THÈSE

En vue de l'obtention du

DOCTORAT DE L'UNIVERSITÉ DE TOULOUSE

Délivré par :

Institut National Polytechnique de Toulouse (INP Toulouse)

Discipline ou spécialité :

Energétique et Transferts

Présentée et soutenue par :

M. DANIEL MEJIA

le mardi 20 mai 2014

Titre :

EFFETS DE LA TEMPERATURE DE PAROI SUR LA REPONSE DE LA FLAMME A DES OSCILLATIONS ACOUSTIQUES

Ecole doctorale :

Mécanique, Energétique, Génie civil, Procédés (MEGeP)

Unité de recherche :

Institut de Mécanique des Fluides de Toulouse (I.M.F.T.)

Directeur(s) de Thèse :

M. RUDY BAZILE

M. LAURENT SELLE

Rapporteurs :

M. FRANCK NICOUD, UNIVERSITE MONTPELLIER 2

Mme FRANÇOISE BAILLOT, UNIVERSITE DE ROUEN

Membre(s) du jury :

Mme DANY ESCUDIE, INSA LYON, Président

M. DANIEL DUROX, ECOLE CENTRALE PARIS, Membre

M. LAURENT SELLE, INP TOULOUSE, Membre

M. RUDY BAZILE, INP TOULOUSE, Membre

A mis viejos.

Acknowledgments

This thesis is the end-product of almost four years of work at the IMFT (Institut de Mécanique des Fluides de Toulouse) laboratory. It is the end-product, but by no means could it contain all the experiences I have had in the past four years. So I would like to take the opportunity now to acknowledge some who have participated, directly and indirectly, in the production of this work.

First, I would like to thank my adviser, Rudy Bazile. I am thankful for his guidance in the development of this work. Most of the work in this thesis was done jointly with Laurent Selle my co-adviser. Undoubtedly, this work would not have come to an end without his help, I really appreciated the fact that he has always believed in me and that he did not lose his mind with all my numerous mistakes. I must say that I am also happy to count him as a friend. I also would like to express my gratitude to Bernard Ferret, for all of his guidance and help, especially in the mechanical conception of the burner. I want to thank Thierry Poinsot for all of his help, constrictive comments and ideas; I wont forget all his help finishing the manuscript (reading and correcting it, several times). I was very lucky to cross paths with this team and I feel really grateful to be able to continue working with them.

Second, I also wish to express my sincere gratitude to my "reporteurs de thèse", Françoise Baillot and Frank Nicoud for having read in such a careful way my work, despite their very busy schedules. I also wish to thank Dany Escudié for agreeing to chair the jury and Daniel Durox for his helpful correction in the last version of the manuscript. The positive comments provided by this jury in respect of my work were very gratifying to me.

My work was certainly made much easier by the staff of the IMFT lab. In particular I will remember Moïse and Sébastien. The time spent with them in "la manip" leave me with really good memories, both in the scientific and human aspect. I cannot forget the rest of the people who always received me with the best disposition when I came with my last minute technical problems: Hervé A., Jean-Marc S, Laurent M., Jean-pierre E., Christophe K., Ruddy S., Charles N., Perre F. and Yannick E., among others. I also thank Catherine and Muriel, they were really nice and helpful during this four years. Finally I would like to thank Forence for all the patience with the administrative procedures, especially considering the fact that I am not and EU resident. I performed this work within the PSC group, it allowed me to meet many interesting people. Thanks to all "les permanents" Pascal F., Eric C., Olivier P. and Franck P. for always being nice and

helpful. Thanks to all the stagiaires, Ph.Ds and post-docs for the engaging discussions during the lunch time. In particular I would like to thank the people whom I shared an office with. I wont forget the first two years in the 315 with Marion, Nico, petit-Jacko and Gigi, just nice memories not much work though haha. Then some fresh blood came to the 315 for the third year: Blaise, Adama and Lucas who, thankfully, talk much less and work more. Then, when I took the bosss chair I had the opportunity to share with Jacko and AnnaFederica Urbano, these last six months were much easier with you guys.

I also want to thank all my friends who made my life in Toulouse so enjoyable: Hanne, Olalla, Amy, Sarah, Emma, Sigve, Andrew, Patt, Mika, Salva and Toño among many many others. I wont forget their amazing present "Helena", which now is a piece of art hanging in my living room and the time when they threw a party for my birthday, party which I did not assist because I was in a very bad-mood, sorry again. I should not forget the US-Ramonville boys, they always put a smile on my face, even when I missed all those goal occasions and finally Carito that from far was always there.

And last but not the least, I want to thank my family, certainly this Ph.D was possible mainly thanks to their support and effort. I am really grateful to be part of such a wonderful family, starting from "los abuelos" Carlos and Fortino who are no longer with us but who left us this wonderful family. Clearly no good results would have come without all the lighted candles and prayers of "mis abuleas" Judith and Dolly and the support of my many aunts and uncles. My education was possible thanks to the support of my "tío Oscar", without it and without his books this thesis wouldnt have been written. At the same time, without the push of "la tía Marta" I certainly wouldnt be here. And how to forget the love of "la tia Genia" who makes me feel what is to have two moms. I also would like to thank my cousins, some of them inspired me to do science, some of them inspire me to travel, some of them inspired me to do sports and some of them inspired me to party and take it easy haha. I wont forget all the help I got from Alejo during my first year in France and Cata during the week of the presentation. Thanks to Toña for bringing the balance to the family and Tatara to bring the balance in my life during this last two years, she is responsible for keeping me from jumping out the window in the hardest moments of this Ph.D. Finally no words can express how grateful I am to my parents, their love is the biggest blessing. I got my character thanks to my mom, her courage and bravery inspired me to never give up. My dad is my biggest hero, he has done more than a normal human being could have done for us to be where we are... I just hope that life is going to give me the opportunity to make it up to both of them.

Gracias.

Abstract

Combustion instabilities, induced by the resonant coupling of acoustics and combustion occur in many practical systems such as domestic boilers, gas turbine and rocket engines. They produce pressure and heat release fluctuations that in some extreme cases can provoke mechanical failure or catastrophic damage. These phenomena have been extensively studied in the past, and the basic driving and coupling mechanisms have already been identified. However, it is well known that most systems behave differently at cold start and in the permanent regime and the coupling between the temperature of the solid material and combustion instabilities still remains unclear. The aim of this thesis is to study this mechanism.

This work presents an experimental investigation of combustion instabilities for a laminar premixed flame stabilized on a slot burner with controlled wall themperature. For certain operating conditions, the system exhibits a combustion instability locked on the Helmholtz mode of the burner. It is shown that this instability can be controlled and even suppressed by changing solely the temperature of the burner rim. A linear stability analysis is used to identify the parameters playing a role in the resonant coupling and retrieves the features observed experimentally. Detailed experimental studies of the different elementary processes involved in the thermo-acoustic coupling are used to evaluate the sensitivity of these parameters to the wall temperature. Finally a theoretical model of unsteady heat transfer from the flame root to the burner-rim and detailed experimental measurements permit to establish the physical mechanism for the temperature dependance on the flame response.

Keywords: *Combustion instability, Flame transfert function, Acoustics, Combustion noise, Flame dynamics, Wall temperature, Unsteady heat transfer, Flame root dynamics.*

Resume

Les instabilités de combustion induites par le couplage combustion-acoustique se produisent dans de nombreux systèmes industriels et domestiques tels que les chaudières, les turbines à gaz et les moteurs de fusée. Ces instabilités se traduisent par des fluctuations de pression et de dégagement de chaleur qui peuvent provoquer une défaillance mécanique ou des dégâts désastreux dans certains cas extrêmes. Ces phénomènes ont été largement étudiés par le passé, et les mécanismes responsables du couplage ont déjà été identifiés. Cependant, il apparaît que la plupart des systèmes se comportent différemment lors du démarrage à froid ou en régime permanent. Le couplage entre la température des parois et les instabilités de combustion reste encore méconnu et n'a pas été étudié en détail jusqu'à présent. Dans le cadre de ces travaux de thèse, on s'intéresse à ce mécanisme.

Ces travaux présentent une étude expérimentale des instabilités de combustion pour une flamme laminaire de pré-mélange stabilisée sur un brûleur à fente. Pour certaines conditions de fonctionnement, le système présente un mode instable autour du mode de Helmholtz du brûleur. Il est démontré que l'instabilité peut être contrôlée, et même supprimée, en changeant uniquement la température de la surface du brûleur. Une analyse de stabilité linéaire est mise en oeuvre afin d'identifier les paramètres jouant un rôle dans la boucle instable, et il est possible de modéliser analytiquement les phénomènes observés expérimentalement. Des études expérimentales détaillées des différents processus élémentaires impliqués dans le couplage thermo-acoustique ont été menées pour évaluer la sensibilité de ces paramètres à la température de la paroi. Enfin un modèle théorique du couplage entre le transfert de chaleur instationnaire à la paroi et le movement du pied de la flamme est proposé. Par ailleurs, d'autres mesures expérimentales ont permis de comprendre les mécanismes physiques responsables de la dépendance de la réponse de la flamme à la température de paroi.

***Mots clés**: Combustion, Thermique parois, Instabilité de combustion, Transfert de chaleur, Dynamique du pied de flamme.*

Contents

Introduction

Our society as we know it today would not be possible without efficient energy generation. Energy generation constitutes one of the major challenges of the new era and comprise electricity generation, industrial processes, transportation and alimentation. Despite the growth of renewable energies, combustion is today, responsible for 90 % of the total energy generate on earth (Sawyer (2009)), and it is likely to remain the main source for a long time.
Combustion systems come in a wide range of scales that goes from huge thermal power stations of 1 GW, to commercial airplane turbofan engines of 100 MW and domestic heat boilers of 10 kW, down to fuel cells of 1 W (*cf.* Fig. 1).

Gaz central power station ∼ 1 GW | Turbofan engine ∼ 100 MW | Domestic boiler ∼ 10 kW | Fuel cell ∼ 1 W

Figure 1: Different scales of thermal power systems.

The main advantages of chemical energy conversion devices is that the raw materials (oil, coal, natural gas, biomass fuels, etc.) have a high energy density and calorific value, are easily stored and may be burned on demand. However, combustion is an exothermic chemical reaction in which products such as CO_2 are inevitable. Pollutants such as NO_x and CO are also produced if the process is not carried out properly. CO_2 emission amplifies the green-house effect (Penner *et al.* (1999)), due to its high absorption and emission of infrared radiations compared to air, the heat coming form the earth surface is trapped in the atmosphere. CO_2 can only be reduced by higher efficiency systems and thermodynamic cycles, so that, less fuel is burnt to produce the same amount of work. NO_x and CO emission can impact the health of plants, animals and humans. Although these emissions can be avoided, they are produced when the reaction zone exceeds determined temperatures. But at the same time high combustion temperature allows increasing system performances.

Among the solutions which can be envisaged to satisfy the progressively more stringent emission regulations for NO_x and CO, one method which is specifically attractive consists on using premixed combustion where the mixing of air and fuel is completed before the reaction zone. Premixed combustion reduces emissions if the mixture is lean (*i.e.* if the proportion of fuel to air is lower than stoichiometry). Formation of NO_x has an exponential dependence on the local temperature and this lean premixing strategy allows: to lower the adiabatic flame temperature in the reaction zone due to the excess of air compared to stoichiometric conditions. Lean-burning processes also releases less CO and unburned hydrocarbons.

Unfortunately, these systems are known to be very likely to develop combustion instabilities (CI). The occurrence of CI is a major problem for the design and operation of many power-generation systems such as gas turbines, aeronautical engines and rocket engines. Combustion dynamics problems are covered in the review proposed by Candel (2002), and in different studies compiled in the book edited by Lieuwen (2012). A document prepared by Culick and Kuentzmann (2006) discusses the many facets of combustion instabilities and combustion oscillations. The book by Poinsot and Veynante (2011) also focuses on combustion instability issues and introduces modern computational methods for predicting these phenomena.

The constructive coupling between acoustic waves and unsteady heat release rate produce CI's, which are responsible for large acoustic pressure levels that may damage system components by inducing structure vibration; heat flux enhancement on ducts linings (the flames may move to unexpected places because of large amplitude flow fluctuations); noise emission induced by the unsteady combustion reaction and global extinction of flames when flow oscillations reach critical threshold values. Figure 2 shows some examples of CI's consequences.

The challenge for understanding and predicting CI lies in the multiplicity of physical phenomena involved in the unstable loop (Culick and Kuentzmann (2006)): acoustics, vortex dynamics, mixing, chemistry, two-phase flows, etc. One of the canonical configurations for the study of CI is the laminar premixed flame, which has been extensively studied (Boyer and Quinard (1990); Baillot *et al.* (1992); Schuller *et al.* (2002); Kornilov *et al.* (2007); Noiray *et al.* (2006); Wang *et al.* (2009)). Recent theoretical developments (Cuquel *et al.* (2011); Blumenthal *et al.* (2013)) propose analytical solutions for the flame response to acoustic perturbation, which is a central element for the prediction of CI.

The ultimate goal of CI studies is to understand the physical mechanisms and anticipate when a combustion chamber will be unstable at the design stage, avoiding the high costs and reducing the time of prototype testing during its development phase. Here we choose the experimental approach to establish the link between theory and experiments, making use of a well controlled generic configuration which represents in a idealized way, the complex geometries found in practice.

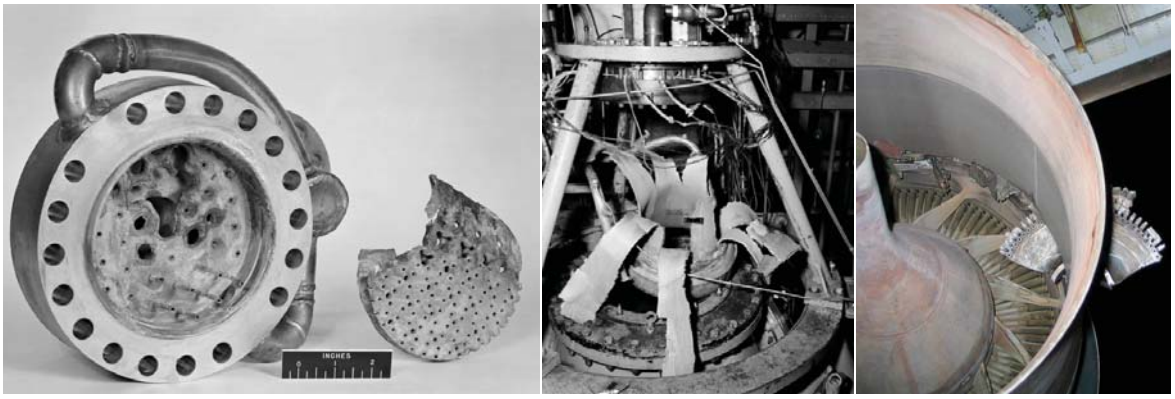

Figure 2: Mechanical damages produced by the occurrence of combustion instabilities. **Left**: burner injectors of a NASA rocked engines, after the flame flashed back from the anchoring point. **Center**: Rocket engines from NASA damaged by explosion on start. **Right**: Turbofan engine after a turbine disc is detached from the opposed engine due to vibrations produce by CI's.

For linear-stability analysis, the flame response is assumed to depend only on the frequency of the incident perturbations, nevertheless its response may depend on many other parameters such as the oscillation amplitude (Noiray *et al.* (2008); Boudy *et al.* (2011); Palies *et al.* (2011)). The present study focuses on the impact of heat transfer on the flame response, based on the experimental observation that most systems behave differently at cold start and in the permanent regime. We therefore investigate the response of a laminar premixed flame stabilized over a slot burner where the temperature of the burner, at the flame anchoring point can be controlled and monitored.

Experimentally CI's can be studied in two different ways: by investigating self-sustained oscillations or by using forced oscillations (Poinsot and Veynante (2011)). Burners may develop self sustained oscillations if the acoustic energy fed into the system, exceeds the dissipation. However, not all systems are naturally unstable and certain conditions should be fulfilled in order for the burner to be naturally unstable. Additionally, this study is limited to only one frequency, which is locked on the Helmholtz mode of the burner. Forced oscillations can be studied by modulating the flow by an external component, permitting an exploration of a wide range of frequencies, but an initially stable flame is necessary. The present study uses both approaches: thanks to the modular design of the burner (*cf.* Fig. 1.1) one can easily change the burner geometry to allow self-sustained combustion oscillations or stable combustion for forced experiments.

The coupling between wall temperature of solid boundaries and CI's has been observed in laboratories but also in industry. Although some studies refer to this phenomena in a indirect way (Rook *et al.* (2002); Preetham and Lieuwen (2004); Altay *et al.* (2009); Kornilov *et al.* (2009); Duchaine *et al.* (2011); Kedia *et al.* (2011); Hong *et al.* (2013) and Cuquel *et al.* (2013)) few of these studies addressed it directly. Figure 3 shows some of

the flames used to study combustion instabilities.

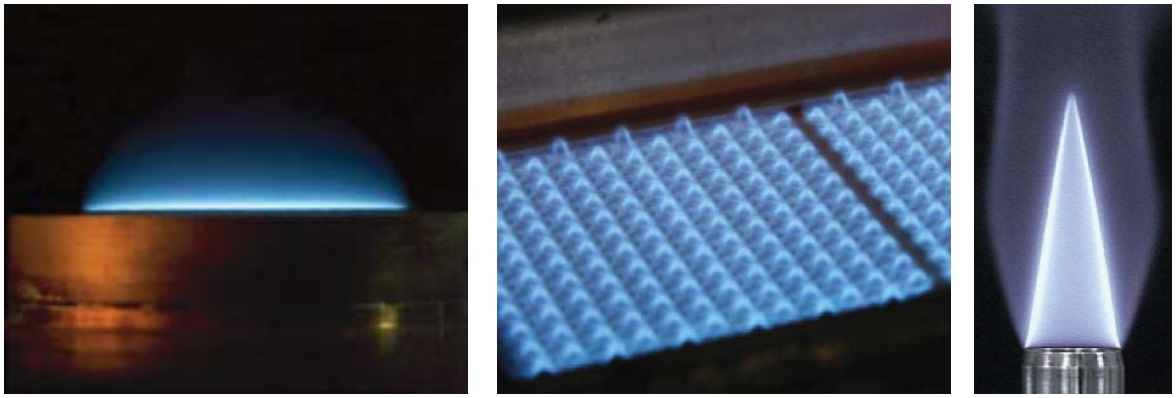

Figure 3: Different types of possibly unstable flames corresponding to their sensitivity to heat transfer. **Left**: planar flame stabilized over a porous media, heat flux burner TU/e (Rook *et al.* (2002)). **Center**: perforated-plate stabilized flame, BOSCH (Kedia *et al.* (2011)). **Right**: Conical flame, EM2C (**?**).

The importance of unsteady heat losses in combustion instabilities has been studied extensively, specially for planar flames stabilized on top of porous media (*e.g.* Rook *et al.* (2002); Rook and de Goey (2003); Schreel *et al.* (2002, 2005)). Refer to de Goey *et al.* (2011) for a review in the current state-of-the-art on premixed planar flames. It has been shown that planar flames (Fig. 3 left) close to a solid boundary can be perturbed in two ways: first, acoustic velocity perturbations produce regular oscillations of the flame stand-off distance with respect to the burner rim; second, these oscillations generate fluctuations of the heat loss to the burner rim, because of changes of the temperature gradient at the solid boundary. This results in an enthalpy wave propagating from the burner to the flame front and the flame dynamics is influenced due to the corresponding flame temperature changes and an associated time lag.

In multidimensional flames, such as the one studied here, heat release rate fluctuations are dominated by flame front fluctuations. On the other hand, for planar flames, heat release rate fluctuations are dominated by heat loss fluctuations to the burner rim. However, the work in two dimensional premixed flames (*e.g.* Altay *et al.* (2009, 2010) and Kedia *et al.* (2011)) has shown that, for low frequencies typically less that 100 Hz, the oscillations of the heat loss rate at the burner rim also plays a critical role and can drive the growth of the perturbations. The flame response to velocity fluctuations at its base takes the form of flame speed oscillations in this region (*cf.* Fig. 4). Flame stand-off distances increase/decrease when the flame-wall interaction strengthens/weakens, impacting the overall dynamics of the heat release. Kedia *et al.* (2011) state, that the main contribution to the phase-lag between the velocity fluctuations and the heat release rate fluctuations, is a convective time lag between the perturbation and the flame root response. The convective lag between the perturbations and the flame tip was found to have a weaker impact

on the heat release rate oscillations for these type of flames.

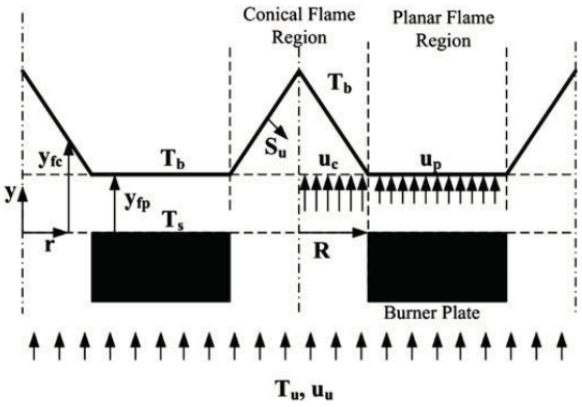

Figure 4: Schematic diagram of the flame surface in perforated-plate stabilized configuration from Altay *et al.* (2009). Here y_{fp} is the flame stand-off distance.

For the configuration of Fig. 4, the burner rim material plays an important role as illustrated by Kedia *et al.* (2011), but this type of flames strongly differs from the one studied here. They deal with a 2D flame stabilized on top of a perforated-plate (*cf.* Fig. 3 center), which has two regions: one planar flame region in contact with the burner plate, and several short conical flames over the injection holes.

For elongated flames (*cf.* Fig. 3 right) the flame dynamics is governed to first order by the stationary flame geometry and the nature of the velocity fluctuation (Ducruix *et al.* (2000); Durox *et al.* (2002); Schuller *et al.* (2003b); Birbaud *et al.* (2006); Cuquel *et al.* (2013)). However, recently Kornilov *et al.* (2007) have shown that for this kind of flames, the flame anchoring point dynamics plays an important role in the flame response to acoustic oscillations, dominated by the heat transfer from the flame to the burner rim (Cuquel *et al.* (2013)). Lee and Lieuwen (2003) identified two sources that contribute to the flame frequency response to velocity fluctuations (Fig. 5):

- One comes from the flame front fluctuations due to flow oscillations impinging on the flame front (which depends mainly on the flame geometry), which we will call **flame front dynamics** from now on.
- And a second one that comes from the oscillation of the anchoring point (which depends mainly on the unsteady heat transfer between the flame root and the burner rim) which we will call **flame root dynamics** from now on.

Although Cuquel *et al.* (2013) aimed to explain the saturation of the phase lag for high frequencies, it highlights the importance of heat transfer between the flame and the burner surface at the anchoring point on the flame dynamics of elongated conical flames.

Figure 3 summarizes the three different types of CI's discussed before. On the left, one can identify the plane flame stabilized over a porous media, where the heat release rate fluctuation is only due to the unsteady heat loss to the burner-rim. In the middle, a

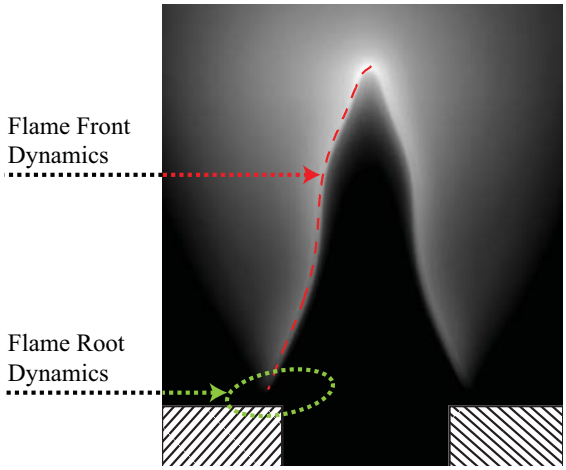

Figure 5: Main mechanisms responsible for the overall flame response.

perforated-plate stabilized flame where the heat release rate fluctuations are mainly due to the unsteady heat loss to the burner-rim but a contribution from the small conical flame surface fluctuation must be take into account. Finally on the right, an elongated conical flame, where the heat release rate fluctuations are mainly due to flame surface fluctuation but a contribution by the flame root fluctuation was identified.

Thesis objectives and contents

This investigation aims to improve the fundamental understanding of combustion dynamics problems. We focus on the understanding of heat transfer to solid boundaries on the flame response. The general organization of the work is presented in Fig. 7. We consider a well controlled configuration where the temperature of the burner at the flame anchoring point can be controlled and monitored to develop systematic experiments, and theoretical analysis to clarify the mechanisms and their coupling.

The manuscript is organized in three parts. In part I, the experimental set-up is presented. Then, the effect of wall temperatures on CI is put in evidence in a well controlled laminar flame experiment where, a self-sustained combustion oscillation is controlled by changes in the temperature of the material at the flame anchoring point. Finally a linear stability analysis is performed in order to identify the parameters susceptible to be affected by the wall temperature and modify the stability of the system.
In Part II, once the parameters have been identified, they will be individually measured through controlled experiments in reacting and non-reacting configurations. For this, the geometry of the burner will be slightly changed in order to have stable combustion for all temperatures of the burner-rim, and the flow will be modulated externally. Here, special attention is put on the sensitivity of these parameters to wall temperature. Subsequently the measured parameters will used in the linear stability model and confronted with the experimental stability map.
Then in part III, once the parameters or mechanisms responsible for modifying the sta-

bility of the system have been identified, we will study the sensitivity of these parameters to the modification of heat transfer to solid boundaries by changes in the burner-rim temperature.

Part I, The burner

The first part is divided in three chapters. In Ch. 1 the experimental setup is presented. It consists of a slot burner with generic features that permits an analysis of fundamental interests. The burner is first described detailing the main components, and the experimental methodology are described; then, diagnostic techniques are presented.

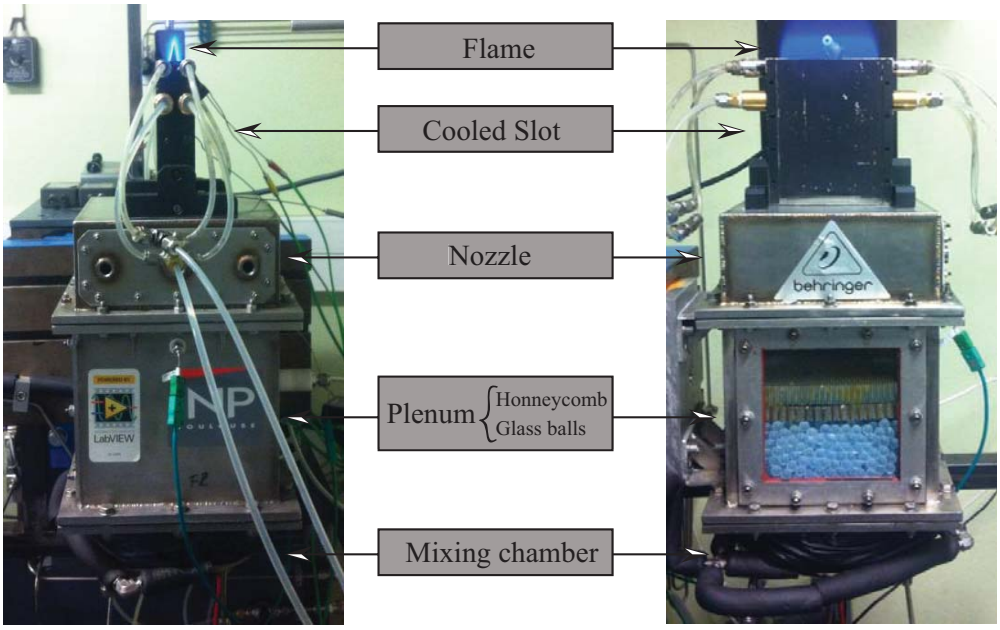

Figure 6: Images of the lateral and frontal view of the slot burner and a schematic longitudinal cut through the front view.

The burner is essentially a flame stabilized on a Helmholtz resonator (Fig. 6). As explained in Durox *et al.* (2002) it typically exhibits instabilities locked on the Helmholtz mode. For a given flame, which has its own response to acoustic perturbations, the stability of the setup depends on the tuning of the Helmholtz frequency and the level of dissipation in the system. Because of its direct impact on both effects, the main parameter controlling the occurrence of instabilities is the heigh of the slot (*cf.* Fig. 1.1). In this study however, an other parameter has been identified: the temperature of the burner rim, T_s. Indeed, for a particular configuration, the flame is unstable when the slot is cold and stable once hot. This behavior will be put in evidence in Ch. 2. Where an experiment is designed to study the coupling between wall-temperature and CI's.

In order to study the role of the slot temperature, T_s, in the combustion instability mechanism, a linear stability analysis can be applied to the burner. Isolating and individually studying the elementary mechanisms of a combustion instability (burner acoustics, combustion dynamics and combustion noise) one can identify which parameters are likely to be affected by the slot temperature, T_s and consequently modify the flame response to acoustic oscillations, which is the objective of Ch. 3.

Part II, Experimental results

This part is divided in four chapters, corresponding to the experimental study of the three elementary mechanisms leading to a combustion instability: burner acoustics; combustion noise and combustion dynamics. An additional chapter is dedicated to the solution of the linear stability system.

Chapter 4 presents the burner acoustic response. We use non-reacting and reacting experiments. The present setup remains at ambient temperature during combustion operation, except in the vicinity of the flame and at the burner rim, which features strong temperature gradients. One may think that the slot temperature, T_s, has a week impact on the burner acoustics, however, tests are performed for different burner-rim temperatures to evaluate the dependency of the burner acoustics to variations on the wall temperature. Two methods are used to characterize the acoustic behavior of the burner: the harmonic response (HR) where a sinusoidal perturbation is send to the burner outlet and the impulse response (IR) where the flow is perturbed by an impulse generated by a loudspeaker placed at the bottom of the plenum.

Combustion noise controls the acoustics feedback process in the CI loop: it is studied in Ch. 5. When combustion is unstable, the flame front motion is accompanied by a high level of noise emission. Acoustic waves are radiated in the whole space and specifically back towards the burner. In order to validate assumptions made in linear stability analysis a validation of the combustion noise theory is performed. The link between the far-field pressure and the unsteady heat release is confirmed experimentally. Likewise, in order to close the linear stability model a good estimation of the flame pinching distance is performed.

Chapter 6 focuses on the experimental determination of the flame response to velocity fluctuations. The flame dynamics constitutes a central element of the resonant feedback which drives CI's. In the case of premixed combustion, the motion of the flame front is generally driven by velocity perturbations impinging on the upstream side of the flame front. This chapter focuses on the influence of the slot temperature on flame dynamics. First, the approach and the experimental setup used to study the combustion dynamics will be presented. Second, the results are presented in the form of a Flame Transfer Function (FTF). Finally, we discuss the velocity fluctuation measurement, through the effect of the reference point location on the final form of the FTF.

Chapter 7 focuses on the determination of the burner stability. The basic mechanisms involved in the coupling were considered separately in the previous chapters, and the parameters needed to complete the linear stability analysis were measured experimentally. Results will be compared to the observations of Ch. 2 to establish the ability of linear stability analysis to predict combustion instabilities and account for other parameters such as wall temperature.

A low order model of the flame dynamics based on the G-equation, in which the principal mechanism affecting the flame response to velocity fluctuations will be exposed as well to clarify the mechanisms responsible for heat release rate fluctuations. Here two types of phenomena are identified (Lee and Lieuwen (2003)) and it is convenient to classify them as: flame front dynamics and flame root dynamics.

Part III, Mechanisms contributing to the flame dynamics

The last part is divided in two chapters focusing on the two contributions to heat release rate fluctuations: flame front dynamics and flame root dynamics.
In Ch. 8 the effects of the slot temperature, T_s, on the flame front dynamics is presented. The study is based on theoretical developments using level-set descriptions to model the flame front kinematic response to flow perturbations (Boyer and Quinard (1990)). Although FTF theoretical approaches are not the subject of this study, a review of the recent results obtained with these developments is of interest to find the mechanisms which could link wall temperature to combustion dynamics.

In Ch. 9, the effect of the slot temperature, T_s, on the flame anchoring point is studied. This study is based on that of Cuquel *et al.* (2013) in which a model for the contribution of the flame base movement to the heat release rate fluctuations is derived. It takes into account unsteady heat losses from the flame base to the burner-rim of the resulting flame wrinkles along the steady flame front. A model for the enthalpy waves traveling between the burner-rim to the flame root is used to derive the flame root displacement transfer function, and its contribution to the global FTF is analyzed.
First a review of the different trends concerning the flame-root dynamics is performed, followed by the description of the mode to describe the flame-root burner rim interaction. Finally the experimental determination of the flame-root dynamics is performed.

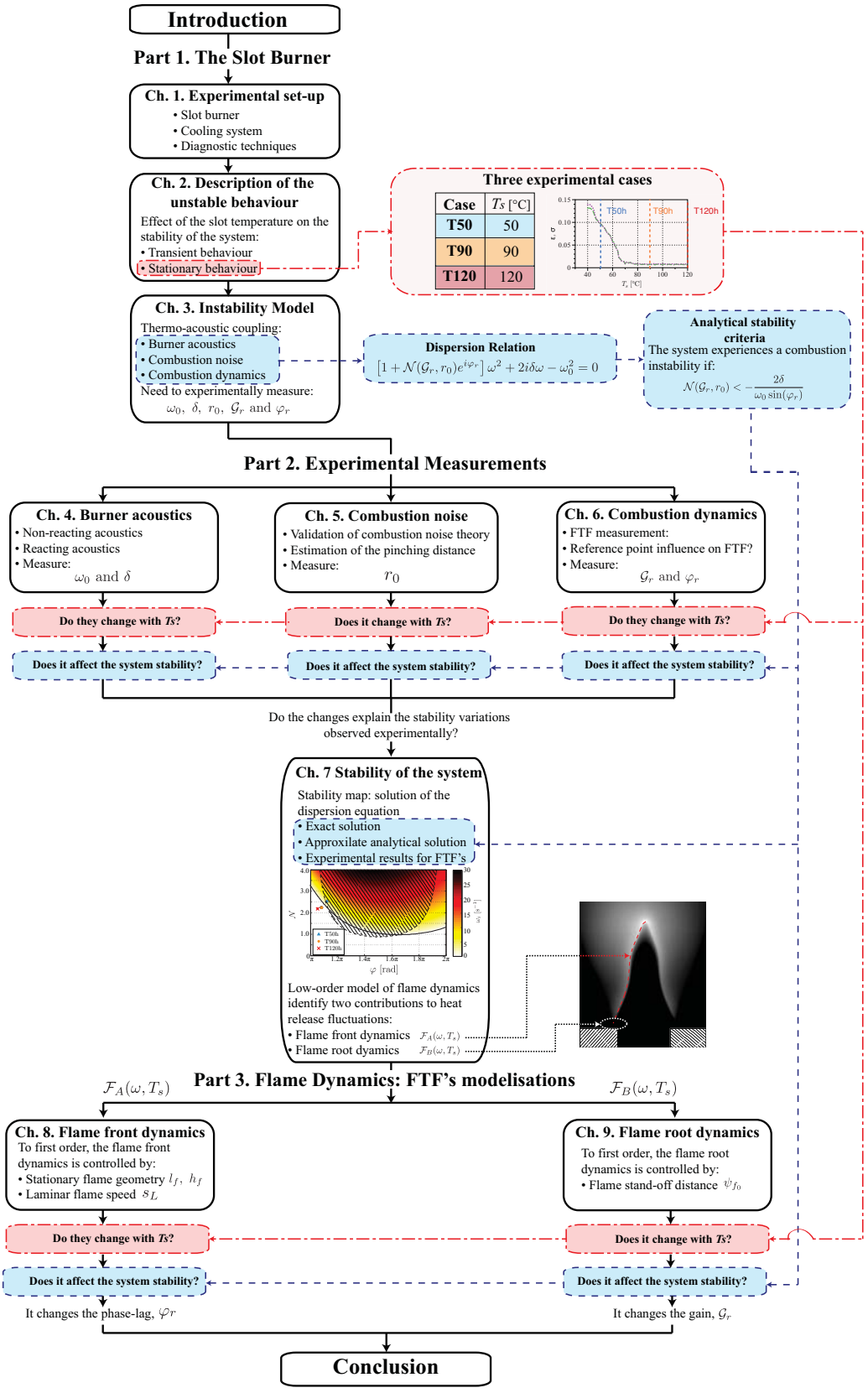

Figure 7: Roadmap and schematic summary of the manuscript.

Nomenclature

Temperature		
T_s	Slot temperature at $y = -1$ mm below burner outlet	[K]
T_2	Slot temperature at $y = -10.5$ mm below burner outlet	[K]
T_3	Slot temperature at the middle of the slot	[K]
T_u	Fresh gases temperature in the slot	[K]
T_h	Burnt gases temperature	[K]
T_p	Fresh gases temperature in the plenum	[K]
T_{wc}	Water temperature close circuit	[K]
T_{wo}	Water temperature open circuit	[K]
T_{ad}	Adiabatic flame temperature	[K]
T_a	Activation temperature	[K]
T_b	Burnt gases temperature	[K]
Velocity		
v	Velocity along y	$[\mathrm{ms}^{-1}]$
v'	Velocity fluctuation	$[\mathrm{ms}^{-1}]$
v^{rms}	RMS velocity fluctuation	$[\mathrm{ms}^{-1}]$
$\tilde{v}$	Amplitude of the velocity fluctuation	$[\mathrm{ms}^{-1}]$
$\bar{v}$	Bulk velocity	$[\mathrm{ms}^{-1}]$
ε	RMS modulation level	
$\mathbf{v}$	Velocity normal to the flame front	$[\mathrm{ms}^{-1}]$
$\mathbf{v}'$	Velocity fluctuation normal to the flame front	$[\mathrm{ms}^{-1}]$
$\mathbf{u}$	Velocity parallel to the flame front	$[\mathrm{ms}^{-1}]$
s_D	Flame speed	$[\mathrm{ms}^{-1}]$
s_L	Laminar flame speed	$[\mathrm{ms}^{-1}]$
$s_{L(\psi_{f0})}$	Flame speed at the flame root	$[\mathrm{ms}^{-1}]$
$s'_{L(\psi_{f0})}$	Flame speed fluctuation at the flame root	$[\mathrm{ms}^{-1}]$
Pressure		
p'_0	Acoustic pressure in the plenum	[Pa]
p'_1	Acoustic pressure at the burner outlet	[Pa]
p'_{M_1}	Acoustic pressure at microphone M_1	[Pa]
Head release		
$\dot{q}$	Heat release rate	[kW]
$\dot{q}'$	Heat release rate fluctuation	[kW]

$\bar{\dot{q}}$	Mean heat release rate	[kW]
$\dot{q}_0$	Steady state Heat release rate	[kW]
Light intensity		
I_{CH^*}	Light intensity emitted by CH^* free radicals	[Volts]
I'_{CH^*}	Light intensity fluctuation emitted by CH^* free radicals	[Volts]
$\bar{I}_{CH^*}$	Mean light intensity emitted by CH^* free radicals	[Volts]
$I_{0\,CH^*}$	Steady satate flame intensity emitted by CH^* free radicals	[Volts]
σ	RMS level of light emission	
Flame geometry		
$\mathcal{A}$	Flame surface	[cm^2]
$\mathcal{A}'$	Flame surface fluctuation	[cm^2]
$\mathcal{A}_0$	Steady state flame surface	[cm^2]
l_f	Flame front length	[mm]
h_f	Flame height	[mm]
w_f	Flame width	[mm]
r	Flame pinching distance	[mm]
r_0	Flame pinching distance at the frequency of the natural instability	[mm]
α	Flame half-tip angle	[°]
ξ	Flame front fluctuation with respect to the stationary flame front	[mm]
ξ_0	Flame front fluctuation at the flame root	[mm]
Ψ_{f_0}	Normalized stand-off distance	
ψ_{f_0}	Stand-off distance	[mm]
δ_f	Flame-front thickness	[mm]
δ_*	Dimensionless flame-front thickness	
Burner geometry		
l_s	Slot length	[mm]
h_s	Slot hight	[mm]
w_s	Slot width	[mm]
S_s	Slot cross section	[cm^2]
l_p	Plenum length	[mm]
h_p	Plenum hight	[mm]
w_p	Plenum width	[mm]
S_p	Plenum cross section	[cm^2]
V_p	Plenum volume	[cm^3]
Frequencies, pulsation frequencies and non-dimensional frequencies		
f_{ex}	Modulation frequency	[Hz]
f_s	Sampling frequency	[Hz]
f_{cam}	Camera sampling frequency	[Hz]
f_0	Natural frequency of the burner	[Hz]
f_r	Resonance frequency of the self-sustained oscillation	[Hz]
f_H	Helmholtz frequency	[Hz]
ω_0	Natural pulsation of the burner	[rad/s]
ω_r	Resonance pulsation	[rad/s]

ω_i	Growth rate	[s^{-1}]
ω_H	Helmholtz pulsation	[rad/s]
ω_{nr}	Pulsation of the system in a non-reacting case	[rad/s]
$\omega_{nr\Re}$	Real part of the pulsation of the system in a non-reacting case	[rad/s]
ω_h	Pulsation of the system in a reacting case	[rad/s]
ω_*	Reduced pulsation	
κ_*	Reduced wave number	
$\hat{\omega}$	Reduced pulsation based on the thermal diffusion time scale	
λ_{ac}	Acoustic wavelength	[m]
λ_c	Convective wavelength	[m]
Damping coefficient		
δ	Damping coefficient in a non-reacting case	[s^{-1}]
δ_h	Damping coefficient in a reacting case	[s^{-1}]
δ_f	Damping coefficient associated to the flame	[s^{-1}]
Time delay		
τ	Time delay between v and I	[s]
τ_{ac}	Acoustic time delay	[s]
τ_{M_1}	Acoustic time delay from the acoustic monopole to M_1	[s]
τ_{r_0}	Acoustic time delay from the acoustic monopole to burner outlet	[s]
τ_f	Convective time delay for enthalpy oscillation to propagates form the burner rim to the flame base	[s]
Transfert functions		
$\mathcal{F}$	Flame transfer function (FTF)	
$\mathcal{V}$	Velocity fluctuation transfer function (VTF)	
$\mathcal{F}_c$	Corrected FTF	
$\mathcal{F}_A$	Contribution of the flame-front fluctuation to the FTF	
$\mathcal{F}_B$	Contribution of the flame-root fluctuation to the FTF	
Ξ	Flame-root transfert function (flame root TF)	
$\mathcal{S}$	Flame speed transfer function at the flame base	
n	Magnitude of the flame response	
$\mathcal{K}$	Combustion acoustics interaction coefficient	
$\mathcal{G}$	FTF gain	
$\mathcal{G}_0$	FTF gain at the natural pulsation of the burner	
$\mathcal{G}_r$	FTF gain at the pulsation of the self-sustained oscillation	
$\mathcal{G}_v$	VTF gain	
$\mathcal{G}_c$	FTF corrected gain	
$\mathcal{G}_f$	Flame root TF function gain	
φ	FTF phase lag	[rad]
φ_v	VTF phase lag	[rad]
φ_c	FTF corrected phase lag	[rad]
φ_f	Flame root TF phase	[rad]
φ_s	Phase between the unsteady heat flux at the burner rim and flame root temperature fluctuation	[rad]

Combustion		
Φ	Equivalence ratio	
s	Stochiometric ratio	
Y_f	Fuel mass fraction	
Δh_f^0	Enthalpy of formation	$[\mathrm{Jkg^{-1}K^{-1}}]$
$\varkappa$	Calibration coefficient of the PM	$[\mathrm{m^3V^{-1}s^{-1}}]$
Spectral analysis		
$\mathcal{S}_{vv}$	Power spectrum of the velocity signal	
$\mathcal{S}_{vq}$	Cross power spectrum between the velocity signal and the heat release signal	
$\mathcal{S}_{ss}$	Power spectrum of the speaker signal	
$\mathcal{S}_{vs}$	Cross power spectrum between the velocity signal and the speaker signal	
$\mathcal{S}_{v\xi_0}$	Cross power spectrum between the velocity signal and the flame root fluctuation	
Constants		
c_p	Specific heat at constant pressure	$[\mathrm{Jkg^{-1}K^{-1}}]$
c_v	Specific heat at constant volume	$[\mathrm{Jkg^{-1}K^{-1}}]$
γ	Ratio of specific heats	
r	Perfect gas constant	$[\mathrm{Jkg^{-1}K^{-1}}]$
Fluid properties		
P_u	Pressure in the plenum	[bars]
ρ_{air}	Density of air	$[\mathrm{kg/m^3}]$
ρ_{CH_4}	Density of methane	$[\mathrm{kg/m^3}]$
ρ_u	Density of fresh gases mixture	$[\mathrm{kg/m^3}]$
ρ_b	Density of burnt gases	$[\mathrm{kg/m^3}]$
k_{air}	Air thermal conductivity	$[\mathrm{Wm^{-1}K^{-1}}]$
k_{CH_4}	Methane thermal conductivity	$[\mathrm{Wm^{-1}K^{-1}}]$
k_u	Fresh gases mixture thermal conductivity	$[\mathrm{Wm^{-1}K^{-1}}]$
ν_{air}	Air kinetic viscosity	$[\mathrm{m^2s^{-1}}]$
ν_{CH_4}	Methane kinetic viscosity	$[\mathrm{m^2s^{-1}}]$
ν_u	Fresh gases mixture kinetic viscosity	$[\mathrm{m^2s^{-1}}]$
c	Sound speed	$[\mathrm{ms^{-1}}]$
E	Density ratio between the fresh and burnt gases	$[\mathrm{kg/m^3}]$
Numbers		
Re	Reynolds number	
$\mathrm{M_a}$	Mach number	
Le	Lewis number	
Ze	Zeldovich number	
$\mathcal{H}$	Helmholtz number	
Abreviations		
CI	Combustion instability	

TF	Transfer Function
FTF	Flame Transfer Function
VTF	Velocity Fluctuation Transfer Function
SPL	Sound pressure level
HR	Harmonic response
IR	Impulse response
M_0	Microphone at the plenum
M_1	Microphone outside the plenum
HW	Hot-wire probe
PM	Photomultiplier
ODE	Ordinary differential equation

Part I

The burner

Chapter 1

Experimental setup

The experimental setup used to study the combustion instabilities is presented in this chapter. It consists of a slot burner with generic features that permit an analysis of fundamental interest. The burner is first described detailing the main components, and the experimental methodology are described; then, diagnostic techniques are presented.

1.1 Slot burner

This experimental setup is similar to that of Selle *et al.* (2011): it consists of a slot burner with a laminar premixed methane/air flame stabilized at the burner outlet (*cf.* Fig. 1.1). The four main components are: a mixing chamber, a plenum, a convergent nozzle and a rectangular-cross-section slot with a height h_s.

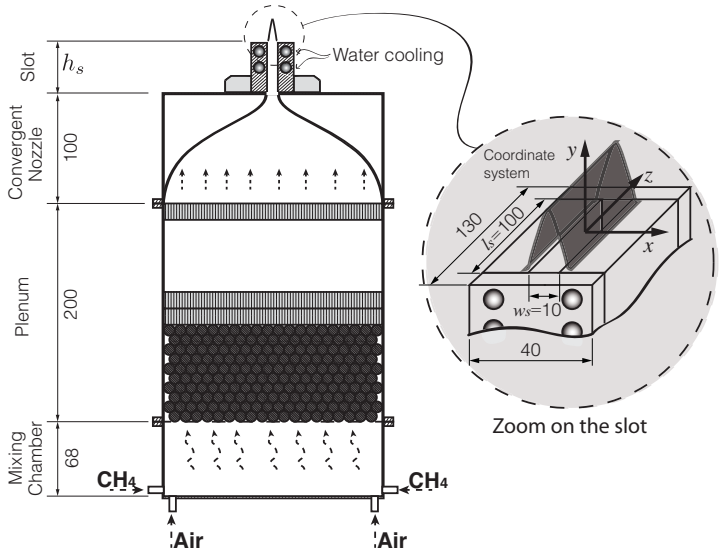

Figure 1.1: Longitudinal cut through the burner, which consists of four main components: the mixing chamber, the plenum, the nozzle and the rectangular slot. A zoom is performed in the rectangular slot and the the coordinate system $(0, x, y, z)$ is introduced.

The flow rates of air and methane are controlled and measured with individual mass-flow meters. The reactants are injected at the bottom of the mixing chamber in a cross-

flow configuration to maximize mixing. The flow is then laminarized in the plenum by an array of small glass balls and three honeycomb panels. Finally, it passes through the converging nozzle and the slot, which has a rectangular cross-section of width $w_s = 10$ mm and length $l_s = 100$ mm.
The massflow rates of air, $\dot{m}_{air}$, and methane, $\dot{m}_{CH_4}$, are controlled and measured electronically by homemade LabVIEW program. The electronic signals are delivered thought a PCI card to a PC. Bulk temperature, T_u, and plenum pressure, P_u, are measured in the plenum chamber, and $\dot{m}_{air}$ and $\dot{m}_{CH_4}$ are calculated in order to impose a bulk velocity, $\bar{v}$, and equivalence ratio, Φ.

$$\dot{m}_{CH_4} = \rho_u \, S_s \, \bar{v} \, Y_F \tag{1.1}$$
$$\dot{m}_{air} = \rho_u \, S_s \, \bar{v} \, (1 - Y_F) \tag{1.2}$$

where, S_s is the slot cross section, ρ_u is the density of the mixture and depends on fresh gases temperature, T_u and the pressure at the plenum, P_u. Y_F is the fuel mass fraction which in Poinsot and Veynante (2011) is given by:

$$Y_F = \frac{1}{1 + (1 + 3.76 W_{N_2}/W_{O_2}) s/\Phi} \, , \tag{1.3}$$

where s is the stoichiometric ratio, W_{N_2} and W_{O_2} are the molecular weight of nitrogen and oxygen respectively. The Bulk velocity, $\bar{u}$, and the equivalence ratio, Φ, can be set respectively between $1.5 - 1.9$ ms^{-1} and $0.7 - 1.3$ allowing a wide range of flame configurations. The equivalent thermal power output is between 3 and 7 kW for the two limit cases. The Burner supply chain is displayed in Fig. 1.2. Filtered dry air is

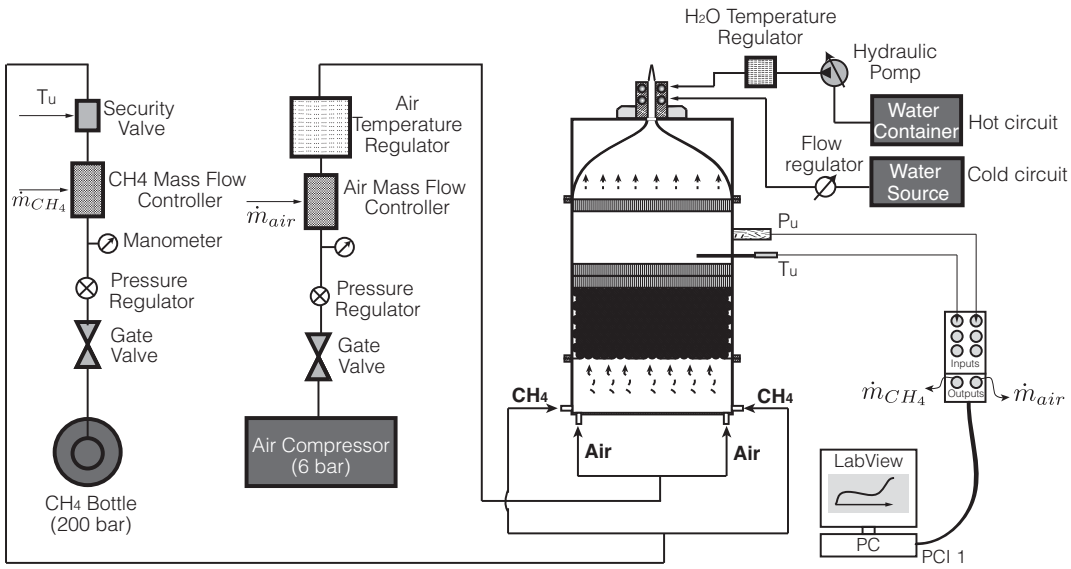

Figure 1.2: Burner supply chain.

provided by the laboratory network at a pressure of 6 bar and ambient temperature. A G20 methane bottle delivers the gas at a pressure of about 200 bar and is stored 50 m away from the burner.

1.2 Cooling system

In order to control the temperature of the burner rim, the long sides of the slot are water-cooled by two pairs of cylindrical passages (*cf.* Fig. 1.3) with a 5 mm cross-section, centered 7 mm and 21 mm below the burner rim, *i.e.* at $x = \pm 12.5$ mm, $y = \pm -7$ mm and $y = \pm -21$ mm in the reference coordinates of Fig. 1.1.

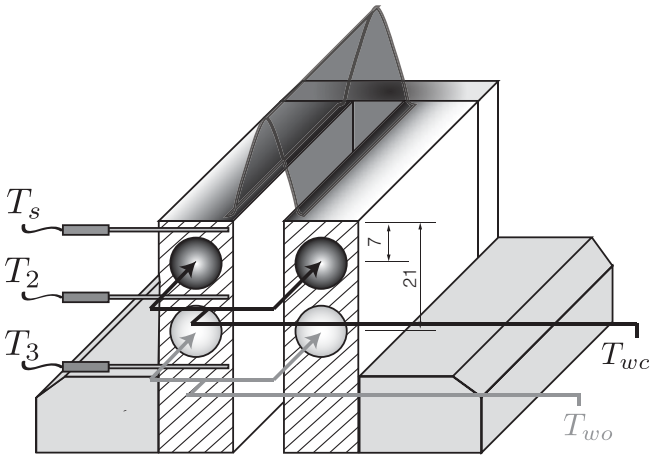

Figure 1.3: Cooling system, two separated circuits.

The upper circuit, ($y = \pm -7$ mm), is a closed circuit, fed by a thermostatic bench. The water temperature, T_{wc}, is controlled and can be set between 1 and 99 °C with a mass flow rate up to 1 min^{-1}. The lower circuit, ($y = \pm -21$ mm), is an open circuit, fed by the laboratory water network. Water is at ambient temperature, T_{wo}, with a mass flow rate up to 5 $\text{kg}\,\text{min}^{-1}$.
This dual channel system allows to control the burner rim temperature over a wide range, going from 40 to 150 °C, while maintaining the lower part of the slot and the plenum at ambient conditions during the experiments. This setup allows a minimal preheating of the fresh gases in the slot.

Three K-type thermocouples are available to monitor the temperature of the slot. The first one, placed 1 mm below the burner outlet ($x = -6$ mm, $y = -1$ mm and $z = 0$ mm), gives the temperature of the burner rim, T_s, as close as possible to the flame anchoring point. The second one reads T_2, is placed between the two channels ($x = -6$ mm, $y = -14$ mm and $z = 0$ mm). The third one T_3, is located in the middle of the slot ($x = -6$ mm, $y = -35$ mm and $z = 0$ mm) and monitors the heat flow from the upper part to the lower part of the slot.

1.3 Experimental methodology

Experimentally, combustion instabilities can be approached in two different ways, self-sustained oscillations (Ducruix *et al.* (2000), Durox *et al.* (2002), Schuller *et al.* (2003a) and Noiray *et al.* (2006)) or forced oscillations (Schreel *et al.* (2002), Kornilov *et al.* (2007), Birbaud *et al.* (2007a), Karimi *et al.* (2009) and Cuquel *et al.* (2013)).
Self-sustained oscillations occur when there is a constructive coupling between the flame and the acoustic eigen modes of the burner. These oscillations may develop in a combustor when certain instability criteria are fulfilled (*cf.* Ch. 3). The study of these systems is usually limited to one frequency for a burner with fixed geometry, or a few frequencies if the burner has variable geometry.
On the other hand, for forced oscillations, the flow is modulated by an external component, usually a loudspeaker. The flow can be excited over a wide range of frequencies and amplitudes. However an initially stable flame is necessary.
Under certain conditions described in Ch. 2 the burner presented in Fig. 1.1 can be either unstable or stable. Consequently, both approaches will be addressed in this study. The self-sustained oscillation method will be exploited in Ch. 2, in order to highlight the physical phenomena that will be addressed in this study, while the forced approach will be adopted in Chs. 4 to 9 to investigate the mechanisms that lead to the particular burner behavior presented in Ch. 2.

1.3.1 Flame stabilization

From observations that will be presented in Ch. 2 we can advance that the burner presented in Fig. 1.1 exhibits instabilities locked on the Helmholtz mode of the cavity (Durox *et al.* (2002) and Schuller *et al.* (2003a)) . For a given flame, which has its own response to acoustic perturbations, the stability of the setup depends on the Helmholtz frequency and the level of dissipation in the system. Because of its direct impact on both effects (Noiray *et al.* (2007)), the main parameter controlling the occurrence of instabilities is the slot height[1], h_s. In this study, however, an other parameter controlling instabilities has been identified: temperature, T_s, of the burner rim. Indeed, for a slot height $h_s = 70$ mm, the flame is unstable when the slot is cold and stable once hot (*cf.* Ch. 2).
In order to able to force the flame it is necessary to have a stable configuration for all temperatures, for this, it is sufficient to increase the height of the slot to $h_s = 150$ mm. Indeed, the resulting decrease in the Helmholtz frequency brings the configuration to an an unconditionally stable region.

Figure 1.4 present the stability map of the two burners used in this study. The stable configurations are represented by circles, the big star represents the unstable configuration, and the little star corresponds to the slightly unstable configuration. Stable regimes correspond to steady mode of burning characterized by a low level of noise emission, a quiet burning process with the flame in a triangular steady shape. Unstable regimes

[1] Here we neglect the effect of the velocity profile modification on the stability of the system.

lead to an oscillatory movement of finite amplitude. When the system operates in this regime, a coupling between the unsteady combustion and burner acoustic occurs. The flame periodically stretches and recoils. This process is accompaigned by a high intensity noise. B07 and B15 are the notations corresponding to the burner with a slot height of $h_s = 70$ and 150 mm respectively. Burner B07 can be either stable or unstable, depending on the reference temperature, T_s, while burner B15 is always stable.

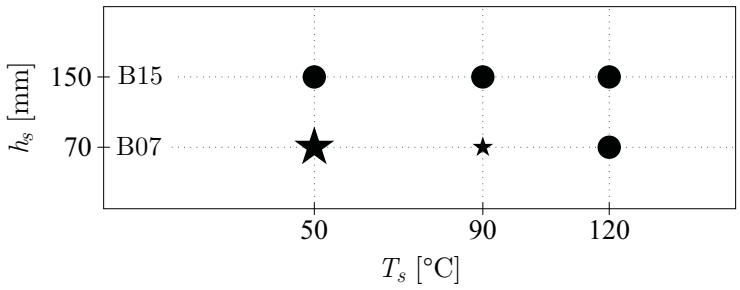

Figure 1.4: Burner stability map: stable configurations (●); unstable configuration (★); and slightly unstable configuration (⋆)

Thanks to the modular conception of the burner, one can easily pass from the burner B07 to B15 and vice-versa by changing the slot. Both slots have exactly the same characteristics in terms of cooling and instrumentation. The cooling system and instrumentation are presented in Fig. 1.5. T_s is placed 1 mm below the burner outlet, T_2, is placed between the two channels and T_3, and is located in the middle of the slot as in the original configuration.

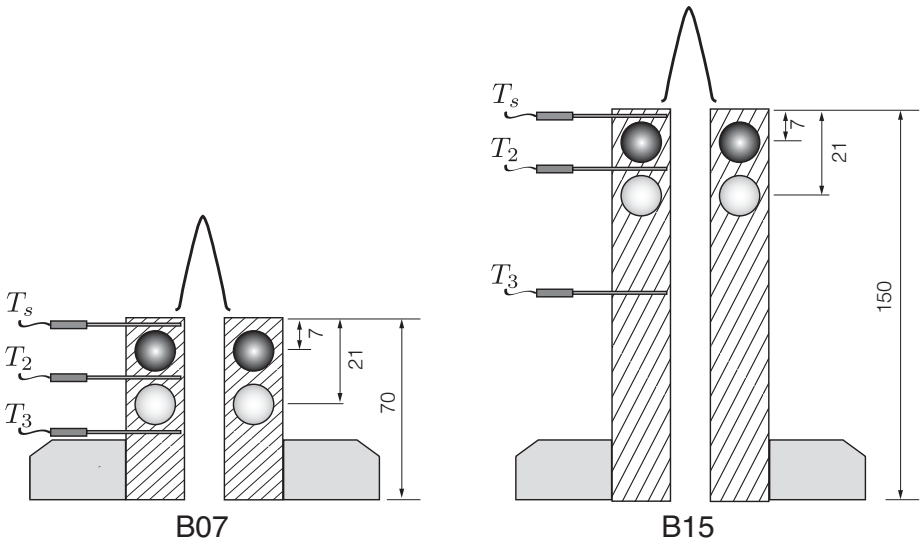

Figure 1.5: Two different slots used in the slot burner. The B07 is a 70 mm high slot that exhibits self-sustained oscillations under certain conditions while the B15 is a 150 mm high slot that is always stable.

1.3.2 Nomenclature for the experiments

Experimental measurements were performed under reacting and non-reacting conditions. In order to reach comparable values of T_s under both conditions, in reacting cases, water from the cooling system is used to cool the walls, whereas, in the non-reacting cases water is used to heat the walls.
In all cases, T_s is considered as the control parameter. For example: T50c, indicates that the test was performed at a burner rim temperature of $T_s = 50$ °C. The subscript "c" and "h" indicate non-reacting and reacting conditions, respectively. Table 1.1 summarises the different experiments performed in this study and the configuration required for the cooling system in order to reach the target burner rim temperature.

Table 1.1: Nomenclature for the experiments

Test	Name	Temperature [°C]				
		T_{wc}	T_{wo}	T_s	T_2	T_3
Non-reacting	T50c	55	20	50	34	20
	T90c	95	20	90	75	21
Reacting	T50h	5	20	50	23	20
	T90h	50	20	90	58	21
	T120h	90	20	120	80	23

Under non-reacting conditions values of T_s larger than 100 °C can not be reached due to the limitation on the water temperature, T_{wc}, in the upper circuit. The burner rim temperature for the reference cases (50, 90 and 120 °C) were carefully chosen according to the observations in Ch. 2.

1.4 Diagnostic techniques

In order to study combustion instabilities the experimental setup of Fig. 1.1 is equipped with a set of diagnostics presented in Fig. 1.6:

1. The flow velocity upstream of the slot outlet is recorded by hot-wire probe.

2. Free radicals CH^* chemiluminescense emited by the flame are detected by means of a photomultiplier.

3. The acoustic pressure inside the plenum and the noise emitted by unsteady combustion are measured with microphones.

4. Temperatures of the slot, water circuits and fresh gases, are measured with K-type thermocouples.

The flow can be modulated by fitting a sealed loudspeaker at the button of the mixing chamber. The flame geometry and movement are monitored by a pco.dimax high speed camera at a rate up to 3000 fps.

Data acquisition is piloted by a single homemade LabVIEW program. Velocity, heat release rate and acoustic pressure signals are recorded and digitalized thanks to a 32 bit PCI analog-to-digital board at a frequency of $f_s = 20$ kHz. The loudspeaker and high-speed camera activity are recorded and monitored by the same board and digitalized at the same frequency f_s. Temperature signals are recorded and digitalized by a 12 bit USB module at a frequency of 2 Hz. In addition, two signal generators are used to drive the loudspeaker and trigger the high-speed camera. The signals are generated by two LabVIEW signal generators at a frequency of 10 kHz and sent to the amplifier and camera through the same analog-to-digital PCI board used to sample the measurements.

1.4.1 Velocity measurements

A CTA (Constant Temperature Anemometry) system is used to measure the axial velocity in the slot. The hot-wire probe, labeled HW, is located 55 mm upstream of the slot outlet ($x = 0$ mm, $y = -55$ mm and $z = 0$ mm) (*cf.* Fig.1.6). Assuming a flat velocity profile at the slot intet. Hot-wire probes are a widely used for the combustion instabilities, (Noiray (2007), Kornilov *et al.* (2009) and Palies *et al.* (2011)).
The CTA delivers a voltage to the data acquisition system function of the flow velocity. In order to determine the flow velocity in [ms^{-1}] a calibration is needed. This calibration is done with an automatic probe calibrator, which blows air at a known velocity v and gives a voltage E to establish the relation $v = f(E)$.

Hot-wire temperature correction

A well-know source of error, measuring velocity using hot-wire anemometry, is the change of hot-wire calibration due to change in flow temperature. As explained in section 1.2 experiments will be performed at different slot temperatures, so, the flow temperature in the slot is susceptible to small but not negligible changes: an accurate correction technique is then necessary. The correction technique used in this study is based on that of Hultmark and Smits (2010), which as been shown to have excellent results in the range of flow temperatures study here.

In the usual hot-wire procedure the velocity v is found as a function of the voltage E delivered by the CTA. The calibration is done so that:

$$\frac{v}{\nu} = f\left(\frac{E^2}{k\Delta T}\right) \tag{1.4}$$

where ν and k are respectively the viscosity and thermal conductivity of the flow, $\Delta T = T_{wc} - T_u$ is the difference between the wire temperature, T_w, and the temperature of the

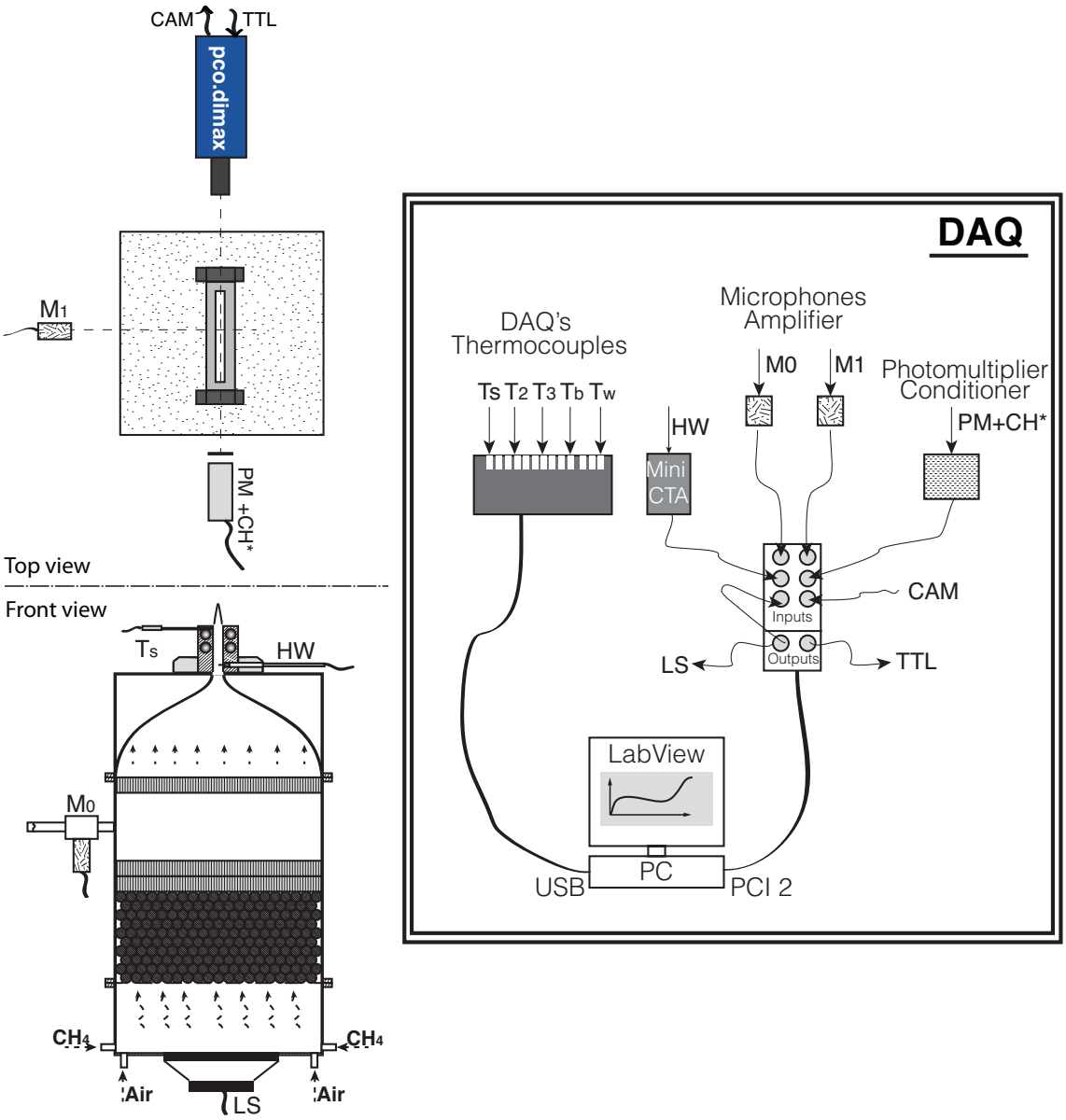

Figure 1.6: Diagnostic techniques: M_0 and M_1: 1/2" microphones. PM + CH*: Photomultiplier equipped with CH* filter. HW: Hot wire. T_s: K-type thermocouple. DAQ: Data acquisition system. LS: loudspeaker. PCO DiMAX: High-speed camera.

flow, T_u. It is then possible to find v, the true velocity over the wire, if ν and k are know as a function of the temperature. The viscosity can be found using the Sutherland law (Sutherland (1893)), and the thermal conductivity of the flow can be found using the correlation given by Kannuluik and Carman (1951).

Figure. 1.11a, shows the effect of the flow temperature on the velocity measurements.

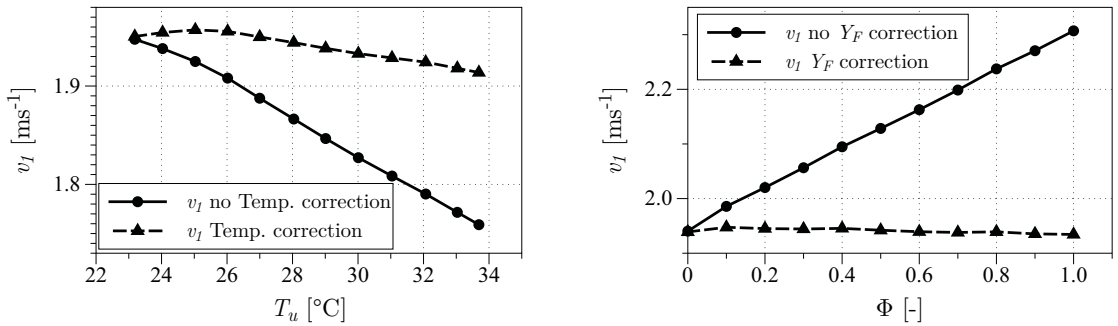

(a) Velocity measured 2 mm downstream of the slot outlet, function of the flow temperature, T_u, for a fixed bulk velocity, $\bar{v} = 1.6$ ms^{-1}, without temperature correction (—●—); with temperature correction (-▲-) .

(b) Velocity measured 2 mm downstream of the slot outlet, function of the equivalence ratio, Φ, for a fixed bulk velocity ,$\bar{v} = 1.6$ ms^{-1}, without fuel fraction correction (—●—) ; with fuel fraction correction (-▲-).

Figure 1.7: Velocity measurements correction

The velocity measured at 20 mm downstream the slot outlet ($y = -20$ mm) is plotted against the flow temperature, T_u, while keeping the bulk velocity constant at $\bar{v} = 1.6$ ms^{-1} in a non reacting configuration. If no temperature correction is applied, an under estimation of almost 10 % is induced in the measurement, due to the effect of the temperature on the fluid properties of the flow. When the temperature correction is applied the error is reduced to less than 2 %.

Hot-wire fuel-mass fraction correction

Another source of error comes from the fact that the the hot-wire is calibrated in air, even though, is used in a CH_4-air mixture. The impossibility to calibrate the hot-wire on a mixture of CH_4 and air calls for an additional correction technique. It consists in calculating the viscosity, ν_u, and thermal conductivity, k_u, of the mix (function of the fuel mass fraction, Y_F) and use them as inputs in the procedure described for the temperature correction. The fuel mass fraction is calculated with equation Eq. 1.3. Then, the gas

properties of the mixture are calculated with:

$$\nu_u = \sum_{k=1}^{n} \nu_k Y_k = \nu_{CH_4} Y_F + \nu_{air}(1 - Y_F) \tag{1.5}$$

$$k_u = \sum_{k=1}^{n} k_k Y_k = k_{CH_4} Y_F + k_{air}(1 - Y_F) \tag{1.6}$$

where ν_u and k_u are at the same time function of the flow temperature, T_u. ν_u is calculated with the Sutherland law for the two species (CH_4 and air). Table 1.2 summarizes the values of the coefficients used in the Sutherland law to calculate the viscosity. Likewise, k_u is calculated with the correlations given by Kannuluik and Carman (1951) and Assael *et al.* (1990) for air and methane respectively. Finally, the hot-wire correction that takes into account the changes in temperature and gas properties of the CH_4-air mixture reads:

$$\frac{v}{\nu_u} = f\left(\frac{E^2}{k_u \Delta T}\right) , \tag{1.7}$$

Figure 1.11b shows the effect of the fuel mass fraction correction on the velocity measurements. The velocity measured at 20 mm downstream the slot outlet ($y = -20$ mm) is plotted against the equivalence ratio Φ while keeping the bulk velocity constant at $\bar{v} = 1.6$ ms^{-1} in a T50c non reacting configuration. For a mixture with $\Phi = 1$, if no correction is applied, an over estimation of 19 % is seen in the measurements. This error is reduced to less than 0.3 % when the change on the fluid properties of the mixture, (ν_u and k_u), is taken into account applying the fuel mass fraction correction of Eq. 1.7.

Table 1.2: Sutherland Constants

Law	Gaz	Constants		
		$T_{ref}[K]$	μ_{ref} [kg/(ms)]	S [K]
$\nu = \frac{\mu_{ref}}{\rho_u}\left(\frac{T}{T_{ref}}\right)^{3/2}\frac{T_{ref}+S}{T+S}$	Air	273.15	$17.16e-06$	110.4
	CH_4	273.15	$12.01e-06$	197.8

1.4.2 Heat release measurement

The heat release rate is determined by a photomultiplier labeled PM. It is placed 400 mm away from the flame, facing the flame longitudinal axis ($x = 0$ mm, $y = 10$ mm and $z = 400$ mm) (*cf.* Fig. 1.6). The PM is equipped with a narrow-band filter centered on a wavelength $\lambda = 430$ nm, this filter only transmits spontaneous emission of CH^* radicals presents in the flame front to the PM. These spontaneous emissions of free CH^* radicals have been shown to be proportional to the heat release rate Price *et al.* (1968), Strahle

(1978), Vagelopoulos and Jonathan (2005) and Schuller *et al.* (2002). The current delivered by the PM is proportional to the photons captured coming from the reaction zone in the flame. This current is then converted into voltage and digitalized through the data acquisitions system.

At a fixed equivalence ratio, Φ, and assuming a lean premixed flame where all the fuel is consumed in the flame front, the heat release rate, $\dot{q}$, will be proportional to the light intensity, I_{CH^*} if the relation, I_{CH^*} vs. $\bar{v}$, follows a linear evolution. Figure 1.8(a) shows this relation, the light intensity, I_{CH^*}, versus the bulk velocity, $\bar{v}$. A linear fit is in excellent agreement with the data which extended pass close to the origine. Therefore, we can use a proportionality relation between the flame heat release rate fluctuations, $\dot{q}'$, and the velocity fluctuations, v'.

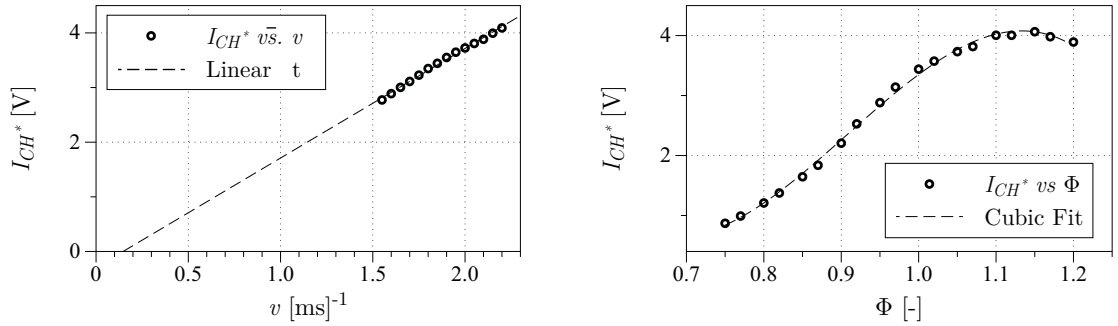

(a) Free radicals CH* chemiluminescence radiated by the flame, I_{CH^*}, function of the bulk velocity, $\bar{v}$, for a fixed equivalence ratio of $\Phi = 0.95$. Data (○); linear fit to the data (----).

(b) Free radicals CH* chemiluminescence radiated by the flame, I_{CH^*}, function of the equivalence ratio, Φ, for a fixed bulk velocity of $\bar{v} = 1.6$ ms^{-1}. Data (○); cubic fit to the data (----).

Figure 1.8: Heat release rate measurements

Figifure 1.8(b) shows the evolution of I_{CH^*} versus the equivalence ratio, Φ, for a fixed mass flow rate. The release of CH* radicals strongly depends on the mix composition in a non linear way, specially for rich flames, (*e.g.* $\Phi > 1$), confirming the conclusion of Schuller (2003) in which variations of the light emission of the flame due to equivalence ratio fluctuations are harder to study than variations of flame light emission induced by velocity fluctuations.

1.4.3 Acoustic pressure measurements

Two microphones M_0 and M_1 are available to monitor the pressure fluctuations in the plenum, p'_0, and the external pressure, p'_{M1} respectively. M_0 is located in the middle of the plenum, connected to a 20 m waveguide that eliminates reflected waves. M_1 is located

300 mm away from the slot outlet facing the lateral side of the flame (*cf.* Fig.1.6) .

1.4.4 Flow modulation system

For forced experiments the bottom of the burner can be replaced by a 13 mm diameter loudspeaker (*cf.* Fig. 1.9) to impose acoustic velocity fluctuations in the plenum that propagate towards the slot outlet.

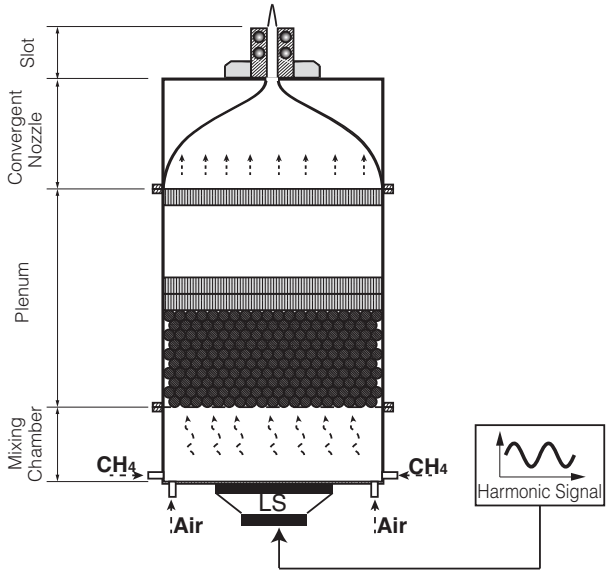

Figure 1.9: Schematic representation of the flow modulation system.

A LabVIEW signal generator program was designed to drive the loudspeaker and automatically sweep the forcing frequency and amplitude. The program generates an harmonic signal sampled at a frequency of $f_{ls} = 10$ kHz that is sent to an amplifier and to the loudspeaker labeled LS in Fig. 1.6. The signal is 8 s long, it has an exponential growth during the first 2 s in order to avoid flow velocity peaks that could blow-off the flame or produce flashbacks. Likewise, the last second is an exponential decay. Therefore, the usable signal sent to the loudspeaker is 5 s long. The signal sent to the amplifier and to the loudspeaker can be described by:

$$s = (1 - e^{-2t})(1 - e^{-4(8-t)}) \sin(\omega_{ex} t) \tag{1.8}$$

here $\omega_{ex} = 2\pi f_{ex}$, where f_{ex} is the excitation frequency. Figure 1.10 shows an example of the signal sent from the LabVIEW signal generator to the amplifier.

Level of modulation

The modulation systems allows rms velocity fluctuations up to 20 % of the mean value in a frequency range of $[10, 300]$ Hz. Beyond $f_{ex} = 300$ Hz this specific flame is not sensitive

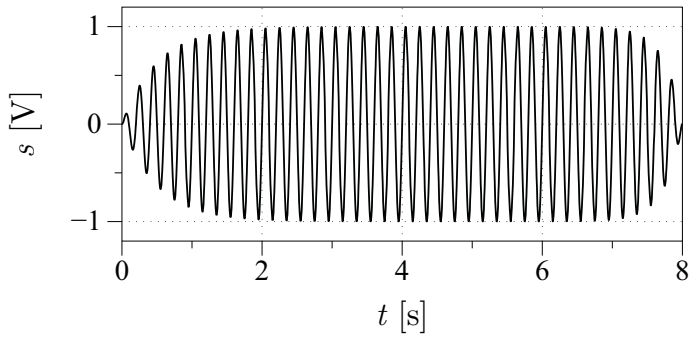

Figure 1.10: Example of the signal sent from the LabVIEW signal generator to the amplifier with an amplitude of $a = 1$ Volts and frequency of $f_{ex} = 5$ Hz.

to acoustic disturbances. This study focuses on linear flame dynamics, as mentioned in the introduction, therefore, the modulation level must be carefully calibrated. First of all, it must be large enough to have a good signal-to-noise ratio. Second of all, it must remain in the linear regime for the flame response.

At this moment it is necessary to define two quantities that will be used often in this work: the heat release rate fluctuation level, σ, and the velocity fluctuation level, ε:

$$\sigma = I^{rms}_{CH^*}/\bar{I}_{CH^*} \tag{1.9}$$

$$\varepsilon = v^{rms}/\bar{v} \tag{1.10}$$

Assuming a flat velocity profile at the slot inlet one can assume that $v_1 \approx \bar{v}$, where v_1 is the local velocity at the axis of the slot. The velocity fluctuation magnitude is often defined in the literature in therms of rms fluctuation magnitude, v^{rms}. The reason for this is that experimentally signals carry some parasite noise and it is easily to measure the rms amplitude that the peak to peak amplitude. This definition is often source of errors when matching experimental results with numerical (LES or DNS) calculations. Indeed, the imposed velocity in the numerical codes is generally expressed as:

$$v = \bar{v} + v' \tag{1.11}$$

where v' is the velocity fluctuation, which can be defined as:

$$v' = \tilde{v}e^{-i\omega t} \tag{1.12}$$

$\tilde{v}$ corresponds to the magnitude of the velocity fluctuation. $\omega = \omega_r + i\omega_i$ designates the complex angular frequency with $\omega_r = 2\pi f$ and ω_i respectively defining the angular frequency and the growth rate. For positive values of ω_i the perturbation grows, while it decays in the opposite case. For a harmonic signal at its limit cycle one can define v' as:

$$v' = \tilde{v}\cos(\omega t) \tag{1.13}$$

We can define a normalized magnitude of velocity fluctuation as $\tilde{v}/\bar{v}$ which is usually the input for the numeral codes. The relation between this amplitude of the velocity fluctuation, $\tilde{v}$, and rms velocity fluctuation level, ε, is defined by:

$$\tilde{v} = \sqrt{2}\,\varepsilon\,\bar{v} \tag{1.14}$$

Thus, when matching experimental and numerical results it is important to know how the magnitude of the velocity fluctuation is defined.

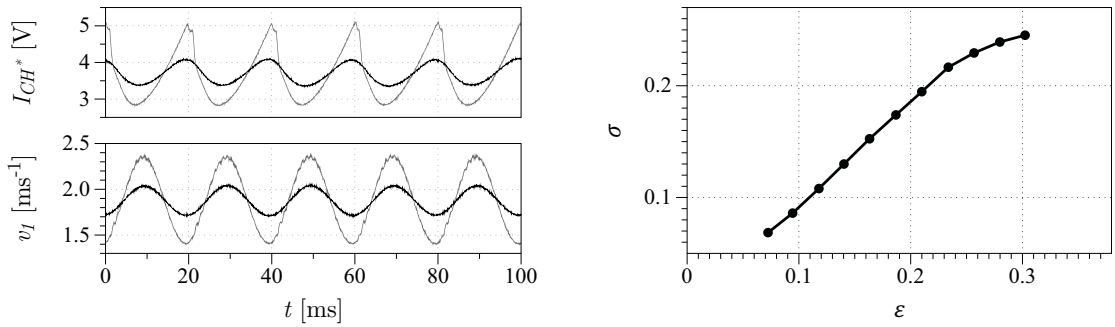

(a) Velocity $v_1(t)$ and heat release rate signals $I_{CH^*}(t)$ during 5 cycles of excitation at a frequency of $f_{ex} = 50$ Hz, for two different modulation levels; $\varepsilon = 0.07$ (——) and $\varepsilon = 0.20$ (——).

(b) Heat release rate fluctuation magnitude, σ, versus the velocity fluctuation magnitude, ε, for a flame excited at $f_{ex} = 50$ Hz and for different amplitudes of modulation.

Figure 1.11: Modulation system operation. The flame is forced by the loudspeaker (*cf.* Fig. 1.9). Equivalence ratio and bulk velocity are $\Phi = 0.95$ and $\bar{v} = 1.6$ ms^{-1} respectively.

Figure 1.11(a) shows typical velocity and heat release rate signals during 5 cycles of modulation at a frequency of $f_{ex} = 50$ Hz, for two different levels of excitation, $\varepsilon = 0.07$ (black), and $\varepsilon = 0.20$ (grey) (T120h case). At a rms modulation level of 0.07 % both signals, $v_1(t)$, and $I_{CH^*}(t)$, are harmonic, however, at 0.20 %, the heat release rate signal is less linear. In both cases, the signal-to-noise ratio is very good.

Figure 1.11(b), shows the heat release fluctuation magnitude, σ, for different velocity fluctuation levels, ε, for a stable flame, in a T120h case, excited at a frequency $f_{ex} = 50$ Hz. The relation σ vs. ε has a linear behavior up to $\varepsilon = 0.2$. Beyond that point, the heat release rate fluctuations start to saturate (*e.g.* Lieuwen (2002), Bellows and Lieuwen (2004), Birbaud *et al.* (2007a) and Noiray *et al.* (2008)).
A modulation level of $\varepsilon = 0.1$ is chosen for the experiments, this value ensures a good signal-to-noise ratio. It is in the linear range (Fig. 1.11(b)) and corresponds to the level of velocity fluctuations seen during a self-sustained operation in a T50h case. $\varepsilon = 0.1$ has been used as amplitude of modulation in similar studies of linear combustion instabilities (Kedia *et al.* (2011)). A calibration of the rms amplifier voltage output is carried out to ensure a constant, ε, at reference measurement point for the whole range of driving frequencies explored in this study.

1.4.5 Flame visualization

Direct flame visualization is used to monitor the flame geometry and dynamics. A high speed pco.dimax camera equipped with a Micro-Nikkor $f/2.8$ 105 mm Nikon lens is used.

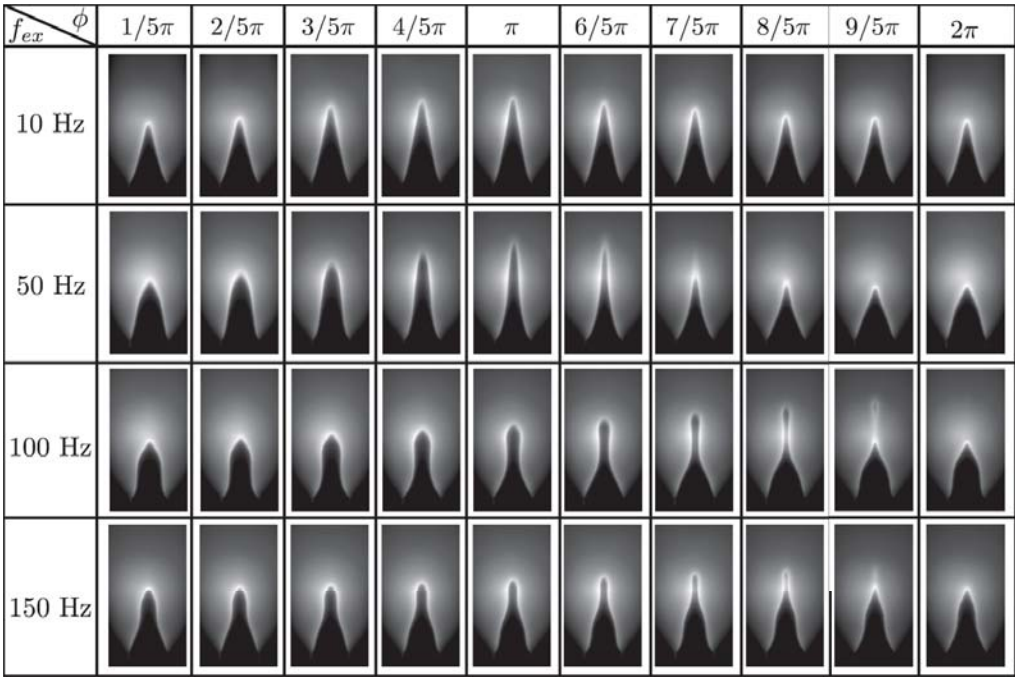

Figure 1.12: Evolution of the flame front for four different frequencies of excitation, $f_{ex} = [10, 50, 100, 150]$ Hz and ten different phases in the one cycle of excitation. The modulation level is $\varepsilon = 0.1$ with a bulk velocity and equivalence ratio of $\bar{v} = 1.6$ ms^{-1} and $\Phi = 0.95$ respectively.

It is placed facing the longitudinal axis of the flame 10 mm above the slot outlet (*cf.* Fig. 1.6).
The camera is controlled through the Camware software set in external trigger synchronization mode. The camera is driven with the same LabVIEW signal generator used to drive the amplifier and loudspeaker. A TTL signal synchronized with the forcing signal is sent directly to the camera to trig the acquisition, an output signal is sent from the camera to the DAQ system in order to monitor and record the camera operation. Figure 1.12 shows snapshots of a stable flame forced at different frequencies of excitation and different phases in one cycle for a modulation level of $\varepsilon = 0.1$.

Flame front recognition

For premixed CH_4-air flames the radiation of OH^*, CH^* and C_2^* is dominating. It has been shown (Armitage *et al.* (2006)) that this radicals are located in the zone of high heat release rate. Therefore, the image of the flame spontaneous emission contains information about the flame front position. It is then natural to assume that the flame front position is located in the pixels where the spontaneous light emission of the flame is maximal. Each pixel in the raw image contains a value proportional to the line of sight integrated over the flame depth l_s light emission. Therefore, the flame front position can be restored

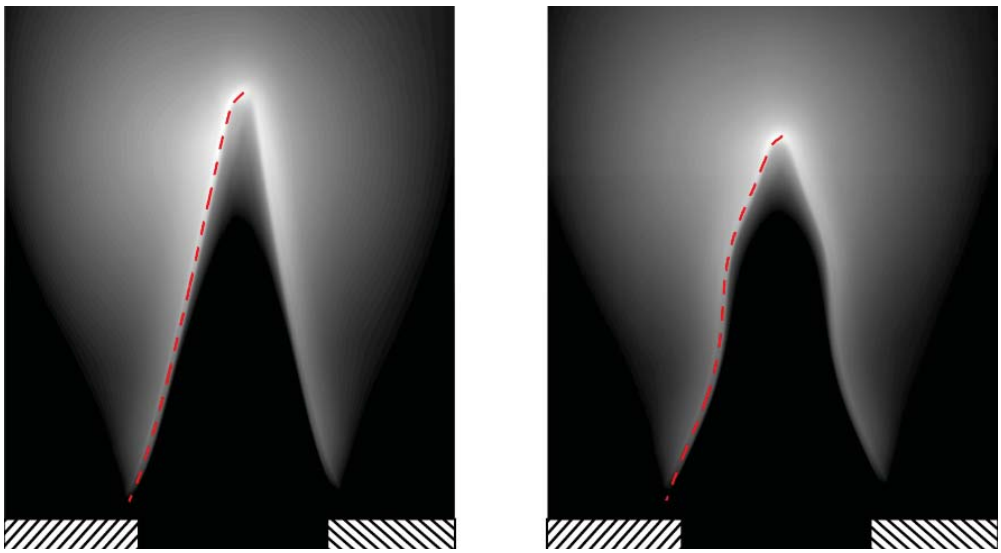

Figure 1.13: Snapshots of a steady (left) and modulated (right) flame. In red dashed line the result of the flame front detection algorithm. Flow conditions are $\bar{v} = 1.6$ ms^{-1} and $\Phi = 0.95$.

as the points where the value of the brightness distribution along the image row has its maximum. Figure 1.13 shows the result of the flame front detection algorithm for two flames, stationary (left) and modulated (right). Flow condition are $\bar{v} = 1.6$ ms^{-1} and $\Phi = 0.95$, frequency of modulation and modulation level are $f_{ex} = 100$ Hz and $\varepsilon = 0.1$ respectively.

Flame tip and flame root recognition

For the flame tip and flame root detection a zoom is performed in the area of interest (tip and root). An example of the zoomed images is presented in Fig. 1.14. The resulting images are 928-by-624 px for the tip and the root, with a resolution of 72 px/mm. The description of the algorithm used to determine the flame end points is explained schematically in Fig. 1.15. The coordinate of the flame tip can be recognized as the point where the image intensity distribution along the flame axis x_{ax} has a maximal value (Fig. 1.15(a)). The flame root location is chosen as the intersection of the flame front with the iso-contour at 65 % of the maximum pixel value over the whole image. A typical image is presented in Fig. 1.15(b). The 65 % threshold was carefully chosen. Tests were performed for several flow and camera configurations and 65 % corresponds to the place along the flame front with maximum rate of change of the pixel intensity (Fig. 1.15(b)).

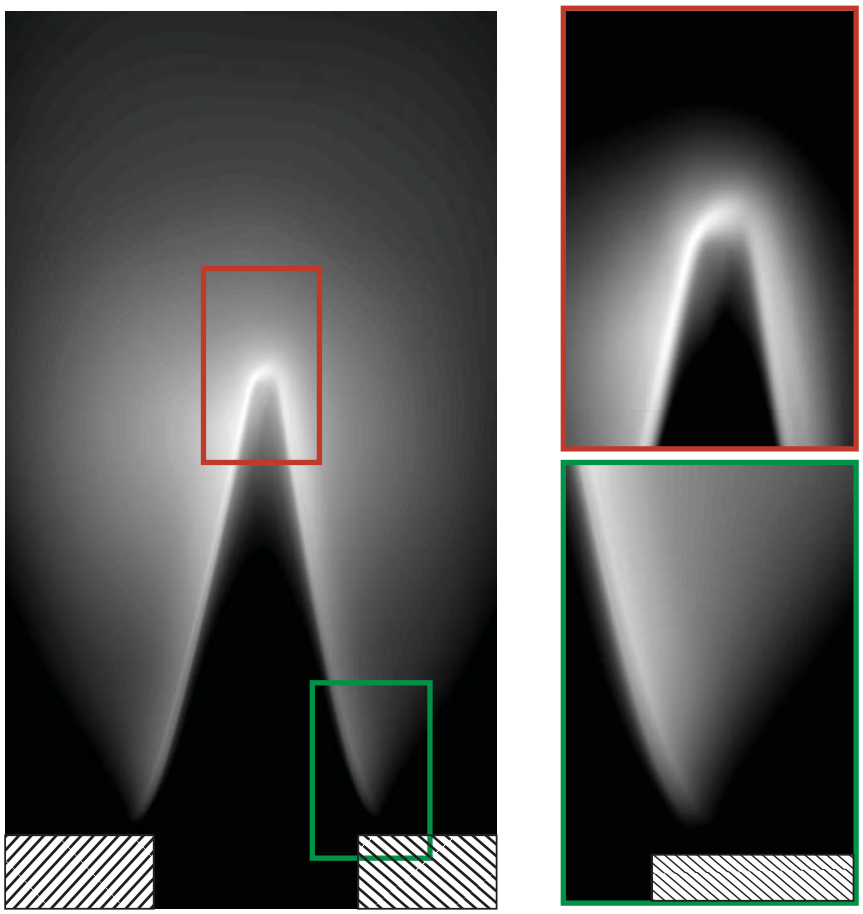

Figure 1.14: Flame tip and rood zoomed images. Flow condition were $\bar{v} = 1.6$ ms^{-1} and $\Phi = 0.95$.

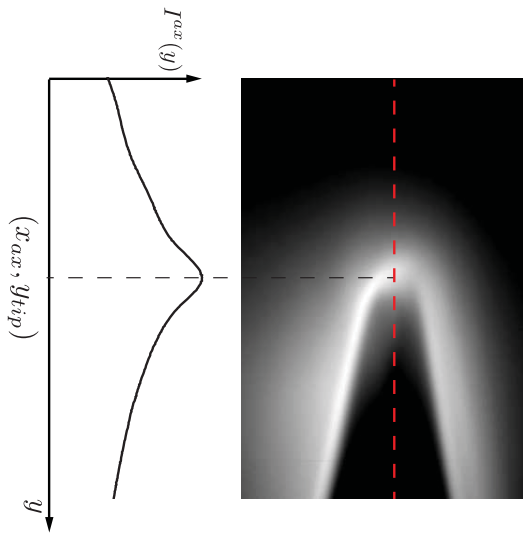

(a) Flame tip detection methodology.

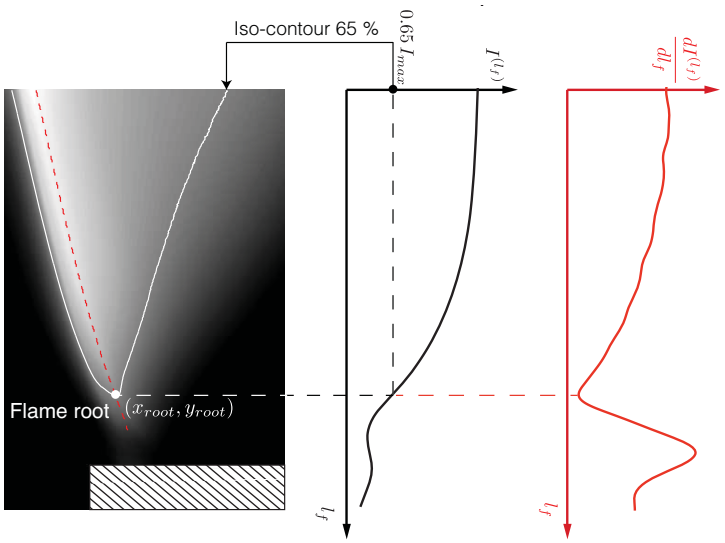

(b) Flame-root detection methodology.

Figure 1.15: Description of the algorithm used to determine the flame end points.

1.5 Conclusion

The experimental setup has been presented in this chapter. It consists of a rectangular slot burner. The methodology adopted for the experiments has been explained as well as the nomenclature used for the experiments. The temperature of the slot, T_s, is controlled and monitored because we want to investigate its effect. The diagnostic techniques have been explained in detail and the algorithm used for the image processing has been presented. Table B.1 gives the list of the technical equipment used in this study. The amplitude of the oscillations for forced experiments has been set to $\varepsilon = 0.1$, it corresponds to the amplitude of the self-sustained oscillations when the slot temperature is 50 °C or which is the same case T50h.

Chapter 2

Description of the unstable behavior

For a given flame configuration the burner presented in Ch. 1 exhibits self-sustained combustion instabilities. In this study these instabilities can be controlled by modifications of the burner rim temperature. Indeed, for a slot height $h_s = 70$ mm, the flame is unstable when the slot is cold and stable once hot.
The purpose of this chapter is to highlight the influence of the burner rim temperature T_s on combustion instability. Experimental results presented in the following sections are obtained on the B07 burner, with fixed equivalence ratio and mass flow rates. In section 2.1 the transient behavior of the combustion instability will be presented, while the steady state behavior will be studied in section 2.2. The general description of the thermo-acoustic coupling will be presented in section 2.3.

2.1 Instabilities in a chamber with variating wall temperatures

The basic observation which pointed out that instabilities and wall temperature were coupled is described in the present section. When the flame is ignited in a cold environment it develops a combustion instability. This behavior is illustrated in Fig. 2.1, which presents the joint evolution of pressure fluctuation in the plenum, p_0, and slot temperature, T_s, versus time, t. The operating point for this test is an equivalence ratio $\Phi = 0.95$ and a bulk velocity in the slot of $\bar{v} = 1.6$ m.s^{-1}. Temperature and pressure correspond to ambient conditions $T_u = 20$ °C $P_u = 0.99$ bar respectively.

At $t = 0$, the whole experiment is at ambient temperature and the cooling system is off. Combustion is initiated at $t = 20$ s and an instability develops immediately at a frequency around $f_r = 58$ Hz. The pressure fluctuation inside the plenum reaches $\tilde{p}_0 = 113$ dB and decreases gradually as the the slot temperature, T_s, increases. Around $t = 300$ s the instability reduces drastically and the flame is fully stable past $t = 400$ s. Meanwhile, T_s is over 100 °C and still increasing. At $t = 480$ s the cooling system is started with water at $T_{wc} = 3$ °C flowing through the slot, resulting in a sharp drop of T_s. The instability rises back up and the whole system reaches a steady state around $t = 800$ s

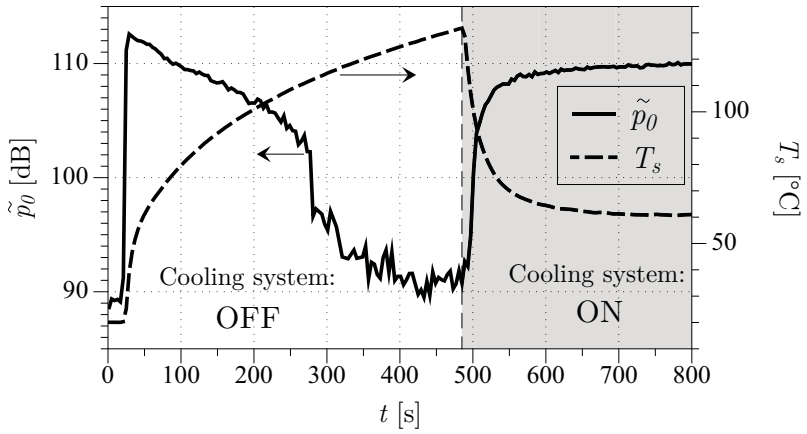

Figure 2.1: Experiment showing the effect of wall temperature on the combustion instability. at $t = 20\ s$ the flame is ignited, with the cooling system OFF and the slot at ambient temperature. At $t = 480\ s$ the cooling system is turned ON. $\tilde{p}_0$ (——) corresponds to the magnitude of the acoustic pressure inside the chamber and T_s (- - - -) corresponds to the slot temperature.

to $\tilde{p}_0 = 110$ dB and $T_s = 60$ °C. This behavior is fully repeatable and the instability can be controlled using only the cooling system.

t \ ϕ	$1/5\pi$	$2/5\pi$	$3/5\pi$	$4/5\pi$	π	$6/5\pi$	$7/5\pi$	$8/5\pi$	$9/5\pi$	2π
40 s										
100 s										
480 s										

Figure 2.2: Snapshots of the flame in ten instants on a unstable cycle and three instants during the test, $t = 40$, 100 and 480 s.

Figure 2.2 shows snapshots of the flame during a unstable cycle for three different instants during the test, $t = 40$, 100 and 480 s. The flame presents strong oscillations at the instant $t = 40$ s, these oscillations are still present at the instant $t = 100$ s but with slightly less amplitude. The flame is completely stable at the instant $t = 480$ s as deduced from Fig. 2.1.

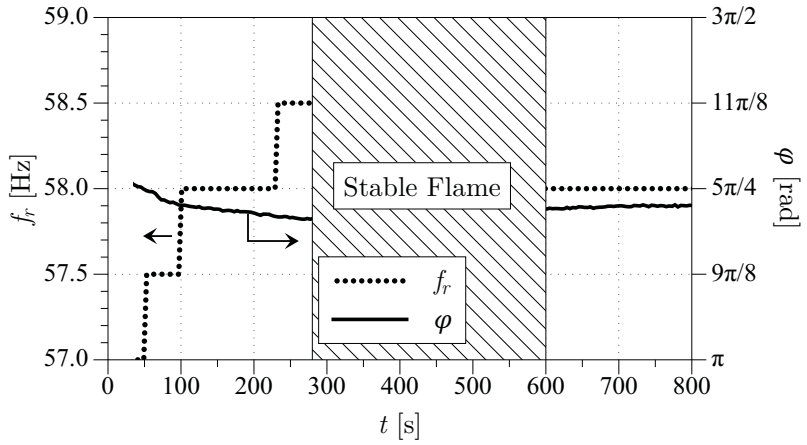

Figure 2.3: Resonance frequency, f_r (·····); phase-lag between velocity and heat release signal, φ (——). At $t = 20$ s the flame is ignited, with the cooling system OFF and the slot at ambient temperature. At $t = 480$ s the cooling system is turned ON.

Figure 2.3 shows the evolution of the resonance frequency, f_r, and phase-lag between the velocity and heat release rate signal, φ, for the experiment described above. The signals are recorded during $t_m = 2$ s. This t_m is sufficiently long in order to have a spectral resolution of $\Delta f = 0.5$ Hz and sufficiently short to assimilate the results at the instant t. The resonance frequency slightly increases with slot temperature before the flame is stabilized. During the period $t \in [280, 600$ s] the level of fluctuations is too low and no information in the resonance frequency can be obtained from the spectral analysis. Once the flame recovers its unstable behavior beyond $t = 600$ s and steady state is reached for the slot temperature at $T_s = 60$°C, the resonance frequency stabilizes at $f_r = 58 \pm 1$ Hz. The phase lag between the velocity and heat release rate signals slightly decreases during the warming-up until the time where the flame becomes stable and no correlation between the signals is possible. At steady state (beyond $t = 700$ s) the phase lag stabilizes at a value of $\varphi = 1.22\pi$ rad.

Figure 2.4 shows the time-resolved signals of $p'_0(t)$, $p'_{M1}(t)$, $v_1(t)$ and $I_{CH^*}(t)$ for two instants in the experiment; $t = 40$ s corresponding to a slot temperature of $T_s = 50$ °C or T50h case, when combustion instabilities are present, and $t = 480$ s corresponding to a slot temperature of $T_s = 120$ °C or T120h case, when the flame is fully stabilized.
At $t = 40$ s strong fluctuations of pressure, velocity and heat release rate are observed. The pressure fluctuation in the plenum and the velocity signal are harmonic and oscillate at the same frequency of $f_r = 58$ Hz. The heat release signal is less regular, it oscillates at the same frequency as $p'_0(t)$ and $v_1(t)$ but differs from a sinusoidal wave. The flame CH* emission increases slowly until the maximum is reached and suddenly drops to its minimum value due to an extinction of a large portion of the flame, producing an intense emission of noise $p'_{M1}(t)$. The heat release rate and the pressure fluctuations inside the plenum are almost in phase, these observations are in agreement with those of Schuller *et*

al. (2003a) for a self-sustained oscillation developed in a conical flame. However a phase difference of $\varphi = 1.23\pi$ rad between $v_1(t)$ and $I_{CH^*}(t)$ is measured, which corresponds to a delay of $\tau = 11$ ms. This delay is the central element for the occurrence of a self-sustained combustion instability. At $t = 480$ s the system is stable and no fluctuations are seen on Fig 2.4 right.

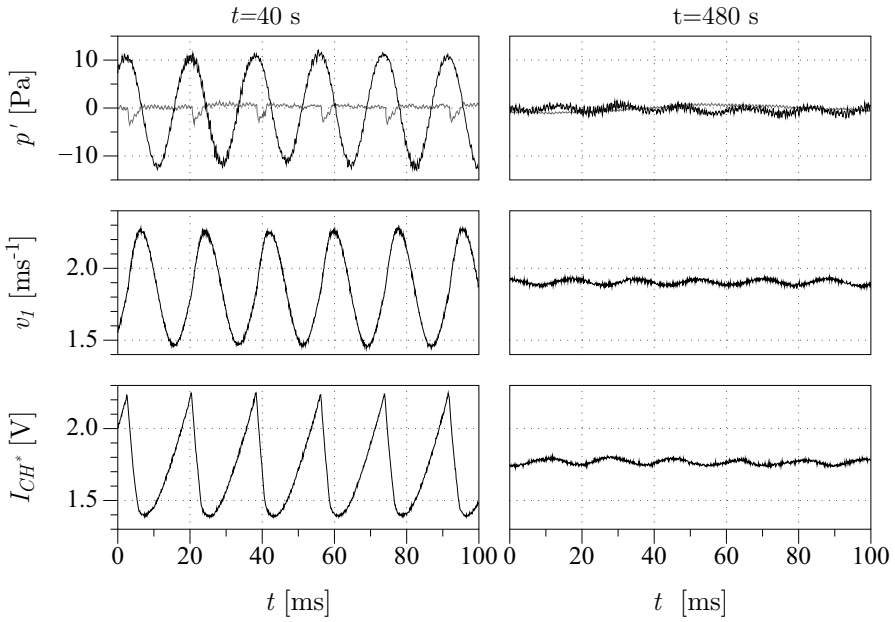

Figure 2.4: Simultanous measurements of pressure (upper row), $p'_0(t)$ (——) and $p'_{M1}(t)$ (——), velocity signal (middle row) and heat release rate (bottom row). For two different instants left $t = 40$ s and right $t = 480$ s. Corresponding to $T_s = 50$ and 120 °C, respectively.

The power spectral density (PSD) of the signals are shown in Fig. 2.5 for the same conditions as Fig 2.4. At $t = 40$ s, corresponding to a cold slot, a strong component at the resonance frequency, f_r, is observed. At $t = 480$ s, the peaks are reduced by at least 50 dB, thus confirming the effect of the slot temperature on the stability of the flame. At the instant $t = 40$ s an energy transfer from the resonant frequency to its harmonics is observed in the signals. However, a 20 dB difference is observed between the main peak and the different harmonics, except for the I'_{CH^*} signal, highlighting the nonlinear nature of the flame described by (Lieuwen, 2005) for example.

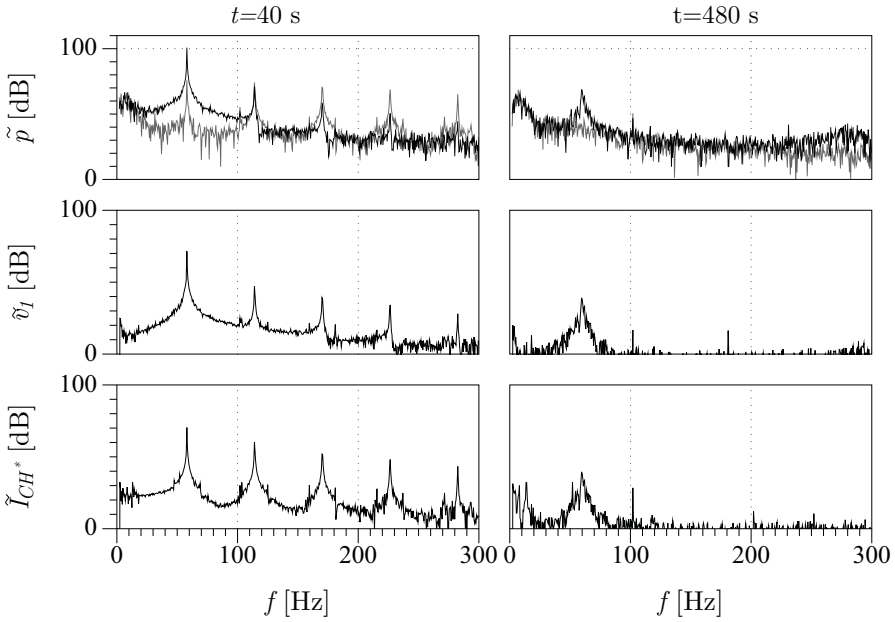

Figure 2.5: Power spectral densities. Upper row, pressure signals, $p'_0(t)$ (——) and $p'_{M1}(t)$ (——). Middle row velocity signal. Bottom row CH* intensity signal. For two different instants in the experiment left $t = 40$ s and right $t = 400$ s.

2.2 Instability in a chamber with controlled wall temperatures

In order to further study the transition between stable and unstable modes, a quasi-steady-state analysis was performed. By varying the cooling-water temperature in the close circuit (*cf.* Fig. 1.3) and waiting for a thermal steady state, one can determine the amplitude of the instability versus slot temperature in a situation where the temperature field in the burner wall is fully stabilized. The velocity and heat release rate fluctuations levels ($\varepsilon = v_1^{rms}/\bar{v}$ and $\sigma = I_{CH^*}^{rms}/\bar{I}_{CH^*}$) are presented in Fig. 2.6 versus T_s. With maximum cooling, corresponding to $T_s = 40$ °C, ε and σ reach as much as 13 %. For $T_s = 60$ °C the fluctuation levels are down to 5 % and lower than 1 % past $T_s = 70$ °C. The instability is shut down by increasing the wall temperature by less than 20 °C showing how sensitive flames can be to heat transfer. Comparing Figs. 2.1 and 2.6 shows that in the quasi-steady state experiment, the instability is damped for lower values of T_s than in the transient case. One can identify in Fig. 2.6 the three cases chosen as reference study cases in Sec. 1.3. T50h corresponds to an unstable case with a velocity fluctuation level of $\varepsilon = 0.1$. T90h corresponds to an unstable case in a transient test (*cf.* Fig. 2.1) and a stable case during the quasi-steady-state test and T120h is a stable case for both tests.

Figure 2.6 shows the evolution of the resonance frequency, f_r, and the phase-lag between velocity and teat reseals signals, φ, with respect to the slot temperature in a quasi

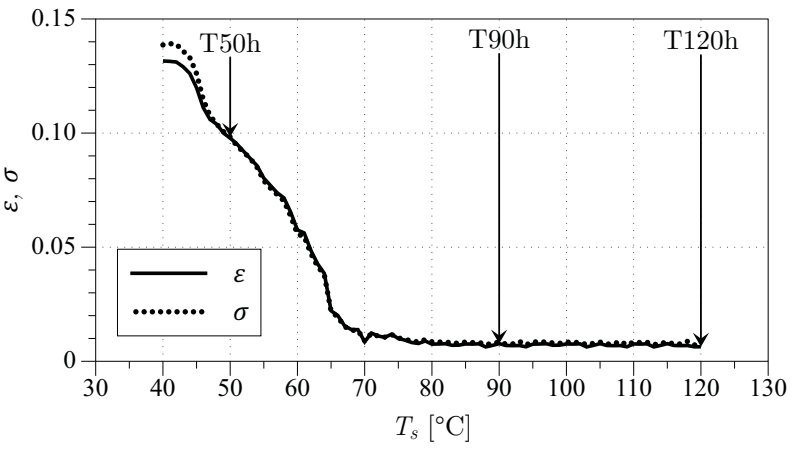

Figure 2.6: Steady state test. Wall temperature was gradually increased in steps of 1 °C from T_s = 40 °C to 120 °C. Steady state was reached at each step. Velocity fluctuation level, ε (———) and heat release fluctuation level, σ (·····) were measured simultaneously using a hot-wire, HW, and a photomultiplier, PM, respectively.

stationary case. The resonance frequency has the same tendency as in the transient case (Fig. 2.7), it slightly increases with slot temperature until T_s exceeds 50 °C, where it stabilizes at f_r = 58 Hz. Beyond T_s = 65 °C no spectral analysis can be performed because the unsteady signal is too weak. The phase lag, φ, slightly decreases with slot temperature, in an almost linear manner, at a rate of 0.0036 rad/s. Assuming this linear relationship between the phase-lag and the slot temperature extends to the places where no correlation is possible, one can interpolate a value for the phase-lag at T_s = 120 °C of $\varphi = 1.15\pi$ rad.

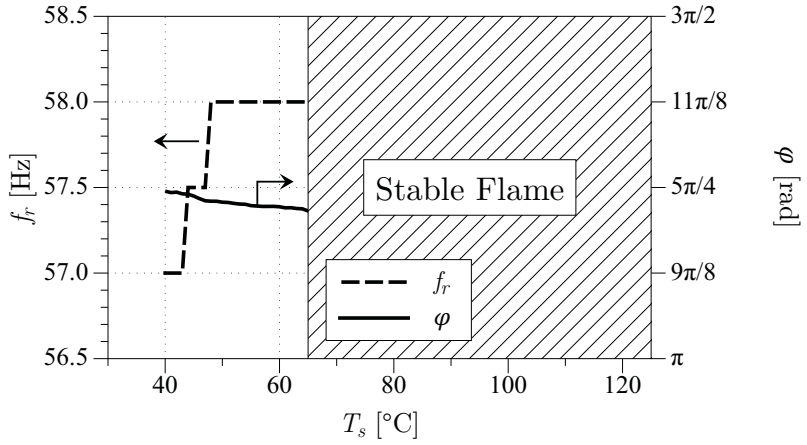

Figure 2.7: Resonance frequency, f_r (- - - -) and phase lag, φ (———) between the velocity and the heat release signals. Beyond T_s = 65 °C the flame is stable so that f_f and φ can not be determined with this method.

2.3 General thermo-acoustic coupling principle

In other to understand the interaction between wall temperature and combustion instabilities we first describe the resonant feedback resulting from the combination of the flame interaction with the burner acoustics.

The resonant coupling mechanism is presented schematically in Fig 2.8: let's first consider a velocity fluctuation v', upstream of the flame. The flame will move in response to this perturbation, resulting in a flame surface perturbation $\mathcal{A}'$ and a corresponding heat release rate fluctuation $\dot{q}'$. This fluctuation is a monopole source of acoustics, so that a pressure fluctuation p' may travel back upstream the flame. If there is a constitutive coupling between the noise emitted by the flame and burner acoustics, a velocity perturbation may be sent towards the flame, thus closing the unstable loop.

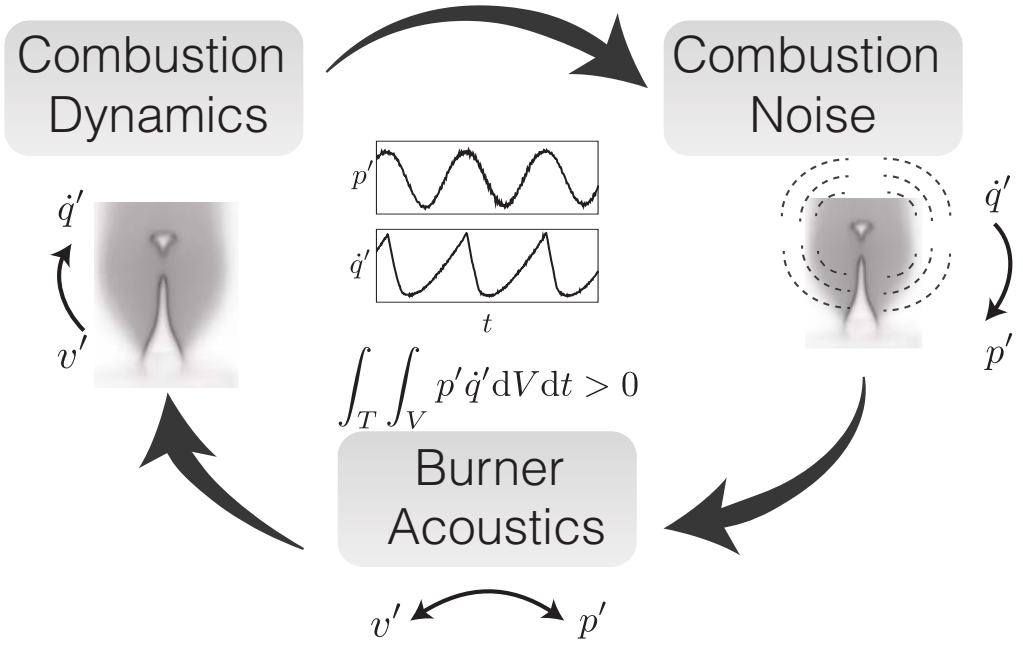

Figure 2.8: Resonant coupling mechanism

From an acoustic energy balance, one shows that a necessary condition for this loop to be unstable is that the product of pressure fluctuation, p', and heat release fluctuation, $\dot{q}'$, over a period of oscillation is positive, $\oint p'q'dt > 0$. This criterion was first introduced by (Rayleigh, 1878), an extension to this criterium was proposed by (Nicoud and Poinsot, 2005) and (Durox *et al.*, 2009a) for unconfined flames. Here, an instability will develop if the energy produced by the thermo-acoustic interaction exceeds the energy dissipated by the system.

2.4 Conclusion

The experiments described in this chapter demonstrate the effect of slot temperature on combustion instabilities. For fixed bulk velocity and equivalence ratio the flame instability can be completely controlled with only modifications on the burner rim temperature. An increase of 20 °C on the burner rim temperature can shut-down the instability.
At this point, the mechanisms through which the burner rim temperature damps the instability is unknown, but we have shown strong indications that the modification of the flame response delay does not suffice to explain the stabilization. A more detailed study will therefore be conducted both theoretically and experimentally in the following chapters.

Chapter 3

Linear stability analysis

In order to study the role of the slot temperature, T_s, on the combustion instability mechanism, a first step is to build a linear stability analysis model for the setup presented in Fig. 1.1. Isolating and studying individually the elementary mechanisms presented in Fig. 2.8 one can identify which parameters are likely to be affected by T_s and consequently modify the flame response to acoustic oscillations.
The objective of this chapter is to derive this low-order model, as a combination of individual blocks, each corresponding to a potential mechanism. In Sec. 3.2 we study the burner acoustics, combustion noise modeling is presented in Sec. 3.3 while flame dynamics is discussed in Sec. 3.4. With the results of these three sections we will derive a dispersion in Sec. 3.5.

3.1 Introduction

The stability of the slot burner is investigated in this chapter, from a linear point of view. This methodology has been used in the combustion community for a while (*e.g.* Dowling (1995); Durox *et al.* (2002); Matveev and Culick (2003); Dowling and Stow (2003); Schuller *et al.* (2003a); Truffin and Poinsot (2005); Fernandes and Leandro (2006); Nicoud *et al.* (2007); Morgans and Dowling (2007); Noiray *et al.* (2008) and Durox *et al.* (2009a)). Besides giving a good understanding of the mechanisms involved in the combustion instability it can also accurately predict the stability of the system.
In a general manner, the thermo-acoustic coupling is an interaction between three different phenomena: combustion noise (the acoustic waves created by unsteady flames), burner acoustics (the propagation and reflection of acoustic waves in the combustor) and combustion dynamics (the response of the flame to the acoustic waves traveling in the combustor). Every one of them has been the subject of detailed studies, too numerous to cite exhaustively. One may refer to the reviews of Candel (2002); Candel *et al.* (2007) for insights in the progress and challenges of flame dynamics and combustion noise as well as Ducruix *et al.* (2003) describing the elementary coupling and the driving mechanism of the combustion instability for example.

It is well known that a combustor or any thermal machine does not perform in the same way during a cold start and in the permanent regime. Some authors have already mentioned this effect for combustion instabilities. For example, Noiray *et al.* (2008) explain that the differences between predicted and measured oscillations frequencies may come from the fact that the temperature of the flame holder plate is not constant during the experiments and this could modify the flame anchoring dynamics. Likewise de Goey *et al.* (2011) state that in order to have an accurate analytical model of the flame dynamics it is necessary to take into account the intrinsic mechanisms of the flame anchoring to the burner, which requires the modeling of conjugate heat transfer between the fluid and the burner. Duchaine *et al.* (2011) performed numerical simulations to highlight the effect of wall temperature on FTF for laminar flames, showing that in order to be able to correctly predict FTF's it is necessary to perform coupled computations of flame and heat transfer to the burner-rim.

The specific issue studied here is the impact of wall temperature on terms-acoustics. The objective is then to establish stability criteria that capture the behavior of the B07 burner seen in Ch. 2. One is not interested in more complicated phenomena such as limit-cycles, instability triggering, mode switching etc... which are only observable by a non-linear stability analysis (*e.g.* Noiray *et al.* (2008) and Boudy *et al.* (2011)). Consequently, we will perform a linear stability analysis.

3.2 Burner Acoustics

To gain insight in the instability mechanism, it is natural to first examine the burner acoustics. One is interested in finding an expression which links the acoustic pressure, p'_1, to the velocity fluctuations at the burner outlet, v'_1. This is done by examining the acoustic properties of the burner.

When the acoustic wavelength is much larger than any burner dimension, the system can be viewed as a Helmholtz resonator (Pierce (1981)), The plenum denoted by (0), has a volume V_p and a transversal section S_p (*cf.* Fig. 3.1). The slot outlet denoted by (1), as a cross section area of S_s and a length of h_s. We are looking for an expression for the velocity fluctuations in the slot as a function of an external pressure perturbation acting at the burner outlet. A mass balance on the volume V_p in the direction y can be written as:

$$\frac{\partial}{\partial t}\int_{V_p}\rho_0 \mathrm{d}V + \int_{S_s}\rho_1 v_1.\mathrm{d}S = 0 \tag{3.1}$$

where $\mathrm{d}S$ is elemental surface area. Integrating over the volume V_p and the surface S_s one obtains:

$$V_p\frac{\mathrm{d}\rho_0}{\mathrm{d}t} = -\rho_1 v_1\, S_s \tag{3.2}$$

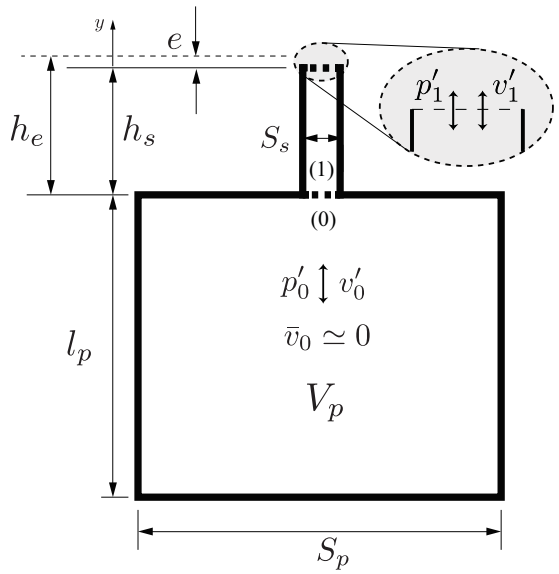

Figure 3.1: Schematic representation of the Helmholtz resonator.

One can decompose the velocity, v, and density, ρ, in mean ($\bar{}$) and first-order fluctuation ($'$)

$$v = \bar{v} + v' \tag{3.3}$$
$$\rho = \bar{\rho} + \rho' \tag{3.4}$$

Assuming that the velocity in the plenum is small ($\bar{v}_0 \backsimeq 0$) and neglecting the second order terms ($\rho'_1 v'_1 \backsimeq 0$) Eq. 3.2 becomes:

$$V_p \frac{\mathrm{d}\rho'_0}{\mathrm{d}t} = -\rho'_1 \bar{v}_1 \, S_s - \bar{\rho}_1 v'_1 \, S_s \tag{3.5}$$

the second term in Eq. 3.5 can be neglected assuming low Mach number in the slot ($M_a \approx 5 \times 10^{-3}$ in our case). Assuming isentropic variations, one can use Laplace's law:

$$\gamma \frac{p}{\rho} = \gamma \frac{p_0}{\rho_0}$$

which can be linearized:

$$p'_0 = c^2 \rho'_0 \tag{3.6}$$

where γ is the ratio of specific heat and c is the speed of sound, defined as:

$$c^2 = \left. \frac{\partial p}{\partial \rho} \right|_s$$

For a perfect gas:

$$c^2 = \gamma \frac{R}{W} T_u = \gamma \frac{\bar{p}}{\bar{\rho}}$$

where R is the perfect gas constant, W is the molecular weight of the mixture and T_u is the temperature of the mixture. Finally the mass balance in the plenum yields:

$$\frac{\mathrm{d}p_0'}{\mathrm{d}t} = -\frac{c^2\bar{\rho}_1 S_s}{V_p} v_1' \tag{3.7}$$

Equation 3.7 tell us that the pressure fluctuations inside the plenum should be in quadrature with the velocity fluctuations at the slot, which is consistent with the experimental observation in Fig. 2.4.

A momentum balance between the slot inlet and the outlet in the y direction can be written as:

$$\frac{\partial}{\partial t}(\rho v) + \bigtriangledown.(\rho v \mathbf{u}) = -\frac{\partial p}{\partial y} + \mathcal{T}_y \tag{3.8}$$

where $\mathcal{T}_y$ is a dissipation term corresponding to the energy losses in the acoustics viscous and thermal bounduary layer at the slot walls. Neglecting the compressibility effects in the slot one can re-write Eq. 3.8 as:

$$\bar{\rho}_1 \frac{\mathrm{d}v_1}{\mathrm{d}t} = -\frac{p_0 - p_1}{h_e} + \mathcal{T}_y \tag{3.9}$$

where $h_e = h_s + e$ is the effective length of the slot, e is an end correction, which corresponds to the impedance adaptation length between the flow at the exit of the slot and the atmosphere (Rienstra (1983)) and is of the order of the half slot width $w_s/2$. Decomposing the velocity, v, and pressure, p, in mean ($^-$) and first-order fluctuation ($'$) one obtains:

$$\bar{\rho}_1 \frac{\mathrm{d}v_1'}{\mathrm{d}t} = -\frac{p_0' - p_1'}{h_e} + \mathcal{T}_y \tag{3.10}$$

For small amplitudes of fluctuation, the dissipation term $\mathcal{T}_y$ is proportional to the velocity fluctuations:

$$\mathcal{T}_y = -2\delta\, \bar{\rho}_1 h_e\, v_1' \tag{3.11}$$

where δ is the damping coefficient (Durox *et al.* (2002, 2009a); Fernandes and Leandro (2006) and Kashinath *et al.* (2013)). Finally the momentum balance yields:

$$\bar{\rho}_1 \frac{\mathrm{d}v_1'}{\mathrm{d}t} = -\frac{p_0' - p_1'}{h_e} - 2\delta\, \bar{\rho}_1 h_e\, v_1' \tag{3.12}$$

Combining Eqs. 3.7 and 3.12 one obtains an expression for the velocity fluctuations in the slot, v_1', function of an external pressure perturbation p_1':

$$\frac{\mathrm{d}^2 v_1'}{\mathrm{d}t^2} + 2\delta \frac{\mathrm{d}v_1'}{\mathrm{d}t} + \omega_0^2 v_1' = -\frac{1}{\rho_u h_e}\frac{\mathrm{d}p_1'}{\mathrm{d}t} \tag{3.13}$$

where we assumed that mean density of the mixture in the plenum, $\bar{\rho}_0$, and in the slot, $\bar{\rho}_1$, are the same and equal to ρ_u. Equation 3.13 is a second order ODE corresponding to a forced mass-spring system with dissipation. Here, $\omega_0^2 = c^2[S_s/(V_p h_e)]$ is the natural resonant pulsation frequency of the burner that will be discussed in more detail in Sec. 4.1.1. Assuming harmonic waves, one can decouple spatial and temporal variations for the acoustic pressure, $p_1' = \tilde{p}_1 e^{-i\omega t}$, and the velocity fluctuation, $v_1' = \tilde{v}_1 e^{-i\omega t}$, which results in an equation for the complex amplitudes:

$$\omega^2 \tilde{v}_1 + 2i\delta\omega\tilde{v}_1 - \omega_0^2 \tilde{v}_1 = -\frac{1}{\rho_u h_e} i\omega \tilde{p}_1 \tag{3.14}$$

According to Eq. 3.14 the resonator is driven by an external pressure fluctuation, $\tilde{p}_1$, that acts at the burner outlet. This equation is the model for the acoustic response of the burner: it will allow us to find the velocity $\tilde{v}_1$ to the pressure $\tilde{p}_1$. Eq. 3.14 can be written in terms of an acoustic impedance at the burner outlet:

$$\mathcal{Z}_1 = \frac{\tilde{p}_1}{\tilde{v}_1} = \frac{i\rho_u h_e}{\omega}\left[\omega^2 + 2i\delta\omega - \omega_0^2\right] \tag{3.15}$$

3.3 Combustion noise

We now move on to the study of the acoustic forcing which will create the $\tilde{p}_1$ term in Eq. 3.14: combustion noise. The sound radiated by unsteady combustion has been the subject of many studies, Candel *et al.* (2007) provide a recent review of the progresses and challenge in combustion noise. Early studies by Strahle (1971) showed that the acoustic pressure p' radiated in the far-field of a compact flame and the net rate of change of the heat release rate in the reacting volume are linked by the following integral:

$$p'(r,t) = \frac{\gamma - 1}{4\pi r c^2} \int_V \frac{\partial \dot{q}}{\partial t}(r_0, t - \tau_{ac}) dV(r_0) \tag{3.16}$$

where r is the distance from the compact combustion zone to the observation point (Fig. 3.2), τ_{ac} the time required for the sound to cover the distance r and V the volume of the combustion region. Compact far-field conditions are fulfilled when the observation distance is large with respect to the acoustic wavelength λ_{ac} and when this wavelength is large with respect to the flame size. For perfectly premixed combustion where all the reactive mixture at the burner outlet enters the reaction zone, it is possible to express the heat release rate $\dot{q}$ in terms of the flame surface area $\mathcal{A}$:

$$\int_V \dot{q}\, dV = \int_{\mathcal{A}} \rho_u Y_F\, s_D(-\Delta h_f^0)\, d\mathcal{A} \tag{3.17}$$

where s_D is the burning velocity, Y_F is the fuel mass fraction in the fresh gases and Δh_f^0 the enthalpy formation of the reactants. In a laminar case, to first order s_D is equivalent to the laminar burning velocity, s_L. Stretch and curvature effects can be ignored (Markstein (1964), Law (1988)), s_L is function of the equivalence ratio Φ, and the injection condition

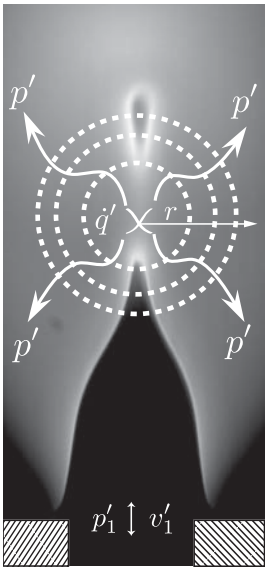

Figure 3.2: Schematic representation of the noise produced by an oscillating flame.

of the premixed reactants T_u and P_u. Equation 3.17, the integration is carried out over the flame surface area $\mathcal{A}(t)$. For a premixed compact laminar flame at a fixed equivalence ratio, Eq. 3.17 reduces to:

$$p'(r,t) = \frac{\gamma - 1}{4\pi r} \frac{\rho_u Y_F(-\Delta h_f^0)}{c^2} s_L \left[\frac{d\,\mathcal{A}}{d\,t}\right]_{t-\tau_{ac}} \tag{3.18}$$

considering $Y_F(-\Delta_f^0) = c_p(T_b - T_u)$ where c_p is the specific heat at constant pressure, T_b and T_u are the burnt and fresh gases temperatures respectively; and noting that $c_p = \gamma R/(\gamma - 1)$ One may write:

$$p'(r,t) = \frac{\rho_u}{4\pi r}\left(\frac{T_b}{T_u} - 1\right) s_L \left[\frac{d\,\mathcal{A}}{d\,t}\right]_{t-\tau_{ac}} \tag{3.19}$$

In addition, most flames are nearly isobaric and one may write $T_b/T_u \simeq \rho_u/\rho_b$, which when inserted in 3.19 finally yields an expression originally derived by Clavin and Siggia (1991):

$$p'(r,t) = \frac{\rho_u(E-1)s_L}{4\pi r} \left[\frac{d\,\mathcal{A}}{d\,t}\right]_{t-\tau_{ac}} \tag{3.20}$$

where $E = \rho_u/\rho_b$ is the volumetric expansion ratio.
Equation 3.20 shows that the mechanism leading to intense noise production is the flame surface fluctuation. In the present flame configuration, the main mechanism leading to high noise levels is the combustion of small pockets of fresh gases created under unstable combustion and located at an altitude r_0 from the burner outlet. Figure 3.3 shows a sequence of 10 images of an oscillating flame, from the moment before the small pocket of fresh gases is detached (somewhere between frames 3-5), to the moment where it is totally burned. Because the flame is compact with respect to the acoustic wavelength and r_0 is

of the order of the flame height ($h_f \simeq 20$ mm), τ_{ac} is then of the other of 10^{-5} s and it can be neglected. Replacing r by r_0 Eq. 3.20 becomes:

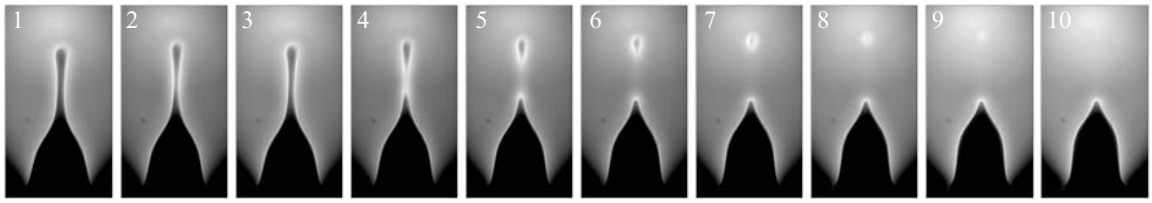

Figure 3.3: Sequence of images of an oscillating flame, from the moment before the pocket of fresh gases is detached until it is consumed. The photos were take at a sampling rate of $f_{cam} = 3000$ fps during an excitation cycle at $f_{ex} = 100$ Hz and $\varepsilon = 0.1$, flow conditions were $\bar{v} = 1.6$ ms^{-1} and $\Phi = 0.95$.

$$p_1'(t) = \frac{\rho_u (E-1) s_L}{4\pi r_0} \left[\frac{d\,\mathcal{A}'}{d\,t} \right]_t \tag{3.21}$$

Considering harmonic fluctuations of acoustic pressure, $p_1' = \tilde{p}_1 e^{-i\omega t}$, and flame surface, $\mathcal{A}' = \tilde{\mathcal{A}} e^{-i\omega t}$, Eq. 3.21 yields:

$$\tilde{p}_1 = -\frac{\rho_u (E-1) s_L}{4\pi r_0} i\omega \tilde{\mathcal{A}} \tag{3.22}$$

A quantitative expression for the acoustic pressure radiated at the burner outlet $\tilde{p}_1$ in terms of the flame surface area fluctuation $\tilde{\mathcal{A}}$ has been derived and the right part of Fig. 2.8 is completed. How velocity fluctuations at the burner outlet (v_1') are linked to the flame surface fluctuation ($\mathcal{A}'$) is the subject of next section.

3.4 Combustion dynamics

Flame dynamics is actually the most important element of the resonant feedback that drives the combustion instabilities. The response to incident flow perturbations induce heat release rate fluctuations which in turn feed acoustic energy back into the system. In the case of premixed combustion, the motion of the flame front, $\mathcal{A}'$, is generally driven by velocity perturbations, v_1' impinging on the flame front the upstream side.

Changes in heat release rate $\dot{q}'$ may be linked to velocity fluctuations v_1' at the burner outlet by the $(n-\tau)$ model proposed by Crocco (1951):

$$\dot{q}'(t) = n\, v_1'(t-\tau) \tag{3.23}$$

where τ is the time lag between the acoustic forcing and the flame response and n is the gain of the flame response. Using this notion of combustion gain and delay, a more

modern way to represent the flame response is the Flame Transfer Function (FTF), $\mathcal{F}$, defined as a function of the excitation frequency f or pulsation frequency $\omega = \omega_r + i\omega_i$ of the oscillation.

$$\mathcal{F}(\omega) = \frac{\dot{q}'/\bar{\dot{q}}}{v_1'/\bar{v}} \tag{3.24}$$

$\mathcal{F}(\omega)$ is a complex number, its magnitude, $\mathcal{G}(\omega) = |\mathcal{F}(\omega)|$, and its argument, $\omega\tau = \varphi(\omega) = \arg(\mathcal{F}(\omega))$, correspond respectively to the gain, $\mathcal{G}$, and the phase-lag, φ, of the flame response. In the case of perfectly premixed combustion, it has been shown (*e.g.* Keller and Saito (1987)) that the flame surface is directly proportional to the heat release rate. Equation 3.24 takes the form:

$$\mathcal{F}(\omega) = \mathcal{G}e^{i\omega\tau} = \frac{\mathcal{A}'/\mathcal{A}_0}{v_1'/\bar{v}} \tag{3.25}$$

where $\mathcal{A}_0$ is the stationary flame surface. For harmonic fluctuations of velocity, $v_1' = \tilde{v}_1 e^{-i\omega t}$, and flame surface, $\mathcal{A}' = \tilde{\mathcal{A}} e^{-i\omega t}$, one obtains:

$$\tilde{\mathcal{A}} = \frac{\mathcal{A}_0}{\bar{v}} \mathcal{G}e^{i\omega\tau}\tilde{v}_1 \tag{3.26}$$

For mean quantities ($\mathcal{A}_0$ and $\bar{v}$), one can establish a relation between the injected flow rate, and the stationary flame surface, $\mathcal{A}_0$ by balancing the fresh gases flow rate at the burner outlet with the consumption of the flame (Selle *et al.* (2011)):

$$\rho_u Y_F \bar{v} S_s = \rho_u Y_F s_L \mathcal{A}_0 \tag{3.27}$$

where S_s is the slot cross-section area. The stationary flame surface can be written as $\mathcal{A}_0 = S_s\bar{v}/s_L$, and Eq. 3.25 becomes

$$\tilde{\mathcal{A}} = \frac{S_s}{s_L} \mathcal{G}e^{i\omega\tau}\tilde{v}_1 \tag{3.28}$$

Finally an expression linking the flame surface fluctuation, $\tilde{\mathcal{A}}$, to the velocity fluctuation at the burner outlet, $\tilde{v}_1$ has been derived. Thus, the left part of Fig. 2.8 is completed, the unsteady loop is now closed and the dispersion relation describing the coupling between combustion and acoustics can be established.

3.5 Dispersion relation

A dispersion relation which describes the combustion acoustics coupling observed experimentally is now derived. Combustion-acoustic coupling is here considered in the sense of system instability. A closed loop is stablished between the combustion process and the system acoustics. The thermo-acoustic system can be represented by a block diagram (Noiray (2007)), as shown in Fig. 3.4. It clearly shows the feedback loop through the burner acoustics, heat release rate and combustion noise. Self-sustained oscillations

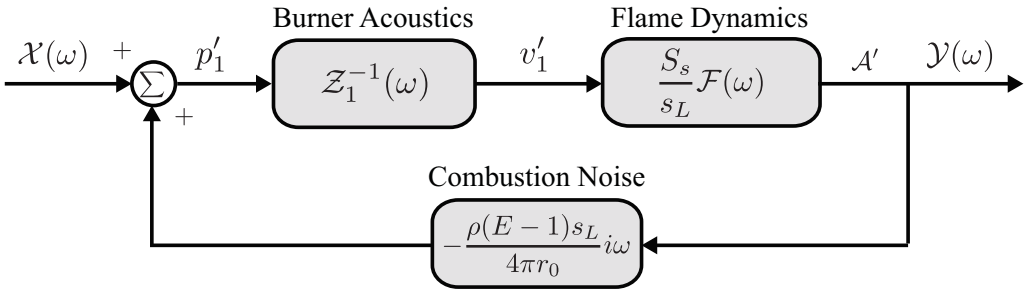

Figure 3.4: Block diagram representation of the feedback loop.

results from the interaction between these basic mechanisms which constitute the different blocks in Fig. 3.4 corresponding to Eqs. 3.15, 3.22 and 3.28. This block diagram corresponds to the qualitative resonant cycle presented in Fig. 2.8.

Making use of control theory concepts one can define the system transfer function ($\mathcal{STF}$) as:

$$\mathcal{STF} = \frac{\mathcal{Y}(\omega)}{\mathcal{X}(\omega)} = \frac{\mathcal{Z}_1^{-1}(\omega)\frac{S_s}{s_L}\mathcal{F}(\omega)}{1 + \mathcal{Z}_1^{-1}(\omega)\mathcal{F}(\omega)\frac{1}{4\pi}\frac{S_s}{r_0}\rho_u(E-1)i\omega} \tag{3.29}$$

the roots, ω, of the close loop system are found when the denominator is zero:

$$1 + \mathcal{Z}_1^{-1}(\omega)\mathcal{F}(\omega)\frac{1}{4\pi}\frac{S_s}{r_0}\rho_u(E-1)i\omega = 0 \tag{3.30}$$

Using the extended form of Eq. 3.5 gives (Durox *et al.* (2002, 2009a)):

$$\omega^2 + 2i\delta\omega - \omega_0^2 = -\frac{S_s}{4\pi h_e}\frac{E-1}{r_0}\omega^2\mathcal{F}(\omega) \tag{3.31}$$

Re-arranging Eq. 3.31 one obtains the final dispersion relation: a second order polynomial expression for the angular frequency ω:

$$\left[1 + \mathcal{N}e^{i\omega\tau}\right]\omega^2 + 2i\delta\omega - \omega_0^2 = 0 \tag{3.32}$$

where $\mathcal{N}$ is a coefficient that represents the magnitude of the interaction between the combustion noise and the flame dynamics and is defined as:

$$\mathcal{N} = \mathcal{C}\frac{1}{r_0}\mathcal{G} \tag{3.33}$$

The $\mathcal{C}$ factor depends only on the burner geometry (S_s and h_e) and the volumetric expansion E:

$$\mathcal{C} = \frac{1}{4\pi}\frac{S_s}{h_e}(E-1) \tag{3.34}$$

The stability of the system is determined by the complex roots of Eq. 3.32, $\omega = \omega_r + i\omega_i$. The burner will develop self-sustained combustion instabilities if the system has a positive growth rate or, $\omega_i > 0$. Figure 3.5 is a state space diagram of Eq. 3.32 that shows the growth rate solutions[1], ω_i, with respect to phase, φ_r, and arbitrary values of the combustion interaction coefficient, $\mathcal{N}$. In Fig. 3.5 colored regions pertain to iso-contours of positive growth rates ($\omega_i > 0$) or unstable regions while the white regions correspond to negative growth rates ($\omega_i < 0$) or stable regions. The system may develop self-sustained oscillations if the intersection between the phase and the interaction coefficient falls on a region where $\omega_i > 0$.

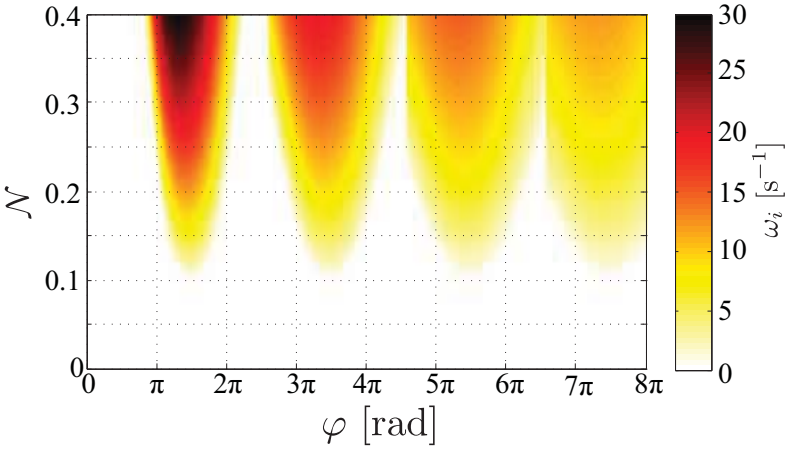

Figure 3.5: Stability map for arbitrary values of $\mathcal{N}$ based on Eq. 3.32. Colored regions pertain to iso-contours of positive values of growth rate ($\omega_i > 0$) or unstable regions while the white regions correspond to negative growth rates ($\omega_i < 0$) or stable regions

Figure 3.5 shows that the unstable regions are not the same for the case $[\pi, 2\pi]$ rad and the the cases $[\pi, 2\pi]$ rad modulo 2π, the reason for this behavior is that the solution of the dispersion equation is only valid around the natural resonance frequency of the burner, ω_0. Thus, for our case, the solution of this dispersion equation is only valid for the region of $\varphi \in [\pi, 2\pi]$ rad.

3.5.1 Parameters involved on the instability mechanism

The stability of the system is determined by the complex roots of Eq. 3.32. The complex roots, ω, are the eigenfrequencies of the system and depend on:

1. The geometry of the slot burner: the slot cross section, S_s, and the slot length, h_e.
2. The volumetric gas expansion E: determined by the thermal power released by the system, fixed by the mean flow characteristics (Φ and $\bar{v}$).
3. The acoustics characteristics of the burner: the natural pulsation frequency under non-reacting conditions ω_0 and the damping coefficient, δ. These two characteristics

[1] To find the complex roots of Eq. 3.32 we use the built in Matlab function "fsolve". $\mathcal{N}$ is discretized from 0 to 0.5 in steps of 0.0025, while φ from 0 to 8π rad in steps of 0.042 rad.

depend on the burner geometry (S_s, h_e and volume of the plenum, V_p) and the physical properties of the gas mixture (sound speed c, density ρ_u and kinematic viscosity ν).

4. The dynamical features of the flame: transfer function gain $\mathcal{G}$ and phase φ (both take at the frequency of oscillation) and the pinching altitude r_0 identified as the location of the acoustic monopole.

We have shown in Ch. 2 that burner stability can be controlled only by modifications on the slot temperature, T_s, which is not directly present in the dispersion relation (Eq. 3.32). It means that T_s has a secondary effect, modifying one or several of the parameters listed above.

In our experiments the burner geometry (S_s, h_e and V_p) and the operating conditions (Φ and $\bar{v}$) are kept constant. Thus items 1 and 2 can be discarded as responsible of the behavior seen in Fig. 2.1. On the other hand, the burner acoustics characteristics depend on the physical properties of the gas mixture (c, ρ_u and ν) which at the same time depend on the fresh gases temperature T_u. Even though the dual channel cooling system (*c.f.* Fig. 1.3) keeps the burner at almost ambient temperature, an increase in T_s may affect T_u and consequently change the acoustics characteristics of the burner (ω_0 and δ), and thus its stability. Thus the their sensitivity to T_s must be examined. Simultaneously, the dynamical features of the flame ($\mathcal{G}$, φ and r_0) depend, at the first order, on the flame geometry (Schuller *et al.* (2003b); Kornilov *et al.* (2007)) and the flame anchoring point dynamics (Rook and de Goey (2003); Kornilov *et al.* (2007); Altay *et al.* (2009); Cuquel *et al.* (2013)). Which at the same time are very sensitive to the laminar flame speed, s_L, and the local flame speed at the flame root, $s_{L(\psi_{f0})}$, respectively. The laminar flame speed, s_L depends on the fresh gases temperature, T_u (Gu *et al.* (2000); Poinsot and Veynante (2011)), that, as we said before, can be affected by the slot temperature T_s. Likewise, the local flame speed at the anchoring point, $s_{L(\psi_{f0})}$, may be affected by the temperature of the solid boundaries as well.

Summarizing: for fixed operating conditions, the system stability may be affected by the indirect effect of the slot temperature, T_s, on one of the following five parameters: the natural pulsation frequency, ω_0, the damping coefficient, δ, the pinching altitude from the source of noise to the burner outlet, r_0 , the gain, $\mathcal{G}$, and the phase lag, $\varphi = \omega\tau$ of the flame response.

3.5.2 Stability criteria: approximate analytical solution

Due to the presence of ω in the exponential term of Eq. 3.32 one can not solve the system directly. However, assuming that combustion only introduces a perturbation so that the eigenfrequencies, ω, remain close to their values in a non-reacting case, ω_{nr}, ($\omega \approx \omega_{nr}$) one can solve the system analytically and have a better idea of the mechanism and the parameters leading to positive growth rate ($\omega_i > 0$). We can re-write Eq. 3.32 as:

$$f(\omega, \mathcal{N}) = \omega^2(1 + \mathcal{N}e^{i\omega_{nr}\tau}) + 2i\delta\omega - \omega_0^2 = 0 \tag{3.35}$$

Considering a solution of Eq. 3.35 without combustion ($\mathcal{N} = 0$):

$$\omega_{nr} = \omega_{nr\Re} - i\delta \tag{3.36}$$

where $\omega_{nr\Re} = \omega_0\sqrt{1-(\delta/\omega_0)^2}$. The damping coefficient is always positive, hence, Eq. 3.36 tell us that in absence of combustion the system is always stable, it can only enter in resonance by the effect of an external excitation.
We reach the solutions of Eq. 3.35 for a weak combustion-acoustic interaction ($\mathcal{N} \ll 1$) as $\omega = \omega_{nr} + \mathrm{d}\omega$, where $\mathrm{d}\omega$ is a first-order expansion that can be expressed using the Implicit Function Theorem:

$$\mathrm{d}f = \left.\frac{\partial f}{\partial \omega}\right|_{(\omega_{nr},\mathcal{N}=0)} \mathrm{d}\omega + \left.\frac{\partial f}{\partial \mathcal{N}}\right|_{(\omega_{nr},\mathcal{N}=0)} \mathrm{d}\mathcal{N} = 0 \tag{3.37}$$

re-arranging Eq. 3.37 one may obtain an expression for $\mathrm{d}\omega$ of the form:

$$\mathrm{d}\omega = -\frac{\partial f/\partial \mathcal{N}}{\partial f/\partial \omega}\mathrm{d}\mathcal{N} = -\frac{\omega_{nr}^2 e^{i\omega_{nr}\tau}}{2\omega_{nr}+2i\delta}\mathrm{d}\mathcal{N} \tag{3.38}$$

Injecting the solution without combustion (Eq. 3.36) in Eq. 3.38

$$\begin{aligned}\mathrm{d}\omega = &\frac{\delta^2\cos(\omega_{nr\Re}\tau) - 2\delta\omega_{nr\Re}\sin(\omega_{nr\Re}\tau) - \omega_{nr\Re}^2\cos(\omega_{nr\Re}\tau)}{2\omega_{nr\Re}} e^{\delta\tau}\mathrm{d}\mathcal{N} \\ &+ \frac{i\delta^2\sin(\omega_{nr\Re}\tau) + 2i\delta\omega_{nr\Re}\cos(\omega_{nr\Re}\tau) - i\omega_{nr\Re}^2\sin(\omega_{nr\Re}\tau)}{2\omega_{nr\Re}} e^{\delta\tau}\mathrm{d}\mathcal{N}\end{aligned} \tag{3.39}$$

Making the reasonable assumption that the damping coefficient, δ, is small compared to the natural pulsation of the burner, ω_0, and that the normalized time delay, $\tau/T_0 = \tau\omega_0/2\pi$, is of the order of unity, ($\delta \ll \omega_0$ and $\delta\tau \ll 1$) then one may develop Eq. 3.39 through the first order Taylor expansion to yield:

$$\mathrm{d}\omega = -\frac{\omega_{nr\Re}\cos(\omega_{nr\Re}\tau)}{2}\mathrm{d}\mathcal{N} - \frac{i\omega_{nr\Re}\sin(\omega_{nr\Re}\tau)}{2}\mathrm{d}\mathcal{N} \tag{3.40}$$

keeping in mind that terms in $\delta\,\mathrm{d}\mathcal{N}$ are of second order and recalling that:

$$\Re\{\omega\} = \Re\{\omega_{nr}\} + \Re\{\mathrm{d}\omega\} \tag{3.41}$$
$$\Im\{\omega\} = \Im\{\omega_{nr}\} + \Im\{\mathrm{d}\omega\} \tag{3.42}$$

one obtains the real and imaginary solution of Eq. 3.35:

$$\Re\{\omega\} = \omega_{nr\Re} - \frac{\omega_{nr\Re}\cos(\omega_{nr\Re}\tau)}{2}\mathrm{d}\mathcal{N} = \omega_0 - \frac{\omega_0\cos(\omega_0\tau)}{2}\mathrm{d}\mathcal{N} \tag{3.43}$$
$$\Im\{\omega\} = -\delta - \frac{\omega_{nr\Re}\sin(\omega_{nr\Re}\tau)}{2}\mathrm{d}\mathcal{N} = -\delta - \frac{\omega_0\sin(\omega_0\tau)}{2}\mathrm{d}\mathcal{N} \tag{3.44}$$

here we assumed that $\omega_{nr\Re} \approx \omega_0$ as $\delta \ll \omega_0$. The complex pulsation of the system is described by its resonance pulsation frequency $\omega_r = \Re\{\omega\}$ and its growth rate $\omega_i = \Im\{\omega\}$.

The system will develop self-sustained combustion oscillations if its complex pulsation has a positive growth rate, thus $\omega_i > 0$:

$$\mathrm{d}\mathcal{N}\sin(\omega_0\tau) < -\frac{2\delta}{\omega_0} \tag{3.45}$$

Taking into account that $\mathrm{d}\mathcal{N} = (\mathcal{C}/r_0)\mathcal{G}(\omega_0)$ one obtains a criteria for the stability of the system:

$$\mathcal{N} < -\frac{2\delta}{\omega_0\sin(\varphi_0)} \quad \text{or} \quad \frac{\mathcal{C}}{r_0}\mathcal{G}_0 < -\frac{2\delta}{\omega_0\sin(\varphi_0)} \tag{3.46}$$

where $\mathcal{G}_0 = \mathcal{G}(\omega_0)$ and $\varphi_0 = \omega_0\tau$ are respectively the gain and phase of the FTF taken at the natural pulsation frequency of the burner ω_0.

Equation 3.46 is a linear stability criterion, which indicates that, in presence of dissipation (*i.e.* $\delta \neq 0$), the occurrence of a combustion instability depends on the phase-lag, φ_0, and the gain, $\mathcal{G}_0$, of the flame response, as well as the pinching distance r_0 and the acoustic characteristics of the burner ω_0 and δ.

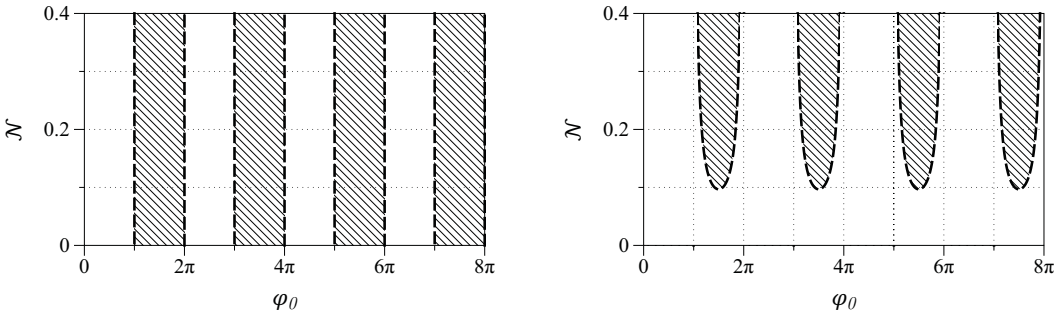

(a) Idealized system without damping $\delta = 0$

(b) System with damping $\delta \neq 0$

Figure 3.6: Stability map for arbitrary values of $\mathcal{N}$ based on Eq. 3.46. The diagonal solid patterns represent the unstable zones.

Figure 3.6 shows the solutions of Eq. 3.46, for arbitrary values of $\mathcal{N}$ and for two different cases: left, when the damping coefficient is zero ($\delta = 0$), and, right, when the damping coefficient is not zero ($\delta \neq 0$). One can think of Fig. 3.6 as a qualitative stability map where the unstable zones are shown in diagonal line pattern bounded by the dashed curve (----) which is the solution of $\mathcal{N} = (\mathcal{C}/r_0)\mathcal{G}_0$, while the stable zones are in white. One can conclude from Fig. 3.6 that without dissipation, ($\delta = 0$) the system may develop self-induced oscillations when the acoustic energy produced by unsteady combustion is fed into the system. This condition is ensured when $\sin(\varphi_0) < 0$, for example for values of φ_0 between $[\pi, 2\pi]$ modulo 2π. In the presence of system dissipation, ($\delta \neq 0$), this condition is necessary to create the oscillations, but it is not sufficient. An oscillation really develops when the energy fed into the system exceeds the energy that is dissipated.

Even if the phase-lag condition is fulfilled the magnitude of the interaction coefficient, $\mathcal{N} = (\mathcal{C}/r_0)\mathcal{G}_0$, must be sufficient to drive the system into an instability.

3.5.3 Comparison between the exact and the approximate solution of the dispersion relation

Now we are interested in evaluating the accuracy of the approximate analytical solution derived in Sec. 3.5.2. We can achieve this by comparing the results of Eq. 3.46 with the numerical solution of Eq. 3.32. The domain chosen for the arbitrary values of the interaction coefficient and the phase was $\mathcal{N} \in [0, 0.4]$ and $\varphi \in [0, 8\pi]$ rad, respectively. For the exact solution the domain was discretized by steps of $\Delta\mathcal{N} = 0.0025$ and $\Delta\varphi = 0.042$ rad for $\mathcal{N}$ and φ, respectively.

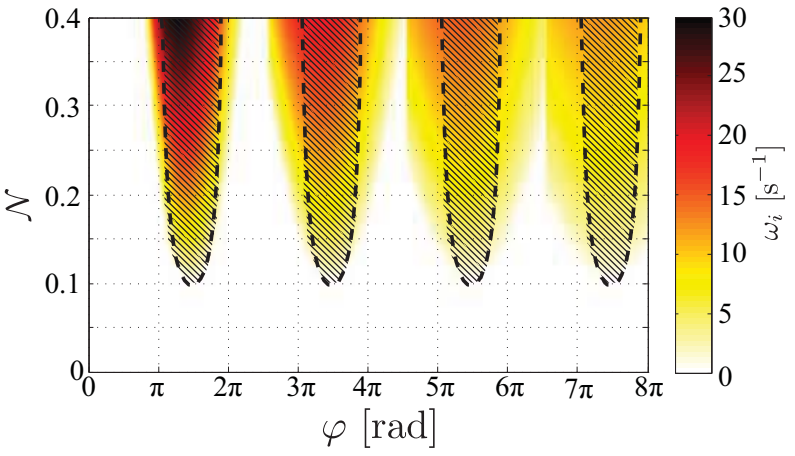

Figure 3.7: Comparison between the exact solution (Eq. 3.32) and the approximate analytical solution (Eq. 3.46). For arbitrary values of $\mathcal{N}$.

Figure. 3.7 presents the superposition of both solutions, the exact and the approximate solution. The exact solution is represented by the iso-contours of the positive values of ω_i, in the white region ω_i has vanished or has negative values. The solution of the approximate solution is superposed, the solid diagonal line patterns represents the values of $\mathcal{N}$ and φ for which ω_i has positive values bounded by the solution of $\mathcal{N}$ (----). The region where the colored regions do not intersect the solid patterns correspond to the potential unstable regions that the approximate analytical solution can not capture. In a global manner the approximate solution is able to capture the stability of the system. At high values of $\mathcal{N}$ the approximate solution may miss some unstable modes, which is logic considering that we assume that $\mathcal{N} \ll 1$. For small values of $\mathcal{N}$ however, the approximate and that exact solution of the dispersion equation have a really good agreement, specially for the range $\varphi \in [\pi, 2\pi]$. This region is where the self sustained instability develops for low slot temperatures[2] ($T_s < 70$ °C). Thus, for this setup the approximate analytical stability criteria can be used to evaluate the stability of the system.

[2] In Ch. 2 we measured the phase-lag, φ, between the velocity and the heat release rate signals and we found that φ is around 1.15π rad *cf.* (Fig. 2.7).

3.6 Conclusion

In this chapter we study the basic mechanisms leading to combustion instabilities: burner acoustic, flame dynamics and combustion noise. These mechanisms are linked in a close loop where the combustion process and the system acoustics interact. Thanks to a block diagram and control theory we were able to establish a system transfer function ($\mathcal{STF}$) which roots represent the complex pulsation of the system ($\omega = \omega_r + i\omega_i$). The sign of the imaginary part of the complex pulsation (ω_i) determines the stability of the system: if ω_i is positive the system will develop self sustained oscillations, on the contrary if ω_i is negative the system will be stable. At the same time we were able to determine several parameters that play a roll in the instability of the system; five of them are susceptible to be affected by the slot temperature T_s:

- ω_0 and δ, related to the acoustics properties of the burner. ω_0 and δ are respectively the natural pulsation and the damping coefficient of the burner with out combustion.
- r_0, from combustion noise. r_0 measures the distance between the slot exit and the acoustic monopole.
- $\mathcal{G}$ and φ, represent the flame response to acoustics. $\mathcal{G}$ and φ are respectively gain and phase-lag of the FTF take at the frequency of the instability.

Because we have shown in Ch. 2 that for this configuration, the occurrence of a combustion instability can be controlled by the burner rim temperature, T_s, our objective is now to elucidate how the five parameters appearing in 3.32 (ω_0, δ, r_0, $\mathcal{G}$ and φ) are affected by, T_s. A chapter is dedicated to each set of parameters: Ch. 4 for acoustics (ω_0 and δ), Ch. 5 for combustion noise (r_0), and Ch. 6 for flame response ($\mathcal{G}$ and φ).

An approximate solution assuming that combustion only introduces a perturbation so that the eigenfrequencies, ω, remain close to their values in a non-reacting case ω_0 has been derived. It describes the stability of combustion in the experimental setup of Fig 1.1. For low values of $\mathcal{N}$ the approximate analytical solution is able to capture almost all the possible unsteady modes described the exact solution of the dispersion equation (Eq. 3.32). Such a derivation is not new and similar derivations can be found in previous studies (Matveev and Culick (2003); Schuller *et al.* (2003a); Morgans and Dowling (2007); Noiray *et al.* (2008)). This approximate stability criteria will be used all along the following chapters to quantify the influence of the five parameters (ω_0, δ, r_0, $\mathcal{G}_0$ and φ_0) on the stability of the system.

Part II

Experimental results

Chapter 4

Burner acoustics

The response of the burner to acoustic perturbations can be characterized in non-reacting and reacting experiments. Tests are performed for the two reference non-reacting cases T50c and T90c and the three reacting cases T50h, T90h and T120h in order to evaluate the influence of the slot temperature on the global acoustic characteristics of the burner. Flow conditions are kept constant: for non-reacting cases the bulk velocity is $\bar{v} = 1.6\ ms^{-1}$*, while in reacting cases the bulk velocity and equivalence ratio are* $\bar{v} = 1.6\ ms^{-1}$ *and* $\Phi = 0.95$*, respectively.*
The objective is to determine experimentally the parameters that play a role in the linear stability analysis (ω_0 *and* δ *in Eq. 3.32 of Ch. 3). Two methods are used to characterize the acoustic properties of the burner: the harmonic response (HR) and the impulse response (IR).*
This chapter is organized as follows: first, the governing equations of the acoustic are presented in Sec 4.1, these equations are used to derive an expression that describes the acoustics of the slot burner, and experimental methodologies are based on this expression. After that the acoustic tests under non-reacting conditions are performed in Sec 4.2, followed by the tests performed under reacting conditions in Sec 4.3, and a summary in Sec 4.4. Finally a general conclusion is presented Sec. 4.6.

4.1 Governing equations

The objective of this section is to derive an equation which will be the base for the experimental determination of the burner acoustic characteristics ω_0 and δ. A burner acoustic analysis was already performed in Sec. 3.2 assuming that the burner was a Helmholtz resonator and that the pulsation ω was close to the first resonance frequency of the system, ω_0. In this section however we intent to derive an expression that is true for all frequencies and we assume that the burner is a network of two compact elements connected by an interface. For this purpose we first start by studying the fundamental equations. The present configuration can be described by the non-reacting equations as the present configuration at ambient temperature during combustion operation, except close to the flame anchoring point where the flame is close to the burner rim. Conservation of mass and

momentum in a non-viscous, non-reacting flow are (Poinsot and Veynante (2011)).

$$\frac{\partial \rho}{\partial t} + \bigtriangledown . \rho \vec{\mathbf{u}} = 0 \tag{4.1}$$

$$\frac{\partial \vec{\mathbf{u}}}{\partial t} + \rho \vec{\mathbf{u}} \bigtriangledown \vec{\mathbf{u}} = - \bigtriangledown p \tag{4.2}$$

In the same way that in Ch. 3, one can decompose the pressure, p, velocity, $\vec{\mathbf{u}}$ and density, ρ, in mean ($^-$) and first-order fluctuation ($'$). Assuming low Mach number $\mathrm{M_a} \ll 1$, the linearization of Eqs. 4.1 and 4.2 yields:

$$\frac{\partial \rho'}{\partial t} + \bar{\rho} \bigtriangledown . \mathbf{u}' = 0 \tag{4.3}$$

$$\bar{\rho} \frac{\partial \mathbf{u}'}{\partial t} + \bigtriangledown p' = 0 \tag{4.4}$$

The linearization of the equation of state yields:

$$\gamma p' = c^2 \rho' + \bar{\rho} \gamma r T'_u \tag{4.5}$$

Equations 4.3, 4.4 and 4.5 combined with the linearized Laplace's law (*cf.* Eq. 3.6) derived in Sec. 3.2 yields the wave equation:

$$\bigtriangledown^2 p' - \frac{1}{c^2} \frac{\partial^2 p'}{\partial t^2} = 0 \tag{4.6}$$

Assuming harmonic oscillations the Helmholtz wave equation becomes:

$$\bigtriangledown^2 \tilde{p} + k \tilde{p} = 0 \tag{4.7}$$

here $k = \omega / c$ is the wave number and ω is the angular frequency.

4.1.1 Acoustic analysis of networks of compact elements

Acoustic networks of compact elements have been widely used in the study of combustion instabilities (*e.g.* Truffin and Poinsot (2005); Palies *et al.* (2011); Poinsot and Veynante (2011); Schuller *et al.* (2012)). A simplification of the experimental setup is presented in Fig. 4.1. One can think of this system as a first duct of cross section S_p and length l_p connected to a second duct of cross section S_s and length h_s, through an abrupt section change.

Considering a plane wave that propagates only in the longitudinal direction $\mathbf{u}' = (0, v', 0)$, a solution to Eq. 4.6 is the superimposition of two traveling waves in each duct of the burner. One is traveling in the positive direction and the other is traveling in the negative direction:

$$p'_j(y,t) = A_j^+ e^{j(ky - \omega t)} + A_j^- e^{j(-ky - \omega t)}$$

$$v'_j(y,t) = \frac{1}{\rho_u c} \left(A_j^+ e^{j(ky - \omega t)} - A_j^- e^{j(-ky - \omega t)} \right)$$

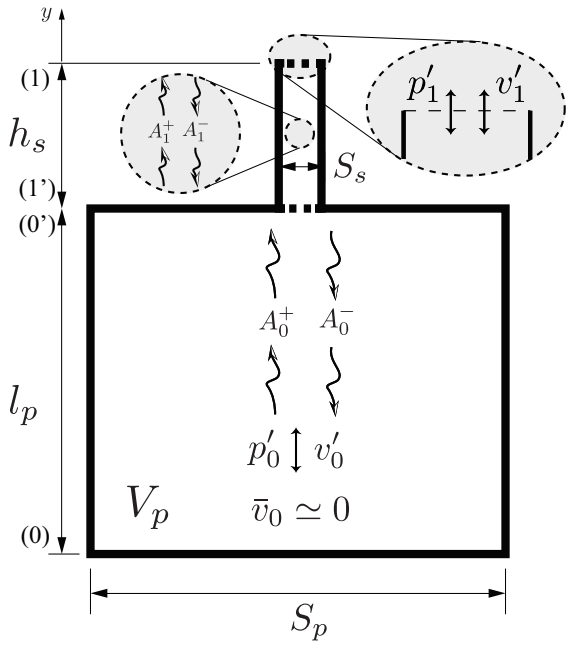

Figure 4.1: Schematic representation of the Helmholtz resonator.

where $j = 0, 1$. In the first segment between sections 0 to $0'$, the harmonic acoustic fluctuations are:

$$\tilde{p}_0 = A_0^+ e^{iky} + A_0^- e^{-iky} \tag{4.8}$$

$$\tilde{v}_0 = \frac{1}{\rho_u c}\left[A_0^+ e^{iky} - A_0^- e^{-iky}\right] \tag{4.9}$$

in the second segment between sections $1'$ to 1 acoustic fluctuations are:

$$\tilde{p}_1 = A_1^+ e^{ik(y-l_p)} + A_1^- e^{-ik(y-l_p)} \tag{4.10}$$

$$\tilde{v}_1 = \frac{1}{\rho_u c}\left[A_1^+ e^{ik(y-l_p)} - A_1^- e^{-ik(y-l_p)}\right] \tag{4.11}$$

In these expressions, A_0^+, A_0^-, A_1^+ and A_1^- are the amplitudes of the incident and reflected traveling waves of each side of the interface $(0' - 1')$. The values of these coefficients are determined by the boundary conditions at the interface.

- section (0) is a rigid wall, and the acoustic velocity goes to zero:

$$\tilde{v}_0(y = 0, t) = 0 \tag{4.12}$$

- at the interface (0'-1'), the acoustic pressure and flow rate are conserved:

$$S_p \tilde{v}_0(y = l_p, t) = S_s \tilde{v}_1(y = l_p, t) \tag{4.13}$$

$$\tilde{p}_0(y = l_p, t) = \tilde{p}_1(y = l_p, t) \tag{4.14}$$

- section (1) is the outlet, the acoustic pressure is in equilibrium with the external acoustic pressure:

$$\tilde{p}_1(y = l_p + h_s, t) = \tilde{p}_1 \tag{4.15}$$

In the absence of an external pressure perturbation $\tilde{p}_1 = 0$.

Combining Eqs. 4.12 to 4.15 with the acoustic fluctuations Eqs. 4.8 to 4.11, one obtains a linear system for the amplitudes A_0^+, A_0^-, A_1^+ and A_1^-. which can be written in matrix form, $T\mathbf{x} = b$, where:

$$\mathbf{x} = [A_0^+ \ A_0^- \ A_1^+ \ A_1^-]^T \tag{4.16}$$

corresponds to the vector formed by the complex wave amplitudes, and, where the right-hand side:

$$b = [0 \ 0 \ 0 \ \tilde{p}_1]^T \tag{4.17}$$

is a source term associated to an acoustic perturbation applied at the burner outlet. These vectors are linked by the transfer matrix T:

$$T = \begin{bmatrix} 1 & -1 & 0 & 0 \\ e^{ikl_p} & e^{-ikl_p} & -1 & -1 \\ e^{ikl_p} & -e^{-ikl_p} & -1/\Gamma & 1/\Gamma \\ 0 & 0 & e^{ikh_s} & e^{-ikh_s} \end{bmatrix} \tag{4.18}$$

where Γ is the interface cross section ratio $\Gamma = S_p/S_s$.

4.1.2 Burner eigenfrequencies

Without external pressure perturbation, $\tilde{p}_1$=0, the modes of the linear system correspond to nontrivial solutions of $\det T = 0$, thus the burner eigenfrequencies are determined by:

$$0 = \cos(kl_p)\cos(kh_s) - \Gamma \sin(kl_p)\sin(kh_s) \tag{4.19}$$

The acoustic wave length is of the order of $\lambda_{ac} = c/f_r \approx 6$ m[1], while the total length of the burner is of the order of $l_p + h_s \approx 0.5$ m. Thus, the acoustic wave length is big relative to the size of the system, $k(l_p + h_s) \ll 1$. A first order Taylor expansion in kl_p and kh_s of this expression give us:

$$1 - \Gamma k^2 \, l_p \, h_s = 0 \tag{4.20}$$

This expression is valid if the cross section ratio is large $\Gamma \gg 1$. The Helmholtz mode corresponds to the first resonance frequency of the system:

$$\omega_H^2 = \frac{c^2}{\Gamma l_p h_s}, \ or \ f_H = \frac{c}{2\pi}\sqrt{\frac{S_s}{h_s V_p}} \tag{4.21}$$

where V_p is the volume of the plenum $V_p = S_p l_p$. Assuming that the natural pulsation of the burner corresponds to the first resonance of the system one can say that $\omega_0 = \omega_H$.

[1]We recall that the frequency of the instability, f_r, was measured in Ch. 2 and it lies around 58 Hz

4.1.3 Internal pressure fluctuation due to external perturbation

We are interested in finding an expression for the induced pressure fluctuation at the plenum, $\tilde{p}_0$, in terms of an acoustic pressure excitation that acts at the burner outlet, $\tilde{p}_1$. This expression will be the base for the determination of the burner acoustic characteristics (ω_0 and δ) for the HR and IR tests. From Eqs. 4.8 and 4.10 one can write:

$$\frac{\tilde{p}_0(y=0)}{\tilde{p}_1(y=l_p+h_s)} = \frac{A_0^+ + A_0^-}{A_1^+ e^{ikh_s} + A_1^- e^{-ikh_s}} \tag{4.22}$$

At the same time, from the boundary conditions (Eq. 4.12 to 4.15) one gets:

$$A_0^+ = A_0^- \tag{4.23}$$

$$A_1^+ = \frac{1}{2}A_0^+ \left[(e^{ik\,l_p} + e^{-ik\,l_p}) + \Gamma(e^{ik\,l_p} - e^{-ik\,l_p})\right] \tag{4.24}$$

$$A_1^- = \frac{1}{2}A_0^+ \left[(e^{ik\,l_p} + e^{-ik\,l_p}) - \Gamma(e^{ik\,l_p} - e^{-ik\,l_p})\right] \tag{4.25}$$

combining Eqs. 4.22 throughout 4.25 one obtains an expression for the pressure fluctuation in the plenum induced by an external pressure perturbation:

$$\frac{\tilde{p}_0}{\tilde{p}_1} = \frac{1}{\cos(kl_p)\cos(kh_s) - \Gamma\sin(kl_p)\sin(kh_s)} \tag{4.26}$$

In the long acoustic wavelength limit a first-order Taylor expansion in kl_p and kh_s of this Eq. 4.26 gives:

$$\frac{\tilde{p}_0}{\tilde{p}_1} = \frac{1}{1 - \Gamma k^2 l_p h_s} = \frac{1}{1 - \omega^2/c^2(V_p h_s/S_s)} \tag{4.27}$$

Injecting Eq. 4.21 in Eq. 4.27 gives us an expression for the internal pressure fluctuation in terms of an external acoustic perturbation, $\tilde{p}_1$:

$$\frac{\tilde{p}_0}{\tilde{p}_1} = \frac{1}{1 - (\omega/\omega_0)^2} \tag{4.28}$$

The interesting case is that corresponding to resonance. When $\omega = \omega_0$, the ratio $\tilde{p}_0/\tilde{p}_1$ goes to infinity. In real applications this ratio is limited by the dissipation of the system that for this case is mainly due to the acoustic loses in the slot and for small amplitude of fluctuations it is proportional to the velocity fluctuation. Taking into account the damping of the system Eq. 4.28 becomes (Fernandes and Leandro (2006); Durox *et al.* (2009a)):

$$\frac{\tilde{p}_0}{\tilde{p}_1} = \frac{1}{1 - (\omega/\omega_0)^2 + 2i\delta\omega/\omega_0^2} \tag{4.29}$$

In the time domain Eq. 4.29 corresponds to a second order differential equation with a forcing term:

$$\frac{\mathrm{d}^2 p_0'}{\mathrm{d}t^2} + 2\delta\frac{\mathrm{d}p_0'}{\mathrm{d}t} + \omega_0^2 p_0' = \omega_0^2 p_1' \tag{4.30}$$

This equation is similar to that derived in Sec. 3.2, however, here we do not assume that the pulsation ω lies around the natural pulsation of the burner ω_0, thus Eq. 4.30 is valid for all frequencies. Equation 4.30 tells us that the burner behaves as a damped harmonic oscillator driven by an external perturbation p'_1. We have seen that under reacting conditions p'_1 comes from unsteady combustion (*c.f.* Sec. 3.3), however, under a non-reacting configuration $p'_1 = 0$, thus the external perturbations should be induced by an external component, a loudspeaker for example.

4.2 Acoustics in non-reacting flow

The study of this system (Eq. 4.30) under non-reacting configuration will provide part of the information information needed to solve the linear stability system proposed in Ch. 3. We recall that the aim of this chapter is to find the acoustic parameters that play a role in the stability of the system (ω_0 and δ) and their sensitivity to T_s. This study relays in Eq. 4.30 which can be studied in two different ways: one can study the response of the burner to a short perturbation without a driving force $p'_1 = 0$. This method is equivalent to the impulse response of the burner; or one can study the response of the burner to an external driving perturbation $p'_1 = \tilde{p}_1 e^{-i\omega t}$, this method is equivalent to the harmonic response of the burner. Here we will explore both approaches by perturbing the plenum with a loudspeaker.

4.2.1 Impulse response IR

When the system is drive out of its steady state by a very short perturbation and in the absence of a maintained external acoustic perturbation $p'_1 = 0$, it behaves as a damped harmonic oscillator, and its response is equivalent to study the homogeneous solution of Eq. 4.30:

$$\frac{\mathrm{d}^2 p'_0}{\mathrm{d}t^2} + 2\delta \frac{\mathrm{d}p'_0}{\mathrm{d}t} + \omega_0^2 p'_0 = 0 \tag{4.31}$$

The characteristic polynomial leads to the eigenfrequencies:

$$\omega_{nr} = -i\delta + \omega_{nr\Re} \tag{4.32}$$

where $\omega_{nr\Re} = \omega_0 \sqrt{1 - (\delta/\omega_0)^2}$. The damping coefficient is always positive $\delta > 0$ and small compared to the natural pulsation of the burner $\delta \ll \omega_0$. The solution to Eq. 4.31 correspons to that of an underdamped system:

$$p'_0(t)/p'_{0_{max}} = e^{-(\delta/2)t} \cos(\omega_{nr\Re} t) \tag{4.33}$$

Or:

$$v'_1(t)/v'_{1_{max}} = e^{-(\delta/2)t} \cos(\omega_{nr\Re} t) \tag{4.34}$$

Equation 4.34 shows that in the case of an underdamped system ($\delta \ll \omega_0$) a perturbation on the mean velocity will drive the system out of its steady state. The system will recover steady after a time τ_{ss} that depends on the natural frequency of the system ω_0 and the damping coefficient δ. The system returns to steady state in an oscillatory motion (with a slightly different frequency $\omega_{nr\Re}$ than the natural frequency, ω_0). The burner response is presented in Fig. 4.2, where an arbitrary value of $\delta/\omega_0 = 0.05$ was chosen to solve Eq. 4.34.

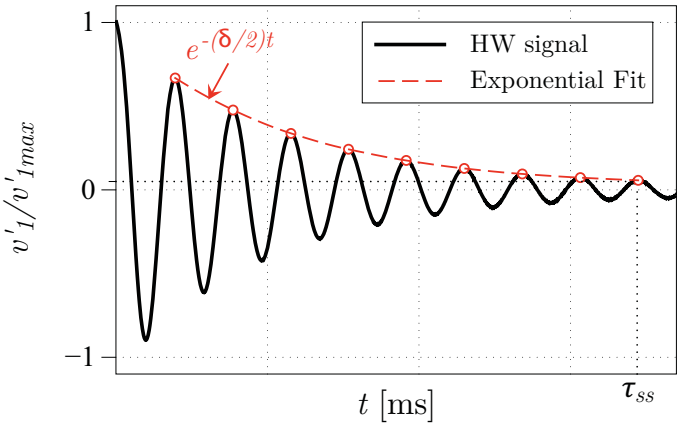

Figure 4.2: Theoretical example of the burner response, $v'_1/v'_{1_{max}}$, submitted to internal impulse perturbation, δ_{IR}.

IR experimental setup

Figure 4.2 suggest that one can determine the acoustic characteristics of the burner by measuring the internal pressure p'_0 or the velocity in the slot v'_1 while the system recovers its steady state after a short perturbation. It can be achieved by sending a short electronic impulse signal δ_{IR} to the loudspeaker placed at the bottom of the chamber and recording the internal pressure with microphone M_0 or the velocity in the slot with the hot-wire (HW). Figure 4.3 shows the experimental setup used to measure the acoustic characteristics of the burner with the IR test.

IR experimental results

Figure 4.4 shows the impulse response for the velocity fluctuation in the slot, v'_1,for the B07 burner and for the cases T50c and T90c, the bulk velocity is kept constant during the experiment at $\bar{v} = 1.6$ ms^{-1}. The impulse signal sent to the amplifier and to the loudspeaker corresponds to a dirac delta function of form:

$$\delta_{IR}(t) = 1/(a\sqrt{\pi})e^{-(5000t)^2/a^2} \tag{4.35}$$

where $a = 2.8209$. The impulse is sent 40 times and spaced by 20 s, for each case. The final impulse response is the averaged velocity signal over the 40 repetitions. Assuming

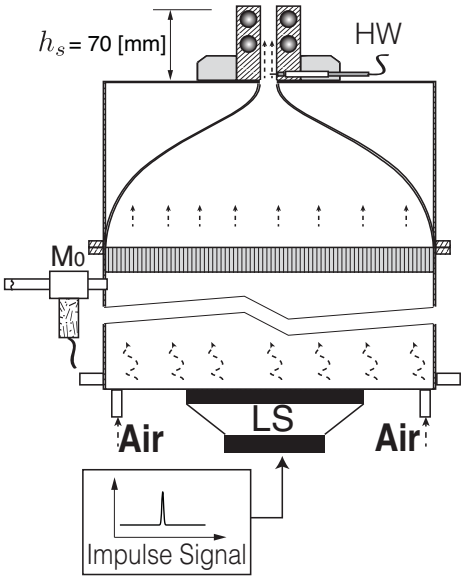

Figure 4.3: Experimental setup used for the impulse response (IR) experiments. The short impulse signal sent to the amplifier and to the loudspeaker place in the bottom of the plenum. A microphone (M_0) and a hot-wire (HW) are used to record the internal pressure and velocity in the slot.

that $\omega_{nr\Re} \approx \omega_0$ as $\delta/\omega_0 \ll 1$ an optimal fit to the averages signal permits to calculate the natural pulsation of the burner, ω_0, and the damping coefficient, δ.

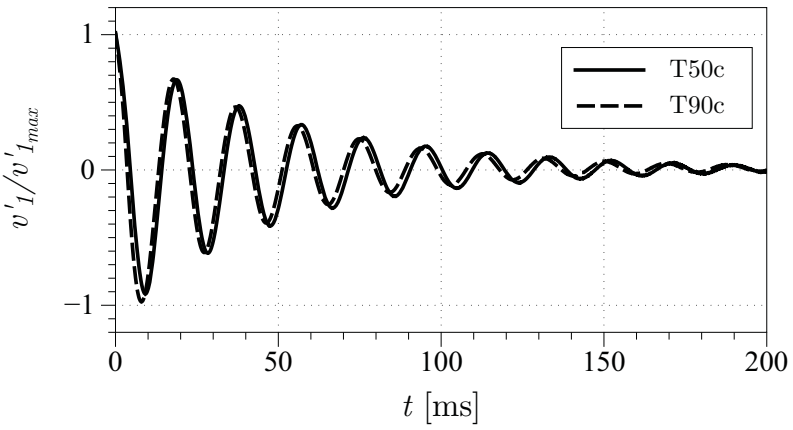

Figure 4.4: Impulse response of the B07 burner under non-reacting conditions. T50c (——), T90c (- - - -). Bulk velocity was $\bar{v} = 1.6$ ms^{-1}.

Figure 4.4 shows the results of the IR test under non-reacting conditions. Results are consistent with Eq. 4.34, the system recovers its steady state in oscillatory motion in 200 ms. Results are practically independent of the slot temperature, T_s, as the curves for T50c and T90c coincide. However, a very little increment in ω_0 and δ is noticed when the slot temperature is increased. Table 4.2 summarizes the results of the IR test, ω_0 increases by only 1.5 % and δ by 0.3 % for case T50c to case T90c. In addition, $\delta/\omega_0 \approx 0.05$ for

both cases, validating the assumption $\delta/\omega_0 \ll 1$ is valid.

Table 4.1: Summary of the results from the impulse test.

Case	B07	
	$\omega_0/2\pi$ [Hz]	δ [s^{-1}]
T50c	52.4	16.3
T90c	53.1	16.8

4.2.2 Harmonic response HR

In the presence of a maintained external acoustic perturbation $p_1' = \tilde{p}_1 e^{-i\omega t}$ one can assume that the burner behaves as a forced damped harmonic oscillator and use Eq. 4.29. The response of the burner is represented by the modulus of Eq. 4.29 ($\mathcal{P}(\omega) = \Re\{(\tilde{p}_0/\tilde{p}_1)^2\}$), which writes:

$$\mathcal{P}(\omega) = \frac{1}{\omega_0^4 \left[\left(1-(\omega/\omega_0)^2\right)^2 + 4\,(\delta/\omega_0)^2\,(\omega/\omega_0)^2\right]} \tag{4.36}$$

Equation 4.36 is plotted in Fig. 4.6 for a value of $\delta/\omega_0 = 0.05$. One can notice that the maximal response of the burner is centered over a frequency $\omega_{nr\Re} = \omega_0\sqrt{1-(\delta/\omega_0)^2}$.

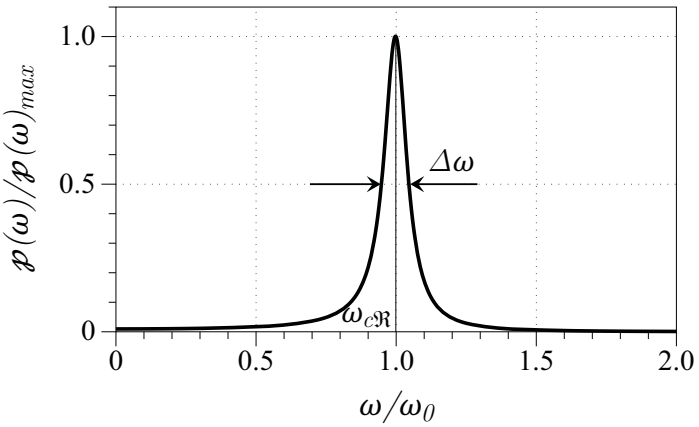

Figure 4.5: Burner response calculated from Eq. 4.36 for $\delta/\omega_0 = 0.05$.

Assuming that the response $\mathcal{P}(\omega)$ is symmetric over $\omega_{nr\Re}$ one can define the full width half maximum as:

$$\Delta\omega = 2(\omega_{nr\Re} - \omega_{1/2}) \tag{4.37}$$

where $\omega_{1/2}$ is the pulsation frequency at the half maximum of burner response with $\mathcal{P}(\omega_{1/2}) = \mathcal{P}(\omega_{nr\Re})/2$:

$$\frac{1}{(\omega_0^2 - \omega_{1/2}^2)^2 + 4\delta^2\omega_{1/2}^2} = \frac{1}{4}\frac{1}{(\omega_0^2 - \omega_{nr\Re}^2)^2 + 4\delta^2\omega_{nr\Re}^2} \tag{4.38}$$

Taking into account that $\omega_{nr\Re}^2 = \omega_0^2 - \delta^2$, one can re-write Eq. 4.38 as:

$$\omega_{1/2}^4 - 2\omega_{1/2}^2\omega_0^2\left[1 - 2(\delta/\omega_0)^2\right] + \omega_0^4\left[1 - 16(\delta/\omega_0)^2 + 16(\delta/\omega_0)^4\right] = 0 \tag{4.39}$$

Ignoring all the terms of $\mathcal{O}(\delta^2/\omega_0^2)$ and $\mathcal{O}(\delta^4/\omega_0^4)$ one finds that $\omega_{1/2} = \omega_0$, therefore the full width half maximum corresponds to:

$$\Delta\omega = 2\delta \tag{4.40}$$

This result demonstrates that the forced response of the system can be used to measure the damping coefficient δ: the burner presents a maximum response to maintained external acoustic perturbation centered over a pulsation frequency $\omega_{nr\Re}$ with a width at the half maximum of 2δ.

HR experimental setup

This experimental methodology has been extensively used in the combustion community, for the measurement of ω_0 and δ, one may refer for example to Durox *et al.* (2002); Schuller *et al.* (2003b) under non-reacting flow and to Palies *et al.* (2011) for reacting flow. From the analysis presented above we can conclude that one can measure the acoustic characteristics of the burner (ω_0 and δ) under non-reacting configuration by measuring the internal, p'_0, and external, p'_1, acoustic pressures, while maintained acoustic waves are sent to the burner outlet at different frequencies. For the practical case, as $\delta \ll \omega_0$ one can assume that $\omega_{nr\Re} \approx \omega_0$, thus, one can locate the natural pulsation of the burner, ω_0, by identifying the position of the maximal response $\mathcal{P}(\omega)_{max}$. Furthermore, the damping coefficient can be measured by determining the frequency width $\Delta\omega$ at the half maximal response, as $\delta = \Delta\omega/2$.

The experimental setup used for the HR test is presented in Fig. 4.6. The signals of two microphones M_0 and M_1 are simultaneously recorded while an harmonic perturbation is applied via a loudspeaker, outside the burner. The external acoustic pressure, p'_{M1} is recorded by microphone M_1 placed at $x = -125$ mm from the burner outlet, facing the loudspeaker, placed at $x = 125$ mm. One can assume that $p'_1 = p'_{M1}$ as the distance from the loudspeaker to the burner and to M_1 is small compared to the acoustic wave length. Internal pressure induced by the loudspeaker p'_0 is recorded by microphone M_0 placed inside the plenum.

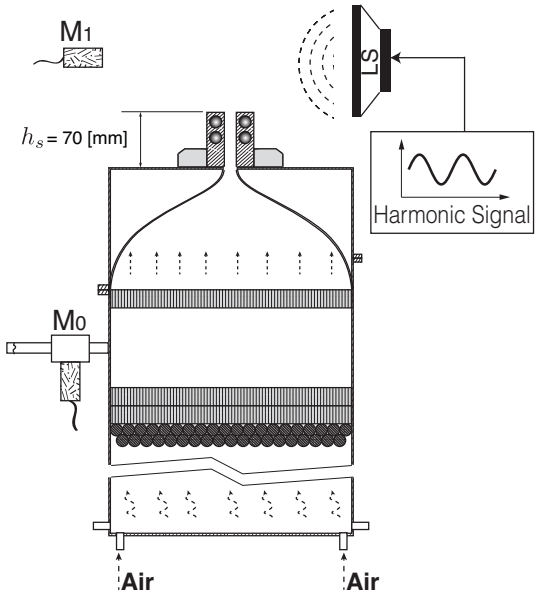

Figure 4.6: Experimental setup used for the harmonic response (HR) tests. The external excitation is generated with the loudspeaker locate at the burner outlet. Two microphones are used to measure the acoustic pressure M_0 and M_1.

HR experimental results

Figure 4.7 shows the harmonic response of the B07 burner for the cases T50c and T90c with a bulk velocity of $\bar{v} = 1.6$ ms^{-1}. The signals were recorded at a frequency rate of $f_s = 20$ kHz during 2 s. A range of frequency $[5, 100]$ Hz is explored in steps of $\Delta f = 0.5$ Hz.

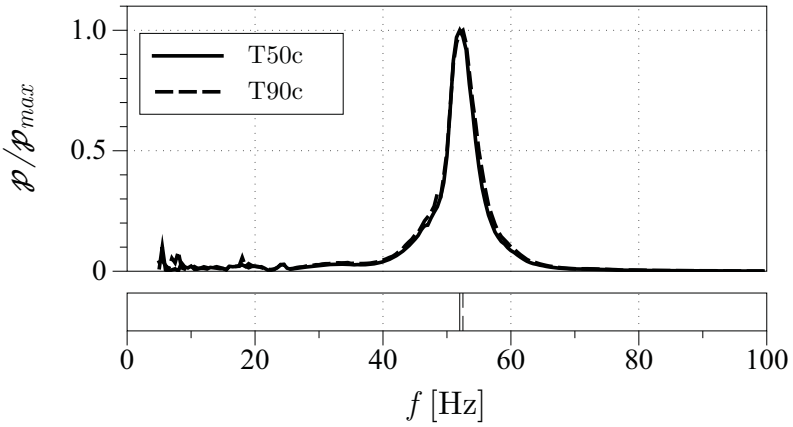

Figure 4.7: Harmonic response of the B07 burner under non-reacting conditions. T50c (——), T90c (- - - -). Bulk velocity was $\bar{v} = 1.6$ ms^{-1}.

The first observation in Fig. 4.7 is that results are consistent with Eq. 4.36, one find a resonance like behavior is centered over a particular frequency, which in this case

corresponds to the Helmholtz mode or the first resonance frequency of the burner. In addition, results are practically independent of the slot temperature T_s as the curves for T50c and T90c are superposed. Case T50c presents a maximum amplitude centered at $f_0 = 52.0$ Hz and a half maximum width of $\Delta f = 4.6$ Hz, while for the T90c one obtains $f_0 = 52.5$ Hz and $\Delta f = 5.0$ Hz for the same parameters respectively. Results are gathered in Table 4.2, and we can see that ω_0 increases by only 0.9 % while δ by 8.2 % from case T50c case T90c. The frequency $f_0 \approx 52$ Hz is close to the frequency of the instability $f_r \approx 58$ Hz (*cf.* Fig. 2.7) which validates the hypothesis made in Sec. 3.5.2 where we found an analytical stability criteria assuming that the complex pulsation frequency of the system lies around the natural pulsation frequency of the burner without combustion.

Table 4.2: Summary of the results from the harmonic test.

Case	**B07**	
	$\omega_0/2\pi$ [Hz]	δ [s^{-1}]
T50c	52.0	14.5
T90c	52.5	15.7

4.2.3 Synthesis of the non-reacting tests results

Performing unit impulse response IR and harmonic response HR tests under non-reacting flow allows to measure the acoustic characteristics of the burner (ω_0 and δ) needed as inputs in the dispersion relation (*cf.* Eq. 3.32) to determine the stability of the system. We have found that the two methods IR and HR are consistent, as summarized in Table 4.3 both methods give practically the same values for ω_0 and δ. One find a maximum dispersion of 11.0 % difference for the damping coefficient in the case T50c between IR and HR tests. This difference may come from the fact that in the IR test the LS is an active component and it may have a small contribution to the global damping coefficient of the burner.

The acoustic characteristics of the burner under non-reacting flow conditions are found to be independent of the slot temperature as the results for ω_0 and δ are practically the same for the cases T50h and T90h. One finds a maximum dispersion of 8.3 % difference for the damping coefficient in the HR test between the cases T50c and T90c. Taking this into account, for the practical case of the solution of Eq. 3.32 ω_0 and δ will be defined as the average of the four results obtained for the cases T50c and T90c and for both methods IR and HR, thus $\omega_0 = 330$ rad/s and $\delta = 15.8$ s^{-1}.
Chapter 2 has shown that for this particular burner the occurrence of combustion instabilities is determined by the slot temperature. At the same time, we have shown that a combustion instability results from the coupling between three different mechanisms:

Table 4.3: Summary of experimental results of the unit impulse IR and harmonic response HR acoustics tests for the B07 slot burner under non-reacting flow.

B07	**Non-reacting acoustics**			
	IR		**HR**	
	$\omega_0/2\pi$ [Hz]	δ [s^{-1}]	$\omega_0/2\pi$ [Hz]	δ [s^{-1}]
T50*c*	52.4	16.3	52.0	14.5
T90*c*	53.1	16.8	52.5	15.7
T120*c*	N/A			

burner acoustics, combustion noise and combustion dynamics. From the results of this section we can conclude that the slot temperature has a direct impact on the combustion process either by affecting the combustion noise or the flame dynamics mechanisms, the burner acoustics is not affected by the slot temperature.

4.3 Acoustics for reacting flow

In order to gain insight in the combustion process, we can perform the same acoustic tests but now we take into account the presence of the flame. In order to this it is necessary to have a stable flame configuration (no of self-sustained oscillations). For this reason we can of course only explore the cases T90h and T120h as the case T50h is always unstable (cf. Fig. 1.4). This approach permits to measured the resonance pulsation frequency[2] ω_h and damping coefficient δ_h of the whole system (burner + flame). Both parameters are measure in the same way as for ω_0 and δ in the non-reacting configuration, using the same procedure described in the previous section for both IR and HR.
In the case of the IR tests ω_h and δ_h are measured from the optimal fit of the velocity fluctuation signal after a short impulse.

$$v_1'(t)/v_{1_{max}}' = e^{-(\delta_h/2)t}\cos(\omega_h t) \tag{4.41}$$

On the other hand, for the HR test ω_h is measured by identifying the position of the maximal response $\mathcal{P}(\omega)_{max}$. and δ_h is measured by determining the frequency width $\Delta\omega$ at the half maximal response, as $\delta_h = \Delta\omega/2$.

Figure 4.8 shows the results of the two acoustic test performed under reacting flow, where the experimental procedures for IR and HR are exactly the same as for the non-reacting flow. Comparing the results for the T90h and T120h cases leads to three main conclusions:

[2] Here the subscript "h" stand for "hot" conditions while in Sec. 4.1.1 the subscript "H" stands for "Heltmholtz".

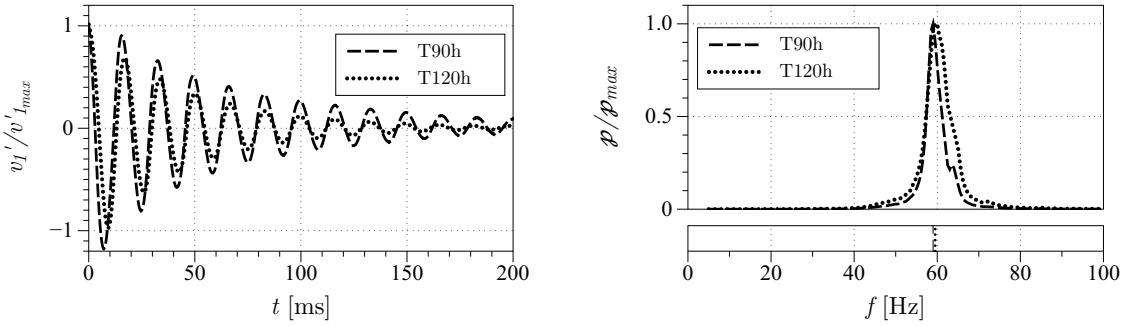

(a) Burner impulse response under reacting configuration.

(b) Burner harmonic response under reacting configuration.

Figure 4.8: Acoustic tests for the B07 slot burner under reacting configurations for two cases, T90h (- - - -) and T120h (·····). Flow velocity and equivalent ratio were $\bar{v} = 1.6$ ms^{-1} and $\Phi = 0.95$ respectively. The impulse and the harmonic signals sent to the loudspeaker correspond to the same signals that the non-reacting cases.

- The resonance pulsation frequency of the system is practically independent of the slot temperature: in Fig. 4.8(b) both curves (T90h and T120h) present a maximum amplitude centered around $\omega_h = 372$ rad/s or $f_h = 59$ Hz.

- On the other hand, the damping coefficient in the reacting configuration, δ_h, changes considerably between the two cases. For example Fig. 4.8(a) shows that in case T120h the velocity fluctuation returns to its steady state faster than the case T90h, meaning that the system has a largest decay growth for the T120h case; in other words, for a reacting flow, the system is "more stable" when the temperature of the slot is increased.

- Finally, we have found that the resonance frequency of the system under reacting flow is around $f_h \approx 59$ Hz, which is very close to the one measured in Ch.2 under unstable combustion $f_r \approx 58$ Hz (*cf.* Fig 2.7). This suggest that measuring ω_h and δ_h is equivalent to measuring the complex pulsation of the system under reacting configuration:

$$\omega = \omega_r + i\omega_i = \omega_h + i\delta_h \tag{4.42}$$

  Hence we can assume the damping of the whole system, δ_h, corresponds to the growth[3] rate of the complex pulsation of the system ω_i ($\delta_h = \omega_i$), and that the resonance pulsation in a reacting test, ω_h, corresponds to the pulsation of the self-sustained oscillation, ω_r ($\omega_h = \omega_r$).

Table 4.4 gathers the results of both IR and HR test under reacting configurations. Both tests give similar results for the resonance frequency and decay rate. For the IR test

[3] One refers to ω_i as a growth rate but it is really a decay rate as the configuration for which we perform the tests corresponds to stable combustion thus ω_i is always negative.

ω_r changes by only 1.3 % while ω_i increases by 59.1 % from case T90h to case T120h. For the HR test ω_r changes by only 0.8 % while ω_i increases by 77.5 % for the same two cases.

Table 4.4: Summary of the results from the IR and HR tests under reacting flow. Case T50h could not be explore because it is naturally unstable.

Case	**IR Test**		**HR Test**	
	$\omega_h/2\pi$ [Hz]	δ_h [s^{-1}]	$\omega_h/2\pi$ [Hz]	δ_h [s^{-1}]
T50h	N/A	$\omega_i > 0$	N/A	$\omega_i > 0$
T90h	60.6	13.7	59.0	12.0
T120h	60.0	21.8	59.5	21.3

4.4 Decoupling the burner acoustic from the combustion process

So far we have seen that the acoustic properties of the burner under non-reacting configuration are not affected by the slot temperature, on the other hand under reacting configuration the system is strongly affected by the slot temperature which controls its damping coefficient δ_h: the increase in the slot temperature has a stabilization effect on the system as δ_h becomes more negative when going from the T90h to the T120h case. This is consistent with the observation of Ch. 2 where the amplitude of the combustion oscillation was decreased when the slot temperature increased.

Thanks to the dual channel cooling system (*cf.* Fig.1.3) one can consider that the setup remains at ambient temperature during reacting operation; except at the flame anchoring point which features strong temperature gradients. Thus, one can decouple the acoustics of the burner from the combustion process if we consider ω_h as the resonance frequency of the whole system including both the natural pulsation of the burner, ω_0 and "natural frequency of the flame" ω_f. Similarly, one can think of δ_h as the global damping of the system, that includes the natural damping of the burner due to acoustic loses, δ and a second damping coefficient associated to the flame itself, δ_f. ω_0 and δ are purely acoustic parameters and independent of the slot temperature while ω_f and δ_f are parameters associated only to the flame itself and are strongly affected by the slot temperature. At the same time, measuring ω_h and δ_h corresponds to measuring ω_r and ω_i respectively, thus we can write:

$$\omega_h = \omega_r = \omega_0 + \omega_f \tag{4.43}$$
$$\delta_h = \omega_i = -(\delta + \delta_f) \tag{4.44}$$

From Eqs. 4.43 and 4.44 one can see that the flame itself has a dynamic behavior described by the sign of δ_f. If $\delta_f > 0$ the flame damps the imposed oscillations; on the other hand, if $\delta_f < 0$, the flame drives the oscillation.

Table 4.5: Summary of the results of the flame influence on the stability of the system.

B07	**IR**		**HR**	
	$\omega_f/2\pi$ [Hz]	δ_f [s^{-1}]	$\omega_f/2\pi$ [Hz]	δ_f [s^{-1}]
T50h	N/A	$-\delta_f > \delta$	N/A	$-\delta_f > \delta$
T90h	8.1	-2.7	6.4	-4.0
T120h	7.3	5.8	6.8	5.3

Table 4.5 shows the results for ω_f and δ_f calculated from Eqs. 4.43 and 4.44 and using $\omega_0 = 330$ rad/s and $\delta = 16$ s^{-1} obtained in Sec. 4.2: the growth rate of the flame itself δ_f has two different dynamic behaviors for the two cases. For case T90h $\delta_f < 0$ while for case T120h $\delta_f > 0$. Although the whole system is stable for both cases ($\omega_i < 1$), in the case T120h the flame is helping to stabilize the system while in the case T90h the flame is destabilizing the system. Moreover, this destabilization effect is not enough to overcome the acoustic losses ($-\delta_f < \delta$) and bring the whole system into a resonance. We are not able to estimate δ_f for the T50h case. As the system is unstable, we know for sure that $\omega_i > 0$, thus we can easily state determine that $-\delta_f > \delta$. Thus, for this case (T50h) the destabilizing effect of the flame is strong enough to drive the whole system into resonance. This is a clear indication that the flame is an active element and it may damp or drive oscillations.

Figure 4.9 shows a comparison between the non-reacting and reacting acoustics tests (IR and HR) for the T90 configuration. In Fig. 4.9(a) one can clearly see the effect that the flame has in this system, after the impulse the velocity fluctuation returns to its steady state faster for the non-reacting configuration than for the reacting configuration, indicating that the presence of the flame has reduced the global damping of the system. The flame is trying to bring the system to a unstable configuration but it can not overcome the acoustic losses. On the other hand, Fig. 4.9(b) shows that the presence of the flame creates a shift to higher frequencies of the maximum amplitude peak of the burner response. The system pass from a resonance frequency of $f_0 = 52$ Hz in a non-reacting case to a resonance frequency of $f_r = 59$ Hz in a reacting case.

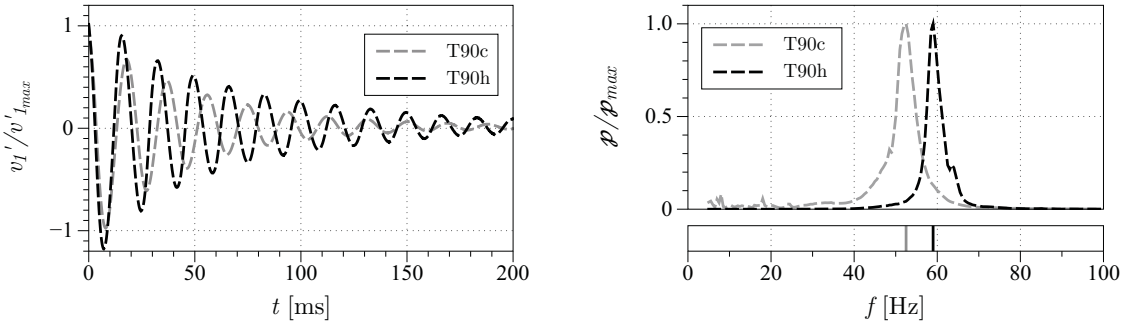

(a) Comparison for the B07 slot burner IR test for the T90 case between a non-reacting and a reacting cases.

(b) Comparison for the B07 slot burner HR test for the T90 case between a non-reacting and a reacting cases.

Figure 4.9: Acoustic tests comparison for the B07 slot burner under non-reacting (----) and reacting (----) configurations for the T90 case.

4.5 Impact of the acoustics parameters on the stability of the system (analytical stability criteria from Eq. 3.46)

Now we are interested in finding what is the impact of the results obtained in this chapter on the stability of the burner. To achieve this, we use the analytical solution of the dispersion relation obtained in Sec. 3.5.2 for which we found that under the hypothesis of: a weak combustion-acoustic interaction, $\mathcal{N} \ll 1$; a damping coefficient small compared to the natural pulsation of the burner, $\delta/\omega_0 \ll 1$; and a pulsation of the system, ω, close to the natural pulsation of the burner, ω_0, one is able to derive an expression for the complex pulsation of the system for which the real part corresponds to the resonance frequency of the system $\omega_r = \Re\{\omega\}$ while the imaginary part corresponds to its decay/growth rate $\omega_i = \Im\{\omega\}$. With this analytical stability criteria is possible to derive expressions for ω_f and δ_f re-writing Eqs. 3.43 and 3.44:

$$\omega_r = \omega_0 + \omega_f = \omega_0 - \frac{\omega_0 \cos(\omega_0 \tau)}{2} \mathrm{d}\mathcal{N} \tag{4.45}$$

$$\omega_i = -(\delta + \delta_f) = -\delta - \frac{\omega_0 \sin(\omega_0 \tau)}{2} \mathrm{d}\mathcal{N} \tag{4.46}$$

where $\mathrm{d}\mathcal{N} = \mathcal{N} = (\mathcal{C}/r_0)\mathcal{G}_0$ is a coefficient that takes into account the interaction between combustion noise and flame dynamics. From Eq. 4.46 we can write δ_f as:

$$\delta_f = -\frac{\omega_0 \sin(\varphi_0)}{2} \frac{\mathcal{C}}{r_0} \mathcal{G}_0 \tag{4.47}$$

where $\mathcal{G}_0$ and $\varphi_0 = \omega_0 \tau$ are the gain and the phase of the flame response to acoustic perturbations at the natural frequency of the burner (ω_0), r_0 is the distance from the

acoustic monopole created under unsteady combustion and the burner outlet and $\mathcal{C}$ is a constant that depends on the burner geometry (S_s and h_s) and the injection conditions ($\bar{v}$ and Φ). One can notice that at the first order, stability of the system is completely determined by δ_f. We have shown that δ is independent of the slot temperature, thus the system will develop self sustained oscillations if δ_f is negative enough to overcome δ ($-\delta_f > \delta$). This tell us that if the system passes from unstable to stable only by increasing the slot temperature, T_s, is because one or several of the following parameters are been affected by the slot temperature: r_0, $\mathcal{G}_0$ and φ_0

Furthermore, the four parameters (ω_0, $\mathcal{C}$, r_0 and $\mathcal{G}_0$) are all positive, which means that if δ_f change sign from T90h to T120h (as it is the case in Table. 4.5) is because the term φ_0 in Eq. 4.47 is been affected by T_s. Therefore the slot temperature has an impact on the phase lag, φ_0, between the velocity perturbation and the heat release rate. However, we can not conclude that this is the effect that stabilizes the flame from case T50h to case T90h. We only know that δ_f is becoming more negative when the slot temperature is increased but it can be either because $\sin(\varphi_0)$ is becoming more negative or because $\sin(\varphi_0)$ is already negative and $\mathcal{G}_0$ is increasing or r_0 is decreasing.

Reacting acoustics tests gave us some important information on the effect of the slot temperature. Although it is not clear how the increment of the slot temperature can damp flame oscillations we can be sure that it affecting the phase lag of the flame response φ_0. However this analysis is not sufficient to discard effects of the slot temperature on the two other parameters $\mathcal{G}_0$ and r_0.

4.6 Conclusion

In this chapter we have studied the acoustic characteristics of the slot burner. Making use of the Helmholtz wave equation and an analysis of compact elements we were able to derive an expression (Eq. 4.30) that describes the acoustics of the burner. This expression was found to be equivalent to the one derived in Sec. 3.2 (Eq. 3.13) which was derived making mass-spring analogy but valid only in the limit of $\omega \simeq \omega_0$. Equation 4.30 was used to derive the experimental metrologies that permit us to measure the burner acoustic characteristics ω_0 and δ, parameters needed as inputs for the solution of the dispersion relation (cf. Eq. 3.32). Two different acoustic test methods were designed and performed; the harmonic response HR and the impulse response IR.

Test were performed under reacting and non-reacting conditions. In both cases the slot temperature was controlled by flowing water at different temperatures in the closed circuit passages (*cf.* Fig. 1.3). Consequently, for the non-reacting cases, values of T_s larger than 100 °C can not be reached so that case T120c could not be explored. Likewise, in reacting conditions for the B07 configuration the case T50h was not tested because it is naturally unstable.

Table 4.6: Experimental results of the harmonic and unit impulse response acoustics tests for the B07 burner for non-reacting and reacts cases.

B07	**Non-reacting**				**Reacting**			
	IR		**HR**		**IR**		**HR**	
	$\omega_0/2\pi$ [Hz]	δ [s^{-1}]	$\omega_0/2\pi$ [Hz]	δ [s^{-1}]	$\omega_r/2\pi$ [Hz]	ω_i [s^{-1}]	$\omega_r/2\pi$ [Hz]	ω_i [s^{-1}]
T50	52.4	16.3	52.0	14.5	N/A			
T90	53.1	16.8	52.5	15.7	60.6	13.7	59.0	12.0
T120	N/A				60.0	21.8	59.5	21.3

Table 4.6 summarizes the results of the burner acoustic study[4]. Both methods IR and HR show similar results. For the practical case of the solution of Eq. 3.32 one is interested in the non-reacting results of the B07 burner, where ω_0 and δ are needed as inputs to solve the relation. These two values will be defined as the average of the four results obtained for the cases T50c and T90c and for both methods IR and HR, thus $\omega_0 = 300$ rad/s and $\delta = 15.8$ s^{-1}. Several conclusions can be obtained from these results:

- The acoustic properties of the slot burner in the non-reacting configuration are independent of the slot temperature, because the results for ω_0 and δ in cases T50c and T90c are practically the same, with a maximum dispersion of 8 % difference in the measurement of δ between cases T50c and T90c in the HR test.

- The natural pulsation frequency of the burner $\omega_0 = 330$ rad/s is close to the pulsation frequency of the instability during unstable conditions $\omega_r = 2\pi f_r = 364$ rad/s measured in Sec. 2.2 which validates the hypothesis made for the analytical stability criteria in Sec. 3.5.2, where we assumed that the real part of the complex pulsation frequency of the system ω_r lies around the natural pulsation frequency of the burner ω_0.

- Likewise the hypothesis made for the analytical stability criteria in which we assumed that $\delta/\omega_0 \ll 1$ is validated as this ratio is of the order of 10^{-3}.

- Evaluating the Helmholtz equation (*cf.* Eq. 4.21)[5] one obtains: $\omega_H = 335$ rad/s, which is close to the first mode measured under non-reacting configuration $\omega_0 = 330$ rad/s, indicating that the first-order approximation gives good results.

[4] In this table we assume that the resonance pulsation frequency of the system under reacting configuration, ω_h, correspond to the real part of the pulsation frequency of the system, ω_r, ($\omega_h = \omega_r$) and that the damping coefficient under reacting configuration, δ_h correspond to the imaginary part of the pulsation frequency of the system, ω_i, ($\delta_h = \omega_i$)

[5] Here we consider V_p, as the sum of the volume of the mixing chamber, the chamber and the converging nozzle then we subtract the volume of the stabilizing glass balls ($N_{\text{balls}} \approx 400$) $V_p = V_m + V_c + V_n - V_b = 13$ cm^2. At the same time h_s corresponds to the B07 slot hight 70 mm and wi take into account a end correction, which corresponds to the impedance adaptation between the flow at the exit of the burner and the atmosphere, that is of the order of the slot width w_s 10 mm.

- The resonance frequency of the system under reacting flow is around $f_h \approx 59$ Hz, which is very close to the one measured in Ch.2 under unstable combustion $f_r \approx 58$ Hz (*cf.* Fig 2.7).
- For the reacting tests δ_h changes considerably with the slot temperature, it becomes more negative when the slot temperature is increased, meaning that the system is "more stable".

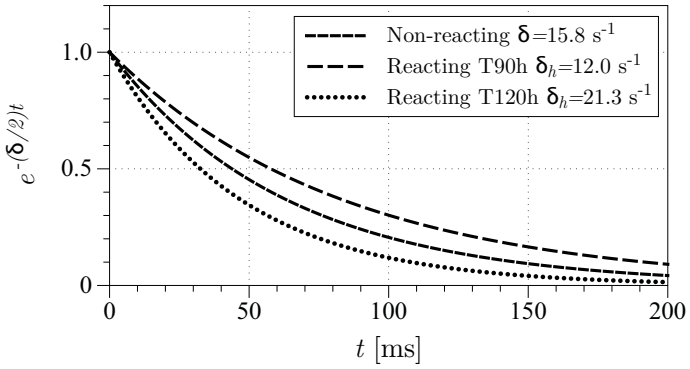

Figure 4.10: Comparison between the damping coefficient of the burner under non-reacting (———) flow and the damping coefficient to the system under reacting flow for the two cases T90h (- - - -) and T120h (·····). The plot corresponds to the envelope of the of the imp use response $e^{-(\delta/2)t}$.

Figure 4.10 shows that the damping of the system under reacting conditions is decreased when the slot temperature is increased, furthermore. At the same time we can see in the case of T90h the system has reduced its global damping while for the case of T120h the system has increased its global damping rate if compared to natural damping of the burner δ.

Considering the influence of the flame on the measurements, we were able to decouple the acoustics of the burner from the combustion process. It was found that the flame itself has a dynamic behavior described by the sign of δ_f, the flame can drive oscillations if $\delta_f < 0$ and damp them if $\delta_f > 0$. Thanks to the analytical stability criteria derived in Sec. 3.5.2 we were able to derive an expression for δ_f. This expression permitted us to conclude that the switch of behavior ($\delta_f < 0$ and $\delta_f > 0$ between cases T90h and T120h, respectively) is a clear indication that the phase-lag φ of the flame response is affected by the slot temperature. However it is still not clear how this mechanism works and from these results we are not able to conclude that this is the only parameter which is affected by the slot temperature as $\mathcal{G}$ and r_0 might be affected as well. The next two chapters will focus on this two issues.

Chapter 5

Combustion Noise Production

We have seen that in the linear stability model (Sec. 3.3) combustion noise controls the acoustics feedback process. When combustion is unstable, the flame front motion is accompanied by a high level of noise emission. Acoustic waves are radiated in the whole space and in particular back towards the burner. In order to validate the assumptions made in Sec. 3.3 a validation of the combustion noise theory is needed. This chapter is organized as follows: A brief review of the combustion noise theory is presented in Sec. 5.1. In Sec. 5.2 we present the experimental setup used in Sec. 5.3 to confirm the link between the far-field pressure and the unsteady heat release rate. Likewise, in order to close the linear stability model a good estimation of the parameter r_0 is necessary: this will take place in Sec. 5.4. Experiments are performed on a reactive stable configuration with the B15 burner for the reference cases T50h, T90h and T120h. Flow conditions are kept constant and correspond to $\bar{v}$ =1.6 ms^{-1} and Φ =0.95 for the bulk velocity and the equivalence ratio, respectively.

5.1 Review of combustion noise theory

Combustion noise theory has been subject of many studies in the past. Early results of Thomas and Williams (1966) on spherical flames to establish a relation to the far-field sound-pressure induced by the volume acceleration created under non-steady combustion:

$$p'(r,t) = \frac{\rho_u}{4\pi r}\frac{\mathrm{d}}{\mathrm{d}t}\left[\frac{\mathrm{d}V}{\mathrm{d}t}\right] \tag{5.1}$$

where r is the distance from the source to the measuring point and $\mathrm{d}V/\mathrm{d}t$ is the rate of value variation of the source and defines the strength of the source. Equation 5.1 propose that the combustion noise results from the flow expansion determined by the heat-release rate. Based on Eq. 5.1 and the observations of Hurle *et al.* (1968) in which turbulent premixed flames can be considered as an assembly of acoustic monopoles, Price *et al.* (1969) proposed an expression for the far-field pressure:

$$p'(r,t) = \frac{\rho_u}{4\pi r}(E-1)\left[\frac{\mathrm{d}\dot{Q}_{CH_4}}{\mathrm{d}t}\right]_{t-\tau_{ac}} \tag{5.2}$$

where E is the volumetric expansion ratio defined as the density ratio between the fresh and burnt gases, $\dot{Q}_{CH_4}$ the total volumetric rate of consumption of gas mixture in the flame, and τ_{ac} is the time required for the sound wave to propagate from the flame to the measuring point r. Equation 5.2 relays on the hypothesis that the flame is compact compared to the acoustic wave length and that the point of measurement is far from the noise source. One may be able to estimate the term $\mathrm{d}\dot{Q}_{CH_4}/\mathrm{d}t$ assuming that $\dot{Q}_{CH_4}$ is proportional to the light-emission intensity of free radicals CH^* in the reaction zone (Hurle *et al.* (1968)):

$$\dot{Q}_{CH_4} = \varkappa I_{CH^*} \tag{5.3}$$

where $\varkappa$ is a coefficient that is constant for a fixed equivalence ratio Φ. Combining Eqs. 5.2 and 5.3 one finds:

$$p'(r,t) = \frac{\rho_u}{4\pi r}(E-1)\varkappa \left[\frac{\mathrm{d}I_{CH^*}}{\mathrm{d}t}\right]_{t-\tau_{ac}} \tag{5.4}$$

A more rigorous expression was proposed by Strahle (1971) (Eq. 3.16 in Ch. 3). It followed the principles of the fluid mechanics and aerodynamics noise and successfully related the far-field pressure to the heat release rate $\dot{q}$, proving Eq 5.4 obtained in a more intuitive way. Taking into account that $\dot{q}$ is proportional to $\dot{Q}_{CH_4}$ one can write:

$$\dot{q} = q_{CH_4}\dot{m}_{CH_4} = q_{CH_4}\frac{\dot{Q}_{CH_4}}{\rho_{CH_4}} \tag{5.5}$$

where q_{CH_4} is the heat of reaction of methane, $\dot{m}_{CH_4}$ is the mass flow rate of methane and ρ_{CH_4} is the density of methane.
In the case of perfectly premixed flames, the heat release rate, $\dot{q}$, is directly related to the instantaneous flame surface, $\mathcal{A}$. Thus, the far-field sound pressure can be linked to the total flame surface fluctuation (Clavin and Siggia (1991)):

$$p'(r,t) = \frac{\rho_u}{4\pi r}(E-1)s_L \left[\frac{\mathrm{d}\mathcal{A}}{\mathrm{d}t}\right]_{t-\tau_{ac}} \tag{5.6}$$

where s_L is the laminar flame speed. Equations 5.4 and 5.6 have been checked in many different recent experiments (e.g Truffaut *et al.* (1998); Rajarama and Lieuwen (2003) and Durox *et al.* (2002)). In a laminar premixed jet flames impinging on a water-cooled plate Schuller *et al.* (2002) successfully proved the results of combustion noise theory linking the far-field pressure, the chemiluminescence and the flame surface. However, the underlying mechanisms leading to intense noise production are less well documented. Schuller *et al.* (2006) listed a set of phenomena leading to fast variations of heat release rate and thus high levels of combustion noise. Indeed, it is possible to distinguish primary mechanisms which induce rapid flame surface fluctuations, like flame vortex interactions, or merging of neighboring flame fronts, or the formation and burning of pockets of fresh gases. This last mechanism, is the main mechanism at play in a slot-type flame, because there are no vortex interactions and no interaction between separate flames, only a periodic creation

of reacting pockets. A kinematic approach was used by Joulin and Sivashinsky (1991) and Truffaut *et al.* (1998) in the case of flame front oscillations induced by harmonic fluctuations at the anchoring point to model the critical conditions of formation of reacting pockets. The burning velocity of pockets has been examined experimentally by Baillot and Bourehla (1997) and Baillot *et al.* (2002).

These studies show the accuracy of Eq. 5.4 in predicting the far-field pressure radiated by an unsteady flame. However, they are mainly based on spherical or conical flame configurations. Here, we work with a 2D slot configuration and a quick validation of this theory is needed in order to approve the use of Eq. 5.4 in the linear stability analysis. This is the subject of Sec. 5.3. The experimental setup is presented in Sec. 5.2 while, Sec. 5.4 is dedicated to the estimation of the pinching distance, r_0.

5.2 Experimental setup

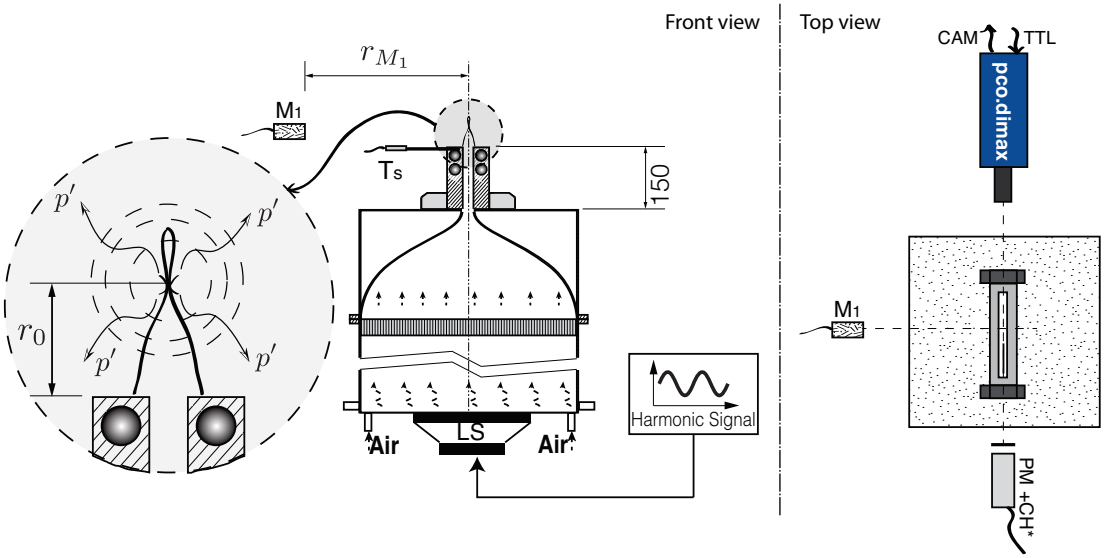

Figure 5.1: Experimental setup used for combustion noise theory validation. A microphone M_1 located outside the plenum at distance $r_{M_1} = 125$ mm from the burner axis records external pressure fluctuation. The intensity of CH* chemiluminescene is measured with a photomultiplier equipped with a filter placed at a distance $z = 400$ mm from the flame, facing the longitudinal axis of the flame. The flame surface fluctuation is monitored with a high speed camera placed at a distance $z = -600$ mm from the flame facing the longitudinal axis of the flame.

The experimental setup presented in Fig 5.1 allows simultaneous measurements of external acoustic pressure, p'_{M_1}, intensity of CH* chemiluminescense, I_{CH^*} and flame surface evolution, $\mathcal{A}$, while the flow is modulated over a range of frequencies $f_{ex} \in [5, 300]$ Hz, for a modulation level of $\varepsilon = 0.1$ (ε is defined by Eq. 1.10). The B15 slot burner configuration

(*cf.* Fig. 1.5) was used in order to have a stable flame for the three reference cases (T50h, T90h and T120h).

The external acoustic pressure is recorded by a microphone, labeled M_1, and located at $r_{M_1} = 125$ mm away form the burner axis. The photomultiplier, labeled PM, is located 400 mm from the burner axis facing the front side (*cf.* Fig. 5.1). Both signals are sampled at a frequency of $f_s = 20$ KHz during 3 s. The flame surface evolution is recorded by a pco.dimax high speed camera at a frequency of $f_{cam} = 4500$ fps.

5.3 Validation of combustion noise theory

First, one is interested in the effect of the slot temperature T_s in the sound pressure level (SPL) emitted by the flame when subjected to acoustic oscillations. Figure 5.2 shows the relative SPL for the three reference cases in the frequency range explored. The relative ΔSPL corresponds to the difference between the external acoustic pressure measured at M_1 during a reacting test and a non-reacting test, which corresponds to the noise produced by the flame when it is submitted to acoustic perturbations.

$$\Delta\text{SPL} = 20\log\left(\frac{p_{M1}^{rms}}{p_{ref}}\right)_{reacting} - 20\log\left(\frac{p_{M1}^{rms}}{p_{ref}}\right)_{non-reacting} \tag{5.7}$$

where $p_{ref} = 20$ μPa (rms) and is the reference sound pressure in air. For all three reactive reference cases Fig. 5.2 shows that the SPL recorded by M_1 is always superior to the reference SPL in the laboratory obtained during a non reacting operation. For frequencies $f_{ex} \in [50, 150]$ Hz there is a difference of at least 15 dB between the noise radiated by the flame and the reference SPL. This particular flame has a preferred frequency band for noise production located between between these frequencies.

Assuming that the acoustic perturbation generates a convective wave that propagates along the flame front at approximately the bulk velocity (Baillot *et al.* (1992)), and for the flow conditions in this experiment one wave is propagating along the flame front for an excitation frequency of $f_{ex} = 70$ Hz. This frequency also corresponds to the maximum of noise production in Fig. 5.2 about 23 dB more than the reference SPL under non-reacting configuration. Figure 5.2 shows that T_s has a small but not negligible impact on the sound radiated by the flame when submitted to acoustic disturbances. At the frequency of the natural instability $f_r = 58$ Hz the relative SPL is 21, 18 and 16 dB for the cases T50h, T90h and T120h respectively. This result is consistent with the observations of Ch. 2 where the amplitude of the oscillations decreased with the increase of the slot temperature.
At the same time Fig.5.2 shows that the acoustic pressure at M_1 for frequencies $f_{ex} \in [50, 130]$ is mainly due to the noise produced by the flame rather than the sound emitted by the loudspeaker as for this frequency range ΔSPL$>$ 15 dB. To check the flame noise production theory more precisely, we will now evaluate two specific frequencies $f_{ex} = 50$ and 100 Hz for a slot temperature corresponding to the reference case T50h.

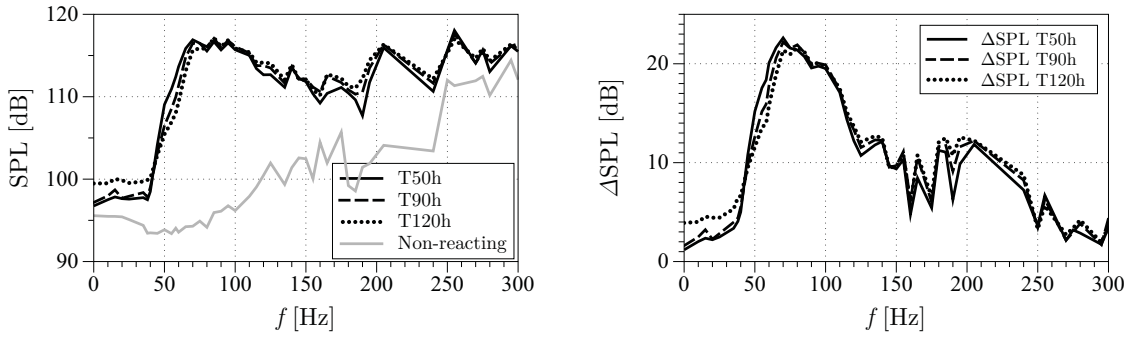

(a) Sound pressure level (SPL) under reacting and non-reacting conditions.

(b) Relative sound pressure level (ΔSPL) under reacting conditions compared to non-reacting conditions.

Figure 5.2: Sound pressure level emitted by the flame when modulated for different frequencies and the three burner-rim temperatures: T50h (——), T90h (- - - -), T120h (·····) and a reference case under non-reacting conditions (——).

5.3.1 Spectral response

Figure 5.3 shows the spectral response for the two cases $f_{ex} = 50$ and 100 Hz and the two signals, p'_{M1} and I_{CH^*} for the T50h case. The evolution of the power spectral density shows that the fundamental frequency corresponds to the excitation frequency f_{ex} in all two cases. The spectrum is filled by the harmonics of the fundamental frequency. For the pressure signal delivered by M_1 these harmonics have almost the same amplitude as the fundamental. However, the sub-harmonics peak amplitude are diminished by almost 20 dB with respect to the fundamental in the CH^* signal. The high quantity of energy stored in the harmonics of p'_{M1} signal is an indication of the non-linearity of the external acoustic pressure. The reason for this non-linearity is, for one part, the reflection of the acoustic waves on the solid walls of the laboratory and, for the second part, the intrinsic non-linear nature of the flame response.

5.3.2 Far-field pressure noise prediction

We are now interested in proving that the classical noise theory is capable of predicting the far-field pressure radiated by the flame. It has ben demonstrated, that for turbulent premixed flames the far-field pressure is proportional to the flame spontaneous emission of CH^* radicals (Eq. 5.4). However, for laminar slot type flames it has not been yet proved. Here, we follow the procedure of Schuller *et al.* (2002). Using the notations of Fig. 5.1 Eq. 5.4 becomes:

$$p'_{M1}(r_{M_1}, t) = \mathcal{K}(r_{M_1}) \left[\frac{d\, I_{CH^*}}{d\, t} \right]_{t-\tau_{M_1}} \tag{5.8}$$

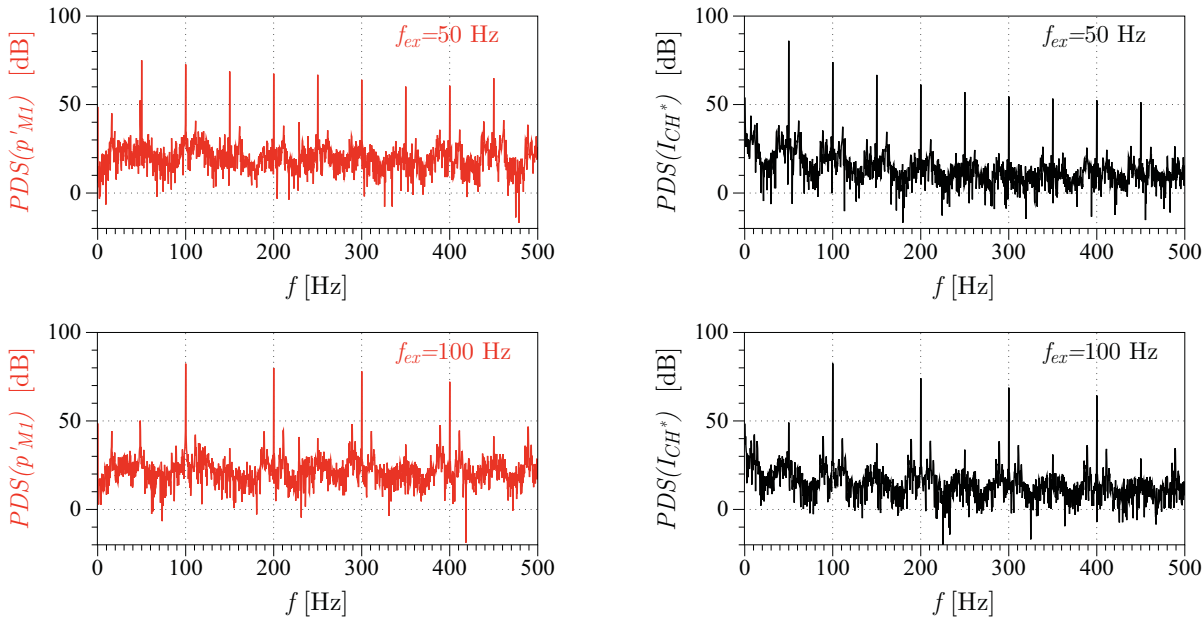

Figure 5.3: Top: $f_{ex} = 50$ Hz. **Bottom**:$f_{ex} = 100$ Hz. **Left**: Spectral response of far-field pressure, p'_{M_1}. **Right**: Spectral response of spontaneous emissions of CH* radicals, I_{CH^*}. The experiment is performed on a stable flame in a T50h case with a bulk velocity of $\bar{v} = 1.6$ ms^{-1} and a equivalence ratio of $\Phi = 0.95$. The magnitude of the modulation is $\varepsilon = 0.1$ for the two frequencies.

where $\mathcal{K}(r_{M_1})$ is a coefficient that depends on the operation conditions and the PM calibration:

$$\mathcal{K}(r_{M_1}) = - \tag{5.9}$$

where p'_{M_1} is the acoustic pressure at the location of M_1, r_{M_1} is the distance from the microphone M_1 to the burner axis and τ_{M_1} is the acoustic time needed to cover this distance at the speed of sound c. In order to solve Eq. 5.8 an estimation of E, τ_{ac} and $\varkappa$ is necessary.

Numerical application

E corresponds to the ratio between burnt and fresh gases temperature, assuming that the fresh gases temperature corresponds to the adiabatic flame temperature one can calculate this ratio as: $E = T_{ad}/T_u$, T_{ad} depends on the equivalence ratio, for $\Phi = 0.95$ the adiabatic flame temperature for the CH_4 corresponds[1] to $T_{ad} = 2189$ K (the fresh gases temperature is $T_u = 300$ K), one obtains: $E = 7.3$.

[1] T_{ad} was calculated using CANTERA with a chemistry GRI-MECH 3.0
http://elearning.cerfacs.fr/combustion/tools/adiabaticflametemperature/index.php

The acoustic time delay, τ_{M_1}, is the main time required for the sound wave to propagate from the acoustic monopole to the measuring point located at a distance of r_{M_1}, the rigorous expression for τ_{M_1} corresponds to:

$$\tau_{M_1} = \int_0^{r_{M_1}} \frac{1}{c(r)} \mathrm{d}r \tag{5.10}$$

where $c(r)$ is the local speed of sound. It is function of the gas temperature along the sound ray path $T(r)$. In this study we assume that the gas temperature is the ambient temperature and that it is constant along the sound ray path $T(r) = T_u$. Thus we can calculate the acoustic time delay has: $\tau_{M_1} = r_{M_1}/c$. Considering that M_1 is placed at a distance of 125 mm from the burner outlet one obtains an acoustics time delay of $\tau_{M_1} = 0.36$ ms.

The link between the heat release rate, $\dot{q}$, and the PM signal, I_{CH^*} is characterized by:

$$\varkappa = \frac{\dot{q}}{\bar{I}_{CH^*}} \tag{5.11}$$

$\varkappa$ can be quantified by measuring the mean voltage delivered by the PM versus the mean heat release rate, $\dot{q}$. Figure 5.4 shows the spontaneous light emission of CH^* radicals, $\bar{I}_{CH^*}$, function of the CH_4 volumetric flow rate, $\dot{Q}_{CH_4}$, and its equivalent heat release rate, $\dot{q}$, for fixed equivalence ratio, $\Phi = 0.95$. Data is well represented by a linear fit. The slope of the linear fit gives $\varkappa$.

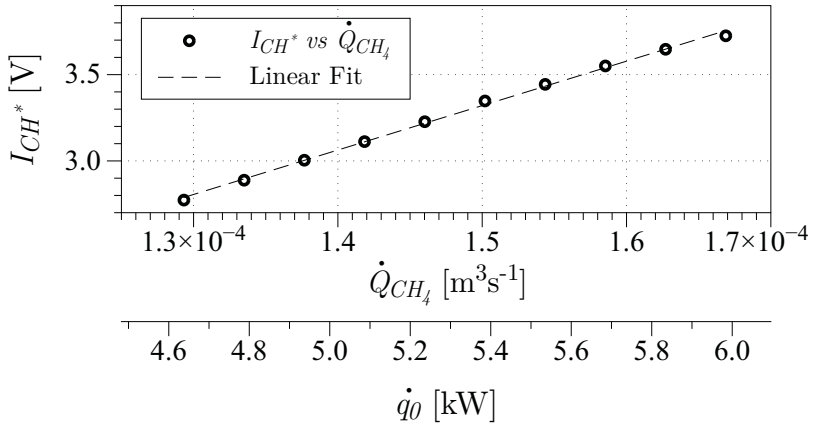

Figure 5.4: Spontaneous light emission of CH^* radicals, $\bar{I}_{CH^*}$, function of the CH_4 volumetric flow rate, $\dot{Q}_{CH_4}$, and the corresponding heat release rate, $\dot{q}_0$, for a fixed equivalence ratio of $\Phi = 0.95$, on a stable T50h case. Data (○); linear fit to the data (----).

Knowing E, τ_{M_1} and the link between I_{CH^*} and $\dot{q}$ ($\varkappa$), it is possible to check link between p'_{M_1} and $\dot{q}'$ suggested by Eq. 5.8. Table 5.1 resumes the numerical values needed

for the calculation of $\mathcal{K}(r_{M_1})$ (*cf.* Eq. 5.9).

Table 5.1: Numerical values for the evaluation of the combustion-noise parameter $\mathcal{K}$ in Eq. 5.9.

ρ_u [Kg/m^3]	T_u [K]	T_{ad} [K]	τ_{M_1} [ms]	$\varkappa$ [m^{3}V^{-1}s^{-1}]	E	r_{M_1} [mm]	$\mathcal{K}(r)$ [Pa s V^{-1}]
1.2	300	2189	0.36	8.6e−05	7.3	125	4.1e−04

Elimination of high frequency noise

Due to the high frequency noise produced by the digitalization of the signals, the term $dI_{CH^*}(t)/dt$ in Eq. 5.9 must be smoothed. The smoothing is done by performing a phase-locked average of the raw signals, $\hat{I}_{CH^*}$ and $\hat{p}'$. The final expression for the far-field pressure obtained from the spontaneous emission of CH* is:

$$\hat{p}'_{I_{CH^*}} = \mathcal{K}(r_{M_1}) \left[\frac{d\,\hat{I}_{CH^*}}{d\,t} \right]_{t-\tau_{M_1}} \tag{5.12}$$

which must be equivalent to the filtered pressure fluctuation measured by M$_1$, $\hat{p}'_{M_1}$.

Far-field noise prediction results

The left column of Fig. 5.5 shows the simultaneous time traces of CH* chimiluminescence, $I_{CH^*}(t)$, and acoustic pressure measured by M$_1$, $p'_{M_1}(t)$ for the two modulation frequencies $f_{ex} = 50$ (top row) and 100 Hz (bottom row). In the right column the comparison between the prediction of the far-field pressure, $\hat{p}'_{I_{CH^*}}$, and the measurement from M$_1$, $\hat{p}'_{M_1}$, is done.

From the raw signals (Fig. 5.5 left) one can conclude that for the two cases $f_{ex} = 50$ and 100 Hz a strong drop in the light intensity signal is followed by an intense noise captured by the microphone M$_1$. The prediction of the far-field pressure from the spontaneous emission of CH* radicals is well correlated to the filtered acoustic pressure. The amplitude and phase of the predicted signals are well replicated, despite a small tendency of the predicted signal to grow before the drop while the pressure signals from M$_1$ decrease before the drop in the $f_{ex} = 100$ Hz case.

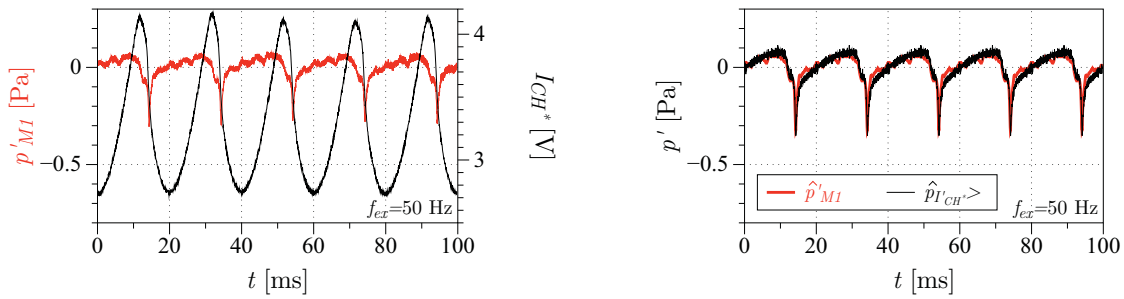

(a) Far-field combustion noise prediction for two frequencies $f_{ex} = 50$ Hz.

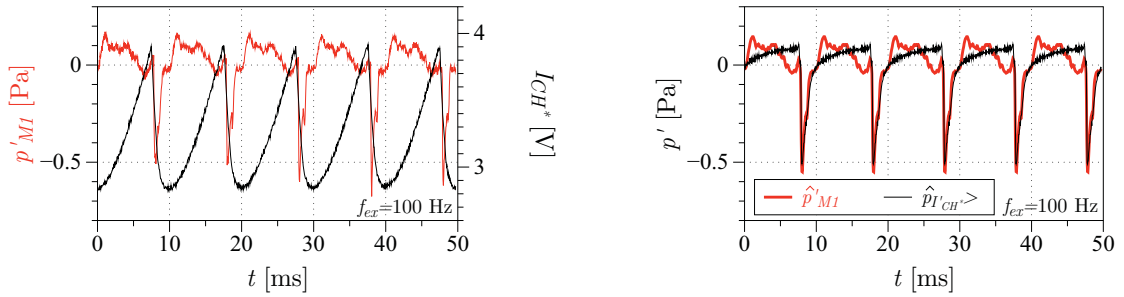

(b) Far-field combustion noise prediction for two frequencies $f_{ex} = 100$ Hz.

Figure 5.5: Left: Simultaneous time traces of CH* chimiluminesence, $I(t)_{CH^*}$ (———) and external acoustic pressure, $p'_1(t)$ (———). **Right**: Comparison between the far-field pressure estimation from the spontaneous emission of CH* radicals, $\langle p'_{I_{CH^*}} \rangle$ (———), and the filtered pressure signals M_1,$\langle p'_1 \rangle$ (———). The experiments were performed on a stable flame in a T50h case with a bulk velocity of $\bar{v} = 1.6$ ms^{-1} and an equivalence ratio of $\Phi = 0.95$. The magnitude of the modulation was $\varepsilon = 0.1$ for the two excitation frequencies.

5.4 Estimation of the pinching distance r_0

Having shown that classical combustion noise theory is suitable for the slot burner, we can proceed to the estimation of the pinching distance r_0 necessary to solve the dispersion relation. Section 3.5 has shown that in order to complete the linear instability analysis a good estimation of r_0 is needed. One recall that here r_0 is the distance of the noise source to the burner outlet (*cf.* Fig. 5.1). This distance is difficult to evaluate. Schuller *et al.* (2003b) defined r_0 has the location along y where the flame pinches. Noiray *et al.* (2006) were more specific and assumed that r_0 is the location of the greatest variation of the volumetric consumption rate in the flame, due to the formation of reacting pockets. They both obtained good results in predicting the potentially unstable flow operations conditions using these definitions. However, finding the point where the flame pinches is not an easy task and the linear instability analysis is sensitive to the determination of r_0. Here we considered equation 5.6 applied at the burner outlet:

$$p'_1(t) = \frac{\rho_u (E-1) s_L}{4\pi r_0} \left[\frac{d\,\mathcal{A}'}{d\,t} \right]_{t-\tau_{r_0}} \tag{5.13}$$

where, τ_{r_0} is the time required for the sound to cover the distance r_0 and $p'_1(t)$ is the acoustic pressure radiated from the flame back to the burner outlet. This acoustic wave is the mechanism responsible for the feedback process in the combustion instability. τ_{r_0} can be neglected if one consider that the flame is compact and that the pinching distance is small, *e.i* of the order of the flame height, thus τ_{r_0} is of the order of 10^{-5} s.

Flame surface variations are measured with a pro.dimax high speed camera. The sampling rate of the camera is $f_{cam} = 4500$ fps, which corresponds to 90 and 45 photos per cycle of oscillation for $f_{ex} = 50$ and 100 Hz, respectively. The photos are simultaneously recorded with the external pressure signal, p'_{M1} measured by M_1 and.CH* measured by the PM, I_{CH^*}; during the 3 s of excitation. The camera is triggered to start the acquisition after the first minimum of the light intensity signal is detected.
A frequency-locked average procedure is performed to increase the signal dynamics of the images. The instantaneous flame surface is calculated with $\mathcal{A} = l_f\, l_s/\eta$. Here, η is a 3D correction factor (Selle *et al.* (2011)) for the slot type burner to account for end effect at slot extremities. In the present configuration $\eta = 1.067$. l_f, is the flame length, measured with the procedure described in Sec. 1.4.5 and, l_s is the slot length.

Figure 5.6 shows the correlation between the light intensity signal and the flame surface oscillation for a frequency of $f_{ex} = 50$ Hz. The flame surface is plotted against the flame spontaneous CH* emission. Data is well represented by a linear fit, that passes through the origin. This correlation between flame surface area and heat release rate supports the assumption of constant flame speed, s_L, along the flame front, despite potential curvature and stretch effects when the flame is pulsated.

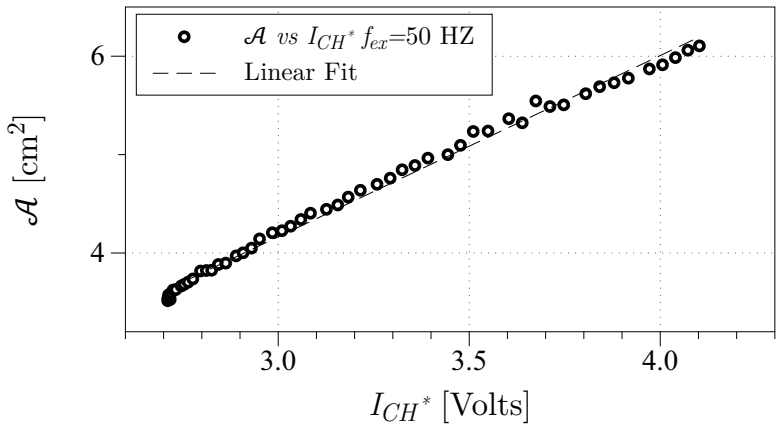

Figure 5.6: Correlation between the flame surface fluctuation and the CH* chimiluminescence. Data (∘); linear fit to the data (----).

Figure 5.7 show the frequency-locked images for a cycle of excitation: images are compared with the light intensity, I_{CH^*}, pressure fluctuation at the burner outlet p'_1, and

normalized flame surface fluctuation, $\mathcal{A}/\mathcal{A}_0$; for the two frequencies 50 (Fig. 5.7(a)) and 100 Hz (Fig. 5.7(b)). The pressure fluctuation at the burner outlet p'_1 is deduced from the external pressure measured with M_1:

$$p'_1 = [p'_{M1}]_{t-\tau_{M_1}} \tag{5.14}$$

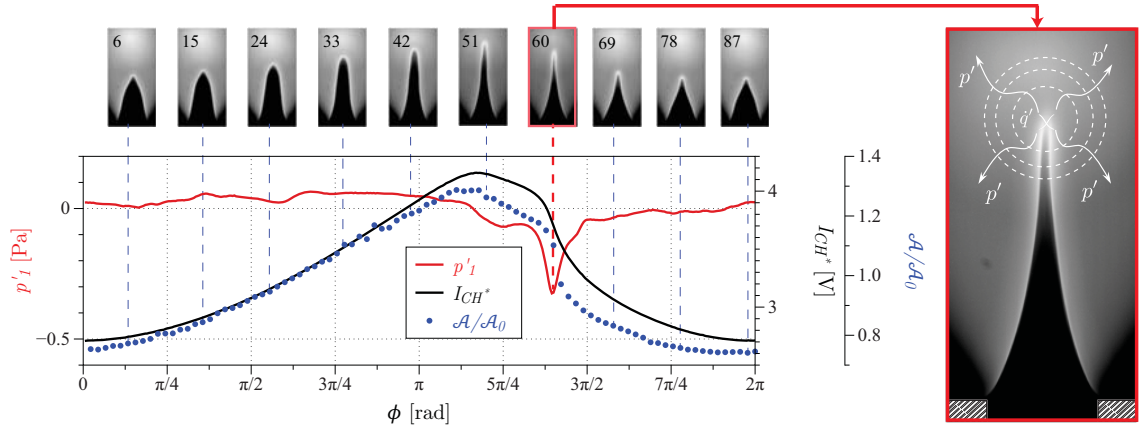

(a) $f_{ex} = 50$ Hz

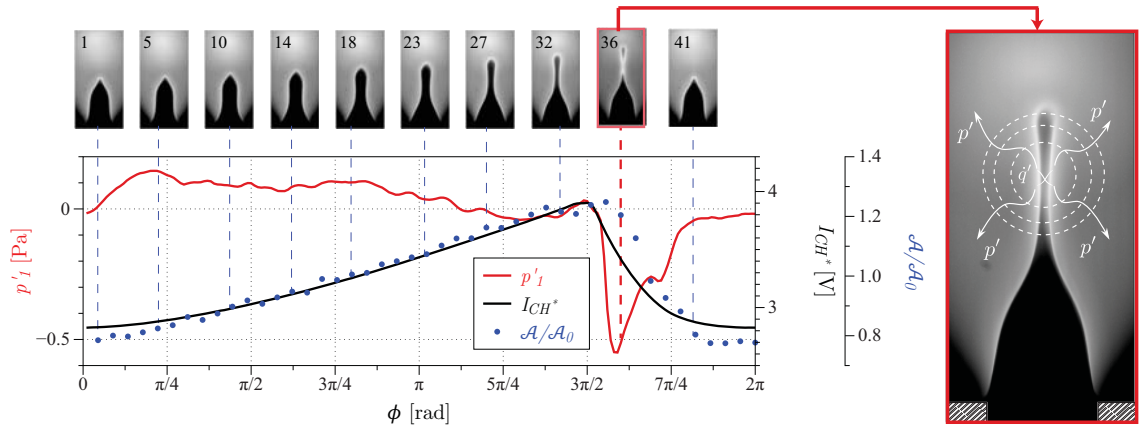

(b) $f_{ex} = 100$ Hz

Figure 5.7: Ten frequency-locked images for a cycle of excitation, the images are compared with the light intensity, I_{CH^*} (——), external acoustic pressure, p'_1 (——), and normalized flame surface fluctuation, $\mathcal{A}/\mathcal{A}_0$ (•). The experiment is performed on a stable flame in a T50h case with a bulk velocity of $\bar{v} = 1.6$ ms^{-1} and an equivalence ratio of $\Phi = 0.95$. The velocity fluctuation level is $\varepsilon = 0.1$.

In both cases the light intensity and the flame surface signal are well correlated. In addition two different flame front dynamics are observed: for a modulation frequency of $f_{ex} = 50$ Hz the flame is deformed but it never pinches and no reacting pockets are detached from the flame front while for the $f_{ex} = 100$ Hz the flame front is strongly deformed and it experiences the apparition of cups and the detachment of reacting pockets.

This behavior is due to the fact that the wave length of the perturbation depends on the excitation frequency and the bulk velocity $\lambda_c = \bar{v}/f_{ex}$ (Baillot *et al.* (1992)). If the bulk velocity is kept constant, the wave length of the perturbation decreases when the excitation frequency increases. λ_c corresponds to 32 mm and 16 mm for $f_{ex} = 50$ and 100 Hz, respectively. If we consider that the stationary flame length is about $l_f = 22\ mm$ one can conclude that in the case of $f_{ex} = 50$ Hz only one convective perturbation is present in the flame front at the same time while in the $f_{ex} = 100$ Hz case one can have more than one perturbation on the flame front at the same time.

In the $f_{ex} = 50$ Hz case the flame is strongly deformed, but no fresh gases pockets are formed. A strong drop in the pressure signal is detected when the two sides of the flame front merge together which for this case corresponds to the 60$^{\text{th}}$ frame. Likewise, for the case $f_{ex} = 100$ Hz two peaks in the external pressure signal are detected, a strong initial peak followed by a weaker peak. The first peak corresponds to the moment when the flame claps somewhere between the 32$^{\text{th}}$ and 36$^{\text{th}}$ frame, while the second peak occurs somewhere between the 36$^{\text{th}}$ and 41$^{\text{th}}$ frame when the pocket of fresh gases is consumed.

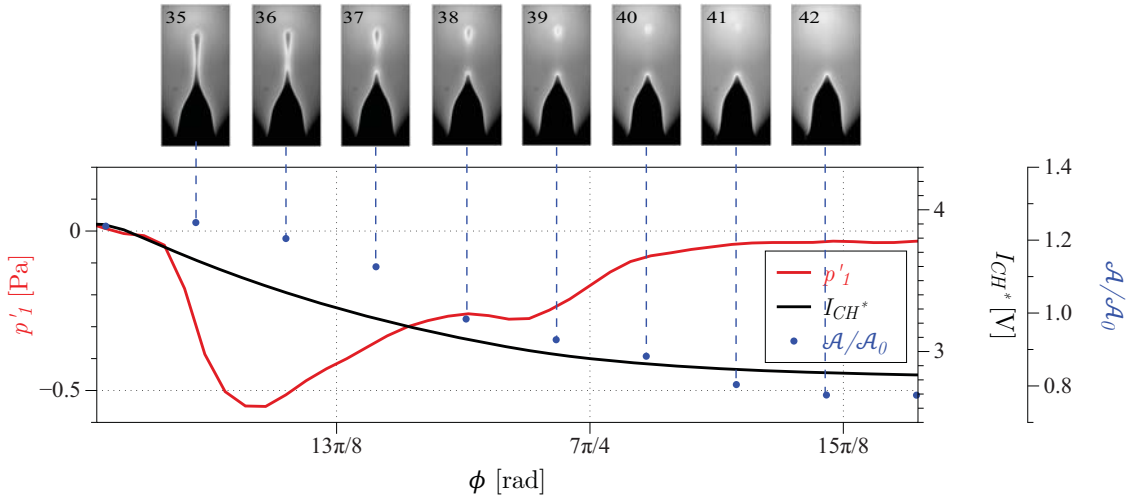

Figure 5.8: Ten frequency-locked images for a cycle of excitation, the images are compared with the light intensity, I_{CH^*} (——), external acoustic pressure, p'_1 (——), and normalized flame surface fluctuation, $\mathcal{A}/\mathcal{A}_0$ (•). The experiment is performed on a stable flame in a T50h case with a bulk velocity of $\bar{v} = 1.6$ ms^{-1} and an equivalence ratio of $\Phi = 0.95$. The frequency of the modulations is $f_{ex} = 100$ Hz and the magnitude $\varepsilon = 0.1$.

Figure 5.8 shows a zoom for the $f_{ex} = 100$ Hz case between the moment when the pocket of fresh gases is created and the moment when it disappears (frame 35$^{\text{th}}$ to 44$^{\text{th}}$). Here the pocket of fresh gases is detached somewhere between the 35$^{\text{th}}$ and 36$^{\text{th}}$ frame. At the same time, one can notice the maximum intensity on the $|p'_1|$ signal. From the 37$^{\text{th}}$ to 42$^{\text{th}}$ frame the pocket of fresh gases is gradually consumed by the flame but during this process the rate of change of the flame surface fluctuation, $d\mathcal{A}'/dt$, is small compared to the rate of change of the flame surface fluctuation between the 35$^{\text{th}}$ and 36$^{\text{th}}$.

These results demonstrated that in this experiment the mechanism responsible for noise production is the flame "clapping". Depending on the frequency of oscillation this "clapping" can either create or not pockets of fresh gases that will be detached from the flame front and gradually consumed. Therefore we can determine the distance between the acoustic monopole and the burner outlet, r_0, using the frame where the flame claps. The point where the flame claps is determined as the altitude from the burner outlet at which the two flame fronts merge together which in practical terms corresponds to the pixel with maximum intensity in the selected photo and it can be easily determined by the imagine processing algorithm.

5.4.1 Dependency of the pinching distance r_0 on slot temperature T_s

Now that we know how to determine r_0 we can focus on the solution of the dispersion relation in which r_0 is needed. We have seen that for the B07 slot burner, at low temperatures of the slot (*e.g.* T50h), the combustion instability develops at a frequency of $f_r = 58$ Hz. It is interesting to measure the pinching distance r_0 at a frequency close to this resonance frequency and determine if this pinching distance is affected by the slot temperature. To do this we repeat the procedure described in Sec. 5.4 but this time we pulsate an initially stable flame (using the B15 slot burner) at a frequency of $f_{ex} = 60$ Hz, and for three temperature of the slot, T50h, T90h and T120h.

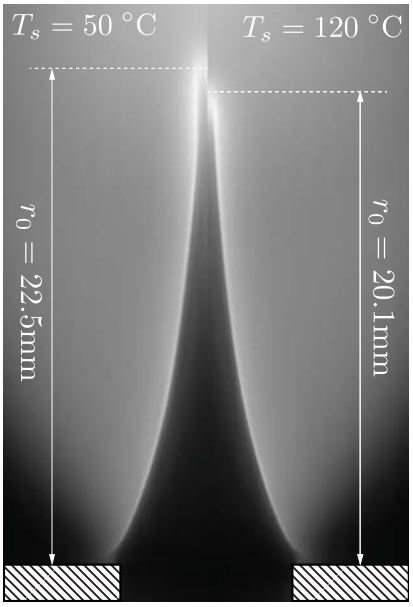

Figure 5.9: Pinching distance for T50h and T120h and a excitation frequency of $f_{ex} = 60$ Hz. The flow conditions were $\bar{v} = 1.6$ ms^{-1} and $\Phi = 0.95$.

Figure 5.9 shows the comparison between cases T50h and T120h: the pinching distance slightly decreases with the temperature of the slot. The pinching distance are $r_0 = 22.5,\ 21.8$ and 20.1 mm for cases T50h, T90h and T120h respectively for $f_{ex} = 60$ Hz.

5.5 Impact of r_0 on the stability of the system (analytical stability criteria form Eq. 3.46)

Now we are interested on how the diminution of r_0 can affect the stability of the system. Equation 5.13 shows that r_0 affects the resonant feedback in two ways: first, it affects the amplitude of the acoustic pressure fluctuation radiated back to the burner outlet; second, it affects the total time delay of the combustion instability process.

If we look at it from the time delay τ_{r_0} point of view, we know that the total time delay of the resonance process is the sum of the convective and acoustic time delays, $\tau = \tau_c + \tau_{r_0}$ (Durox *et al.* (2009a)). A diminution of 2.4 mm on r_0 between the case T50h and T120h would decrease the acoustic time delay by 7 μs which is negligible compared to the convective time delay which is of the order of $\tau_c = 14$ ms if we consider a first order approximation where $\tau_c = l_f/\bar{v}$. Thus one can conclude that the reduction on the acoustic time delay τ_{r_0} would not have any effect on the stability of the system.

On the other hand, the effect of r_0 on the amplitude of the acoustic pressure fluctuation radiated back to the burner can be study recalling Eq. 3.46. This analytical stability criteria was obtained in Sec. 3.5.2 and it was already used on the reacting acoustics study in Sec. 4.5. We can re-write Eq 3.46 as:

$$\omega_i = -\delta - \frac{\omega_0 \sin(\omega_0 \tau)}{2}\mathcal{N} \tag{5.15}$$

where δ is the damping coefficient of the burner, ω_0 is the natural pulsation of the burner, and $\mathcal{N} \propto \mathcal{G}_0/r_0$ is an interaction coefficient that depends on the pinching distance, r_0 and the gain $\mathcal{G}_0$. From Eq. 5.15 we can easy see the effect that a decrease of r_0 would have in the stability of the system: assuming that $\mathcal{G}_0$ does not change and that the system is initially unstable ($\sin(\omega_0\tau) < 0$) a diminution of r_0 by the effect of T_s would produce a growth of ω_i. In other words it would make the system more unstable.

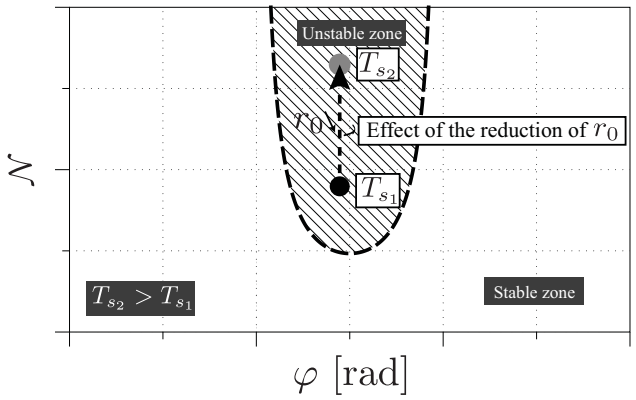

Figure 5.10: Schematic representation of the r_0 effect on the stability of the system.

Fig. 5.10 shows, in a schematic way, the effect mentioned above. If r_0 decreases when

the slot temperature is increased from T_{s_1} to T_{s_2} the interaction coefficient $\mathcal{N}$ is increased. Thus, if we start from the T50h case where the system is initially unstable the increase on the slot temperature, T_s, will decrease the pinching distance r_0 and consequently increase the interaction coefficient $\mathcal{N}$, which will make the system even more unstable. This in contradiction with the observation of Ch. 2 in which the increase of the slot temperature has a stabilizing effect on the system.

Consequently, the dependency on the pinching distance with the slot temperature appears to be a consequence of the effect of the slot temperature on the combustion instability rather that the cause. It is more likely that r_0 depends on the amplitude of the flame oscillations, if the amplitude decreases by the increase in T_s, r_0 decreases.

5.6 Conclusion

An experiment was setup to study the combustion noise produced by a stable laminar premix flame when submitted to acoustic oscillations, this study follows the protocol of Schuller *et al.* (2002) for a jet flame impinging on a cooled plate. The objective was: first, to validate the classical combustion theory used in Ch. 3 to establish a linear stability system; and second, to determine the distance r_0 from the slot outlet to the place where the acoustic monopole is located.

Experiments are in good agreement with the theoretical prediction of Clavin and Siggia (1991) and the experimental work of Schuller *et al.* (2002). One can conclude that for the slot burner used in this study, the noise radiated by this 2D slot premixed laminar excited flame is directly proportional to the rate of change of the total flame surface. The predicted far-field pressure obtained from the flame light emission is in good agreement with external pressure measured by M_1. Tests were performed over a wide range of frequencies although only two representative cases where shown 50 and 100 Hz. The cases not presented in this document have the same trend.

A procedure was developed in which joint measurements of external acoustic pressure, p'_1, flame spontaneous emission of CH^* radicals, I_{CH^*}, and flame surface, $\mathcal{A}$, are used to accurately determine the position of the pinching distance downstream the burner outlet r_0. The pinching distance r_0 was defined as the point where the flame claps, or, more precisely, the point where the two sides of the flame front merge together.

The pinching distance, r_0, was calculated for an excitation frequency of $f_{ex} = 60$ Hz and for the three slot temperature cases it corresponds to: $r_0 = 22.5,\ 21.8$ and 20.1 mm for T50h, T90h and T120h respectively. It has been shown that the pinching distance slightly depends on the slot temperature. For an excitation frequency close to that of the natural instability r_0 slightly decreases with T_s. For the practical case of the solution of Eq. 3.32 we will use the mean value of the three results as small variations on r_0 are

negligible on the stability of the system compared to the effects that the flame dynamics has on it as demonstrated from Eq. 4.46. Thus r_0 will be set to 21.5 mm. This is the value that will be used to solve the dispersion relation.

In Ch. 4 the acoustics of the burner was studied, two parameters (ω_0 and δ) were measured experimentally and were found to be independent of the slot temperature. The present chapter studied the combustion noise and one more parameter (r_0) was experimentally measured: it shows small dependency on T_s, nevertheless, thanks to the analytical stability criteria, we were able to concluded that this effect is negligible on the stability of the system. From the results of this chapter and taking into account that the acoustic properties of the burner under non-reacting operation are not affected by the slot temperature one can conclude that the increase on the slot temperature has a direct impact on the combustion process and specifically on the flame dynamics. At the same time, in Sec. 4.4 we conclude that the slot temperature modifies the phase-lag of the flame response, φ. However we still do not know how big this impact is and more importantly we do not know if the magnitude of the flame response, $\mathcal{G}$, is also affected by T_s. The purpose of the next chapter is to quantify the effect of the slot temperature on the flame dynamics by measuring the effects of φ and $\mathcal{G}$ on T_s and how these two parameters along which the ones already calculated control the dispersion relation Eq. 3.32.

Chapter 6

Combustion dynamics: effects of the slot temperature and reference point location on the FTF

This chapter focuses on the experimental determination of the flame response to velocity fluctuations introduced in the upstream duct. These flame dynamics constitute a central element of the resonant feedback that drives combustion instabilities. In the case of premixed combustion, the motion of the flame front is generally driven by velocity perturbations impinging on the flame front. This chapter aims at determining the influence of the slot temperature on the flame dynamics. First, in Sec. 6.1 the approach and the experimental setup used to study the combustion dynamics will be presented. Second, in Sec. 6.2 the results are presented. In Sec. 6.3 we will confront this results with the analytical stability criteria. Finally a discussion of the reference point location where velocity fluctuations are measured is presented in Sec. 6.4.

6.1 Introduction

The early work of Crocco (1951) links the velocity fluctuation to the heat release rate fluctuations by an interaction index, n, and a time lag, τ. A velocity perturbation produces a perturbation of the heat release after a time lag, τ, and the coefficient n characterizes the strength of this coupling:

$$\dot{q}'(t) = n\, v'(t-\tau) \tag{6.1}$$

This idea can be generalized by defining the Flame Transfer Function (FTF) which is defined as the ratio of the relative heat release rate perturbations $\dot{q}'/\bar{\dot{q}}$, to the upstream velocity fluctuations, $v'/\bar{v}$:

$$\mathcal{F}(\omega) = \frac{\dot{q}'/\bar{\dot{q}}}{v'/\bar{v}} \tag{6.2}$$

$\mathcal{F}(\omega)$ is a complex number, its magnitude, $\mathcal{G}(\omega) = |\mathcal{F}(\omega)|$, and its argument, $\varphi(\omega) = \omega\tau = \arg(\mathcal{F}(\omega))$, correspond respectively to the gain and the phase-lag of the flame response:

$$\mathcal{F}\,(\omega) = \mathcal{G}(\omega) e^{i\varphi(\omega)} \tag{6.3}$$

The FTF concept has ben used for many years in the study of combustion dynamics e.g. Boyer and Quinard (1990); Fleifil *et al.* (1996); Dowling (1999); Ducruix *et al.* (2000); Schuller *et al.* (2003a); Kornilov *et al.* (2007); Wang *et al.* (2009); Cuquel *et al.* (2011); Kedia *et al.* (2011) among others.
For linear-stability analysis, the FTF is a function of a single variable: the pulsation ω. In order to predict limit-cycle amplitudes and more complex phenomena, the dependance to the amplitude of the velocity fluctuation magnitude may be added, resulting in a so-called Flame Describing Function FDF. One may refer to the following studies on non-linear FTF: Noiray *et al.* (2008); Durox *et al.* (2009b); Boudy *et al.* (2011); Palies *et al.* (2011) and Kashinath *et al.* (2013).
The objective of this chapter is to find the two missing parameters ($\mathcal{G}$ and φ at the oscillation frequency of the self-sustained operation) to solve the dispersion relation Eq. 3.32 and determine the stability of the system. This information can be determined by studying the linear flame transfer function.
The influence of the slot temperature, T_s, on the flame response is of central interest in this chapter. So far, none of the studies mentioned above have directly addressed this issue. Nevertheless, some studies deal with the unsteady heat loss to the burner rim and highlight the importance of the wall temperature in the flame response to acoustic oscillations (Schreel *et al.* (2002); Rook and de Goey (2003); Altay *et al.* (2009) and Kedia *et al.* (2011)). However, the mechanisms of this interaction between wall temperature and flame dynamics remains unclear.

6.1.1 Linear Flame Transfer Function definition

For premixed systems at constant equivalence ratio, flame dynamics are strongly correlated to the velocity fluctuations at the flame base, v_1'. Here, we explore how the FTF may depend on the slot temperature $\mathcal{F}(\omega, T_s)$.
For premixed combustion at a given equivalence ratio, it has been demonstrated that the heat release rate $\dot{q}$ is proportional to the flame surface $\mathcal{A}$ and to the light emission from free radicals CH* (Price *et al.* (1969); Schuller *et al.* (2002)), and it is possible to determine the transfer function from one of the following expressions:

$$\mathcal{F}(\omega, T_s) = \frac{\dot{q}'/\bar{\dot{q}}}{v_1'/\bar{v}} = \frac{\mathcal{A}'/\bar{\mathcal{A}}}{v_1'/\bar{v}} = \frac{I'_{CH^*}/\bar{I}_{CH^*}}{v_1'/\bar{v}} \tag{6.4}$$

Measuring the complex number $\mathcal{F}(\omega, T_s)$, requires a stable configuration that can be pulsated over the range of frequencies where the flame is sensitive to acoustic perturbations. For this purpose, the burner B15 (*cf.* Fig. 1.5) is chosen for the FTF measurements.

6.1.2 Transfer function determination

Light emission from CH* free radicals, I'_{CH^*} and velocity fluctuations v_1' are recorded simultaneously by the photomultiplier (PM) and the hot-wire probe (HW) represented in Fig. 6.1, respectively. In the B15 slot burner the HW is placed along the slot axis at the

reference point located 142 mm upstream of the burner outlet. A test no present in this document was performed to confirm that the introduction of the HW at the slit inlet has not an impact in the resulting velocity fluctuation at the slot outlet.

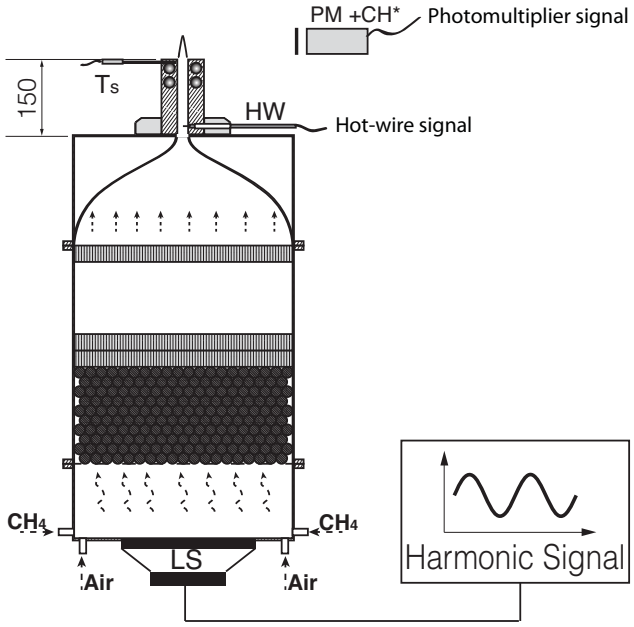

Figure 6.1: Experimental setup for FTF measurements. Simultaneous measurements of heat release rate and velocity fluctuations are recorded during 5 s of harmonic excitation for a frequency range of $[5, 300]$ Hz.

A spectral analysis of the normalized temporal signals, $v_1'(t)/\bar{v}$ and $I'_{CH^*}(t)/\bar{I}_{CH^*}$, is sufficient to determine the experimental FTF. For this, the ratio $\mathcal{S}_{vq}/\mathcal{S}_{vv}$ is calculated, here $\mathcal{S}_{vq}$ is the cross power spectral density between the $v_1'(t)/\bar{v}$ and $I'_{CH^*}(t)/\bar{I}_{CH^*}$ signals and $\mathcal{S}_{vv}$ is the power spectral density of the velocity signal, $v_1'(t)/\bar{v}$ at the excitation frequency f_{ex}. This procedure is repeated for every excitation frequency between $f_{ex} = 10$ and 300 Hz in steps of $\Delta f_{ex} = 5$ Hz and for the three reference cases T50h, T90h and T120h.

$$\mathcal{F}(\omega, T_s) = \frac{\mathcal{S}_{vq}}{\mathcal{S}_{vv}} \tag{6.5}$$

The gain is defined as the magnitude of $\mathcal{F}(\omega, T_s)$, $\mathcal{G} = |\mathcal{F}(\omega, T_s)|$ while the phase is its argument, $\varphi = \arg[\mathcal{F}(\omega, T_s)]$.

6.2 Experimental results

The FTF is measured by acquiring the signals with a sampling frequency $f_s = 20$ kHz during an acquisition time of 5 s. The forcing signal is generated with the modulation system described in Sec. 1.4.4. The frequency range is $[10, 300]$ Hz. The level of rms

velocity fluctuation is kept constant at $\varepsilon = 0.1$ (defined by Eq. 1.10) for all frequencies, which corresponds to the value observed in the self-sustained oscillation test when the slot is cold (*cf.* Fig. 2.6) and still is in the linear regime (*cf.* Fig. A.1). The bulk velocity and equivalence ratio are $\bar{v} = 1.6$ m/s and $\Phi = 0.95$, respectively. Three relevant temperatures were chosen to measure the FTF which corresponds to the cases T50h, T90h and T120h.

6.2.1 Input signals for the FTF determination

Typical normalized signals of velocity fluctuation, $v_1'/\bar{v}$, measured by the HW and flame light intensity fluctuation $I'_{CH^*}/\bar{I}_{CH^*}$ recorded by the PM are presented in Fig. 6.2. Three different frequencies of excitation $f_{ex} = 50,\ 125$ and 200 Hz and three cases T50h, T90h and T120h are shown.

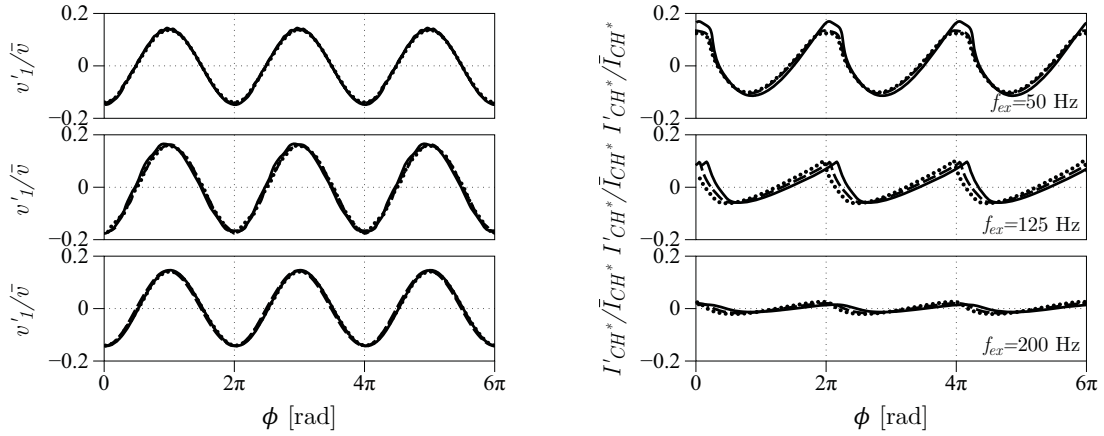

(a) Normalized velocity fluctuation $v_1'/\bar{v}$.

(b) Normalized flame light intensity fluctuation, $I'_{CH^*}/\bar{I}_{CH^*}$.

Figure 6.2: Flame transfer functions signals during three cycles of oscillations for three different frequencies of excitation $f_{ex} = 50$ Hz (top row), 125 Hz (middle row) and 200 Hz (bottom row) and for three slot temperatures: T50h (——); T90h (- - - -) and T120h (·····). Flow velocity and equivalent ratio where $\bar{v} = 1.6$ ms^{-1} and $\Phi = 0.95$, respectively. The modulation level was kept constant at $\varepsilon = 0.1$.

Figure 6.2(a) presents the velocity signals. Velocity fluctuations have a sinusoidal shape and the amplitude, $\tilde{v}_1$, is constant for all three frequencies and all three slot temperatures ($\tilde{v}_1/\bar{v} = \sqrt{2}\varepsilon \approx 0.14$) [1]. On the other hand, Fig. 6.2(b) shows that the light intensity fluctuation signals are less linear and the magnitude is not constant with the frequency nor the slot temperature. The I'_{CH^*} signal dependency with frequency is expected:

[1] We recall that the velocity was defined in Sec. 1.4.4 as: $v_1 = \bar{v} + v_1'$, where v_1' is the velocity fluctuation at the reference point, defined by $v_1' = \tilde{v}_1 \cos(\omega t)$. Here $\tilde{v}_1$ is the amplitude of the fluctuation, which in terms of ε correspond to $\tilde{v}_1 = \sqrt{2}\,\bar{v}\,\varepsilon$.

all these flames act as a low-pass filter. The dependence on the slot temperature is more difficult to identify but it is present: for low frequencies, typically $f_{ex} < 125$ Hz, the flame have a slightly weaker response to velocity fluctuations when the temperature of the slot is increased. This behavior is in qualitative agreement with the experiments of Ch. 2 where the natural instability of the flame was gradually attenuated with the increase of the slot temperature. One may recall that the frequency of the natural instability was $f_r = 58$ Hz for the B07 burner. On the other hand, for high frequencies, typically $f_{ex} > 125$ Hz this characteristic is inverted, the flame tends to have a stronger response to the same velocity fluctuations when the temperature of the slot is increased.

6.2.2 Flame transfer function

An example of FTF (determined experimentally) is shown in Fig. 6.3. For all slot temperatures, the gain features a characteristic low-pass-filter shape and the phase grows almost linearly with frequency. However, as T_s is increased, $\mathcal{G}$ decreases for frequencies below 125 Hz while it increases past 125 Hz. The phase, φ, is however marginally affected despite a slight decrease as T_s increases. These results can be repeated (on different days for example, or from high slot temperatures to cold slot temperatures and vice-versa) so that the difference obtained in Fig. 6.3 correspond to real physical mechanisms and are not due to experimental uncertainties.

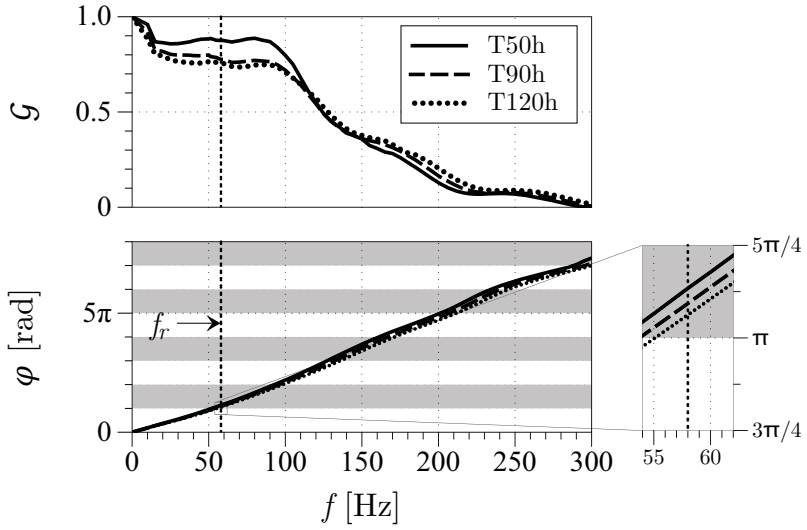

Figure 6.3: Flame transfer function for three different slot temperatures, T_s, corresponding to the cases T50h (——); T90h (- - - -) and T120h (·····). Flow velocity and equivalent ratio are $\bar{v} = 1.6$ ms^{-1} and $\Phi = 0.95$, respectively. Velocity fluctuations are kept constant for all frequencies at $\varepsilon = 0.1$. The reference point is located at $y = -142$ mm upstream of the flame.

The shades zones in Fig. 6.3 correspond to potentially unstable zones that fill linear stability criteria in an ideal system without dissipation ($\delta = 0$ or $\sin(\varphi) < 0$). However,

this is a necessary condition for instability but it is not sufficient, a real system will develop self-sustained oscillation if the energy fed to the system overcome its losses.

6.3 Impact of the flame dynamics on the stability of the system (analytical stability criteria form Eq. 3.46)

We now focus on the effect of the flame dynamics on the stability of the system. The analytical stability criteria (*cf.* Eq. 3.46) depends on the gain, $\mathcal{G}_0$, and the phase, φ_0, which are the gain and the phase of the FTF measured at the natural natural pulsation frequency of the burner, ω_0. However, to derive the approximate analytical solution it was necessary to assume that the pulsation frequency of the system, ω, was close to the natural pulsation of the burner, ω_0. In order to obtain more accurate results one can evaluate $\mathcal{G}$ and φ at the actual pulsation frequency of the instability, $\omega = \omega_r + i\omega_i$. This is difficult to do experimentally. However, one can measure the frequency of oscillation under self-sustained oscillations operation and obtain $\omega_r = 2\pi f_r$ and then assume that $\omega = \omega_r$. This assumption is based on calculations that indicate that ω_i is one order of magnitude smaller than ω_r. The self-sustained frequency of oscillation, f_r, was measured in Ch. 2. It was found to be around 58 Hz for the slots temperature where the flame is unstable (*cf.* Fig 2.7). It is then more convenient to use the values of the gain and phase of the FTF at $\omega_r = 2\pi f_r$: $\mathcal{G}_r = \mathcal{G}(\omega_r)$ and $\varphi_r = \varphi(\omega_r) = \omega_r \tau$.

Table 6.1: Phase-lag φ_r at the frequency of the instability (f_r = 58 Hz), compared to the observations of Ch. 2. The analytical stability criteria states that a necessary conditions for a system to develop an instability is that the phase lag $\varphi_r \in [\pi, 2\pi]$ modulo 2π, this is the case for all slot temperatures.

FTF	$\mathcal{G}$	φ_r [rad]	**Experimental observation**
T50h	0.88	1.13π	Unstable
T90h	0.78	1.09π	Stable
T120h	0.75	1.06π	Stable

Table 6.1 summarizes the results of the FTF for the three different slot temperatures corresponding to: T50h, T90h and T120h. Results shows that at the frequency of the natural instability the magnitude of the flame response, $\mathcal{G}_r$, decreases by almost 14 % from the case T50h to the case T120h. At the same time, but in a less proportion, the phase lag, φ_r, decreases by 7 % from the same two cases. Moreover, the three values of φ_r, for the three different slot temperature (T50h, T90h and T120h) remain between the limits of $[\pi, 2\pi]$. In Ch. 2 we have seen experimentally that only case T50h is unstable (Fig. 2.1). This is still consistent with Table 6.1: this table shows that the linear criterion

for instability is satisfied for all cases[2]. We know however that this is not sufficient to lead to instability in the real world: the gain must also be large enough and the losses small enough for an unstable mode to grow (Fig. 3.6). We know that the gain is affected by the slot temperature (Fig. 6.3). On the other hand, the other parameters involved in the dispersion equation (Eq. 3.32) are not modified by the slot temperature: Chs. 4 and 5 have shown that the damping coefficient δ, the Helmholtz frequency ω_0 and the pinching distance, r_0, were not modified when the slot temperature varies. Therefore, Eq. 3.46 hints that the mechanism responsible for the stabilization is the combined effect of the modification of $\mathcal{G}$ and φ (at the frequency of the self-sustained oscillation) when T_s is increased.

Through the stability map (Fig. 3.6(b)) build from the analytical stability criteria (Eq. 3.46) we can study the impact of this change on the flame dynamics with the increase of T_s on the stability of the system. Figure 6.4 is a zoomed version of Fig. 3.6(b), here a diminution of the gain, $\mathcal{G}_r$, produces a proportional diminution of the interaction coefficient, $\mathcal{N}$, this effect narrows the unstable zones (diagonal pattern zones in Fig. 6.4). On the other hand we saw in Table 6.1 that all the values of the phase-lag, φ_r, are close to π, meaning that the system is located in the left bounduary of the unstable band of Fig. 6.4 close to the stability threshold. Therefore, a reduction on φ_r may drag the system out of the unstable zones. In conclusion, for this experimental set-up, the increase of the slot temperature has an affect on the flame dynamics ($\mathcal{G}$ and φ) which has as consequence a stabilization impact on the whole system.

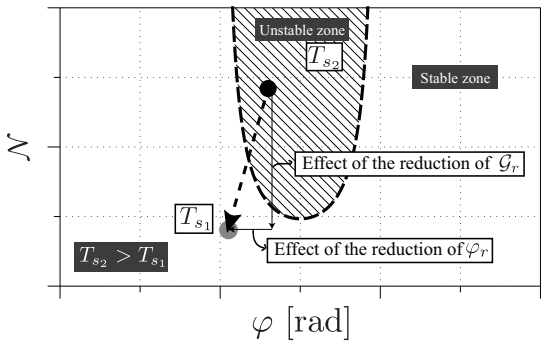

Figure 6.4: Stability map for arbitrary values of $\mathcal{N}$ based on Eq. 3.46. The diagonal solid patterns represent the unstable zones.

Now that we suspect which mechanisms explain the effect of the slot temperature on the overall flame stability, we will proceed in two directions:

- First we will gather all the experimental results (ω_r, δ, r_0, $\mathcal{G}_r$ and φ_r) obtained in the present and the two previous chapters and introduce them in the dispersion equation to check whether these changes really explain the stability variations observed experimentally. This will be done in Chapter 7.

[2] Taking into account the acoustic time delay between the perturbation at the HW reference point and the burner outlet, we found a $\Delta\tau = 0.5$ ms, this acoustic time delay doest not affect the stability criteria and the phase-lag remain in the unstable band $\varphi \in [\pi, 2\pi]$ for the three cases.

- In the following chapters (8 and 9), we will then see whether we can explain why the FTF's measured experimentally change when the slot temperature is changing. This will require models for the flame front response to forcing but also for the flame root (the place where the flame is anchored) because this is an important part of the process.

Before proceeding to Chs. 7 to 9, the end of the present chapter will be devoted to an experimental question which might jeopardize the present FTF results: is the location where the reference velocity is measured, an important factor in the FTF? In other words, could the position of the reference point play a role which we would have missed? This could be the case in our problem because we know that the effects we are investigating are small and very close to the stability threshold where oscillations can grow or be damped.

6.4 Discussion on the velocity fluctuation measurement

We will show in the next chapter that the FTF measured in the present section can be used in models to explain the burner stability sensitivity to slot temperature. Before doing this, we would like to study a problem which may control the accuracy of this FTF data: the position of the reference point. Indeed, one controversial question for FTF measurements is: where is the "input" of the burner-flame system, or more precisely, where should the velocity perturbation be measured? Truffin and Poinsot (2005) recommended that the velocity fluctuation must be measured as close as possible to the flame using the Helmholtz number:

$$\mathcal{H} = 2\pi \frac{l_c}{\lambda_{ac}} \tag{6.6}$$

where l_c is the distance between the reference point and the flame cone (Fig. 6.5) and λ_{ac} is the acoustic wave length. Truffin and Poinsot (2005) stated that $\mathcal{H}$ must be smaller that 0.01 to obtain consistent results. In practice, this implies that transfer functions measured for reference points which are not located close enough to the flame base are not intrinsic parameters of the burner but depend also on upstream and downstream conditions.

Schuller *et al.* (2003a) measure the velocity fluctuation 0.6 mm downstream the burner outlet (corresponding to $\mathcal{H} = 0.003$) while Kornilov *et al.* (2007) measure v' between $l_c = 3$ and 20 mm upstream the burner rim (corresponding to $\mathcal{H} = 0.1$ for the limit case of $l_c = 20$ mm) and found that between these limits this distance does not affect the FTF. However, in this study, due to geometrical constraints we had to measure v'_1 at the base of the slot, hence $l_c = 142$ mm. This gives us a $\mathcal{H} = 0.8$ for the limit case of a excitation frequency of $f_{ex} = 300$ Hz. The Helmholtz number is considerably larger than the limit stated in Truffin and Poinsot (2005), suggesting a possible problem for the model.

6.4.1 Velocity fluctuation along the slot axis

The discussion above suggest that reference point in our measurements is too far upstream the flame. Therefore, one is interested in how the position of the velocity fluctuation measurement affects the results of the FTF. For this purpose we designed a non-reacting experimental in which we modulate the flow with a loudspeaker (LS) placed at the bottom of the plenum and use a hot-wire (HW) to measure the velocity fluctuation at several stream-wise locations along the burner axis. Then, the velocity signal, $v_1(y,t)$, is compared to a reference signal, $s(t)$, that corresponds to the signal sent to loudspeaker. Figure 6.5 shows the experimental setup: the HW is set initially at the reference point, $y = -142$ mm, and it is moved downstream until $y = 20$ mm, in steps of $y = 0.2$ mm. This procedure is repeated for the two non-reacting cases T50c and T90c and for two frequencies of excitation $f_{ex} = 50$ and 130 Hz.

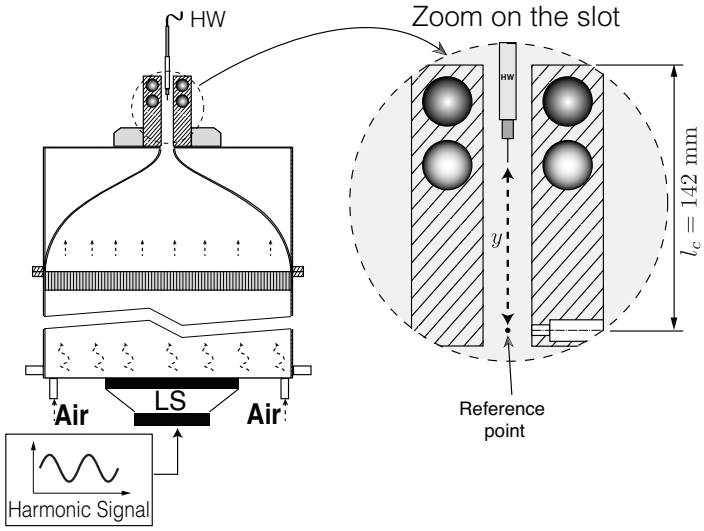

Figure 6.5: Experimental setup for measurements of the velocity fluctuation transfer function

To determine the flow dynamics we use a procedure similar to that of Birbaud *et al.* (2007b). Velocity signals are recorded by a HW at several stream-wise locations. The amplitude of the velocity fluctuation compared with the reference signal amplitude recorded at $y = -142$ mm gives the gain. The phase shift is evaluated between the HW and LS signals at the driving frequency. The flow transfer function, $\mathcal{V}$, between the velocity signal at the current point and the loudspeaker excitation signal is first determined by $\mathcal{T}_y = \mathcal{S}_{us}(y)/\mathcal{S}_{ss}$, where, $\mathcal{S}_{us}$ is the cross power power spectrum and $\mathcal{S}_{ss}$ is the power spectrum of the excitation signal. This quantity is then compared to the transfer function between the velocity signal at the reference point and the loudspeaker, $\mathcal{T}_{ref} = \mathcal{S}_{us}(y_{ref})/\mathcal{S}_{ss}$, to determine the transfer function between the two locations.

$$\mathcal{V}(f_{ex}) = \frac{\mathcal{T}_y}{\mathcal{T}_{ref}} \tag{6.7}$$

This transfer function provides information on the flow receptivity to the upstream acoustic modulation. The response at the excitation frequency is characterized in terms of gain,

$\mathcal{G}_v = |\mathcal{V}(f_{ex})|$, and phase, $\varphi_v = \arg[\mathcal{V}(f_{ex})]$. The amplitude of the perturbation at the reference point is kept constant at $\varepsilon = 0.1$ for the two explored frequencies.

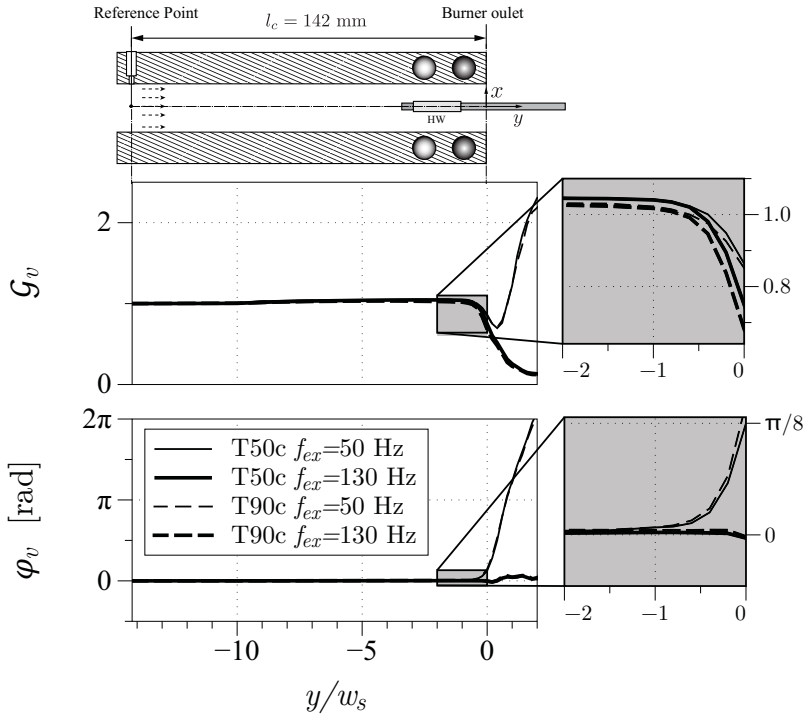

Figure 6.6: Axial flow transfer function for two different slot temperatures, T_s, corresponding to the cases T50c (——) and T90c (- - - -), and two different frequencies of excitation $f_{ex} = 50$ (thin line) and 130 Hz (thick line). Bulk velocity was kept constant at $\bar{v} = 1.6$ ms^{-1}. Velocity fluctuation at the reference point was kept constant at $\varepsilon = 0.1$ for the two frequencies explored.

The gain $\mathcal{G}_v$ and the phase φ_v are shown in Fig. 6.6: results are independent of the slot temperature, T_s, but, the excitation frequency has a big impact on the dynamics of the flow, especially in the vicinity of the burner outlet. The velocity transfer function gain and phase do not change with the axial distance until 10 mm upstream the burner outlet. At the burner outlet, the gain $\mathcal{G}_v$ has dropped by almost 20 % in all four cases, and the phase, φ_v increases for the low frequency case $f_{ex} = 50$ Hz while it remains almost constant for the high frequency case $f_{ex} = 130$ Hz.

These results agree with those of Kornilov *et al.* (2009), who conclude that close to the burner outlet (zoom in the right of Fig. 6.6) there is an area of impedance adaptation where a convective flow perturbation is generated (specially for low frequencies) and the plane acoustic behavior is affected.

6.4.2 Velocity fluctuation Trasnfer Function (VTF)

The previous results (Sec. 6.4.1) show that the velocity signal is strongly affected near the slot outlet, suggesting that the location of the reference point might have a strong influence on the FTF: here the velocity fluctuation is measured with a hot-wire. Even though the wire is very small, it can create an anchoring point for the flame and the high temperature will burn it. For this reason one must place the HW as far as possible from the flame base. For reacting experiments we placed the HW at 142 mm downstream the burner outlet. This geometrical constraint gives rise to the question: is the FTF affected by the position along the burner axis where the velocity fluctuation is measured? and if yes is it necessary to correct the FTF measurement to account for the distance between flame and reference point?

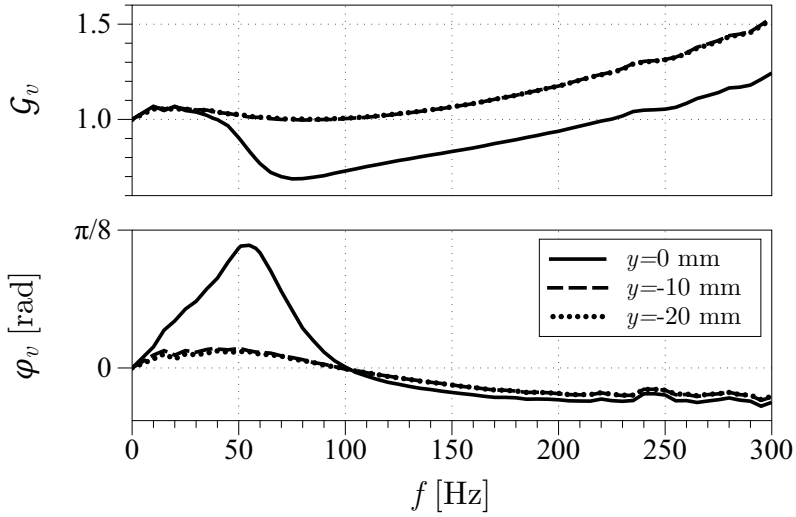

Figure 6.7: Velocity fluctuation transfer function for T50c case and three different longitudinal positions in the slot: $y = 0$ mm (——); $y = -10$ mm (- - - -) and $y = -20$ mm (·····). Bulk velocity was kept constant at $\bar{v} = 1.6$ ms^{-1}. Velocity fluctuation at the reference point was kept constant at $\varepsilon = 0.1$ for all frequencies.

In order to answer these questions, we define a velocity fluctuation transfer function VTF between velocity signals at different points along the duct. The gain, $\mathcal{G}_v$ and the phase, φ_v between the reference point where the velocity fluctuation is actually measured in the reacting tests ($y = -142$ mm) and three points downstream $y = -20$ mm, $y = -10$ mm and $y = 0$ mm which are the point where some authors (*e.g.* Truffin and Poinsot (2005); Kornilov *et al.* (2009)) recommend to measure it. The same procedure described in the previous subsection is performed, but this time we explore the same range of frequencies explored for the FTF measurement ($f_{ex} \in [10, 300]$ Hz). We explore only the T50c non-reacting case because it has been demonstrated (Fig. 6.6) that the cold flow dynamics is not influenced by the slot temperature.

Figure 6.7 show the results of the VTF. For $y = -20$ mm and $y = -10$ mm the perturbation remains an acoustic plane wave, and the phase and gain between the two points do not really change, while the phase, φ_v, remains almost invariable for all frequencies and the gain, $\mathcal{G}_v$, remains constant up to $f_{ex} = 150$ Hz then starts to increase. On the other hand, for $y = 0$ mm the behavior is completely different. The phase increases for low frequencies, typically $f_{ex} < 100$ Hz. Likewise, the gain drops to values of less than 0.8 for frequencies between $f_{ex} \in [50, 150]$ Hz. This is a clear indication that at the burner outlet the perturbation is no longer acoustic but becomes convective. These results are in agreement with those of Birbaud *et al.* (2007b) in which close to the burner outlet there is a transition from an acoustic perturbation to a convective perturbation for low frequencies. This also suggest that using a reference point close to the slot outlet ($y = 0$ mm) might introduce a supplementary bias on the FTF method.

6.4.3 Influence of the reference point on the FTF

We have seen that amplitude and phase of the velocity perturbation depend on the position along the burner axis where the velocity is measured. Close to the burner outlet the magnitude of the velocity fluctuation is reduced and the perturbation experiences a transition from acoustic (traveling at the speed of sound c) to convective (traveling at a velocity close to the bulk velocity $\bar{v}$). For this reason, and taking into account that in the combustion community the velocity fluctuation is usually measured close or in the flame cone we proceed now to correct the FTF with the VTF to be able to use the model with reference point close to the flame (without having to actually install the hot-wire near the flame during reacting tests).

Figure 6.8 shows the block diagram of the procedure used to correct the FTF. Fist we measure the flame transfer function (FTF) $\mathcal{F}(\omega, T_s)$ at the reference point. Then we measure the velocity fluctuation transfer function (VTF) $\mathcal{V}(\omega, y)$ between the reference point and different stream-wise locations along the slot axis, y. Finally we use both results to calculate the corrected flame transfer functions $\mathcal{F}_c(\omega, T_s, y)$. The corrected gain, $\mathcal{G}_c$, and phase, φ_c, for the new transfer functions are calculated as follows:

$$\mathcal{G}_c = \frac{\mathcal{G}}{\mathcal{G}_v} \tag{6.8}$$

$$\varphi_c = \varphi - \varphi_v \tag{6.9}$$

Figure 6.9 shows two transfer functions corrected for the velocity measurement position. Figure 6.9(a) is a FTF for a velocity measurement at 10 mm upstream of the burner outlet ($y = -10$ mm), while Fig. 6.9(b) is corrected for a velocity measurement at the burner outlet ($y = 0$ mm).

Figure 6.9(a) shows that at a distance upstream of the burner of $w_s = 10$ mm, the FTF is not affected by the position of the velocity measurement. Indeed, the FTF measured

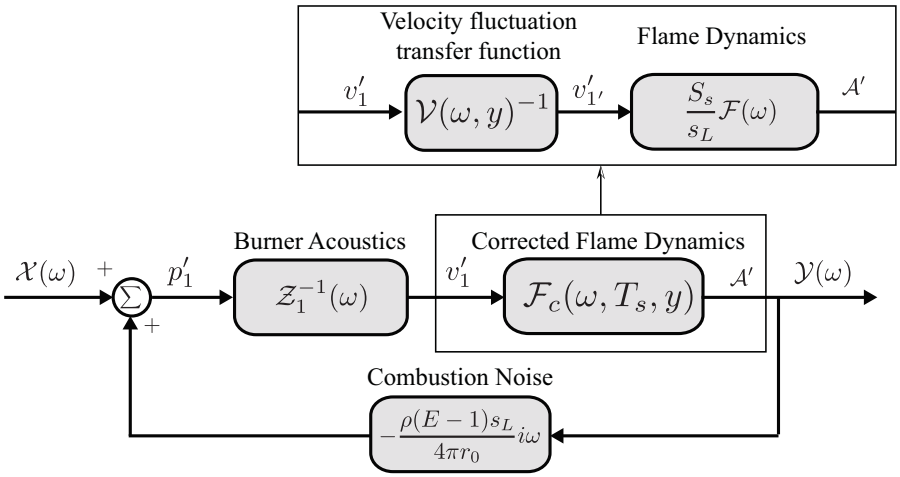

Figure 6.8: Block digram of the procedure used to correct the flame transfer function, $v_{1'}'$ correspond to the corrected velocity fluctuation. Refer to Fig. 3.4 to the original block diagram of the feedback loop.

at $y = -10$ mm is equivalent to the FTF measured at $y = -142$ mm. On the other hand, Fig. 6.9(b) shows that close to burner outlet the velocity measurement position has a big impact on the FTF measurement, especially for the gain, which goes beyond unity for $f_{ex} \in [50, 100]$ Hz. The phase φ presents a small reduction for the three slot temperatures. Although the values of the gain can change depending on where the velocity fluctuations is measured, the tendency of the flame to have a weaker response for $f_{ex} < 130$ Hz when the slot temperature is increased does not change.

Table 6.2 gather the results of the FTF at the frequency of the self-sustained oscillation for the three slot temperatures (T50h, T90h and T120h) and the three different reference points ($y = -142$, -10 and 0 mm). For cases where the velocity was measured at $y = -142$ mm and $y = -10$ mm results are equivalent, the magnitude of the flame response, $\mathcal{G}_r$, decreases by almost 14 % from the case T50h to the case T120h and the phase lag, φ_r, decreases by 7 % from the same two cases. Moreover, the six values of φ_r, remain between the limits of $[\pi, 2\pi]$ modulo 2π.

The same trend is observed in the case of the FTF measured at the burner outlet ($y = 0$ mm). The gain $\mathcal{G}_r$, decreases by 14 % from case T50h to T120h, while the phase φ_r decreases by 10 % from the same two slot temperatures. However, the results of the FTF measured at the burner outlet show a different dynamic behavior of the flame response. Indeed, for cases T50h and T90h the phase φ_r remains between the limits of $[\pi, 2\pi]$ modulo 2π: if enough acoustic energy is fed into the system, the system will develop self-sustained oscillations. On the other hand, in the case of T120h φ_r is not between the limits of $[\pi, 2\pi]$ modulo 2π as one can see in Table 6.2. Therefore, considering the stability criteria (Eq. 3.46) derived from the approximate analytical solution in Ch. 3, the

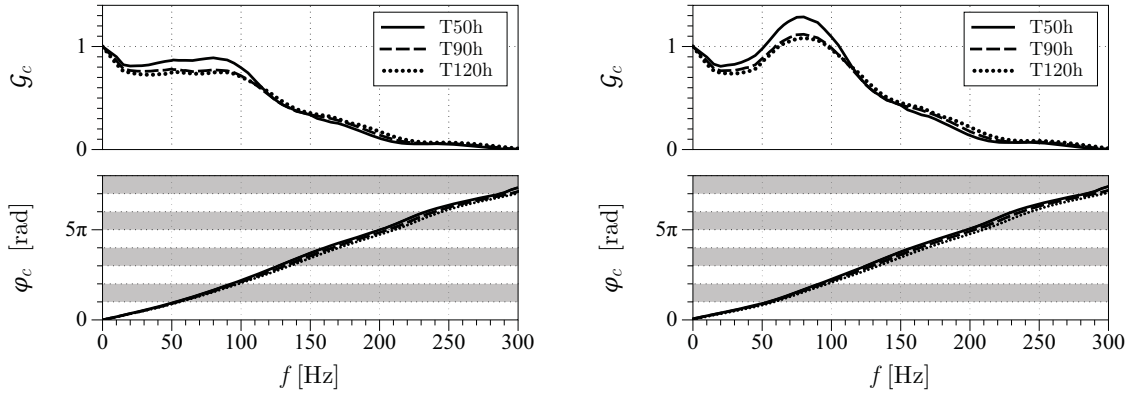

(a) FTF calculated for velocity fluctuations 10 mm upstream of the burner outlet.

(b) FTF calculated for velocity fluctuations at the burner outlet.

Figure 6.9: Flame transfer functions for three different slot temperatures, T_s, corresponding to the cases T50h (——); T90h (- - - -) and T120h (·····). Flow velocity and equivalent ratio were $\bar{v} = 1.6$ ms^{-1} and $\Phi = 0.95$ respectively. Velocity fluctuation was kept constant for all frequencies at $\varepsilon = 0.1$.

system will be always stable.

The results of the FTF measured at the burner outlet capture the dynamics behavior observed during the acoustic analysis performed under reacting configuration (*cf.* Sec. 4.4). In this acoustic study we conclude that between the cases T90h and T120h there is a switch on the flame behavior. In case T90h the flame is trying to drive the system into resonance, while for T120h the flame is helping stabilize the system. In Sec. 4.4 we concluded the dynamics of the flame is described by the sign of δ_f. If $\delta_f > 0$ the flame is helping to stabilize the system but if $\delta_f < 0$ the flame is destabilizing the system (Eq. 4.47):

$$\delta_f = \frac{\omega_0 \sin(\varphi_r)}{2} \frac{\mathcal{C}}{r_0} \mathcal{G}_r$$

The switch in the flame behavior is possible if the term $\sin(\varphi_r)$ in the equation above changes sign, which for this case happens when φ_r decreases to values under π. This is the case of the T120h FTF measured at the burner outlet: as the phase φ_r passes from 1.04π to 0.98π from T90h to T120h.

These results re-open the discussion on where the reference point must be placed in order to correctly describe the flame dynamics through the $n - \tau$ model. Some authors (Schuller *et al.* (2003a); Durox *et al.* (2009a)) have performed stability analysis assuming that the perturbations propagate as acoustic planar waves in the slot. However, they placed the reference point in the flame cone, where the propagation loses its acoustic nature for some frequencies. These studies are accurate because their experimental setups exhibit resonant frequencies considerable larger than the frequency band for which the

Table 6.2: Experimental results of the FTF for the three different slot temperatures corresponding to: T50h, T90h and T120h. Three different methods of measurement were used caring the position along the slot axis where the velocity is measured. The results of Gain $\mathcal{G}$ and phase φ were take at the resonance frequency of the natural instability of the B07 slot burner $f_r = 58$ Hz.

FTF	**y = −142 mm**		**y = −10 mm**		**y = 0 mm**	
	$\mathcal{G}_r$	φ_r	$\mathcal{G}_r$	φ_r	$\mathcal{G}_r$	φ_r
T50h	0.88	1.13π	0.87	1.12π	1.10	1.09π
T90h	0.78	1.09π	0.77	1.08π	0.98	1.04π
T120h	0.75	1.06π	0.75	1.05π	0.95	0.98π

planar wave assumption is affected. This is not our case, the resonance frequency of the instability is around $f_r = 58$ Hz which is between the limits $f_{ex} \in [0, 100]$ Hz (*cf.* Fig. 6.7) for which the propagation is no longer acoustic. We therefore suggest that in order to be coherent with the stability model it is necessary to place the reference point where the propagation is still an acoustic planar wave with the minimum Helmholtz number, $\mathcal{H}$ (Fig. 6.10).

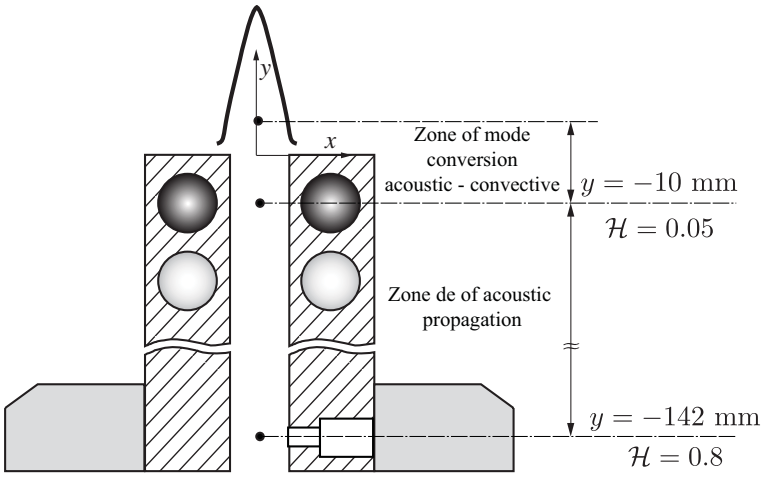

Figure 6.10: Identifications of the propagation zones in the B07 slot burner. $\mathcal{H}$ is calculated for the maximum driving frequency explored in this study $f_{max} = 300$ Hz.

We will consequently study the stability of the system with the results of the FTF measured at $y = -10$ mm; for which the propagation has an acoustic nature for all frequencies. At $y = -10$ mm one finds a Helmholtz number of $\mathcal{H} = 0.05$, which suggest that the limit of $\mathcal{H} < 0.01$ proposed by Truffin and Poinsot (2005) is too conservative. As a matter of fact, the FTF's measured at $y = -142$ and $y = -10$ mm are equivalent even though they correspond to two very different Helmholtz numbers $\mathcal{H} = 0.8$ and 0.05 respectively.

6.5 Conclusion

In this chapter, the approach used to determine the flame dynamics was exposed as well as the experimental setup. The Flame Transfer Function FTF has ben determined experimentally and a discussion on where the velocity should be measured was presented.

It has been demonstrated that the position where the velocity fluctuation measurement is performed has a big impact on the final form of the FTF. The initial perturbation propagates as a plane acoustic wave up to approximately 10 mm upstream the burner outlet (corresponding to one slot width $w_s = 10$ mm). Here, the perturbation loses its acoustic nature and thanks to a mode conversion mechanism (Schuller *et al.* (2003b); Birbaud *et al.* (2006)), it becomes a convective perturbation. The place where this mode conversion takes places strongly depends on the frequency. For low frequencies (when the acoustic wave length is large compared to the flame size $\lambda_{ac \gg l_f}$) the convective wave develops earlier upstream of the burner outlet, while, for high frequencies (when the acoustic wave length is of the flame size $\lambda_{ac \approx l_f}$) the acoustic behavior might propagate several centimeters downstream of the burner outlet. This mechanism of mode conversion was studied by Birbaud *et al.* (2006) and Birbaud *et al.* (2007b) and these studies are in agreement with the results presented here.

The FTF's measured at $y = -142$, -10 and 0 mm show the same trent for caring slot temperatures. At the resonance frequency of the self-sustained oscillation the gain, $\mathcal{G}_r$ and phase φ_r decrease with the increase of the slot temperature, T_s. However, the FTF measured at the burner outlet ($y = 0$ mm) has different characteristics. The gain goes beyond unity for $f_{ex} \in [50, 100]$ Hz and the phase goes under π for the T120h case. When the FTF is measured close to the flame cone, one is able to reproduce the dynamics behavior of the flame at different slot temperatures seen in Ch. 4 under reacting acoustics tests. Here we notice that at T90h the flame is trying to destabilize the system while at T120h the flame is helping stabilize the system. The same trend observed for the FTF measured at $y = 0$ mm as the phase φ_r passes from 1.04π to 0.98π from T90h to T120h.

For the solution of Eq. 3.32 one is interested in the FTF measured at $y = -10$ mm (Fig. 6.9(a)). This idea follows the hypotheses used in the linear stability model, where one assumes that the perturbation propagates as a planar acoustic wave. However, the discussion on where should the velocity measurement take place is still open. Big differences are noticed for the FTF's measured at different stream wise positions along the slot axis. One must take this into account if one is interested in capturing more complicated effects on the flame dynamics.

Table 6.3 summarizes the results of gain and phase at $f_r = 58$ Hz when measured at $y = -10$ mm. Results show that the flame response to acoustic oscillations has a strong dependency on the slot temperature. One find differences of 14 % and 7 % for the gain and the phase respectively, for the same operating point between cases T50h and T120h. These results will be used in next chapter along with the experimental results of

Table 6.3: Experimental results of the FTF measured at $y = -10$ mm for the three slot temperatures at the frequency of resonance of the burner B07.

		T50h	**T90h**	**T120h**
FTF at	$\mathcal{G}_r$	0.87	0.77	0.75
y = −10 mm	φ_r	1.12π	1.08π	1.05π

the burner acoustic Ch. 4 and combustion noise Ch. 5 to evaluate the dependency of the burner stability to the slot temperature T_s.

Chapter 7

Burner stability: resolution of the dispersion equation using experimental data

This chapter focuses on the determination of the B07 burner stability. The basic mechanisms involved in the coupling have been considered separately in Chs. 4, 5 and 6. It is now possible to use the analytical model of the combustion-acoustic coupling derived in Ch. 3 to determine the system stability. These results will be compared to the observations of Ch. 2 to establish the ability of the linear stability analysis in the prediction of combustion instabilities.
In Sec. 7.1 the solution of the linear system is performed. While Sec 7.2 presents a low-order model of the flame dynamics, in which, the principal mechanism affecting the flame response to velocity fluctuations will be exposed.

7.1 Solution of the dispersion equation

In Ch. 4 the acoustics of the burner was studied, and, ω_0 and δ were determined. It was also shown that the slot temperature, T_s, has no impact on the natural frequency ω_0 nor the damping coefficient, δ. Chapter 5 focused in the combustion noise and the pinching distance, r_0, was found to be independent of the slot temperature as well. Finally, Ch. 6 studied the combustion dynamics and $\mathcal{G}$ and φ were found. Observations show a strong dependency of the combustion dynamics to the slot temperature, specially in the gain, $\mathcal{G}_r$, which for frequencies close to the resonant frequency of the instability $f_r = 58$ Hz decreases with the slot temperature. The phase, φ_r was proved to be affected to a lesser extent.

Combining these results it is possible to solve Eq. 3.32 derived in Ch. 3 and determine the stability of the system for the three cases (T50h, T90h and T120h). It is also possible to use these experimental results to evaluate the accuracy of the approximate solution (Eqs. 3.43 and 3.44) obtained assuming a small combustion interaction coefficient ($\mathcal{N} \ll 1$).

Table 7.1: Experimental results for the burner acoustics, combustion noise and flame dynamics for the three cases T50, T90 and T120.

Case	Burner acoustics		Combustion Noise	Flame dynamics		Interaction Coefficient
	$\omega_0/2\pi$ [Hz]	δ [s^{-1}]	r_0 [mm]	$\mathcal{G}_r$ [-]	φ_r [rad]	$\mathcal{N}$
T50	52.5	15.80	21.5	0.87	1.12π	0.253
T90				0.77	1.08π	0.224
T120				0.75	1.05π	0.218

Table 7.2: Comparison between the exact and the approximate analytical solution of the dispersion relation with the observations.

Case	Solution of the dispersion relation				Experimental observation
	Analytical (Eqs. 3.43 and 3.44)		Exact (Eq. 3.32)		
	$\omega_r/2\pi$ [Hz]	ω_i [s^{-1}]	$\omega_r/2\pi$ [Hz]	ω_i [s^{-1}]	
T50	59.1	0.6	60.0	2.4	Unstable
T90	58.6	-6.0	59.4	-6.9	Stable
T120	58.5	-9.8	59.3	-12.0	Stable

Table 7.1 gathers the experimental results of the previous chapters while Table 7.2 compares the solutions of both, exact (Eq. 3.32) and the approximate analytical solution (Eq. 3.46), of the dispersion relation with the experimental observations of Ch. 2. The exact and approximate solution of Eq. 3.32 are in agreement with the observations, the solutions have positive growth rate for T50 case while negative growth rate are obtained for cases T90 and T120, indicating that the system will be unstable for the case T50 and stable for cases T90 and T120 as observed experimentally (Fig. 2.6).

Figure 7.1 presents the superposition of both solutions, the exact solution of Eq. 3.32 and the approximate analytical solution (Eq. 3.44). The domain chosen for the interaction coefficient and the phase is $\mathcal{N} \in [0, 0.4]$ and $\varphi \in [\pi, 2\pi]$ rad, respectively. For the exact solution the domain was discretized by steps of $\Delta\mathcal{N} = 0.0025$ and $\Delta\varphi = 0.042$ rad for $\mathcal{N}$ and φ, respectively. The exact solution is represented by the iso-contours of the positive values of ω_i: in the white region ω_i has negative values, the iso-contour $\omega_i = 0$ is represented by the solid black curve (——). The solution of the approximate analytical solution is superposed: the dashed black line (----) makes the unstable regions represented by diagonal patterns. The three experimental cases are represented as symbols, T50h (▲), T90h (●) and T120h (×).

In Fig. 7.1 the experimental points are close to the boundaries of the system stability map, for both solutions exact solution and the approximate analytical solution. Therefore, small changes in any of the five parameters (ω_0, δ, r_0, $\mathcal{G}_r$ and φ_r) can bring the system

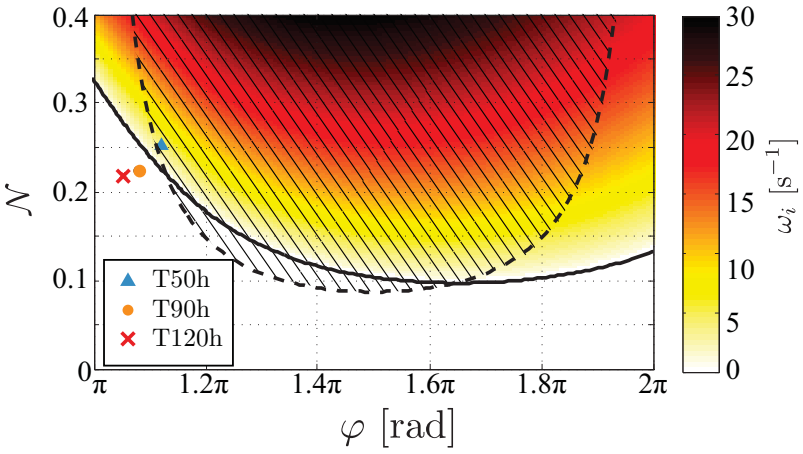

Figure 7.1: The exact solution of the dispersion equation (Eq. 3.32) is represented by the iso-contours of the positive values of ω_i, in the white region ω_i has vanished or has negative values, the iso-contour $\omega_i = 0$ is represented by the solid black curve (——). The solution of the approximate analytical solution (Eq. 3.46) is superposed, the dashed black line (----) and the solid patterns represent the unstable zones for the analytical stability criteria. The three experimental cases are represented as symbols, T50h (▲), T90h (●) and T120h (×)

from an unstable to a stable operation or vice-versa. Nevertheless, the tendency observed in Ch. 2 is well reproduced with both solutions. Case T50h is bounded in the unstable regions while cases T90h and T120h are bounded in the stable regions.

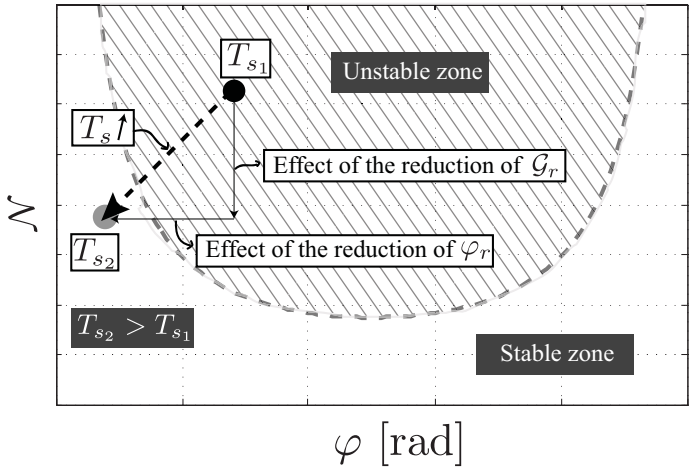

Figure 7.2: Description of the effect of increase of T_s on the stability of the system.

The gain, $\mathcal{G}_r$, is reduced by the effect of an increased slot temperature, T_s, from T50h to T120h. This phenomenon has a stabilizing effect on the system. Indeed, a reduction of $\mathcal{G}_r$ produces a proportional reduction of $\mathcal{N} = (\mathcal{N}/r_0)\mathcal{G}_r$. If the interaction coefficient, $\mathcal{N}$, is reduced the experimental points exit the unstable domain.

At the same time the reduction of the phase lag, φ_r, with the increase in T_s also has a stabilizing effect on the system. Indeed, as the experimental points are close to the left boundaries on the stability map, a reduction on the phase lag tends to bring the system out of the unstable domain.
However the reduction of $\mathcal{G}_r$ or φ_r would not be sufficient to stabilize the system. The flame is actually stabilized by the combined effects of T_s on both $\mathcal{G}_r$ and φ_r. Figure 7.2 shows a schematic representation of the effect of the slot temperature increase on the stability of the system, when T_s is increased the system goes from the initially unstable point (T_{s_1}) to a stable point (T_{s_2}).

Thanks to this analysis one can conclude that the mechanism leading to the attenuation of the instability is the effect of the slot temperature on the dynamics of the flame which is quantified and correctly captured by using FTF's as shown by Fig. 7.1. Indeed, the acoustics of the burner is not affected by the slot temperature. The combustion noise is marginally affected by the increase of the slot temperature but it is a consequence of the attenuation of the instability not the cause.

7.2 Low-order model for flame dynamics FTF's

We have shown that flame dynamics (measured by the FTF's) is the mechanism responsible for the attenuation of the instability when the slot temperature increases. However, it is not clear how the slot temperature affects the flame dynamics, as measured by the gain and the phase of the flame response to velocity oscillations. A joint approach to aboard this question is to study the response of a perfectly premixed flame front using the G-equation formulation and a level set analysis.

The level-set description of flame front motion was initially motivated by the discrepancies between the theory and the experimental observations. Over the last two decades this field has seen great advances, it went from the first models *e.g.* Boyer and Quinard (1990); Fleifil *et al.* (1996); Dowling (1999); Ducruix *et al.* (2000) which used uniform velocity perturbations to most sophisticated models like the one in Baillot *et al.* (1992) and Schuller *et al.* (2003b) using convective velocity perturbations, that did not satisfy the continuity equation, to the most recent (Cuquel *et al.* (2013)) in which a model using a convective velocity perturbation satisfying the continuity equation and including the flame anchoring point movement was developed.

The following section and chapters of this study are based on the modern theoretical developments using level-set descriptions to model the flame front kinematic response to flow perturbations represented by the G-equation. Although this theoretical approach is not the subject of this study, a review of the last results obtained with this theoretical development is of interest in finding the mechanisms which could link the wall temperature to the combustion dynamics.

7.2.1 G equation

Consider the case of a premixed flame stabilized over a rectangular slot burner of cross section area $S_s = l_s\, w_s$, where l_s is the slot length and w_s is the slot width. The flame takes the form of a triangular wedge Fig. (7.3). In the (x, y) coordinates the flame takes the form of a triangle.

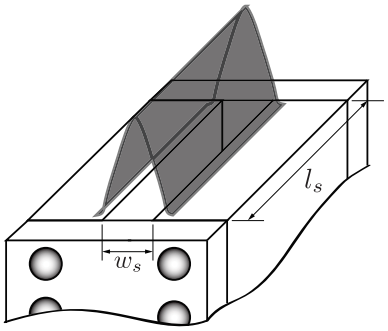

Figure 7.3: Schematic representation of a flame stabilized over a rectangular slot burner.

The flame front corresponds to a particular level, $G = (x, t) = 0$[1], of a scalar field G. The front consumes the fresh gases located on the $G < 0$ side by moving in the normal direction at a rate given by the laminar flame speed, s_L. The front is also convected by the incident axial velocity field $\vec{v}$:

$$\vec{v}(x,t) = u'(x,t)\mathbf{e_x} + (\bar{v} + v'(x,y))\mathbf{e_y}. \tag{7.1}$$

A transport equation for the iso-line $G = 0$ writes:

$$\frac{\partial G}{\partial t} + \vec{v}.\nabla G = s_L|\nabla G|, \tag{7.2}$$

which can be expressed in the frame attached to the steady flame front (Schuller *et al.* (2003b); Lieuwen and Preetham (2004)) (*cf.* Fig. 7.4):

$$\frac{\partial \xi}{\partial t} + \bar{\mathbf{u}}.\nabla \xi = \mathbf{v}'(\mathbf{x}, t) \tag{7.3}$$

where, $\mathbf{x} = x/\sin(\alpha)$ is the component normal to the steady flame front, $\bar{\mathbf{u}} = \bar{v}\cos\alpha$ is the mean flow velocity component tangential to the steady flame front, $\mathbf{v}'$ is the velocity perturbation component normal to the steady flame front and ξ is the displacement of the perturbed flame front respect to the stationary position. The solution of this partial

[1]In order to simplify the calculations, from now on, the coordinate system (x, y, z) will be moved to the left lip of the burner rim. The burner axis will be now placed at $x = 5$ mm and $y = z = 0$ mm

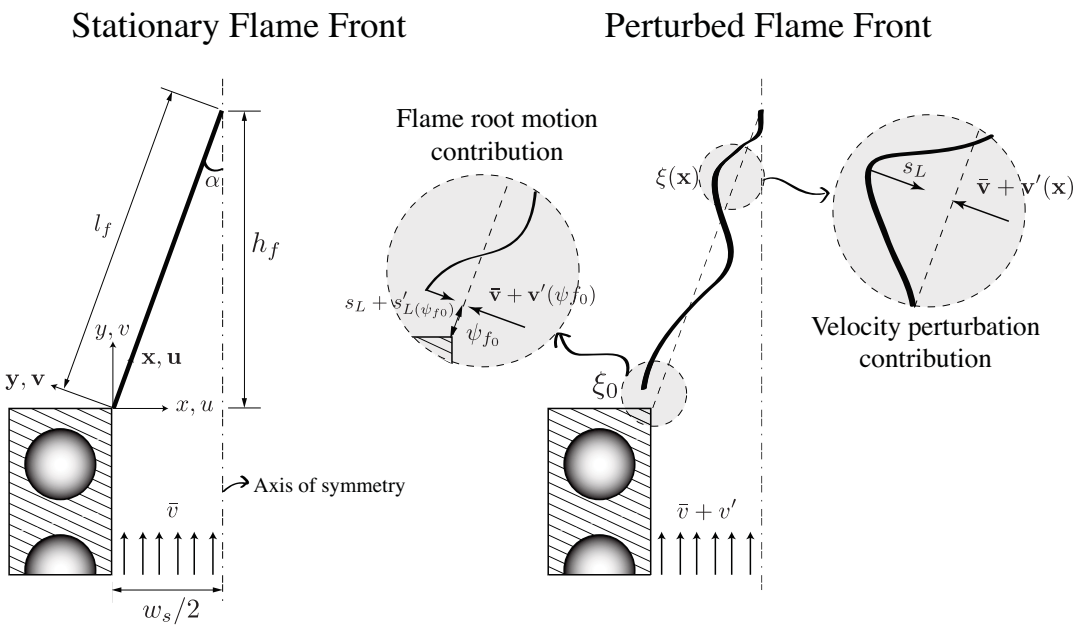

Figure 7.4: Schematic representation of the stationary flame front and the perturbed flame front.

derivative equation is given by the telegraph integral (Boyer and Quinard (1990); Schuller *et al.* (2003b) and Preetham and Lieuwen (2004)) and in the frequency domain is:

$$\tilde{\xi}(\mathbf{x}) = \frac{e^{i\kappa\mathbf{x}}}{\bar{\mathbf{u}}} \int_0^{\mathbf{x}} \tilde{\mathbf{v}}(\mathbf{x}') e^{-i\kappa\mathbf{x}'} \mathrm{d}\mathbf{x}' + \tilde{\xi}_0 \mathrm{e}^{\mathrm{i}\tilde{\omega}\mathbf{x}} \tag{7.4}$$

here, $\kappa = \omega/\bar{\mathbf{u}}$ is the wavenumber associated to the convection of the flame wrinkles along the steady flame front and $\tilde{\xi}_0$ is the flame front displacement at the flame base at $\mathbf{x} = 0$. Equation 7.4 exhibits two contributions to flame wrinkling (Fig. 7.4):

- The first contribution results from the velocity perturbation component that is normal to the steady flame front in the fresh gases, which is acting as a forcing therm in Eq. 7.3. This contribution has been the subject of several studies in the past *e.g.* Boyer and Quinard (1990); Fleifil *et al.* (1996); Ducruix *et al.* (2000); Schuller *et al.* (2003b); Lieuwen and Preetham (2004).

- The second contribution results from the flame root motion at $\mathbf{x} = 0$ that produces perturbations convected along the steady flame front Lee and Lieuwen (2003). Until recently, this contribution was thought to be negligible. However, Baillot *et al.* (1992); Kornilov *et al.* (2007) and Cuquel *et al.* (2013) have shown that in order to have a better description of the flame dynamics it is necessary to take this flame root motion into account.

7.2.2 Incompressible convective velocity model

When the stationary flame is submitted to velocity perturbations the flame front wrinkles due to the forcing term in Eq. 7.3. The perturbed flow in the vicinity of the flame base can be considered incompressible, if the acoustic wave length of the perturbation is large compared to the flame size $\lambda_{ac} >> l_f$ (Baillot *et al.* (1992); Schuller *et al.* (2003b); Birbaud *et al.* (2006)). These perturbations are convected from the burner outlet to the flame front at a velocity of the order of $\bar{v}$. The perturbed velocity field can be described by:

$$\tilde{u} = i\kappa(w_s/2 - x)\sqrt{2}\,\varepsilon\bar{v}e^{i\kappa y} \tag{7.5}$$

$$\tilde{v} = \sqrt{2}\,\varepsilon\bar{v}e^{i\kappa y} \tag{7.6}$$

where $\kappa = \omega/\bar{v}$ is the wave number of the flow disturbances convected along the burner axis and the term $\sqrt{2}\,\varepsilon\bar{v}$ is the amplitude of the axial velocity perturbation at the burner outlet in terms of the rms fluctuation level. The velocity perturbation normal to the flame front takes the form of:

$$\tilde{\mathbf{v}}(x) = \tilde{v}\sin\alpha - \tilde{u}\cos\alpha, \tag{7.7}$$

which in the reference frame attached to the steady flame front gives:

$$\tilde{\mathbf{v}}(\mathbf{x}) = \sqrt{2}\,\varepsilon\bar{v}\sin\alpha\left[1 - i\kappa_*\left(1 - \frac{\mathbf{x}}{l_f}\right)\right]e^{i\kappa_*\frac{\mathbf{x}}{l_f}}. \tag{7.8}$$

where κ_* is a dimensionless frequency (Cuquel *et al.* (2013)), that takes into account the perturbations propagating at the velocity $\bar{v}$ along the axial direction over a distance equal to the flame height.

7.2.3 Flame surface perturbation for 2D wedged flames

Flame surface fluctuations obtained by integrating Eq. 7.4 over the flame surface area in the frame associated to the steady flame front leads to:

$$\mathcal{A} = \int_0^{\mathbf{x}} \mathrm{d}\mathcal{A} = 2l_s\int_0^{l_f}\sqrt{1 + \left(\frac{\mathrm{d}\tilde{\xi}(\mathbf{x})}{\mathrm{d}\mathbf{x}}\right)^2}\,\mathrm{d}\mathbf{x}, \tag{7.9}$$

where, l_s is the slot length and l_f is the flame length. Expanding this expression to first order, one obtains:

$$\mathcal{A} \simeq 2\,l_s\,l_f + \frac{1}{2}\int_0^{l_f}\left(\frac{\mathrm{d}\tilde{\xi}(\mathbf{x})}{\mathrm{d}\mathbf{x}}\right)^2\mathrm{d}\mathbf{x} = \mathcal{A}_0 + \tilde{\mathcal{A}}, \tag{7.10}$$

The first term of Eq. 7.10 corresponds to the stationary flame surface area, $\mathcal{A}_0$, and the second term is the perturbed flame surface area $\tilde{\mathcal{A}}$. It is well known that, in the case of

premixed flames and in the absence of mixture composition inhomogeneities, the flame surface is proportional to the heat release rate (Clavin and Siggia (1991); Schuller *et al.* (2002)):

$$\frac{\tilde{\mathcal{A}}}{\mathcal{A}_0} = \frac{\tilde{\dot{q}}}{\bar{\dot{q}}}. \tag{7.11}$$

The contributions to the flame surface oscillations can be separated in two parts: one coming from the velocity contribution over the flame front dynamics (first term in Eq. 7.4), and a second one coming from a flame root dynamics (second term in Eq. 7.4). This leads to an expression of the FTF as the sum of two contributions (Lee and Lieuwen (2003); Cuquel *et al.* (2013)):

$$\mathcal{F}(\omega) = \frac{\tilde{\dot{q}}/\bar{\dot{q}}}{\tilde{v}/\bar{v}} = \mathcal{F}_A(\omega) + \mathcal{F}_B(\omega), \tag{7.12}$$

This development permits to identify and separate the mechanisms that control the flame dynamics. We can classify the two phenomena as follows (Fig. 5):

- Flame front dynamics: this is the usual field where the movements of a premixed laminar flame front are studied when this front is submitted to acoustic waves.
- Flame root dynamics: this is a field which is less studied where the flame root (the place where the flame is anchored) response to acoustic waves is considered.

Of course, both mechanisms are coupled: the flame root dynamics control part of the flame front dynamics. In the limit case where the acoustic oscillations would quench the flame root, the flame front itself would obviously disappear too. But for the purpose of separating and understanding effects, this separation is a convenient way to analyze the global flame stability.

7.2.4 Mechanisms contributing to the flame dynamics: flame front versus flame root dynamics

To find how the slot temperature change the flame dynamics one must look into the mechanisms by which an acoustic wave creates a heat release perturbation (*e.g.* Ducruix *et al.* (2003)). Several studies over the years have looked into these mechanisms and it was synthesized in the work of Cuquel (2013). Figure 7.5 presents a block diagram of how an acoustic perturbation produce a heat release perturbation. This diagram is similar to that proposed in Cuquel (2013), however, in this study we focus only on the physical mechanisms that may be affected by the slot temperature, T_s.

In Fig. 7.5, the upper part of the diagram correspond to the contribution of the flame front dynamics, while the lower part corresponds to the contribution of the flame root dynamics.

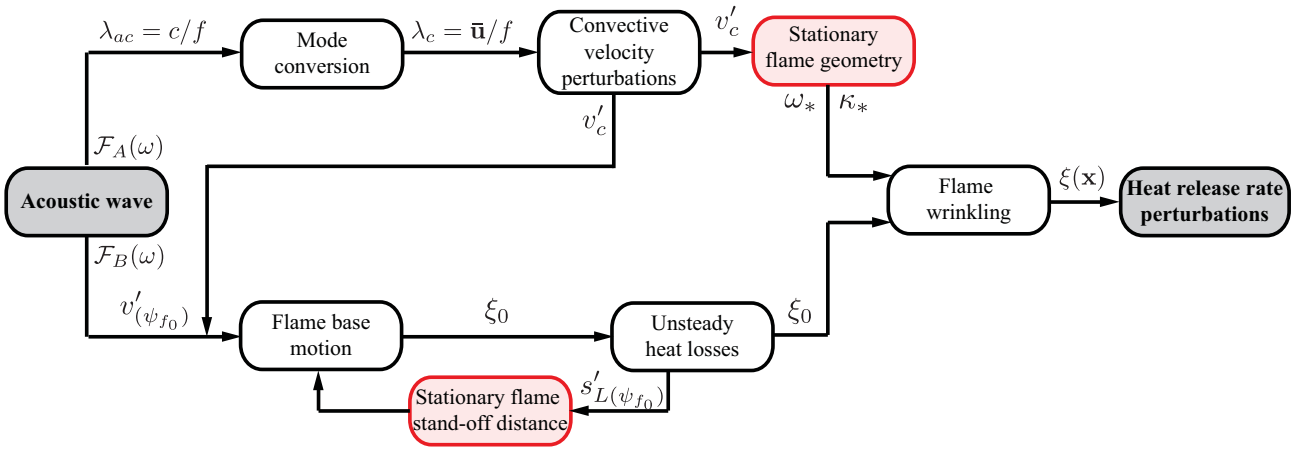

Figure 7.5: Main mechanism contributing to flame dynamics when submitted to acoustic perturbations.

Flame front dynamics contribution ($\mathcal{F}_A$) to heat release rate oscillation

The contribution of the flame front dynamics, $\mathcal{F}_A$, to the heat release rate oscillation is described as follows: an acoustic perturbation propagates from the plenum to the burner outlet at the speed of sound. When the acoustic wave is large compared to the flame size[2] $\lambda_{ac} \ll h_f$, thanks to a mode conversion (Birbaud *et al.* (2006)) the propagation changes its nature and becomes convective. The propagation, that can be acoustic or convective depending on the excitation frequency, impacts the flame front and creates flame wrinkles that propagate along the flame front and produce heat release rate fluctuations. The amplitude and wavelength of the flame wrinkles determine the magnitude of the heat release rate oscillations. Two non-dimensional numbers (ω_* and κ_*)[3] based on the flame geometry describe the interaction between the perturbation, the flame wrinkles and the heat release rate oscillations (Cuquel *et al.* (2013)). Consequently, we can study the influence of the slot temperature on flame front dynamics by analyzing the dependency of ω_* and κ_* on T_s. This is the subject of Ch. 8.

Flame front dynamics has been extensively studied in the past and many authors have addressed this issue *e.g.* Boyer and Quinard (1990); Baillot *et al.* (1992); Fleifil *et al.* (1996); Ducruix *et al.* (2000); Schuller *et al.* (2003b); Wang *et al.* (2009); Cuquel *et al.* (2011) from a linear point of view and Dowling (1999); Preetham and Lieuwen (2004); Lieuwen (2005) from the non-linear point of view. These studies show that flame front dynamics have a strong dependency on the nature of the velocity perturbation impinging on the flame. This phenomenon was studied in Birbaud *et al.* (2006) and three

[2] The flame size can be represented by the flame height h_f of flame length l_f. Either h_f or l_f are of the order of 20 mm, thus for frequencies bellow 70 Hz one can assume a convective propagation and for frequencies above 70 Hz one can assume acoustic propagations.

[3] We wall come back to the definition of ω_* and κ_* in Ch. 8 for now we are just interested in describing the physical mechanisms.

propagation modes were identified (convective, convective-acoustic and acoustic) based on the Strouhal number involving the burner diameter and the upstream flow velocity. A parametric study conducted in Kornilov (2006) explored the dependency of the FTF to different parameters such as: the mean flow velocity and radial velocity profile; the equivalence ratio; burner tube diameter, material and opening geometry, flame confinement and co-flow. This study concluded that to the first order, the flame FTF gain and phase are controlled by the flame aspect ratio or equivalently, by the flame half-tip angle ($\alpha = \arcsin(s_L/\bar{v})$). All these results suggest that the flame front dynamics is very sensitive to the stationary flame geometry which is determined by the burner outlet cross-section and competition between the bulk velocity, $\bar{v}$, and the laminar flame speed, s_L.

Flame root dynamics contribution ($\mathcal{F}_B$) to heat release rate oscillation

The contribution of the flame root dynamics, $\mathcal{F}_B$, to the heat release rate oscillation was first studied by Lee and Lieuwen (2003) and is described as follows: first, a velocity perturbation at the burner outlet, v', produces regular oscillations of the flame anchoring point, ξ_0; second, these oscillations ξ_0 generate oscillations of the heat loss to the burner rim, because of changes of the temperature gradient at the burner material. This results in an enthalpy wave propagating from the burner to the flame base at a velocity close to the laminar flame speed, s_L. This enthalpy wave generates fluctuations of flame temperature, T_b, at the flame base, that at the same time produce local flame speed fluctuations $s'_{L(\psi_{f0})}$. Depending on the flame stand-off distance ψ_{f0} this local flame speed fluctuation can couple with the imposed velocity fluctuations to amplify or damp the flame root oscillation. These flame root oscillations propagate along the flame front creating flame wrinkles and consequently heat release rate oscillations. We can study the flame root contribution to the heat release rate fluctuations by studying the dependency of the flame anchoring point fluctuation to the slot temperature, T_s. This is the subject of Ch. 9.

The physical mechanism associated to the flame root motion was studied by Petersen and Emmons (1961); Kornilov *et al.* (2007); Karimi *et al.* (2009); Shin and Lieuwen (2012). The unsteady heat transfer between the flame and the burner rim was studied by Schreel *et al.* (2002); Rook *et al.* (2002); Rook and de Goey (2003); Altay *et al.* (2009); Kedia *et al.* (2011). Recently in Cuquel *et al.* (2013) a flame base transfer function for a conical flame was derived and they successfully link these two phenomena.

7.3 Conclusion

In this chapter we used the experimental results found in Ch. 4, 5 and 6 to solve the dispersion relation (Eq. 3.32) derived in Ch. 3. The solution of Eq. 3.32 reproduces the observations described in Ch. 2: the flame is unstable for the case T50h and stable for the cases T90h and T120h. At the same time, these results were compared to the approximate analytical solution (Eq. 3.46). The analytical stability criteria is also able to predict the

stability of the system.
This results shows the ability of low-order models or more generally acoustic solvers to describe the flame response to account for additional parameters, such as the slot temperature when the proper FTF is used (here it was measured experimentally). Despite their versatility these methods still require input parameters, from the FTF which can only be obtained through experiments or detailed numerical simulations.

One can conclude that the flame is stabilized by the effect of the slot temperature on the flame dynamics ($\mathcal{G}$ and φ). This effect can be explained from the stability map presented in Fig. 7.1. Here the two solutions (exact and the approximate analytical solution) of the dispersion equation are superposed. The stable regions are represented in white while the unstable region of exact solution is colored with iso-contours of positive values of ω_i and the unstable regions of the analytical stability criteria is represented by diagonal patterns. The experimental points are represented by symbols: T50h (▲), T90h (●) and T120h (×). At the frequency of the self-sustained oscillation the gain, $\mathcal{G}_r$, and the phase, φ_r, of the FTF are reduced. This effect pushes the system out of the unstable regions. In the case of $\mathcal{G}_r$ this effect is straight forward: a reduction on $\mathcal{G}_r$ produces a proportional reduction of the combustion interaction coefficient $\mathcal{N}$ and this effect reduces the gap of φ for which the system is unstable. On the other hand, the effect of φ_r is more complicated. A reduction on φ_r can eider stabilize or destabilize the system, depending on its initial location on the stability map. For our particular case, the phase is initially located close to the left boundary of the instability map (Fig. 7.1), so that a reduction on φ_r due to the increase on T_s brings the system to "more stable" zones, where a stronger combustion-acoustic interaction ($\mathcal{N}$) would be needed to bring the system into instability.

Although the flame dynamics has been largely studied, theoretically, experimentally and numerically; none of these studies directly related the effect of the wall temperature on the flame dynamics. Level-set descriptions of the flame front kinematic allow to explore all the mechanism contributing to the flame wrinkling and thus, the heat release fluctuation: two principal contributions to the heat release rate fluctuation were identified and will be addressed in next part of this study. The two contributions ("flame front dynamics" and "flame root dynamics") and their mechanisms are summarized in Fig. 7.5.

In the next part, the problem is divided in two chapters corresponding to the two contributions to flame dynamics described by Lee and Lieuwen (2003) and Cuquel *et al.* (2013) (Eq. 7.12). First, one is interested in the effect of the slot temperature on the flame front dynamics. Second, the mechanism associated to the flame base motion and the unsteady heat transfer to burner rim is addressed because it controls flame root dynamics.

Part III

Mechanism contributing to the flame dynamics

Chapter 8

Effects of slot temperature on flame front dynamics and FTF

In this chapter the effects of the slot temperature, T_s, on the flame front dynamics and the associated FTF is studied. The study is based on level-set description to model the flame front kinematic response to flow perturbations represented by the G-equation. This chapter is organized as follows: first, Sec. 8.1 presents some theoretical results (mainly obtained at the EM2C laboratory in paris) obtained for laminar conical flames; then the effect of the slot temperature on the fresh gases temperature profile is discussed in Sec. 8.2 and finally the possible effects this change on the temperature profile is presented in Sec. 8.3 and 8.4 respectively.

8.1 Introduction

The previous chapter has shown that it is possible to separate the FTF in two main contributions ($\mathcal{F} = \mathcal{F}_A + \mathcal{F}_B$): one from flame front dynamics ($\mathcal{F}_A$) and a second from flame root dynamics ($\mathcal{F}_B$). In this chapter we focus on the flame front dynamics contribution, and two main questions arise: does the slot temperature, T_s, modify the flame front dynamics? and if yes is this effect responsible for the attenuation on the instability with the increase of the slot temperature observed experimentally in Ch. 2?
To answer the questions we use two approaches:

- First, theory provides simple rules based on the steady flame geometry to identify which parameters control the FTF. These parameters can be measured on a stable flame. We will describe theory in the present section and see how T_s modifies these control parameters.

- Second, we will directly measure the FTF varying the control parameters which are influenced by T_s (fresh gases temperature, bulk velocity, flame speed) and see if they are the cause of the changes on the stability of the system.

The first theoretical attempts to derive exact expressions for FFT were conducted with conical flames assuming a uniform acoustic velocity perturbation Merk (1987); Matsui (1981); Fleifil *et al.* (1996). These study were extended by Ducruix *et al.* (2000) to

account for any flame tip angle. They found that, in the low frequency range, flame dynamics is controlled by one single dimensionless frequency $\omega_* = (\omega R)/(s_L \cos\alpha)$, where R is the burner radius and α is the tip half-angle (Fig. 8.1).

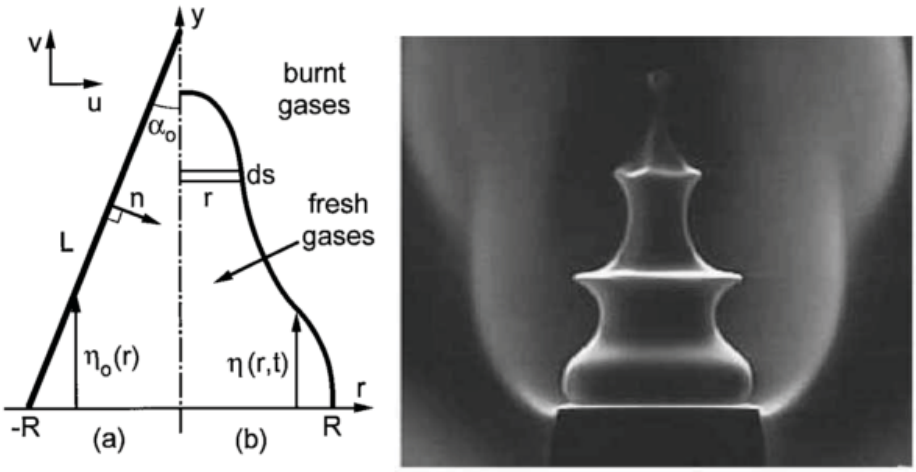

Figure 8.1: Sketch of the flame and flow parameters in the steady situation (a) and in the perturbed situation (b), taken from Ducruix *et al.* (2003).

However, this model failed to predict the phase for the high frequency range. The discrepancy between model and experiments come from the definition of the velocity perturbation. Schuller *et al.* (2003b) proposed a FTF model based on the observation that the velocity perturbations in the reactants stream are not only acoustic, but are convected by the mean flow (Baillot *et al.* (1992)). This model retrieves the regular increasing behavior of the phase lag on the FTF. The FTF is found to be dependent on two parameters, the reduced frequency, ω_*, and the tip half-angle, α.

Unfortunately, in the low frequency range this model fails to predict the phase-lag. Cuquel *et al.* (2011) proposed a FTF model with a convective velocity perturbation that satisfies the continuity and was able to reproduce the phase-lag at low frequencies. This model depends on two dimensionless numbers, the reduced frequency, ω_*, and the reduced flow wave number, $\kappa_* = \omega_* \cos^2\alpha$ which takes into account the perturbations propagating at the velocity $\bar{v}$ along the axial direction over a distance equal to the flame height.

Although this model predicts the FTF phase in the low frequency range, it fails in predicting the gain. This discrepancy was corrected in Cuquel (2013) by taking into account the spatial decay of the velocity fluctuation. It was found by Durox *et al.* (2005) and Birbaud *et al.* (2006) that the velocity perturbation decays exponentially with the distance from the burner outlet. Thanks to this observation they introduced a complex component in the flow wave number, $\kappa_* = \kappa_*(1 - i\,b)$, where b is a decay parameter, which is of the order of $b = 0.4$ for elongated flames.

Recently, Blumenthal *et al.* (2013) extended the frequency domain models of Ducruix *et al.* (2000) and Schuller *et al.* (2003b) to a time domain model of the impulse response of the flame. They found two different time scales, a "restoration" time scale and a "convection" time scale. The restoration time scale is defined as $\tau_r = l_f/(\bar{v}\cos\alpha)$. It comes from a uniform velocity perturbation model, and it is equivalent to the reduced frequency ω_* in the frequency domain. This response is obtained by assuming that, at the initial instant, the flame front is uniformly displaced from its steady position and comes back to its steady position after a restoration time τ_r. When a convective velocity perturbation model is used, two characteristics time scales are found: (1) a restoration time scale, τ_r identified previously and (2) a convection time scale, $\tau_c = \tau_r \cos^2\alpha$ which can be associated to the flow wave number, κ_*, in the frequency domain. This impulse response exhibits a linear increase from $t = 0$ to $t = \tau_c$ and a linear decrease from τ_c to τ_r.

To summarize, the current state of the art in theoretical flame dynamics based mainly on the G-equation states that the contribution of the flame front fluctuations $\mathcal{F}_A$ (*c.f.* Sec. 7.2) to the FTF, $\mathcal{F}(\omega)$, should be a function of two dimensionless frequencies:

$$\omega_* = \frac{\omega}{s_L\cos\alpha}\frac{w_s}{2} = \frac{\omega}{\bar{v}\cos\alpha}l_f, \tag{8.1}$$

$$\kappa_* = \omega_*\cos^2\alpha(1-ib) = \frac{\omega}{\bar{v}}h_f(1-ib), \tag{8.2}$$

where ω is the pulsation frequency, s_L is the flame speed, α is the half-tip angle, w_s is the slot width, $\bar{v}$ is the bulk velocity, l_f is the flame length and h_f is the flame height. Therefore, if the flame front dynamics is affected by the slot temperature, it must be because one or many of the parameters ($\bar{v}$, s_L, l_f, h_f, α or b) depends on the slot temperature.

We can already discard a dependance of b on T_s. Indeed, Fig. 6.6 showed that the gain decay along y downstream of the burner outlet is independent of the slot temperature. We can conclude that flame front dynamics is controlled to first-order only by stationary flame parameters (l_f, h_f and α) which are themselves determined by $\bar{v}$ and s_L. In our experimental tests (T50h, T90h and T120h) the operating point ($\bar{v}$ and Φ) are kept constant. However, changes in T_s may induce changes in the fresh gases temperature, T_u, and consequently modify the flow conditions ($\bar{v}$ and s_L) at the burner outlet. This effect may eventually modify the flame front dynamics. Thus, the first question we will try to answer will be: is the fresh gases temperature profile affected by changes in the slot temperature?

8.2 Effect of the slot temperature T_s on the fresh gases temperature T_u

The dual-channel cooling system of Fig. 8.2(a) is designed to keep the lower part of the slot at ambient temperature, while the upper part, between the lower channel and the

burner outlet heats up. Changes in the slot temperature, T_s, can modify the heat transfer from the top surface of the burner rim to the side walls of the slot and heat back the fresh gases, changing the temperature profile of the fresh gases. Figure 8.2(b) shows profiles of fresh gases temperature, T_u, for the two non-reactiing cases T50c and T90c. The profiles are measured with a thermocouple at $y = 2$ mm downstream of the burner outlet in steps of $\Delta x = 0.1$ mm (*cf.* Fig. 8.2(a)).

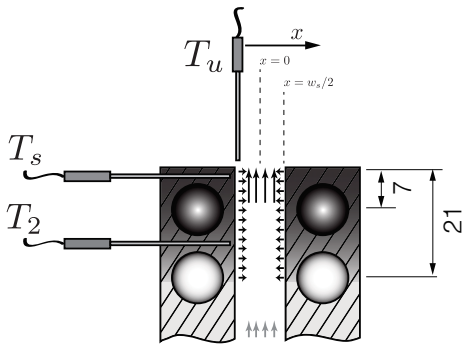

(a) Schematic representation of the temperature profile test.

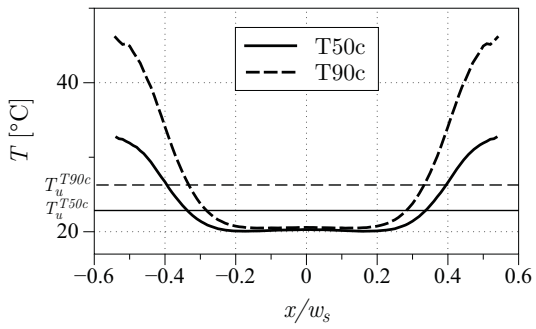

(b) Temperature profile for two different slot temperatures, corresponding to the cases T50c (——); T90c (- - - -).

Figure 8.2: Fresh gases temperature profile. B15 burner, under non-reacting configuration with a bulk velocity of $\bar{v} = 1.60$ ms^{-1} at $y = 2$ mm downstream of the burner outlet.

Figure 8.2(b) reveals that the increase in slot temperature, T_s, has a non-negligible effect on the fresh gases temperature profile, especially close to the solid boundaries. However, the fresh gases mean temperature, T_u, does not vary considerably: it goes from $T_u^{T50c} = 296.00$ K in the T50c case to $T_u^{T90c} = 299.42$ K in the T90c case. Indeed, thanks to the dual cooling system used in this study (*cf.* Fig. 1.3), the process between the inlet and the outlet of the slot is almost isothermal as 7/8 of the slot remains at ambient temperature.

The pre-heating of the fresh gases can have two effects:

1. First, it can change the velocity profile and the bulk velocity, $\bar{v}$ because density will change: the expansion of the gases due to the higher temperature close to the solid boundaries can accelerate the fresh gases.

2. The flame speed is also very sensible to the fresh gases temperature (Poinsot and Veynante (2011)) and a modification of the flame speed will affect the geometry of the flame.

It is possible to study these two effects separately: first in Sec. 8.3 we will investigate the effect velocity profile on the flame front dynamics and on the FTF. Then in Sec. 8.4 we will repeat this procedure but in this case we will study the effect of a variation on the flame speed.

8.3 Effect of the fresh gases temperature T_u on the bulk velocity $\bar{v}$

The acceleration of the fresh gases will change the density and therefore the bulk velocity, and as consequence it will modify the flame geometry. Thus, the two parameters controlling the flame front dynamics ω_* and κ_* will be modified by the direct effect of the $\bar{v}$ variation and by the secondary effect of the flame geometry variation, h_f, l_f and α.

The effect of the acceleration of the fresh gases was mentioned in Kedia *et al.* (2011) who stated that it is one of the causes of the decreasing time delay when they use a more conductive material as flame holder. Duchaine *et al.* (2011) mentioned that an increase in the fresh gases temperature induces a diminution on the phase-lag due to the acceleration of the fresh gases and local flame speed.

Considering cases T50c and T90c, and assuming an isentropic expansion, an increase in the bulk temperature produces an increase of the fresh gases bulk velocity of the order of:

$$\frac{\bar{v}^{T90c}}{\bar{v}^{T50c}} = \frac{T_u^{T90c}}{T_u^{T50c}} \tag{8.3}$$

Taking into account the results of Fig. 8.2(b) one can conclude that the bulk velocity will be increased by 1.2 % from the case T50c to T90c. Figure 8.3(b) shows the velocity profile for the two cases. The profiles are measured with a HW prove at $y = 2$ mm downstream the burner outlet in steps of $\Delta x = 0.1$ mm (*cf.* Fig. 8.3(a)): the bulk velocity is increased from $\bar{v} = 1.66$ ms^{-1} in the T50c case to $\bar{v} = 1.68$ ms^{-1} in the T90c case[1].

Now it is interesting to see whether changes in the bulk velocity of the order of 1.2 % can have an influence of the flame-front dynamics and the FTF.

The effect of the bulk velocity, $\bar{v}$, on the flame front dynamics is complicated, because of its direct influence on both parameters ω_* and κ_*, and on the flame geometry. An experiment was designed to study this effect in a more detailed way. This experiment consists in:

1. Determining the effect of small variations of bulk velocity on the stationary flame geometry, for a fixed equivalence ratio.
2. Study the effect of small variations of the bulk velocity on the FTF for a fixed excitation frequency and a fixed equivalence ratio.

8.3.1 Effect of the bulk velocity on stationary flame geometry

The reduced parameters of ω_* and κ_* of Eqs. 8.1 and 8.2 depend on the mean flame properties such as the flame length, l_f, and half-tip angle α. Therefore, in a first step, it

[1]The velocity signal is corrected by the mean temperature profile at each point

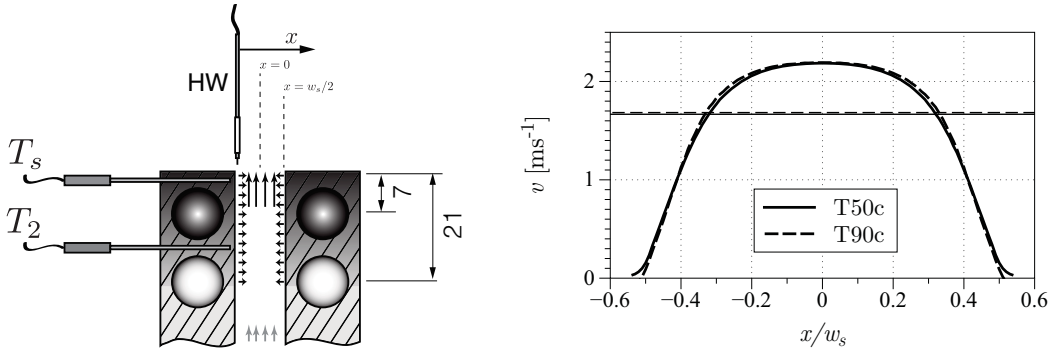

(a) Schematic representation of the velocity profile test.

(b) Velocity profile for two different slot temperatures, corresponding to cases T50c (——) and T90c (- - - -).

Figure 8.3: Velocity profile without flame. B15 burner, under non-reacting configuration with a nominal bulk velocity of $\bar{v} = 1.60$ ms^{-1} at $y = 2$ mm downstream the burner outlet and in steps of $\Delta x = 0.1$ mm.

is useful to verify how these parameters are affected by $\bar{v}$: the effect of $\bar{v}$ on the stationary flame geometry is studied by varying the bulk velocity from $\bar{v} = 1.51$ to 1.69 ms^{-1} in steps of $\Delta\bar{v} = 0.01$ ms^{-1} and measuring the flame geometry from pictures taken with a camera. Note that, even though these changes are small (0.01 ms^{-1} variation), we know that we are looking a stable/unstable transition which is triggered or not for very small variations.

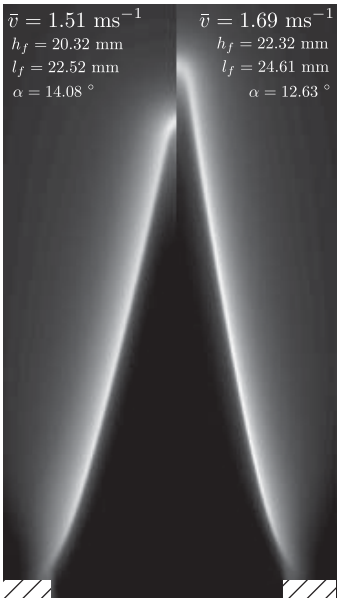

Figure 8.4: Comparison between steady flames for case T90h for two different bulk velocities $\bar{v} = 1.51$ and 1.69 ms^{-1}. Equivalence ratio is $\Phi = 0.95$.

Figure 8.4 shows a comparison between the pictures of the stationary flame for the limit cases of the experiment $\bar{v} = 1.51$ and 1.69 ms^{-1}. The surface temperature is set to

have $T_s = 90$ °C when the flow conditions are $\bar{v} = 1.6$ ms^{-1} and $\Phi = 0.95$. One can see that increasing the bulk velocity increases the flame height, h_f, and the flame length, l_f. However, as the flame is anchored to the burner rim, the half-tip angle, α, decreases when the bulk velocity is increased.

Figure 8.5(a) shows that the flame height, length and half-tip angle vary linear with $\bar{v}$, which is to be expected from mass conservation. However, because the parameters ω_* and κ_*, which control the flame response depend on ratios of these quantities, it turns out that they are marginally affected by variations in $\bar{v}$ as seen in Fig. 8.5(b). Consequently, this steady state analysis suggests that $\bar{v}$ will have little impact on the flame response and that this effect is not dominant to explain the influence of T_s.

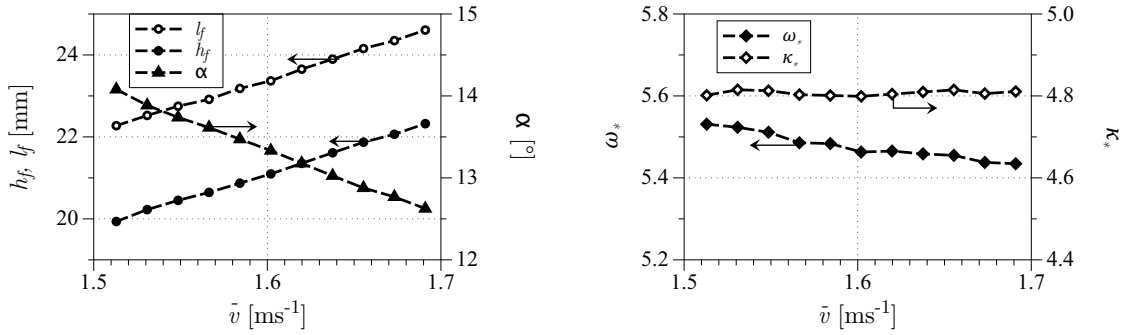

(a) Stationary flame geometry for different bulk velocities. Flame length l_f (--○--); flame hight h_f (--●--); flame half-tip angle α (--▲--)

(b) ω_* (--◆--) and κ_* (--◇--) for different bulk velocities.

Figure 8.5: Bulk velocity effect on the flame size (left) and on the reduced parameters (right). Stable flame with the B15 burner, with for a fixed equivalence ratio of $\Phi = 0.95$. Surface temperature is set to have $T_s = 90$ °C when the flow conditions are $\bar{v} = 1.6$ ms^{-1} and $\Phi = 0.95$, or the equivalent to the T90h test.

8.3.2 Effect of the bulk velocity on the FTF

Of course, a second and direct method to study the effect of $\bar{v}$ is to really measure the FTF and not relay in the theory presented in Sec. 8.1 is to study the effect of $\bar{v}$ on the FTF by varying the bulk velocity from $\bar{v} = 1.51$ to 1.69 ms^{-1} in steps of $\Delta\bar{v} = 0.01$ ms^{-1}. This is done for a fixed equivalence ratio and a fixed excitation frequency, f_{ex} set to 58 Hz, which is the resonance frequency of the natural instability.

Figure 8.6 shows that the gain increases slightly with the bulk velocity, $\bar{v}$, while the phase remains constant. We have seen (*cf.* Fig. 8.3(b)) that from a T50c to T90c test case, the bulk velocity increases of 1.2 %. According to the results of Fig. 8.6, the effect fresh gases acceleration does not have any impact on the phase, and it increases the gain

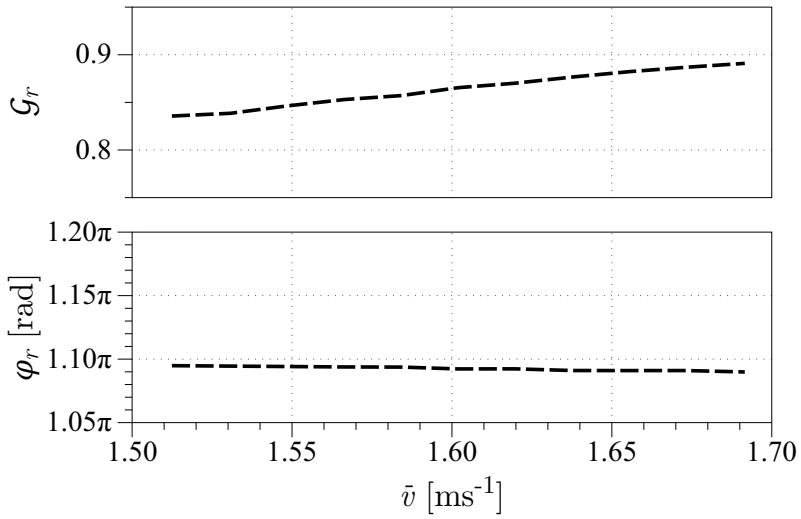

Figure 8.6: Flame response versus bulk velocities at the frequency of the instability (f_r = 58 Hz). Test performed with a stable flame with the B15 burner, for a fixed equivalence ratio of $\Phi = 0.95$. Surface temperature is set to $T_s = 90$ °C when the flow conditions are $\bar{v} = 1.6$ ms^{-1} and $\Phi = 0.95$. Velocity fluctuations are keep constant to $\varepsilon = 0.1$.

by 0.5 %. This effect of the bulk velocity on the gain was first remarked by Kornilov (2006) and was recently confirmed by Kashinath *et al.* (2013). However, in the present case, given the modest increase in $\bar{v}$ due to pre-heating of the reactants (±1.2 %), the corresponding increase in the FTF gain would be marginal. More importantly, this effect is opposite to the reduction in the FTF gain at the frequency of the instability observed in Fig. 6.3 when the slot heats walls up. Consequently, the damping of the instability when T_s is increases can not be attributed to the effects of the pre-heating of the reactants on $\bar{v}$.

8.4 Effect of the fresh gases temperature T_u on the laminar flame speed s_L

Figure 8.2(b) shows that the temperature profile is affected by the slot temperature. This effect induces changes in the local flame speed. Experiments of Gu *et al.* (2000) in methane/air premixed flames show that the flame speed increases rapidly with temperature. Simple theoretical arguments (Poinsot and Veynante (2011)), show that s_L scales like T^{α_T}:

$$s_L \propto \left(\frac{T_{fg}}{T^0_{fg}}\right)^{\alpha_T}, \tag{8.4}$$

where T^0_{fg} is a reference temperature and α_T is the a temperature exponent which depends on the fuel and operation conditions $\alpha_T = 1.9$ for an atmospheric methane flame at

$\Phi = 0.95$. If we take the bulk fresh gases temperature (*cf.* Fig. 8.2(b)) as the controlling one in Eq. 8.4 the flame speed varies by 2.2 % from case T50h to case T90h. An increase in the flame speed, s_L, while keeping the bulk velocity constant will yield a proportional decrease in the flame length, which at the same time will increase the half-tip angle, α. If we look at the two stationary flames in cases T50h and T90h (*cf.* Fig 8.7) we can see that the flame in the T90h case is slightly shorter than the flame in the T50h case. The flame length decreases by 2.6 % which matches the increase in flame speed due to the change in the fresh gases bulk temperature.

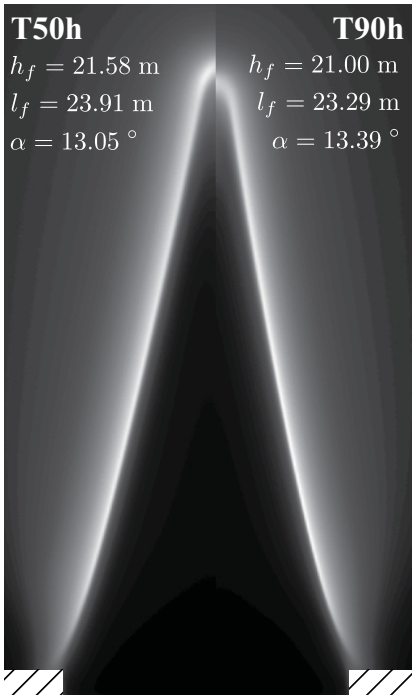

Figure 8.7: Comparison between steady flames for cases T50h and T90h. Bulk velocity and equivalence ratio are $\bar{v} = 1.6$ ms^{-1} and $\Phi = 0.95$ respectively.

Now it is interesting to investigate if changes in the flame speed of the order of 2.2 % could change the flame front dynamics, and bring the flame from unstable configuration at T50h to an stable configuration at T90h as seen in Ch. 2.

As explained previously (*cf.* Subsec. 8.3), flame speed variations have a direct influence on both parameters ω_* and κ_*. We can study now the effect of s_L as follows:

1. Determining the effect of flame speed on the stationary flame geometry, for a fixed bulk velocity, and different flame speeds. Flame speed changes are created through modifications of the equivalence ratio Φ.

2. Study the effect of small variations of the flame speed, s_L, on the flame response (FTF) at the frequency of the resonance and a fixed bulk velocity.

8.4.1 Effect of the flame speed on stationary flame geometry

The effect of s_L on the stationary flame geometry is studied by varying the equivalence ratio from $\Phi = 0.9$ to 1.02 in steps of $\Delta\Phi = 0.02$ and measuring the flame geometry from direct vision.

For this type of flames, the flame speed, s_L, can be calculated from the flame length as indicated in Selle *et al.* (2011):

$$s_L = \bar{v}\frac{w_s}{2l_f}\eta, \tag{8.5}$$

where η is a 3D correction factor due to the finite length of the 2D slot, that for this configuration was determined to be 1.067. From Fig. 8.7 one can deduce the flame speed using Eq. 8.5: $s_L = 0.36$ and 0.37 ms^{-1} for two cases T50h and T90h respectively.

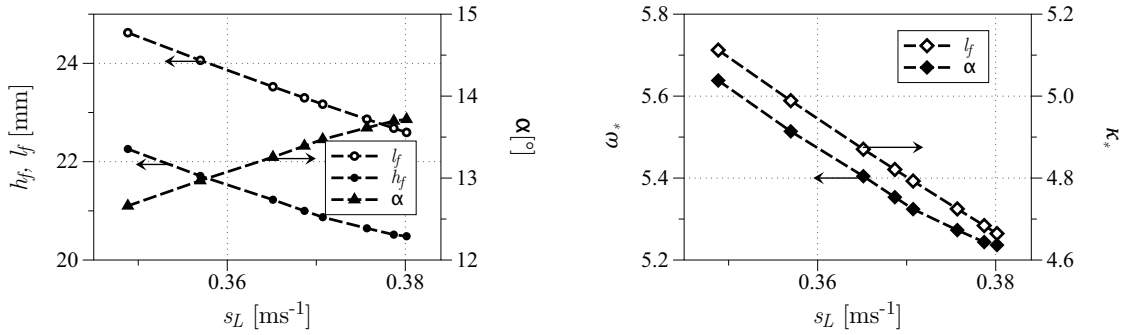

(a) Stationary flame geometry for different flame speeds. flame hight h_f (--●--); flame half-tip angle α (--▲--)

(b) ω_* (--◆--) and κ_* (--◈--) for different flame speeds.

Figure 8.8: Flame speed effect on the flame size (left) and on the reduced parameters (right). Stable flame with the B15 burner, with a fixed bulk velocity of $\bar{v} = 1.60$ ms^{-1}. Surface temperature is set to $T_s = 90$ °C. The flow conditions are $\bar{v} = 1.6$ ms^{-1} and $\Phi = 0.95$, or the equivalent to T90h test.

Figure 8.8 show the results of the stationary test: increasing the flame speed has the opposite effect on the flame geometry than increasing the bulk velocity. The flame height and length are decreased while the half-tip angle is increased. Concerning the two parameters ω_* and κ_* one can notice that they both are highly affected by the flame speed, contrary to the effect of the bulk velocity, where only ω_* was slightly affected (see Fig. 8.5(b)).
The parameters κ_* (*cf.* Fig. 8.8(b)) decreases by the direct effect of s_L in the flame height, h_f, when T_s is increased. Concerning ω_* one can identify two contributions. The first comes from the $1/\cos(\alpha)$, which increases with s_L due to the increase of α. The second contribution comes from the $l_f/\bar{v}$ factor which decreases due to the decreasing values on l_f. As the global effect is the decreasing of ω_* with s_L one can conclude that the main

factor controlling the flame front dynamics is the so-called flame aspect ratio $l_f/\bar{v}$.

8.4.2 Effect of the flame speed on the FTF

It is now clear that the two parameters controlling the flame front dynamics (ω_* and κ_*) are affected by the modification of the flame aspect ratio $l_f/\bar{v}$, and that this flame aspect ratio is slightly modified by the increase of the slot temperature, T_s through its effect on the fresh gases temperature profile. However, it is still not clear, if this mechanism is strong enough to change the FTF and stabilize the flame when the slot temperature is increased. Thus, an experiment was designed where the effect of s_L on the FTF is studied varying the equivalence ratio from $\Phi = 0.9$ to 1.02 in steps of $\Delta\Phi = 0.02$ and measuring the gain, $\mathcal{G}_r$, and the phase, φ_r. This is done for a fixed bulk velocity and a fixed excitation frequency of 58 Hz which is the resonance frequency of the natural instability $f_{ex} = f_r$.

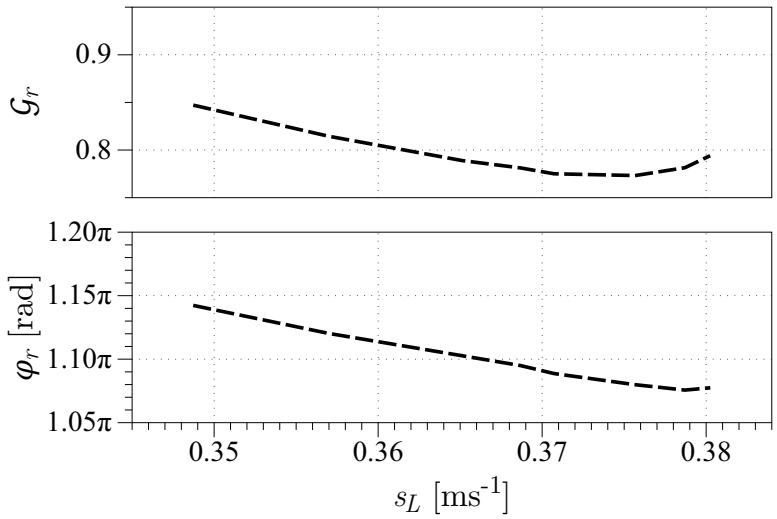

Figure 8.9: FTF for a fixed frequency ($f_r = 58$ Hz) and different flame speeds s_L. Stable flame with the B15 burner, for a fixed bulk velocity of $\bar{v} = 1.6$ ms^{-1}. Surface temperature is set to have $T_s = 90$ °C when the flow conditions are $\bar{v} = 1.6$ ms^{-1} and $\Phi = 0.95$, or the equivalent to the T90h test. The velocity fluctuations levels are kept constant to $\varepsilon = 0.1$.

Figure 8.9 shows the dependency of the measured gain, $\mathcal{G}_r$ and phase, φ_r, on the flame speed. They both decrease with the flame speed. The phase, φ_r, decreases linearly at a rate of 2.13π rad for every increment 1 ms^{-1} on the flame speed. Since the flame speeds increases of 0.01 ms^{-1} from the case T50h to the case T90h[2], one can conclude that the phase will decrease of 0.21π between these two cases. This variation is similar to the

[2]Calculate from the stationary flame in for flow conditions of $\bar{v} = 1.6$ ms^{-1} and $\Phi = 0.95$ corresponding to the cases T50h and T90h used in the calculation of the FTF (*cf.* Ch. 6)

phase difference found in the FTF results for the same two cases (*cf.* Table 7.1). The gain, $\mathcal{G}_r$, exhibit a less monotonic behavior. It decreases almost in a linear way up until $s_L = 0.37$ ms^{-1} and then it starts to increase. Taking into account only the linear part of the gain response (between the limits $s_L = [0.35, 0.37]$ ms^{-1}), it decreases at a rate of 2.90 for every increment 1 ms^{-1} of the flame speed. One can extrapolate that the gain will decrease of 0.03, between case T50h to T90h. This unfortunately does not explain why the difference of 0.1 in the gain, $\mathcal{G}_r$ for the two cases found in Ch. 6.

We can then conclude that the reduction of the phase-lag φ_r found on the FTF's of Ch. 6, which is partially responsible for the attenuation of the natural instability with the increase on the slot temperature, is due to the increase of the flame speed s_L (which at the same time reduces the flame size, l_f and h_f) produced by the pre-heating of the fresh gases induced by the increase of the slot temperature. This induced reduction of the flame size (l_f and h_f) reduces the convective time delay, τ, that the flame takes to respond to a velocity fluctuation consequently reducing the phase-lag φ_r (Fig. 8.10).

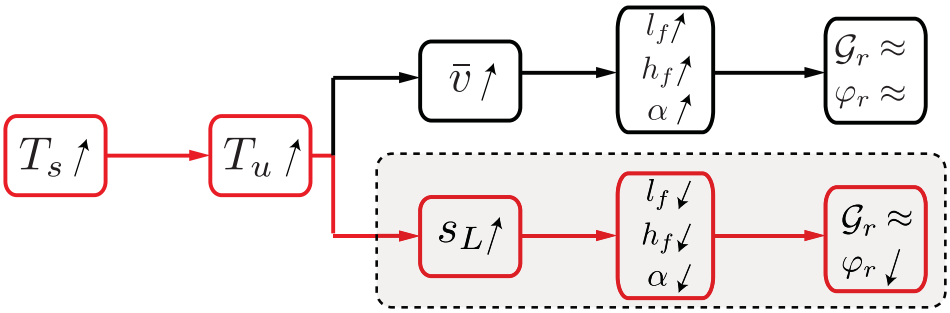

Figure 8.10: Effect of the slot temperature on the stationary flame geometry. The dashed rectangle represents the mechanism responsible for the reduction on the phase-lag, φ_r, due to increase of the slot temperature, T_s.

8.5 Conclusion

In this chapter, the influence of the wall temperature on the flame front dynamics was studied. The main parameters controlling the flame front dynamics were deduced thanks to the analytical work of previous researchers in the study of flame front dynamics through the G-equation (Boyer and Quinard (1990); Baillot *et al.* (1992); Fleifil *et al.* (1996); Dowling (1999); Ducruix *et al.* (2000); Schuller *et al.* (2003b); Lieuwen (2005) and Cuquel *et al.* (2013)). Two parameters were found to control the flame front dynamics, ω_* and κ_*. These two parameters depend only the flow conditions and the flame stationary geometry.

It was also shown that the fresh gases temperature profile differs for the three different cases T50h, T90h and T120h. This is due to the pre-heating of the fresh gases by the

heat flux from the side wall. This mechanism has two effects:

1. it increases the bulk velocity due to the expansion of the fresh gases,
2. it also the increases the flame speed

Both effects were studied separately. It was found that the increase of the bulk velocity due to the pre-heating of the free gases is negligible. This effect has no influence on the phase, and it is not the reason why the gain decreases with increasing slot temperature (*cf.* Ch. 6). On the other hand the effect of the pre-heating of the fresh gases on the flame speed was found to be the mechanism that decreases the phase in the results of Ch. 6. The mechanism works in the following way: due to the increase in T_s the heat-flux from the slot walls to the fresh gases is increased and the temperature profile of fresh gases is affected. The consequent increase in the bulk temperature of the fresh gases increases the flame speed which at the same time decreases the flame height. As the bulk velocity is not altered, the convective time delay decreases as it is proportional to $\tau \sim h_f/\bar{v}$ and finally the phase lag between the velocity fluctuation and the heat release fluctuation decreases. Direct FTF measurements confirm this analysis.

It is now clear that the mechanism linking the slot temperature to the phase is the one presented above. However, the mechanism linking the gain to the slot temperature is still unknown. From Fig. 7.1 one can see that in the hypothetical case, where only the phase would be affected by T_s the system would still be stable in the T50h case. The observations of Ch. 2 contradict this hypothesis. As the flame front dynamics path is unable to explain way the gain of the FTF decreases with the slot temperature, one is interested now in looking at the interaction of the flame root with burner rim. This is the purpose of the next chapter.

Chapter 9

Effects of slot temperature on flame root dynamics and FTF

In this chapter, the effect of the slot temperature, T_s, on the flame anchoring point is studied. This study is based on that of Cuquel et al. (2013) in which a model for the $\mathcal{F}_B$ contribution to the FTF is derived. It takes into account unsteady heat losses form the flame base to the burner-rim on the resulting flame wrinkles along the steady flame front. A model for the enthalpy waves traveling from the burner-rim to the flame root (Rook et al. (2002)) is used to derive the flame root displacement transfer function, and its contribution to the global FTF is analyzed.
First a review of the existing flame root dynamics theories is performed in Sec. 9.1, followed by the description of the model used to describe the flame root burner-rim interaction in Sec. 9.2. Finally the experimental determination of the flame root dynamics is performed in Sec. 9.3.

9.1 Introduction

The flame studied here is an elongated 2D wedged flame, with a relatively small half-tip angle, typically $\alpha < 15$ °. As a result, the dynamics of the flame is mainly controlled by the two dimensionless parameters, ω_* and κ_* studied in Ch. 8, where it was found that increasing the slot temperature increases the fresh gases temperature profile and consequently the flame speed, which at the same time has an impact on phase-lag response of the flame, φ_r. Unfortunately, this analysis does not explain why the gain of the flame response at the frequency of the instability, $\mathcal{G}_r$, decreases with increasing the slot temperature. This problem gives rise to two questions: is the dynamics of the flame anchoring point affected by slot temperature? and if yes, is this the mechanism responsible for the attenuation of the instability seen in Ch. 2?

To understand how the flame root dynamics is controlled by the heat losses to the burner walls, it is useful to consider also the literature on flames stabilized on porous plates (Fig. 9.1 left) for which the link between flame speed and heat losses to the solid plate walls has been analyzed in depth (de Goey *et al.* (2011)). We will use this results

in the present study.

First let us consider a conical flame stabilized in on a burner rim. Early studies of such laminar flames suggested that the flame anchoring point is motionless and fixed to the burner rim. But it has been shown by Petersen and Emmons (1961) that the flame response to velocity fluctuations (FTF) is very sensitive to the flame root point dynamics. Imposing an oscillatory motion on an inclined premixed flame, a convective undulation develops along the flame front in an uniform flow.

Recently, Kornilov *et al.* (2007) compared the response of conical flames anchored to a fixed rim and submitted to flow modulations and the response of the same flame to a vibration of the anchoring rim in a uniform flow field. They found that the same kind of waves propagate along the flame front but different phase-lag behaviors were observed for the FTF. The phase-lag saturates between $\varphi = [\pi/2, \pi]$ for the moving rim, while it grows linearly for the modulated flow. In the present study, the physical mechanism associated with the flame root motion is assumed to be linked to unsteady heat transfer between the flame and the burner rim.

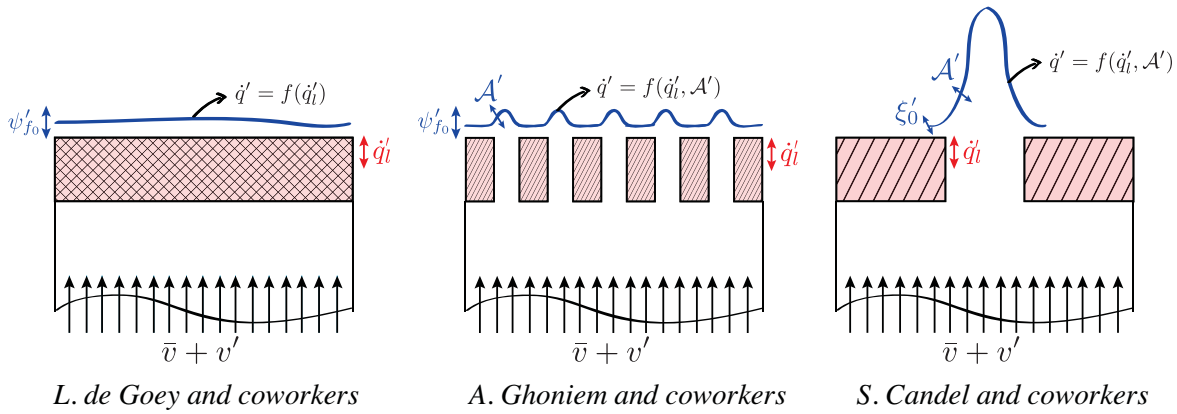

L. de Goey and coworkers *A. Ghoniem and coworkers* *S. Candel and coworkers*

Figure 9.1: Different types of flames corresponding to their combustion instability nature. **Left**: planar flame stabilized over a porous media. **Center**: perforated-plate stabilized flame. **Right**: Conical flame. ψ'_{f_0} is the stand-off distance fluctuation, $\dot{q}'$ is the heat release rate fluctuation, $\dot{q}'_l$ is the heat loss fluctuation, $\mathcal{A}'$ is the flame surface fluctuation and ξ'_0 is the flame root fluctuation.

The importance of unsteady heat losses in combustion instabilities has been studied extensibly by L. de Goey and coworkers, specially for planar flames stabilized on porous plate (*e.g.* Rook *et al.* (2002); Rook and de Goey (2003); Schreel *et al.* (2002, 2005)). Refer to de Goey *et al.* (2011) for a review of the current state-of-the-art on the effect hot unsteady heat transfer from the flame to solid boundaries.
It has been shown that planar flames (*cf.* Fig. 3 left) close to a solid boundary can be perturbed in two ways:

- First, acoustic velocity perturbations produce regular oscillations of the flame stand-off distance, ψ'_{f_0}, with respect to the burner rim.

- Second, these oscillations generate oscillations of the heat loss to the burner rim, $\dot{q}'$, because of changes of the temperature gradient at the burner material.

This results in an enthalpy wave propagating from the burner walls to the flame front and the flame dynamics is influenced due to the corresponding changes and an associated time-lag.

For elongated flames, such as the one studied here, heat release rate fluctuations are governed by flame front fluctuations. On the other hand, in planar flames, heat release rate fluctuations are governed by heat loss fluctuations at the burner. However, the work of A. Ghoniem and coworkers (*e.g.* Altay *et al.* (2009, 2010) and Kedia *et al.* (2011)) in two dimensional premixed flames, have shown that, for low frequencies typically less that 100 Hz, the oscillations of heat loss rate at the burner rim plays a critical role in driving the growth of the perturbations. The flame response to velocity fluctuations at its base takes the form of flame speed oscillations in this region. Flame stand-off distance increase when the flame-wall interaction strengthens, impacting the overall dynamics of the heat release. Kedia *et al.* (2011) state that the main contribution to the phase-lag between velocity fluctuations and heat release rate fluctuations, is a convective time lag between the perturbation and the flame base response. The convective lag between the perturbations and the base and the flame tip was found to have a weaker impact on the heat release rate oscillations. This observation is, of course, critical in a configuration where the wall temperature T_s directly controls the flame root position.
Here, the burner rim temperature plays an important role as illustrated by Schreel *et al.* (2005), but this type of flames strongly differ from the one studied here. They deal with a 2D flame stabilized on top of a porous plate, which has two regions: one planar flame region in contact with the burner plate, and several short conical flames over the injection holes, with large half-tip angles, α.
Recently Cuquel *et al.* (2013) integrated a model for the flame root oscillations, which are dominated by the heat transfer from the flame to the burner-rim, into the kinematic description of the flame front oscillations of an elongated conical premixed flame. It highlight the importance of heat transfer between the flame and the burner surface at the anchoring point on the flame dynamics of elongated conical flames.

Figure 9.1 summarizes the three different natures of combustion instability discussed before. On the left, one can identify the plane flame stabilized over a porous media, where the heat release rate fluctuation is only due to unsteady heat loss to the burner-rim (the flame surface is constant). In the middle, a perforated-plate stabilized flame where the heat release rate fluctuations are mainly due to the unsteady heat loss to the burner-rim but a contribution of the small conical flame surface fluctuation must be taken into account. Finally on the right, an elongated conical flame, where the heat release rate fluctuations are mainly due to flame surface fluctuations but a contribution by the flame

root fluctuation was identified. This last is what we want to study here.

9.2 Modelisation of the flame root dynamics

Taking into account that the flame root fluctuations are convected along the fame front and generate heat release rate fluctuations (Kornilov *et al.* (2007); Cuquel *et al.* (2013)), one may think, that if the amplitude of flame root oscillations is modified by the slot temperature, the FFT will be affected. In order to check this hypothesis we are going to combine the theoretical developments of Rook *et al.* (2002); Altay *et al.* (2009) and Cuquel *et al.* (2013) to model the flame root TF. The flame root TF corresponds to the frequency response of the flame root oscillations to a velocity fluctuation.

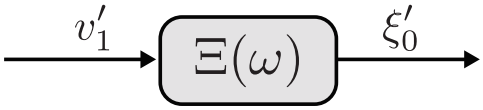

Figure 9.2: Block diagram representation of the flame root transfer function.

In the flame root zone, the heat loss of the flame to the burner-rim and the local flame speed are coupled: when the flame anchoring point moves, as a consequence of the velocity fluctuation, the heat loss will change. This will influence the temperature of the flame, and consequently, the local flame speed. If this heat loss gives positive feedback to the local flame speed, this might lead to resonance in the flame anchoring point response, this mechanism was initially studied by McIntosh and Clarke (1984); McIntosh (1987). Later on Rook *et al.* (2002) derived a transfer function between the flame speed and the inlet velocity for planar perforated stabilized flames. This model and the subsequent adaptations are explained in the following section.

9.2.1 Local flame speed transfer function

The Rook *et al.* (2002) transfer function between the flame speed and the inlet velocity for planar perforated model is based on the transport of enthalpy $h = \Delta h_f^0 Y_f + c_p T_u$ between the flame front and the burner plate, where Δh_f^0 is the heat value per unit mass of fuel, Y_f is the fuel mass fraction of the mixture, c_p is the specific heat at constant pressure, and T_u is the fresh gases temperature. The physical mechanism relies on the following hypothesis:

- planar premixed flame,
- low-Mach number,

- one-step chemistry,
- unity Lewis number (Le = 1),
- constant c_p for all species,
- the specific heat of the solid is assumed to be infinite, which implies that its temperature is constant,
- the heat transfer coefficient is assumed to be infinite as well, which implies that the gas temperature is equal to the solid temperature at the interface,
- the fuel mass fraction consumed by the flame is keep constant as well,
- zero-flame stretch rate is assumed. Thus, the flame structure behaves as a rigid oscillating structure, without internal dynamics,

Using these hypothesis the balance equations for the fuel mass fraction, Y_f, and enthalpy, h, reduce to (Rook *et al.* (2002)):

$$\frac{\partial \rho Y_f}{\partial t} + \frac{\partial \rho u Y_f}{\partial y} - \frac{\partial}{\partial y}\left(\frac{k_u}{c_p}\frac{\partial Y_f}{\partial y}\right) = \dot{\omega}_f \tag{9.1}$$

$$\frac{\partial \rho h}{\partial t} + \frac{\partial \rho u h}{\partial y} - \frac{\partial}{\partial y}\left(\frac{k_u}{c_p}\frac{\partial h}{\partial y}\right) = 0 \tag{9.2}$$

where k_u is the thermal conductivity of the mixture and $\dot{\omega}_f$ is the fuel consumption rate. Although Rook *et al.* (2002) obtained reasonable good results at low inlet velocity, they ignored the increase in the flame surface area as a results of the formation of conical flame surfaces. Therefore, the model is only valid when the mean inlet velocity is equal to the main flame speed. At higher inlet velocities the flame is strongly curved and the model is not valid any more.

Altay *et al.* (2009) solved the 2D conservation equations (Eqs. 9.1 and 9.2). They used Rook's planar model (Rook *et al.* (2002)) to estimate the flame speed response of the 2D (Fig. 9.1 center) flame and used the following hypothesis:

- the heat and mass diffusion in the tangential direction of the flame surface are assumed to be negligible compared to the normal direction,
- the impact of flame area oscillations on the flame speed response is neglected, which is consistent with assuming a uniform flame speed response at the entire flame surface.

Using these assumptions, the temperature in the normal direction to the flame surfaces of the 2D flame is the same as the temperature obtained in Rooks planar model, giving an expression for flame speed frequency response of the from (Altay *et al.* (2009))[1]:

$$\mathcal{S}(\hat{\omega}) = \frac{s'_L}{\mathbf{v}'_{(\psi_{f0})}} \left[1 + \frac{\hat{\omega}}{2\mathrm{Ze}} \left(\frac{T_b - T_u}{T_{ad} - T_u} \right) e^{\frac{\psi_{f0}}{\delta_f}} e^{-\frac{\psi_{f0}}{2\delta_f}(1-\sqrt{1+\hat{\omega}})} \right]^{-1} \tag{9.3}$$

where s'_L is the flame speed fluctuation, $\mathbf{v}_{(\psi_{f_0})}$ is the velocity fluctuation normal to the flame front evaluated at the flame base, $\hat{\omega} = 4\omega\delta_f/s_L$ is the acoustic frequency normalized by the thermal diffusion time scale, $\delta_f = k_u/(\rho_u s_L c_p)$ is the thermal flame thickness, T_b is the burnt gas temperature, ψ_{f_0} is the flame stand-off distance and Ze is the Zeldovich number defined as:

$$\mathrm{Ze} = \frac{T_a}{T_b} \frac{T_b - T_u}{T_b} \tag{9.4}$$

here T_a is the activation temperature. This model gives good results, but it is limited to short conical flames, *e.g.* flames with large half-tip angle, α. Unfortunately, this is not the case in our study, where we deal with elongated 2D wedged flames with small half-tip angle (Fig. 9.1 right). Thus, the impact of the flame area oscillations on the flame speed can not be neglected. Cuquel *et al.* (2013) tackle this problem by modeling the flame root displacement frequency response assuming only local flame speed fluctuations at flame root. They assume the local flame speed at the flame root is the sum of the laminar flame speed and the flame speed fluctuations due to the instationary heat loss to the burner rim:

$$s_{L(\psi_{f0})} = s_L + s'_{L(\psi_{f0})} \tag{9.5}$$

where $s_{L(\psi_{f0})}$ and $s'_{L(\psi_{f0})}$ are the local flame speed and local flame speed fluctuation at the flame root respectively. With these hypothesis the flame speed oscillations at the flame root are defined by (Cuquel *et al.* (2013)):

$$\mathcal{S}(\hat{\omega}) = \frac{\tilde{s}_{L(\psi_{f_0})}}{\tilde{\mathbf{v}}_{(\psi_{f_0})}} = \left[1 - \frac{i\hat{\omega}}{\mathrm{Ze}} \left(\frac{T_b - T_u}{T_{ad} - T_u} \right) e^{\frac{\psi_{f_0}}{2\delta_f}(1-i\hat{\omega})^{1/2})} \right]^{-1} \tag{9.6}$$

where $\tilde{s}_{L(\psi_{f_0})}$ is the harmonic flame speed fluctuation at the flame root. The difference between Eq. 9.3 and Eq. 9.6 is only the definition of the flame speed fluctuation: in the case of Altay *et al.* (2009) the flame speed fluctuations acts in the whole flame while in the case of Cuquel *et al.* (2013) it acts locally in the flame root zone. In this model however, Cuquel *et al.* (2013) assumed an isothermal burner, meaning that the burner absorbs heat from the flame infinitely fast. The result is that the burner remains at

[1] Here we changed the notations in order to be coherent with the previous notations

ambient temperature, T_u. Unfortunately this is not the case of a real burner, and as the interest of this study is to understand the influence of the slot temperature, T_s, on the flame dynamics, we propose to include the slot temperature in the procedure developed by Cuquel *et al.* (2013). This can be done using the results of Schreel *et al.* (2002) in which the stand-off distance ψ_{f_0} was defined in function of the surface temperature of the burner-rim[2], T_s:

$$\psi_{f_0} = \delta_f \log\left(\frac{T_{ad} - T_u}{T_{ad} - T_b + T_s - T_u}\right) \tag{9.7}$$

The main difference between this model and the one derived in Cuquel *et al.* (2013) is the dependency of the flame stand-off distance, ψ_{f_0}, on the surface temperature, T_s. From Eq. 9.7 we can notice that the stand-off distance decreases when the surface temperature is increased and vice versa as expected. With the flame speed response to acoustic oscillations at the flame root it now possible to study the frequency response of the flame root oscillations.

9.2.2 Flame root transfer function

From now on we follow the procedure of Cuquel *et al.* (2013) modified to 2D wedged flames. Using Eq. 9.6 it is possible to model the flame anchoring point motion using the kinematic equation of the perturbed flame front (*cf.* Eq. 7.3) applied at the flame base $\mathbf{x} = \psi_{f_0}$:

$$\frac{\partial \xi_0}{\partial t} + \bar{\mathbf{u}}(\psi_{f0}).\nabla\xi_0 = \mathbf{v}'(\psi_{f0}, t) - s'_{L(\psi_{f0})}(t), \tag{9.8}$$

From Fig. 8.3(b) we can conclude that at the flame base the mean flow velocity is close to zero, which makes the second term of the left-hand side of Eq. 9.8 vanish:

$$\frac{\partial \xi_0}{\partial t} = \mathbf{v}'(\psi_{f0}, t) - s'_{L(\psi_{f0})}(t), \tag{9.9}$$

The Fourier transform of Eq. 9.9 gives the model for the flame base motion transfer function, and it is defined as the amplitude of the flame root oscillation normal to the flame front for an incoming velocity fluctuation:

$$\Xi(\omega) = \frac{\tilde{\xi}_0/(w_s/2)}{\tilde{v}/\bar{v}} = -\frac{\bar{v}}{i\omega(w_s/2)}\left(1 - \mathcal{S}(\hat{\omega})\right)\frac{\tilde{\mathbf{v}}_{(\psi_{f_0})}}{\tilde{v}}. \tag{9.10}$$

From Eq. 7.8 one can obtain the term $\tilde{\mathbf{v}}_{(\psi_{f_0})}/\tilde{v}$ needed to complete the model:

$$\frac{\tilde{\mathbf{v}}(\psi_{f_0})}{\tilde{v}} = \sin\alpha\left[1 - i\kappa_*\left(1 - \frac{\psi_{f_0}}{l_f}\right)\right]e^{i\kappa_*\frac{\psi_{f_0}}{l_f}}. \tag{9.11}$$

[2] Until now we have referred to T_s as the slot temperature. For this chapter we will assume that slot temperature and surface temperature are the same, which is a reasonable assumption if we take into account that the thermocouple is only 1 mm below the burner rim surface.

Combining Eqs. 9.10 and 9.11 gives the expression linking the flame anchoring point movement to the incoming velocity perturbations taking into account the unsteady heat loss to the burner rim for a slot flame:

$$\Xi(\hat{\omega}) = -4\delta_* \frac{1-\mathcal{S}(\hat{\omega})}{i\hat{\omega}\cos\alpha}\left(1 - i\frac{1}{4}\frac{\hat{\omega}}{\delta_*}\cos^2\alpha\,(1-2\delta_*\Psi_f\tan\alpha)\right)e^{i\frac{1}{2}\hat{\omega}\Psi_f\cos\alpha\sin\alpha} \tag{9.12}$$

where $\delta_* = \delta_f\cos\alpha/(w_s/2)$ is the dimensionless projection of the flame thickness along the horizontal direction and $\Psi_f = \psi_{f_0}/(2\delta_f)$ is the dimensionless flame stand-off distance. Far from the solid boundary the dynamics of the flame is controlled by ω_* and κ_*, while close to the solid bounduary $\hat{\omega}$ controls the dynamics of the flame base. Indeed, the dynamics of the flame base is controlled to first order by $\hat{\omega}$: other parameters play a secondary role: Ze, δ_*, α and Ψ_f.
For fixed operating conditions of bulk velocity and equivalence ratio, and taking into account the results of Ch. 8 where α and $\bar{v}$ are marginally affected by T_s, one can conclude that Ze and δ_* are independent of the slot temperature. On the other hand, Eq. 9.7 shows that the flame stand-off distance is strongly dependent on the slot temperature. Thus, in our case, the flame base fluctuation transfer function will depend only on the reduced frequency associated with the flame time scale, $\hat{\omega}$, and the flame stand-off distance ψ_{f0}. $\Xi(\hat{\omega},\psi_{f0})$ is a complex number, with a gain $\mathcal{G}_f = |\Xi(\hat{\omega},\psi_{f0})|$ and the phase $\varphi_f = \arg(\Xi(\hat{\omega},\psi_{f0}))$.

Figure 9.3 shows the prediction of flame root transfer function Ξ based on Eq. 9.12 versus the excitation frequency for four different surface temperatures $T = 50$, 90 and 120 °C, corresponding to cases T50h, T90h and T120h. The numerical application is based on the experimental case flow conditions $\bar{v} = 1.6$ ms^{-1} and $\Phi = 0.95$, which gives a flame speed of $s_L = 0.36$ ms^{-1} (for the T50h case) and a flame half-tip angle of $\alpha = 13$ °. The adiabatic temperature, $T_{ad} = 2189$ °C and the flame thickness, $\delta_f = 0.47$ mm, were calculated with CANTERA. The activation and the burnt gases temperature at the base were set[3] to $T_a = 24000$ °C and $T_b = 2000$ °C respectively. This gives a Zeldovich number of Ze = 10.2.

The gain, $\mathcal{G}_f$, of the response can be seen as a frequency band-pass filter with a resonance-like behavior. The phase, φ_f, decreases at low frequencies, before increasing again reaching a small and almost constant value at high frequencies. The location of the peak of the gain $\mathcal{G}_f$ versus frequency strongly depends on the stand-off distance. The peak moves to higher frequencies when the surface temperature is increased.
This resonance-like behavior of the gain, $\mathcal{G}_f$, can be explained if we take into account that the enthalpy oscillations resulting from the heat loss to the burner-rim are transported to the base of the flame after a convective time delay of the order of $\tau_f \sim \psi_{f_0}/s_L$. Since the burning rate is assumed to respond instantaneously to fluctuations in the temperature (Rook *et al.* (2002)), the flame speed oscillates in phase with the enthalpy fluctuations reaching the flame front. Depending on the frequency of the imposed oscillations, f_{ex}, the

[3]These values are taken from the values used in the models of Rook *et al.* (2002) and Cuquel *et al.* (2013) which have similar flow configurations to the one studied here.

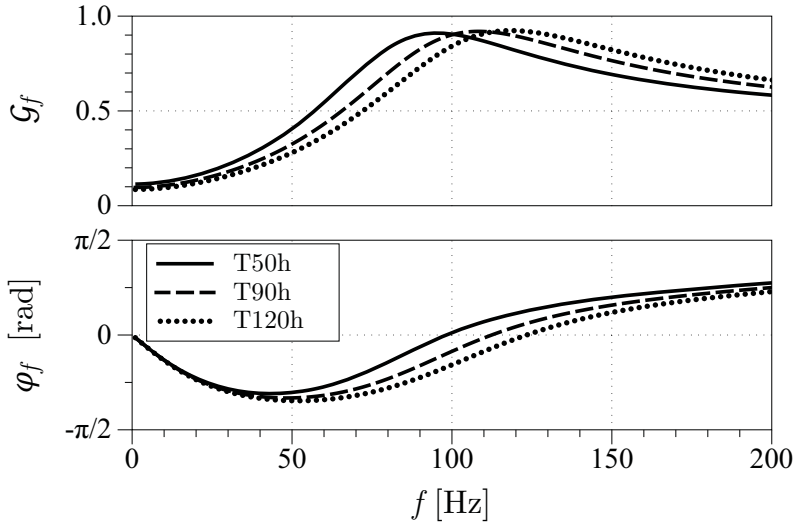

Figure 9.3: Flame base movement transfer functions based on Eq. 9.12 for four different surface temperatures, T_s, corresponding to the cases T50h (——); T90h (- - - -) and T120h (·····).

convective time delay, τ_f, results in a phase difference $\varphi_s = 2\pi\tau_f f_{ex}$ between the flame speed and the heat loss fluctuation. When $\varphi_s = \pi/2$, the flame base reaches its absolute minimum or maximum distance from the burner. The resonant frequency correspond to:

$$f_f = \frac{1}{4\tau_r} \sim \frac{s_L}{4\psi_{f_0}} \tag{9.13}$$

While the surface temperature rises, the flame stand-off distance, ψ_{f_0}, decreases, as a consequence the convective time delay τ_f decreases resulting in a resonance peak that moves to lower frequencies (*cf.* Fig. 9.3).

In a qualitative manner it is interesting to compare the flame root TF with the global FTF of the flame, of course, the flame root is not the only contribution to the global FTF but is certainly plays a role. Here, the gain $\mathcal{G}_f$ of the flame root transfer function obtained from Eq. 9.3 (*cf.* Fig. 9.3) and the gain $\mathcal{G}$ of experimental transfer function measured in Ch. 6 (Fig. 6.9(a)) present similar characteristics: at low frequencies ($f_e x < 100$ Hz) the gain is increased with the increase of the slot temperature while the opposite behavior is found for high frequencies ($f_e x > 100$ Hz). At the resonance frequency of the self-sustained oscillation ($f_r = 58$ Hz) the gain $\mathcal{G}_f$ in Fig. 9.3 decreases from 0.51 to 0.34 from case T50h to T120h respectively. This behavior suggests that the decrease of the gain $\mathcal{G}_r$ (from the FTF's of Ch. 6 at the frequency of the instability) may come from the reduction of the amplitude of the flame root oscillation due to the increase of the slot temperature.

Therefore this amplitude reduction of the flame root oscillation along with the already confirmed reduction of the phase lag φ_r due to pre-heating of the fresh gases may be the reasons of the attenuation for the instability. In order to confirm this results we will now

directly measure the flame root TF experimentally in the next section.

9.3 Experimental flame root dynamics

The model presented above suggests a shift to higher frequencies in the resonance peak of the flame base response gain, $\mathcal{G}_f$, when the slot temperature is increased. We try to verify this prediction experimentally, by measuring the flame root transfer function: This requires to track the position of the flame root when the flame if forced acoustically.

9.3.1 Experimental setup

Figure 9.4 shows the experimental setup used for the measurement of the flame foot transfer function. A high-speed camera (pco.dimax) is used to track the flame root position when submitted to an acoustic modulation. The camera is equipped with a Micro-Nikkor $f/2.8$ 105 mm Nikon lens, located at $x = 0$ mm, $y = 10$ mm and $z = 350$ mm. Images zoomed on the flame base of 624-by-928 pixel with a resolution of 70 px/mm were acquired at a sampling frequency of $f_{cam} = 3000$ fps and an exposure time of 0.30 ms, during 2 s. For each pulsating frequency, 6000 images are acquired. A LabVIEW program is used as a signal generator, to drive the loudspeaker at the bottom of the burner and to send a synchronized TTL signal to trigger the camera. Thanks to this synchronization, the images can be phase-averaged with respect to the acoustic modulation. A flame-front detection algorithm is designed to track the flame root during the harmonic excitation. The flame-root location is chosen as the intersection of the crest of light intensity with the iso-contour at 65 % of the maximum pixel value over the whole image (*cf.* Fig. 1.15).

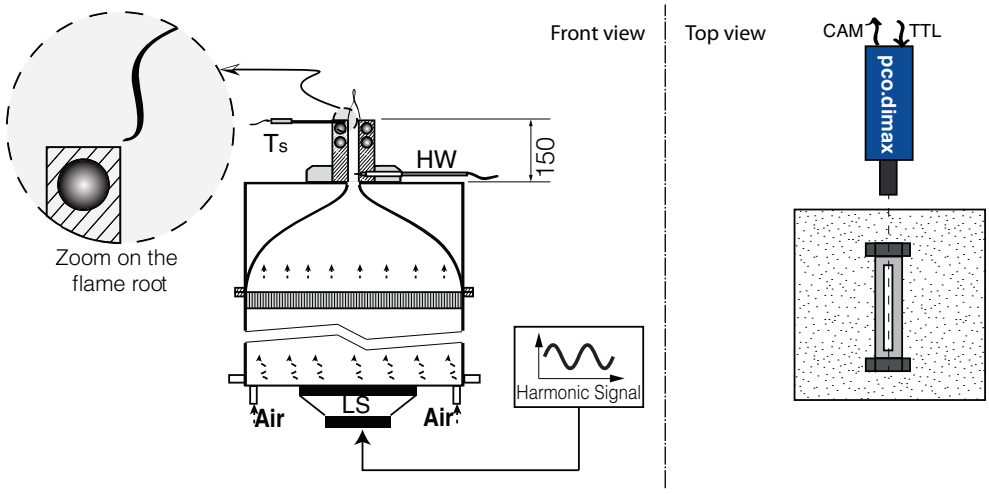

Figure 9.4: Experimental setup used to measure the flame root transfert function

The B15 burner is used and the three reference cases are explored: T50h, T90h and T120h. The flow conditions are $\bar{v} = 1.6$ ms^{-1} and $\Phi = 0.95$ for the bulk velocity and the equivalence ratio respectively. The velocity fluctuation level is $\varepsilon = 0.1$ while the frequency range explored is $f_{ex} = [10, 200]$ Hz.

Figure 9.5(a) show the comparison between the stationary stand-off distance, ψ_{f_0} for two different cases T50h and T120h. In a qualitative manner one can see that the flame gets closer to the burner rim when the surface temperature is increased. Figure 9.5(b) shows the comparison between the stand-off distance obtained experimentally and the results of the model calculated with Eq. 9.7. One can see that the model underestimates ψ_{f_0}. However, the trend is well described: when T_s increases, the flame gets closer to the burner rim.

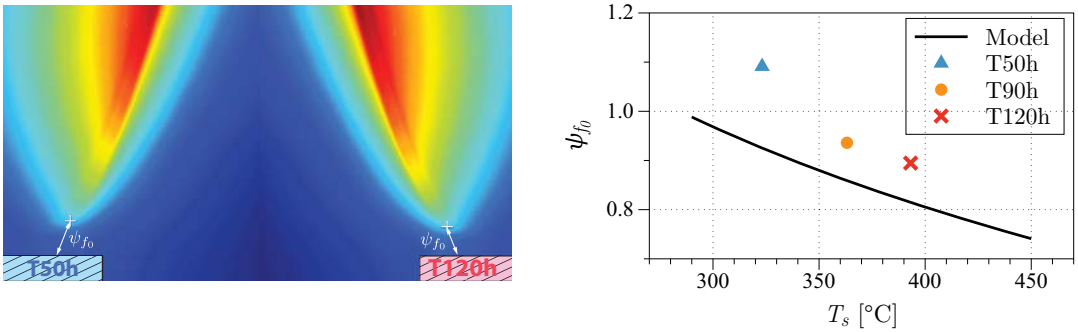

(a) Stationary flame stand-off distance, comparison between T50h and T120h cases.

(b) Stand-off distance comparison between model of Eq. 9.7 and experimental results.

Figure 9.5: Stationary flame stand-off distance. B15 burner stationary flame. The flow conditions are $\bar{v} = 1.6$ ms^{-1} and $\Phi = 0.95$ for the bulk velocity and the equivalence ratio respectively.

Nine phase-average images are presented in Fig. 9.6 over a cycle of modulation at an excitation frequency of $f_{ex} = 100$ Hz. These images are in agreement with the observations of Kornilov *et al.* (2007) and Cuquel *et al.* (2013) in which the flame root follows a periodic oscillation around its stationary position. These perturbations are then convected along the flame front through the mechanism described by Kornilov *et al.* (2007).

9.3.2 Flame root trajectories

The trajectories of the flame root are plotted in Fig. 9.7 for four different modulation frequencies $f_{ex} = [50, 100, 150, 200]$ Hz and for the three reference cases T50h, T90h and T120h. Data is phase averaged to eliminate high frequency noise and the coordinates (x', y') are relative to the location of the flame root without excitation, which means that the influence of T_s on the stationary flame root position has been removed.
Several conclusions can be obtained from these trajectories. First, they depend on the

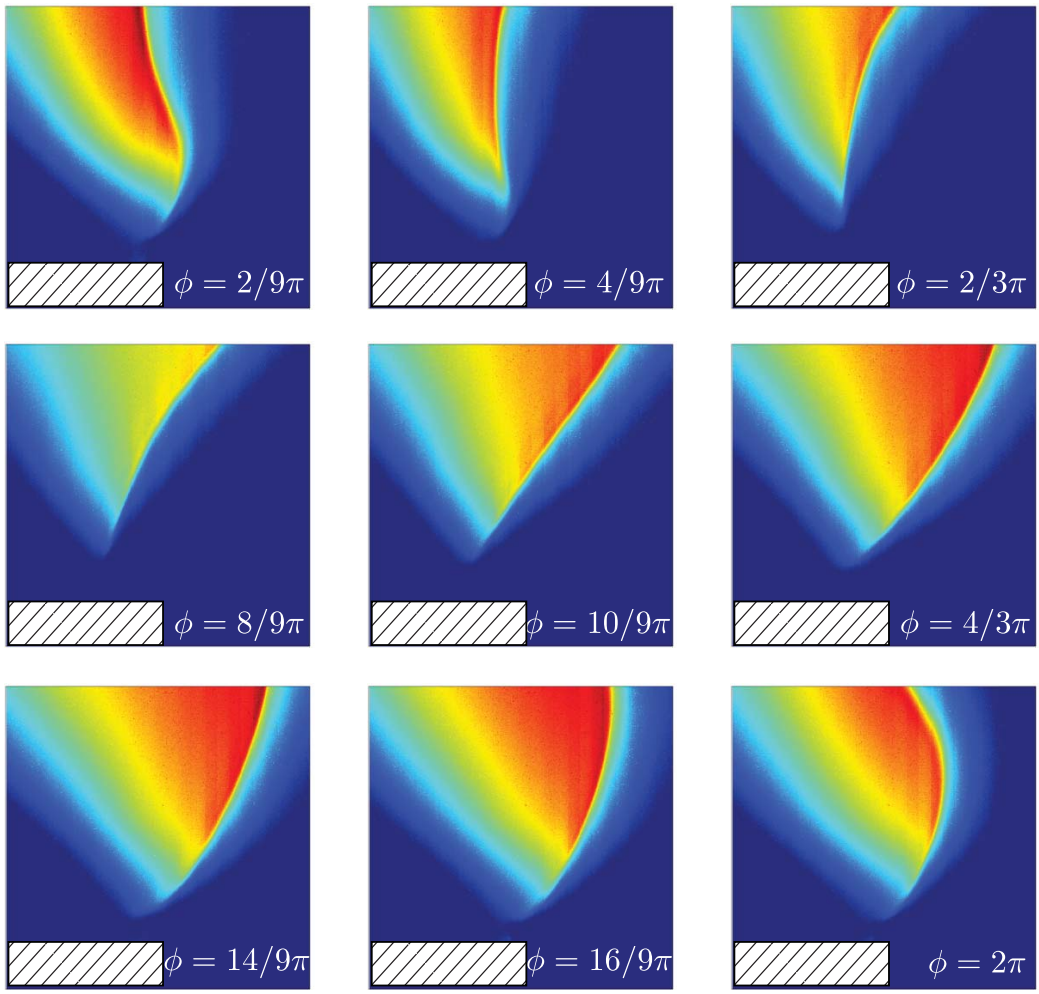

Figure 9.6: Phase-average images over a cycle of modulation at an excitation frequency of $f_{ex} = 100$ Hz and a velocity fluctuation level of $\varepsilon = 0.1$. B15 burner. The flow conditions are $\bar{v} = 1.6$ ms^{-1} and $\Phi = 0.95$ for the bulk velocity and the equivalence ratio respectively.

frequency of modulation, so that the flame root does not follow the same path for all frequencies. For low frequencies, typically $f_{ex} < 70$ Hz the trajectory is elliptical, whereas for high frequencies $f_{ex} > 120$ Hz the trajectory describes a shape of an "airfoil wing". Close to frequencies of $f_{ex} \simeq 100$ Hz the flame root moves along a line. For $f_{ex} > 150$ Hz the amplitude of the trajectory is significantly reduced. One can also mention the fact that the trajectory described by the flame root when submitted to velocity fluctuations is mainly horizontal: the amplitude of the movement in the horizontal x' direction is almost four times the amplitude in the vertical direction y' for all frequencies.

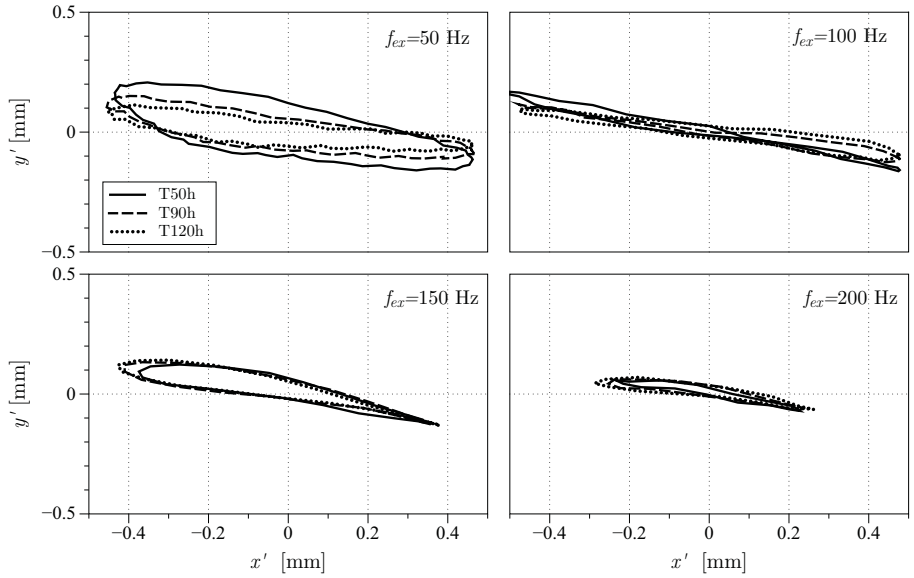

Figure 9.7: Phase-averaged flame base trajectory, relative to the flame root position without excitation, for four frequencies of excitation, $f_{ex} = [50, 100, 150, 200]$ Hz, and the three reference cases T50h (——), T90h (- - - -) and T120h (·····). Tests were performed on the B15 burner. The flow conditions are $\bar{v} = 1.6$ ms^{-1} and $\Phi = 0.95$ for the bulk velocity and the equivalence ratio respectively and velocity fluctuation level of $\varepsilon = 0.1$.

Figures 9.8 and 9.9 show the flame root displacement plotted with respect to the phase of the forcing signal for the vertical, y', and horizontal, x', direction respectively. They all feature a periodic behavior which is harmonic in time. The amplitude of these flame root displacements also depend on the slot temperature. Especially in the vertical direction, for frequencies below $f_{ex} < 120$ Hz the amplitude of the flame foot displacement in the vertical direction is decreased by a factor of 3, from case T50h to case T120h. For frequencies above $f_{ex} > 120$ Hz they have practically the same amplitude for the three cases.

In the horizontal direction (Fig. 9.9) the behavior is slightly different, the amplitude of the flame root displacement is independent of the slot temperature for frequencies below

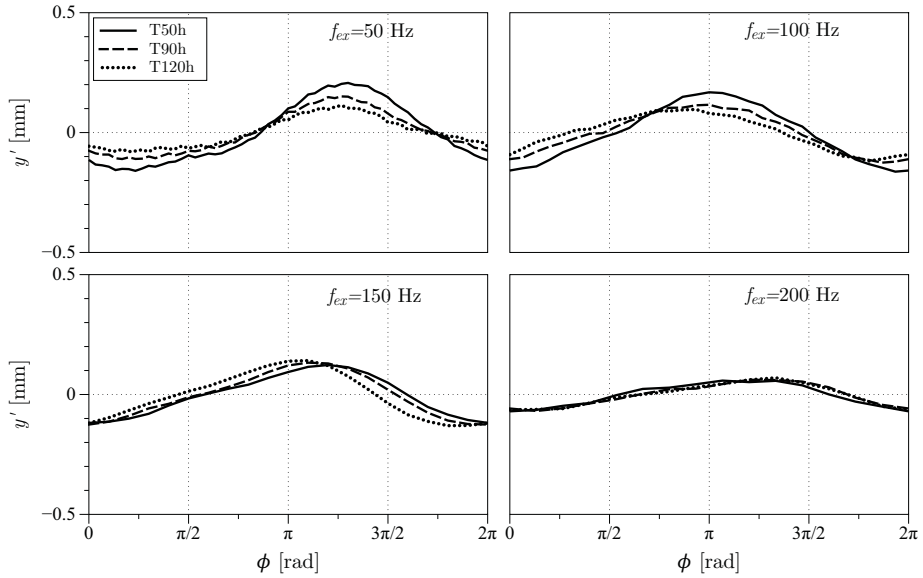

Figure 9.8: Phase-averaged flame base trajectory in the vertical direction, relative to the flame root position without excitation, for four frequencies of excitation, $f_{ex} = [50, 100, 150, 200]$ Hz, and the three reference cases T50h (——), T90h (- - - -) and T120h (·····). Tests were performed on the B15 burner. The flow conditions are $\bar{v} = 1.6$ ms^{-1} and $\Phi = 0.95$ for the bulk velocity and the equivalence ratio respectively and velocity fluctuation level of $\varepsilon = 0.1$.

$f_{ex} < 120$ Hz. For frequencies above $f_{ex} > 120$ Hz the amplitude slightly increases with the increase of the slot temperature.

The phase differences between the vertical and horizontal displacements are very close to phase opposition: the flame root reaches its more negative position along the vertical direction (y') at the same time that reaches its more positive position along the horizontal direction (x') as evidenced in Fig. 9.10, where the difference between the vertical and horizontal displacements, ϕ_{xy}, is plotted versus the excitation frequency for the three reference cases: ϕ_{xy} remains close to π for all frequencies. The flame root motion is mainly oriented along a single direction, which in the model was assumed to be normal to the flame front position.

9.3.3 Definition of the normal to the flame front

In order to measure the experimental flame root transfer function it is necessary to determine the normal direction to the flame front. In the model (*cf.* Sec. 9.2.2), it is defined by the half-tip angle $\alpha = \arcsin(s_L/\bar{v})$. However experimentally, this definition is more complicated.
Based on the stationary flame heigh h_f, one finds $\alpha = \arctan[(w/2)/h_f] = 0.23$, 0.24 and 0.25 rad for the three reference cases. On the other hand, if measured from the stationary flame images zoomed on the flame root, one finds $\alpha_b = 0.35$, 0.38 and 0.41 rad (*cf.*

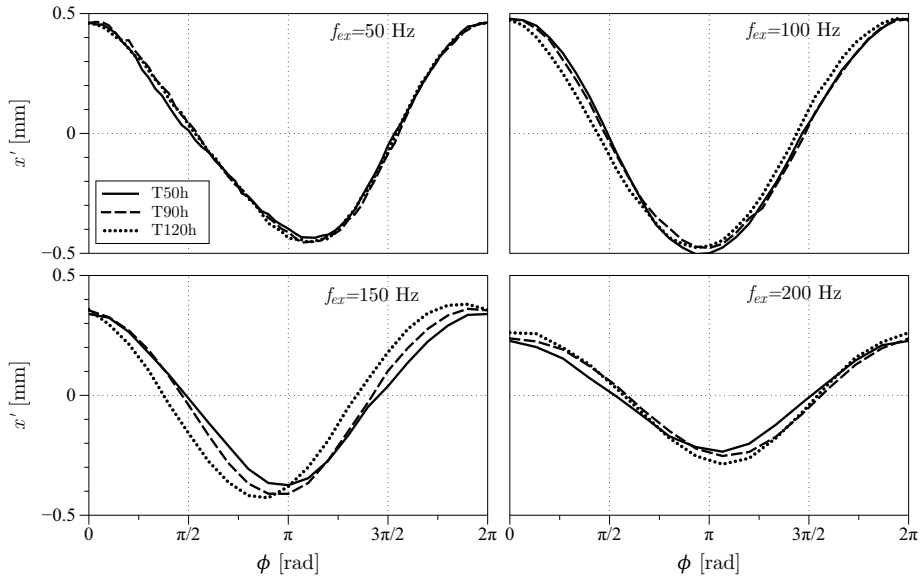

Figure 9.9: Phase-averaged flame base trajectory in the horizontal direction, relative to the flame root position without excitation, for four frequencies of excitation, $f_{ex} = [50, 100, 150, 200]$ Hz, and the three reference cases T50h (———), T90h (- - - -) and T120h (·····). Tests were performed on the B15 burner. The flow conditions are $\bar{v} = 1.6$ ms^{-1} and $\Phi = 0.95$ for the bulk velocity and the equivalence ratio respectively and velocity fluctuation level of $\varepsilon = 0.1$.

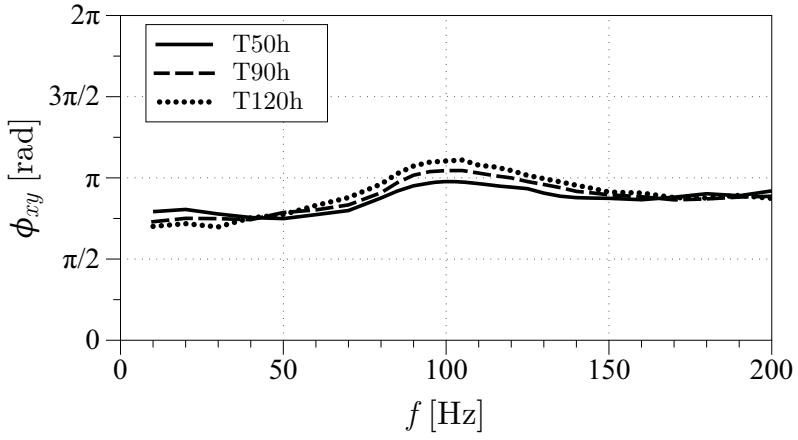

Figure 9.10: Phase difference between the vertical and horizontal displacements for the three reference cases T50h (———), T90h (- - - -) and T120h (·····). Tests were performed on the B15 burner. The flow conditions are $\bar{v} = 1.6$ ms^{-1} and $\Phi = 0.95$ for the bulk velocity and the equivalence ratio respectively and velocity fluctuation level of $\varepsilon = 0.1$.

Fig. 9.11(a)). It is natural to find $\alpha < \alpha_b$, due to the fact that the value of the angle at the flame base is determined by a balance between the flow velocity and the flame burning velocity at this location. The burning velocity at the flame base is reduced due to heat losses to the burner rim and the flow velocity in the wake of the burner edge takes also small values. These effects combine and modify the flame angle with respect to its value far from the burner edges.
A way to determine the actual normal displacement of the flame base is to take into account the amplitude of displacement of the flame root in the vertical (ξ_0^y) and horizontal (ξ_0^x) direction $\alpha_n = \arctan(\xi_0^y/\xi_0^y)$. These results are summarized in Fig. 9.11.

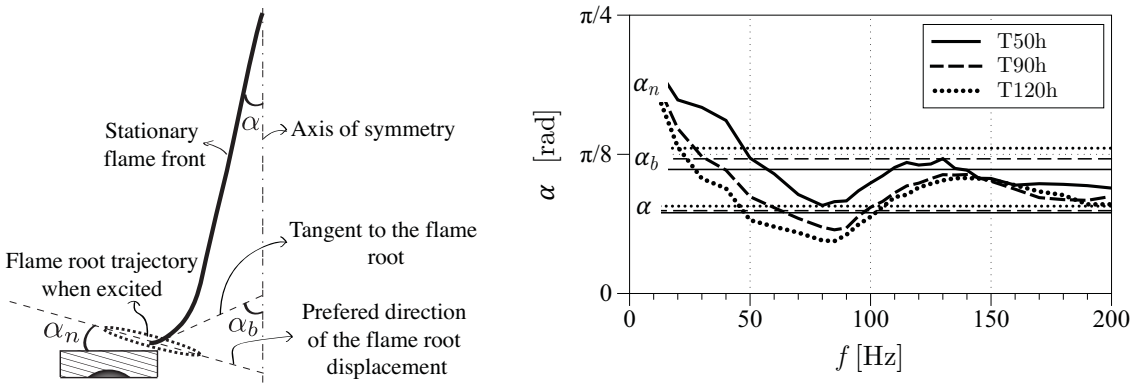

(a) Schematic representation showing the difference between the three angles: flame half-tip angle, α, flame base angle, α_b and flame root trajectory angle α_n

(b) Results for the three angles. α and α_b are measure in steady flame, while α_n is measured excited flame. T50h (——), T90h (- - - -) and T120h (·····).

Figure 9.11: B15 burner for the three reference cases T50h, T90h and T120h. The flow conditions are $\bar{v} = 1.6$ ms^{-1} and $\Phi = 0.95$ for the bulk velocity and the equivalence ratio respectively and velocity fluctuation level of $\varepsilon = 0.1$ was used for the calculation of α_n

Figure 9.11(b) shows that α_n oscillates between α and α_b for the range of frequencies studied here. α and α_b have the tendency to increase with the slot temperature, due to the increase on the $s_L/\bar{v}$ factor in both cases. However, for α_n this tendency is inverted. α_n decreases with T_s, which is mainly due to the fact that the amplitude of the flame root oscillation in the vertical direction ξ_0^y decreases with the slot temperature.

9.3.4 Experimental flame root transfer function

The experimental flame root transfer function is defined as:

$$\Xi_{exp}(\omega, T_s) = \frac{\tilde{\xi}_0/(w_s/2)}{\tilde{v}/\bar{v}} \tag{9.14}$$

In order to calculate the flame root transfer function, Ξ_{exp}, the images are post-procesed to obtain the flame root displacement in the burner reference plane, ξ_0^x and ξ_0^y. The normal

flame root displacement can be defined either by half-tip angle, α, the flame base angle, α_b or the normal base displacement angle, α_n. Nevertheless, in order to be consistent with the model of Sec. 9.2, the flame half tip angle α is chosen to determine the normal flame root displacement.

$$\xi_0 = \xi_0^x \cos\alpha + \xi_0^y \sin\alpha \tag{9.15}$$

After the image post-processing one obtains a 2 s long signal for $\xi_0(t)$ sampled at a frequency of $f_s = 3$ kHz. This signal is correlated to the velocity signal delivered by the HW to determine the experimental flame root transfer function:

$$\Xi_{exp}(\omega, T_s) = \frac{S_{v\xi_0}}{S_{vv}} \tag{9.16}$$

As well as for the FTF an spectral analysis of the normalized temporal signals, $v_1(t)/\bar{v}$ and $\xi_0(t)/(w_s/2)$, permits us to determine the experimental Ξ_{exp}. For this, the ratio $S_{v\xi_0}/S_{vv}$ is calculated, here $S_{v\xi_0}$ is the cross power spectral density between the $v_1(t)/\bar{v}$ and $\xi_0(t)/(w_s/2)$ signals and S_{vv} is the power spectral density of the velocity signal, $v_1(t)/\bar{v}$ taken at the excitation frequency f_{ex}. This procedure is repeated for every excitation frequency to determine the flame root response over the whole frequency range explored and for the three reference cases T50h, T90h and T120h.
The gain is defined as the magnitude of Ξ_{exp}, $\mathcal{G}_f = |\Xi_{exp}(\omega, T_s)|$ while the phase is its argument $\varphi_f = \arg[\Xi_{exp}(\omega, T_s)]$.

Results of the experimental flame root transfer function are presented in Fig. 9.12. The phase lag, φ_f, initially increases with increasing frequency for all three cases, before reaching a constant value for all frequencies higher than 150 Hz. φ_f slightly changes for the three reference cases, despite a small tendency to decrease with increasing T_s for frequencies between 75 and 150 Hz. On the other hand, the gain, $\mathcal{G}_f$, presents a resonance behavior with a peak which varies for the three cases. The resonance peak is shifted to the higher values of frequency when the slot temperature is increased. This is in agreement with the model and the theoretical analysis that stated that when the slot temperature is increased, the stand-off distance is reduces, which reduced the time taken by the enthalpy wave to propagate from the burner rim to the flame root and consequently increase the resonance frequency. Another interesting feature is that while for frequencies below 120 Hz the gain $\mathcal{G}_f$ decreases with increasing T_s, the opposite trend is observed adobe 120 Hz. This feature replicates the trends observed on the FTF in Fig. 6.9(a) which are compared side by side in Fig. 9.13.

These experimental results confirm the predictions of the model presented in Sec. 9.2.2 and permit to conclude that the reduction of the FTF gain ($\mathcal{G}_r$) at the resonance frequency comes from a reduction of the amplitude of the flame root fluctuations due to the increase of the slot temperature. At the frequency of the instability, $f_{ex} = 58$ Hz, the gain, $\mathcal{G}_f$ of the experimental flame root TF $\Xi(\omega)_{exp}$ decreases of about 11 % from the T50h to the T120h cases. This diminution of $\mathcal{G}_f$ is comparable to that of the FTF gain diminution $\mathcal{G}_r$ at the same frequency of 14 % for the same two cases found in Ch. 6.

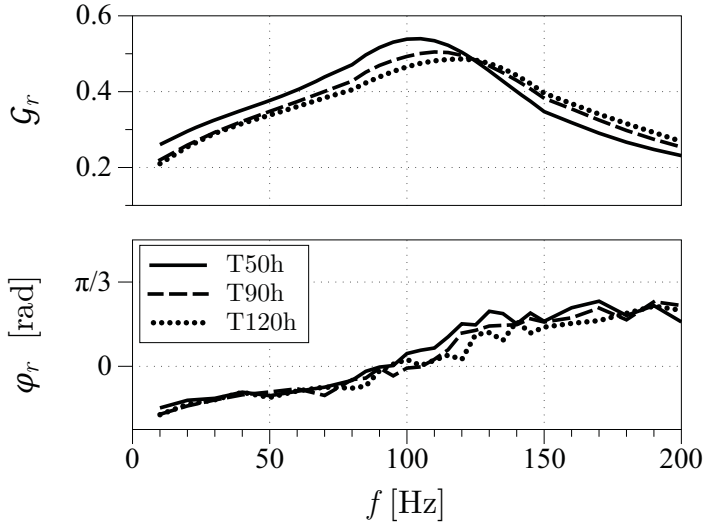

Figure 9.12: Experimental flame base movement transfer functions for four different surface temperatures, T_s, corresponding to the cases T50h (——); T90h (- - - -) and T120h (·····). Tests were performed on the B15 burner. The flow conditions are $\bar{v} = 1.6$ ms^{-1} and $\Phi = 0.95$ for the bulk velocity and the equivalence ratio respectively and a velocity fluctuation level of $\varepsilon = 0.1$

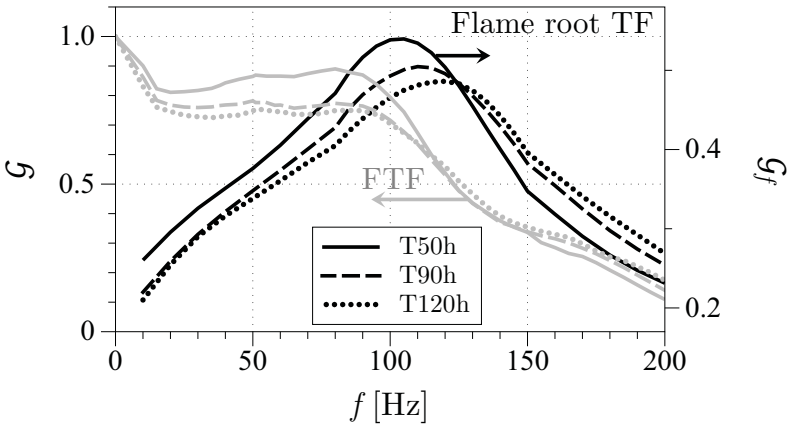

Figure 9.13: Comparison between the global FTF gain $\mathcal{G}$ (in gray lines) of the flame and the flame root TF gain $\mathcal{G}_f$ (in black lines).

9.4 Comparison between analytical and experimental flame root transfer functions

Wa have seen that in a qualitative manner the modeled (Ξ) and the experimental (Ξ_{exp}) flame root transfer functions show the same trend. Figure 9.14 shows both results Ξ and Ξ_{exp}, to allow a quantitative comparison: the gain, $\mathcal{G}_f$, is over-predicted by the model by a factor of two. The phase, φ_f, however is generally well reproduced especially for frequencies over 100 Hz.

The difference in the amplitude between the predicted gain and the measurements can

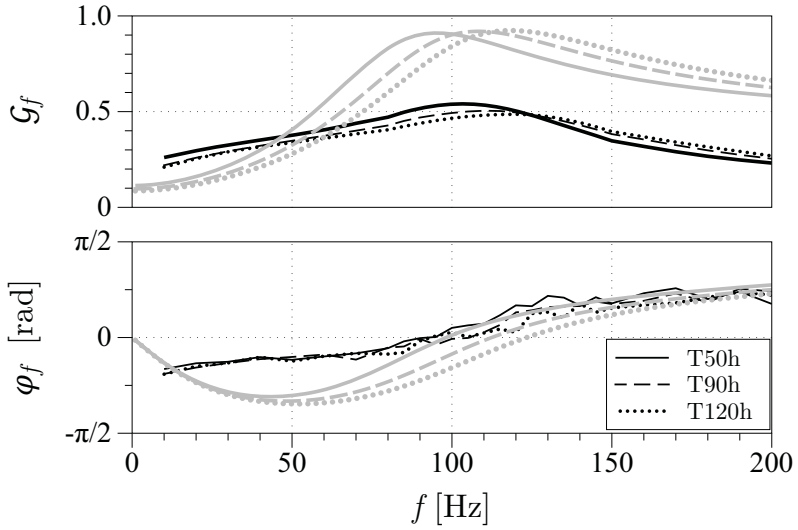

Figure 9.14: Comparison between the analytical (in thick gray lines) and the experimental (in thin black lines) flame root transfer function.

be explained, if one takes into account that the magnitude of velocity fluctuation at the flame root differs strongly from the one measured by the HW. It was previously remarked that close to the burner outlet there is a mode velocity conversion from acoustic to convective, which in the axis can decreases the gain by almost 30 % for certain frequencies (*cf.* Fig. 6.7). At the same time the flame root is located in the wake created by the interaction between the jet and the burner-lip. TYhis wake can modify the magnitude of the velocity fluctuation impinging on the flame root.

9.5 Conclusions

The flame root dynamics has been studied in this chapter to try to elucidate the variation of the FTF gain with the slot temperature. First an adaptation of the model developed by Cuquel *et al.* (2013) was performed in order to account for a 2D flame and include the

slot temperature as a new variable. This model shows a strong dependency of the flame root frequency response on the slot temperature especially for the gain, $\mathcal{G}_f$ defined as the magnitude of the amplitude normal to the flame front of the flame root displacement for a given velocity fluctuation. This flame-root displacement shows a preferred frequency that depends mainly on the stand-off distance. At the same time the stand-off distance is shown to be a function of the slot temperature, T_s. It decreases with the increase of T_s. For frequencies below 120 Hz the gain decreases with increasing T_s, the opposite trend is observed past 120 Hz. This feature strongly suggests that the alteration of the flame-root movement by the burner-rim temperature is the key to the modification of the gain in the global FTF.

These observations were successfully reproduced by the experiments in which the flame root frequency response was obtained from high speed zoomed photos of the excited flame root. However some discrepancies are found. First, the stand-off distance is under-estimated by the model and second, the magnitude of the gain is over-estimated.

One of the reasons for the discrepancy between the experiments and the theory of the stand-off distance is the definition of the flame root from the photos: these photos integrate all the light in the visible spectra coming from the flame, and although it is a good estimation, it is not the reaction rate. However, the position of the gain resonance peak coincides in the model and in the experiments (*cf.* Table. 9.1) underlining the fact that the stand-off distance coincide in both cases even though the definition of ψ_{f_0} from the photos is not exact.

Table 9.1: Comparison between the gain resonance peak frequency from the prediction of Eq. 9.13 and the experimental flame root TF.

f_f	**T50h**	**T90h**	**T120h**
Model	96 Hz	108 Hz	118 Hz
Measurements	105 Hz	110 Hz	120 Hz

From the results of this chapter one can conclude that the mechanism responsible for decreasing the gain $\mathcal{G}_r$ of the FTF at the frequency of the instability, which is partially responsible for stabilizing the system when T_s increases, is the flame root dynamics. Indeed, the flame root fluctuations, $\tilde{\xi}_0$, present a resonance behavior due to the coupling between the unsteady heat loss to the burner rim, q_l, and the local flame speed fluctuations at the flame root, $s_{L(\psi_{f_0})}$. The resonance peak is centered at a frequency f_f that depends on the flame stand-off distance, ψ_{f_0}. The increase on the slot temperature, T_s, reduces the flame stand-off distance. When the stand-off distance is reduced the peak, f_f, shifts to higher frequencies. Therefore for frequencies to the left of these peaks, as it is the case for the resonance frequency of the self-sustained oscillation, f_r, the gain, $\mathcal{G}_f$, decreases. This means that the amplitude of the flame foot oscillations are decreased when the slot temperature is increased. As the perturbations are convected along the flame front from the

flame root to the flame tip, the reduction of the flame root fluctuation amplitudes reduces the global magnitude of the flame response to acoustic oscillations and consequently the gain, $\mathcal{G}_r$, of the FTF.

Conclusions

A laminar premixed flame stabilized on a slot burner has been investigated experimentally. It exhibits a combustion instability that depends on the temperature of the burner at the flame anchoring point. When the slot is cold, the flame is unstable but as it heats up the instability is damped. For a fixed bulk velocity and equivalence ratio the flame instability can be completely controlled with only modifications of the burner-rim temperature. An increase of 20 °C on the burner-rim temperature can shut-down the instability completely.

An experiment with joint measurements of velocity and heat release rate was designed to study this phenomena. It was found that the flame during its unstable operation oscillates at a frequency around $f_r = 58$ Hz (or $\omega_r = 364$ rad/s). Three experimental cases with different dynamic characteristics are chosen depending on the slot temperature. The three cases correspond to a slot temperature of $T_s = 50$, 90 and 120 °C and are designated as T50h, T90h and T120h. T50h is always unstable; T90h is unstable in a transient regime while stable in a stationary regime and finally T120h is always stable. This cases were used all along the study for the experimental tests.

A linear stability model was developed in order to identify the parameters playing a role in the instability mechanisms. Five different parameters were identified: the natural pulsation of the burner, ω_0, the dissipation, δ, the pinching distance, r_0, the magnitude of the flame response, $\mathcal{G}_r$, and the phase-lag, φ_r at the resonance frequency. Thanks to an approximate analytical solution of this model it was possible to investigate the effect of each individual parameter in the stability of the system. Then these parameters were individually studied by well controlled experiments and their dependency to the burner rim temperature, T_s, was determined.

The acoustics of the burner was studied because the natural pulsation frequency of the burner and the dissipation are inherent characteristics of the burner acoustics. Acoustic tests were initially performed under reacting conditions. The slot temperature is controlled by injecting water at different temperatures in the closed circuit passages (*cf.* 1.3). Two methods were explored: the harmonic response (HR) and the impulse response (IR). They both give practically the same results: for $\omega_0 = 330$ rad/s and for $\delta = 15.8$ s^{-1}. The acoustic response of the burner was found to be independent of the slot temperature for both methods.

The same procedure was performed in a reacting configuration, for the experimental cases T90h and T120h (where the flame is stable). Here it was found that the resonance pulsation frequency under reacting configuration (ω_r) increases compared to the natu-

ral pulsation of the burner under non reacting configuration (ω_0), however they remain relatively close. At the same time it was found that ω_r does not depend on the slot temperature as it was the identical for T90h and T120h. The damping coefficient under reacting configuration however was found to increase with the slot temperature because the presence of the flame drives the system into resonance for low slot temperatures and stabilize the system for high slot temperatures.

Combustion noise was studied in order to validate the hypothesis made in the linear stability model. It was verified that the far-field acoustic pressure produced by an unstable flame can be reconstructed from its light intensity signal of CH^* radicals. The pinching distance r_0 was defined as the altitude from the burner outlet where the flame claps. It has been shown that r_0 depends on the excitation frequency and the slot temperature. For an excitation frequency close to that of the natural instability, r_0 slightly decreases with T_s. Thanks to the approximate analytical model of the linear stability system we were able to conclude that this decrease in r_0 with T_s is a consequence of the attenuation of the instability and not the cause. A diminution in r_0 would actually have an amplifying effect on the instability, not the contrary.

Flame Transfer Functions for various burner-rim temperatures were measured showing that the phase of the FTF is slightly reduced while its gain is reduced at low frequency and increased at higher frequencies when the T_s increased. From the FTF results one can conclude that the magnitude of the flame response to acoustic oscillation has a strong dependency on the slot temperature. At the frequency of the instability the magnitude of the flame response, $\mathcal{G}_r$, decreases by almost 14 % from the case T50h to the case T120h. On the other hand, the phase lag, φ_r, is however less affected, it decreases by 7 % from the T50h to the T120h case.
On the other hand, the FTF was found to be very sensitive to the reference point where the velocity measurement takes place. Due to a mode conversion (acoustic to convective) at the burner outlet, the amplitude of the velocity fluctuations is considerably reduced when the reference point gets closer and passes the burner outlet. This effect has a major impact on the form of the FTF gain. In this study we place the reference point 10 mm upstream the burner outlet in order to avoid the effects of the convective mode conversion.

Together with measurements of acoustic and combustion noise, a low-order model of the burner linear stability was able to retrieve the experimental observations. The system is unstable for low temperature of the slot (T50h) and stable for high temperatures of the slot (T90h and T120h). The approximate analytical solution of the low-order model reproduces the experimental observations as well. A synthesis in the state of the art of the level-set description of the flame front kinematic permitted to identify the mechanisms contributing to the flame wrinkling and so, the heat release fluctuation. Here, two principal mechanisms were identified and it was concluded from previous theoretical studied that the FTF is the sum of two contributions: the flame front dynamics and the flame root dynamics. These two contributions were studied separately in order to find out which is the mechanism that stabilize the flame when the slot temperature is increased (*cf.* Ch. 2).

The sensibility of the flame front dynamics to the slot temperature was studied in Ch. 8 using the analytical work on flame front kinematics through the G-equation of previous studies (*e.g.* Fleifil *et al.* (1996); Ducruix *et al.* (2000); Schuller *et al.* (2003b); Lieuwen (2005) and Cuquel *et al.* (2013)). Two parameters were found to control the flame front dynamics, ω_* and κ_*. These two parameters depend only on the flame stationary geometry which is set by the operating point ($\bar{v}$ and Φ). However, for the same operating point the flame geometry can change from T50h to T90h if the fresh gases temperature profile is affected by the slot temperature, which was the case when it was measured for the T50c and T90c under a non-reacting configuration. The fresh gases temperature profile was found to change with T_s due to the pre-heating of the fresh gases by the heat flux from the side walls. This has as consequence two secondary effects: the first one is the increasing bulk velocity due to the expansion of the fresh gases, and the second one is the increase of the flame speed. Both effects where studied separately. It was found that the increase on the bulk velocity due to the pre-heating of the gases is negligible. This effect has no influence on the phase, and it is not the reason why the gain decreases with increasing the slot temperature as it actually increases with the bulk velocity. On the other hand, the effect of the pre-heating of the fresh gases on the flame speed it was found to be the mechanism that decreases the phase lag. The mechanisms works in the following way: due to the increase in T_s the heat-flux from the slot walls to the flow is increased and the temperature profile of fresh gases is affected; the increase in the bulk temperature of the fresh gases increases the flame speed (Gu *et al.* (2000)) which at the same time decreases the flame height. As the bulk velocity is not altered, the convective time delay decreases as it is proportional to $\tau \sim h_f/\bar{v}$ and finally the phase lag between the velocity fluctuation and the heat release fluctuation (φ_r) decreases.

The flame root dynamics is an important contribution to the global flame frequency response to velocity fluctuations studied in Ch. 9. The flame anchoring point fluctuations are convected along the flame front and generate heat release rate fluctuations (Kornilov *et al.* (2007); Cuquel *et al.* (2013)). One may think, that a modification of the flame-root burner-rim interaction will actually have an effect on the global flame response. Thus, the dependency of the flame root dynamics on the slot temperature was studied in order to check this hypothesis. This study was done by an adaptation of the model developed by Cuquel *et al.* (2013) based on the analytical results of Rook (2001). This model shows a strong dependency of the flame root frequency response on the slot temperature. Specially on the gain, $\mathcal{G}_f$ defined as the magnitude of the amplitude normal to the flame front of the flame root displacement for a given velocity fluctuation. This flame-root displacement shows a preferred frequency that depends mainly on the stand-off distance (defined as the altitude from the burner to the flame base), depends directly on the slot temperature (the flame gets closer to the burner when the slot temperature is increased and vice versa). For frequencies below 120 Hz the gain decreases with increasing T_s, the opposite trend is observed past 120 Hz. This feature strongly suggests that the alteration of the flame-root movement by the burner-rim temperature is the key to the modification of the gain at the resonance frequency of the instability ($\mathcal{G}_r$) on the global FTF.

This observations were successfully reproduced by the experiments in which the flame root frequency response was obtained from high speed zoomed photos of the flame root. However some discrepancies are found: first, the stand-off distance is under-estimated in the model; second, the gain $\mathcal{G}_f$ is under estimated in the experiments. However the trent of the model was well captured by the experiments and we were able to conclude mechanism that decreases the gain of the FTF is the alteration of the flame root dynamics due to the increase on the slot temperature.

Summarizing, this study was motivated by the following question: why an initially unstable flame is stabilized when the temperature of the burner rim increases? Now we are able to answer this question. The system is stabilized by the effect of the wall temperature on the flame dynamics: when the slot walls became warmer, the FTF changes. This effect brings the system to a stable zone in the stability map (*cf.* Fig. 7.2). The gain and the phase change with the slot temperature thanks to two different mechanisms (Fig. 9.15):

1. The mechanism that acts on the phase is described as follows. The increase on the slot temperature increases the heat flux from the walls to the fresh gases that pass through the slot. This increase in the heat flux increases the fresh gases temperature, which at the same time increases the flame speed. This increase in the flame speed reduces the flame size. As the time delay that a flame takes to respond to a velocity oscillation is proportional to the flame height, a reduction on the flame size imposes a reduction on the delay which consequently reduces the phase-lag of the FTF.

2. The mechanism that acts on the gain is described as follows: the flame root fluctuations present a resonance behavior due to the coupling between the unsteady heat loss to the burner rim and the local flame speed fluctuations at the flame root. The resonance peak is centered at a frequency that depends on the stand-off distance. The increase of the slot temperature reduces the flame stand-off distance. When the stand-off distance is reduced the peak shifts to higher frequencies. Therefore for frequencies to the left of these flame root induced resonance peaks (as the resonance frequency of the self-sustained oscillation in this study) the gain decreases when the slot temperature is increased. As the perturbations are convected along the flame front from the flame root to the flame tip, the reduction of the flame root fluctuation amplitudes reduces the global magnitude of the flame response to acoustic oscillations and consequently the gain on the FTF.

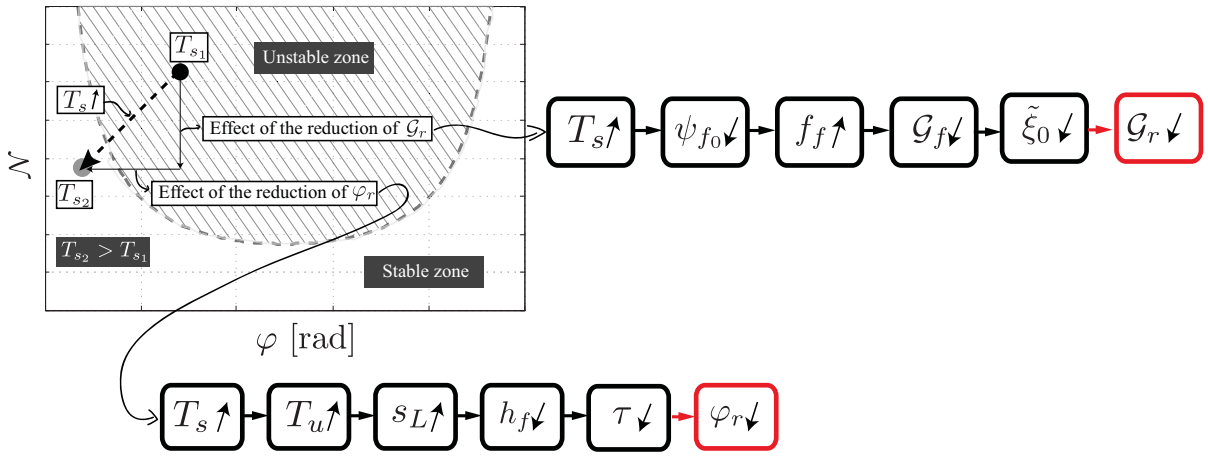

Figure 9.15: Description of the effect of the increase of the wall temperature, T_s, on the stability of the system and its associated mechanism on the gain, $\mathcal{G}_r$ and the phase, φ_r. T_u is the fresh gases bulk temperature, s_L is the flame speed, h_f is the flame height, τ is the time delay that the flame takes to react after a perturbation, ψ_{f_0}, is the stand-off distance, f_f is the frequency at the resonance peak, $\tilde{\xi}_0$ is the amplitude of the flame root oscillations and $\mathcal{G}_f$ is the flame root TF gain.

Perspectives

This study could be pursued in various directions. The first one is to perform DNS simulations of the same configuration and evaluate the ability of CFD solvers to account for parameters such as the slot temperature in the prediction of combustion instabilities. This could be done with simple thermal boundary conditions based on experimental temperature measurements, or by coupling with a solid heat conduction solver such as AVTP to account for more realistic temperature fields and fluxes in the solid material. This study is already an ongoing investigation in the IMFT lab. In the same way, it would be enriching to determine numerically the stability of the system, by the use of a Helmholtz solver such as AVSP and to compared with the results of the linear stability analysis derived in this thesis.

The location where the velocity fluctuation should be measured to defined FTF's is still open, and it would be very interesting to explore it more in detail. One can envisage to explore a wider frequency range and a cover a larger part of the $x-y$ plane. It will also be convenient to study the nature of the velocity fluctuation dependency on the fresh gases temperature with LDA and time resolved PIV that are not affected by the fresh gases temperature. It will also be convenient to study the effect of the slot temperature on the velocity fluctuation close to the solid boundaries. It has been said that one of the reasons for the discrepancy between the flame root fluctuation model and the experiments could be the different nature of the velocity fluctuation. The velocity fluctuation was actually measured downstream of the slot outlet where the velocity fluctuation is of an acoustic

nature and it should be taken close to the burner outlet where a velocity conversion mode could change the nature of the velocity fluctuation.

Another identified source of error between the flame root transfer function model and the experiments is the poor definition of the flame anchoring point position. Experimentally it was defined as the point along the flame front that has the maximum rate decay of light intensity in the flame root zone. However taking into account that the photos integrate the whole light spectrum emitted by the flame this definition is unclear. It would be interesting to perform the same test with an intensified high speed camera and a CH^* or OH^* filter that will only show information on the heat release rate.

In order to keep the lower part of the slot at ambient temperature it was necessary to design a dual channel cooling system. This configuration does not allow slot temperature higher that 120 °C. It will also be interesting to explore higher slot temperatures. It can be done by heating up the surface temperature by external means. In the same way one may thing to employ confined configurations and evaluate the effect of the wall temperature in the confinement wall on the combustion instabilities.

Bibliography

H. Altay, S. Park, D. Wu, D. Wee, A. Annaswamy, and A. Ghoniem. Modeling the dynamic response of a laminar perforated-plate stabilized flame. *Proc. Combust. Inst.* , 32(1):1359–1366, 2009.

H. Altay, K. Kedia, R. Speth, and A. Ghoniem. Two-dimensional simulations of steady perforated-plate stabilized premixed flames. *Combust. Theory and Modelling* , 14(1):125–154, 2010.

C. Armitage, R. Balachandran, E. Mastorakos, and R. Cant. Investigation of the non-linear response of turbulent premixed flames to imposed inlet velocity oscillations. *Combust. Flame* , 146:419–436, 2006.

M. Assael, J. Millat, V. Vesovic, and W. Wakerham. The thermal conductivity of methane and tetrafluoromethane in the limit of zero density. *J. Phys. Chem. A*, 19(5), 1990.

F. Baillot and A. Bourehla. Burning velocity of pockets from a vibrating flame experiment. *Combust. Sci. Tech.* , 162:201–224, 1997.

F. Baillot, D. Durox, and R. Prud'homme. Experimental and theoretical study of a premixed vibrating flame. *Combust. Flame* , pages 149–168, 1992.

F. Baillot, D. Durox, and D. Demare. Experiments on imploding spherical flames: effects of curvature. *Proc. Combust. Inst.* , 29:1453–1460, 2002.

B Bellows and T Lieuwen. Nonlinear response of a premixed combustor to forced acoustic oscillations. *AIAA Paper* , (0455), 2004.

A. Birbaud, D. Durox, and S. Candel. Upstream flow dynamics of a laminar premixed conical flame submitted to acoustic modulations. *Combust. Flame* , 146(3):541–552, 2006.

A. Birbaud, D. Durox, S. Ducruix, and S. Candel. Dynamics of confined premixed flames submitted to upstream acoustic modulations. *Proc. Combust. Inst.* , 31:1257–1265, 2007.

A. Birbaud, D. Durox, S. Ducruix, and S. Candel. Dynamics of free jets submitted to upstream acoustic modulations. *Phys. Fluids* , 19(1), 2007.

R. Blumenthal, P. Subramanian, R. Sujith, and W. Polifke. Novel perspectives on the dynamics of premixed flames. *Combust. Flame* , 160(7):1215–1224, 2013.

F. Boudy, D. Durox, T. Schuller, and S. Candel. Nonlinear mode triggering in a multiple flame combustor. *Proc. Combust. Inst.* , 33:1121–1128, 2011.

L. Boyer and J. Quinard. On the dynamics of anchored flames. *Combust. Flame* , 82(1):51–65, 1990.

S. Candel, D. Durox, D. Ducruix, A. Birbaud, N. Noiray, and T. Schuller. Flame dynamics and combustion noise: Progress and challenges. *CEAS Combustion Noise Workshop*, pages 49–51, 2007.

S. Candel. Combustion dynamics and control: Progress and challenges. *Proc. Combust. Inst.* , 29(1):1–28, 2002.

P. Clavin and E. Siggia. Turbulent premixed flames and sound generation. *Combust. Sci. Tech.* , 78:147–155, 1991.

L. Crocco. Aspects of combustion instability in liquid propellant rocket motors. Part I. *J. American Rocket Society* , 21:163–178, 1951.

F. Culick and P. Kuentzmann. *Unsteady Motions in Combustion Chambers for Propulsion Systems*. NATO Research and Technology Organization, 2006.

A. Cuquel, D. Durox, and T. Schuller. Theoretical and experimental determination of the flame transfer function of confined premixed conical flames. 7th Mediterranean Combustion Symposium, 2011.

A Cuquel, D Durox, and T Schuller. Impact of flame base dynamics on the nonlinear frequency response of conical flames. *Comptes Rendus Mécanique*, 341:171–180, 2013.

A. Cuquel. *Dynamics and nonlinear thermo-acoustic stability analysis of premixed conical flames*. Phd thesis, Ecole Centrale Paris, 2013.

L. de Goey, J. van Oijen, V. Kornilov, and J. ten Thije Boonkkamp. Propagation, dynamics and control of laminar premixed flames. *Proc. Combust. Inst.* , 33:863–886, 2011.

P. Dowling and R. Stow. Acoustic analysis of gas turbine combustors. *J. Prop. Power* , 19(5):751–764, 2014/01/27 2003.

A. Dowling. The calculation of thermoacoustic oscillations. *J. Sound Vib.* , 180(4):557 – 581, 1995.

A. Dowling. A kinematic model of ducted flame. *J. Fluid Mech.* , 394:51–72, 1999.

F. Duchaine, L. Selle, and T. Poinsot. Sensitivity analysis of transfer functions of laminar flames. *Combust. Flame* , 158(12):2384–2394, 2011.

S. Ducruix, D. Durox, and S. Candel. Theoretical and experimental determinations of the transfer function of a laminar premixed flame. *Proc. Combust. Inst.* , 28:765–773, 2000.

S. Ducruix, T. Schuller, D. Durox, and S. Candel. Combustion dynamics and instabilities: Elementary coupling and driving mechanisms. *J. Prop. Power* , 19(5):722–734, 2003.

D. Durox, T. Schuller, and S. Candel. Self-induced instability of a premixed jet flame impining on a plate. *Proc. Combust. Inst.* , 29:69–75, 2002.

D. Durox, T. Schuller, and S. Candel. Combustion dynamics of inverted conical flames. *Proc. Combust. Inst.* , 30(2):1717–1724, 2005.

D. Durox, T. Schuller, N. Noiray, A. Birbaud, and S. Candel. Rayleigh criterion and acoustic energy balance in unconfined self-sustained oscillating flames. *Combust. Flame* , 155(3):416–429, 2009.

D. Durox, T. Schuller, N. Noiray, and S. Candel. Experimental analysis of nonlinear flame transfer functions for different flame geometries. *Proc. Combust. Inst.* , 32(1):1391 – 1398, 2009.

E. Fernandes and R. Leandro. Modeling and experimental validation of unsteady impinging flames. *Combust. Flame* , 146(4):674 – 686, 2006.

M. Fleifil, A. Annaswamy, Z. Ghoneim, and A. Ghoniem. Response of a laminar premixed flame to flow oscillations: A kinematic model and thermoacoustic instability results. *Combust. Flame* , 106(4):487–510, 1996.

X. Gu, M. Haq, M. Lawes, and R. Woolley. Laminar burning velocity and Markstein lengths of methane-air mixtures. *Combust. Flame* , 121:41–58, 2000.

S. Hong, S. Shanbhogue, K. Kedia, and A. Ghoniem. Impact of the flame-holder heat-transfer characteristics on the onset of combustion instability. *Combust. Sci. Tech.* , 185:1541–1567, 2013.

M. Hultmark and A. Smits. Temperature corrections for constant temperature and constant current hot-wire anemometers. *Measurement Science and Technology.*, 21(10), 2010.

I. Hurle, R. Price, T. Sugden, and A. Thomas. Sound emission from open turbulent premixed flames. *Proc. R. Soc. Lond. A* , 303(409), 1968.

G. Joulin and G. Sivashinsky. Pockets in premixed flames and combustion rate. *Combust. Sci. Tech.* , 77:329–335, 1991.

W. Kannuluik and E. Carman. The temperature dependence of the thermal conductivity of air. *Aust. J. Sci. Res. A: Phys. Sci.*, 4:305–14, 1951.

N. Karimi, M. Brear, S. Jin, and J. Monty. Linear and non-linear forced response of a conical, ducted, laminar premixed flame. *Combust. Flame* , pages 2201–2212, 2009.

K. Kashinath, S. Hemchandra, and M. Juniper. Nonlinear thermoacoustics of ducted premixed flames: The influence of perturbation convection speed. *Combust. Flame* , 160(12):2856–2865, 2013.

K. Kedia, H. Altay, and A. Ghoniem. Impact of flame-wall interaction on premixed flame dynamics and transfer function characteristics. *Proc. Combust. Inst.* , 33:1113–1120, 2011.

J. Keller and K. Saito. Measurements of the combustion flow in a pulse combusor. *Combust. Sci. Tech.* , 53(137-163), 1987.

V. Kornilov, K. Schreel, and L. de Goey. Experimental assessment of the acoustic response of laminar premixed bunsen flames. *Proc. Combust. Inst.* , 31:1239–1246, 2007.

V. Kornilov, M. Manohar, and L. de Goey. Thermo-acoustic behaviour of multiple flame burner decks: Transfer function (de)composition. *Proc. Combust. Inst.* , 32(1):1383–1390, 2009.

V. Kornilov. *Dynamics and nonlinear thermo-acoustic stability analysis of premixed conical flames*. Phd thesis, Technische Universiteit Eindhoven, 2006.

C. Law. Dynamics of stretched flames. *Proc. Combust. Inst.* , 22:1381–1402, 1988.

D. Lee and T. Lieuwen. Premixed flame kinematics in a longitudinal acoustic field. *J. Prop. Power* , 19(5):837–846, 2003.

T. Lieuwen and S. Preetham. Nonlinear flame-flow transfer function calculations: Flow disturbance celerity effects. part i. *AIAA Paper* , pages 1–16, 2004.

T. Lieuwen. Analysis of acoustic wave interactions with turbulent premixed flames. *Proc. Combust. Inst.* , 29:1817–1824, 2002.

T. Lieuwen. Nonlinear kinematic response of premixed flames to harmonic velocity disturbances. *Proc. Combust. Inst.* , 30(2):1725–1732, 2005.

T. Lieuwen. *Unsteady Combustor Physics*. Cambridge University Press, 2012.

G. Markstein. Non steady flame propagation. *Pergamon Press.*, page 50, 1964.

Y. Matsui. An experimental study on pyro-acoustic amplification of premixed laminar flames. *Combust. Flame* , 43:199 – 209, 1981.

K. Matveev and F. Culick. A study of the transition to instability in a rijke tube with axial temperature gradient. *J. Sound Vib.* , 264(3):689 – 706, 2003.

A. McIntosh and J. Clarke. Second order theory of unsteady burner-anchored flames with arbitrary lewis number. *Combust. Sci. Tech.* , 38:161–196, 1984.

A. McIntosh. The effect of upstream acoustic forcing and feedback on the stability and resonance behaviour of anchored flamest. *Combust. Sci. Tech.* , 54(217-236), 1987.

H. Merk. An analysis of unstable combustion of premixed gases. *Proc. Combust. Inst.* , 6:500–512, 1987.

A. Morgans and A. Dowling. Model-based control of combustion instabilities. *J. Sound Vib.* , 299(1–2):261 – 282, 2007.

F. Nicoud and T. Poinsot. Thermoacoustic instabilities: should the Rayleigh criterion be extended to include entropy changes ? *Combust. Flame* , 142:153–159, 2005.

F. Nicoud, L. Benoit, C. Sensiau, and T. Poinsot. Acoustic modes in combustors with complex impedances and multidimensional active flames. *AIAA Journal* , 45:426–441, 2007.

N. Noiray, D. Durox, T. Schuller, and S. Candel. Self-induced instabilities of premixed flames in a multiple injection configuration. *Combust. Flame* , 145(3):435–446, 2006.

N. Noiray, D. Durox, T. Schuller, and S. Candel. Passive control of combustion instabilities involving premixed flames anchored on perforated plates. *Proc. Combust. Inst.* , 31(1):1283–1290, 2007.

N. Noiray, D. Durox, T. Schuller, and S. Candel. A unified framework for nonlinear combustion instability analysis based on the flame describing function. *J. Fluid Mech.* , 615:139–167, 2008.

N. Noiray. *Analyse linéaire et non-linéaire des instabilités de combustion, application aux systèmes à injection multipoints et stratégies de contrôle.* Phd thesis, Ecole Centrale Paris, 2007.

P. Palies, D. Durox, T. Schuller, and S. Candel. Nonlinear combustion instability analysis based on the flame describing function applied to turbulent premixed swirling flames. *Combust. Flame* , 158(10):1980–1991, 2011.

J. Penner, D. Lister, D. Griggs, D. Dokken, and M. McFarland. Aviation and the global atmosphere. Technical report, Intergovermental Panel on Climate Change (WMO and UNEP), 1999.

R. Petersen and W. Emmons. Stability of laminar flmaes. *Phys. Fluids* , 4(456-464), 1961.

A. Pierce. *Acoustics: an introduction to its physical principles and applications.* McGraw Hill, New York, 1981.

T. Poinsot and D. Veynante. *Theoretical and Numerical Combustion.* Third Edition (www.cerfacs.fr/elearning), 2011.

S. Preetham and T. Lieuwen. Nonlinear flame-flow transfer function calculations: flow disturbances celerity effects. *AIAA Paper* , 2004.

R. Price, I. Hurle, and T. Sudgen. Optical studies of the generation of noise in turbulent flames. *Proc. Combust. Inst.* , 12:1093–1102, 1968.

R. Price, I. Hurle, and T. Sugden. Optical studies of the generation of noise in turbulent flames. *Proc. Combust. Inst.* , 12(1):1093 – 1102, 1969.

R. Rajarama and T. Lieuwen. Parametric studies of acoustic radiation from premixed flames. *Combust. Sci. Tech.* , 175:2269–2298, 2003.

L. Rayleigh. The explanation of certain acoustic phenomena. *Nature*, pages 319–321, 1878.

S. Rienstra. A small Strouhal number analysis for acoustic wave-jet flow-pipe interaction. *J. Sound Vib.* , 86:539–556, 1983.

R. Rook and L. de Goey. The acoustic response of burner-stabilized flat flames: a two-dimensional numerical analysis. *Combust. Flame* , 133(1-2):119–132, 2003.

R. Rook, L. de Goey, L. Somers, K. Schreel, and R. Parchen. Response of burner-stabilized flat flames to acoustic perturbations. *Combust. Theory and Modelling* , pages 37–41, 2002.

R. Rook. *Acoustics in Burner-Stabilised Flames*. PhD thesis, Eindhoven University of Technology, 2001.

F. Sawyer. Science based policy for addressing energy and environmental problems. *Proc. Combust. Inst.* , 32(1):45–56, 2009.

K. Schreel, R. Rook, and L. de Goey. The acoustic response of burner-stabilized premixed flat flames. *Proc. Combust. Inst.* , 29:115–122, 2002.

K. Schreel, V. van den Tillaart, and L. de Goey. The influence of burner material properties on the acoustical transfer function of radiant surface burners. *Proc. Combust. Inst.* , 30:1741–1784, 2005.

T. Schuller, D. Durox, and S. Candel. Dynamics of and noise radiated by a perturbed impinging premixed jet flame. *Combust. Flame* , 128:88–110, 2002.

T. Schuller, D. Durox, and S. Candel. Self-induced combustion oscillations of laminar premixed flames stabilized on annular burners. *Combust. Flame* , 135:525–537, 2003.

T. Schuller, D. Durox, and S. Candel. A unified model for the prediction of laminar flame transfer functions: comparisons between conical and v-flames dynamics. *Combust. Flame* , 134:21–34, 2003.

T. Schuller, N. Noiray, D. Durox, and S. Candel. On mechanisms of intense combustion noise emition. *International Congres of Sound and Vibration*, 2006.

T. Schuller, D. Durox, P. Palies, and S. Candel. Acoustic decoupling of longitudinal modes in generic combustion systems. *Combust. Flame* , 159(5):1921–1931, 2012.

T. Schuller. *Mécanismes de Couplage dans les Interactions Acoustique-Combustion*. Phd thesis, Ecole Centrale Paris, 2003.

L. Selle, T. Poinsot, and B. Ferret. Experimental and numerical study of the accuracy of flame-speed measurements for methane/air combustion in a slot burner. *Combust. Flame* , 158(1):146–154, 2011.

D. Shin and T. Lieuwen. Flame wrinkle destruction processes in harmonically forced, laminar premixed flames. *Combust. Flame* , 159(11):3312–3322, 2012.

W. Strahle. On combustion generated noise. *J. Fluid Mech.* , 49:399–414, 1971.

W. Strahle. Combustion noise. *Prog. Energy Comb. Sci.* , 4:157–176, 1978.

W. Sutherland. The viscosity of gases and molecular force. *Philosophical Magazine*, 5:507–531, 1893.

A. Thomas and G. Williams. Flame noise: sound emission from spark-ignited bubbles of combustible gas. *Proc. R. Soc. Lond. A* , 294:449–466, 1966.

J. Truffaut, G. Searby, and L. Boyer. Sound emissions by non-isomolar combustion at low Mach number. *Combust. Theory and Modelling* , 2:423–428, 1998.

K. Truffin and T. Poinsot. Comparison and extension of methods for acoustic identification of burners. *Combust. Flame* , 142(4):388–400, 2005.

M.C. Vagelopoulos and F. H. Jonathan. An experimental and numerical study on the adequacy of CH as a flame marker in premixed methane flames. *Proc. Combust. Inst.* , 30(1):241–249, 2005.

H. Wang, C. Law, and T. Lieuwen. Linear response of stretch-affected premixed flames to flow oscillations. *Combust. Flame* , 156(4):889–895, 2009.

Appendix A

Comments on the linearity of the flame response

We have seen that flame dynamics is strongly dependent on the slot temperature, however how this interaction wall-temperature flame dynamics works is still unknown. At this point the one question question arises: is the linearity of the flame affected by the slot temperature ? and if yes, is this the reason for the attenuation of the instability when T_s is increased ? In order to answer these questions we will explore the dependency of the flame linearity to the slot temperature.
The nonlinear effects of the flame response to flow perturbation have been studied both theoretically (Lieuwen (2005)) and experimentally (Bellows and Lieuwen (2004)). It has been demonstrated that for small amplitudes of velocity fluctuations, typically less than $\varepsilon < 0.2$ (*cf.* Fig. A.1) the flame heat release rate fluctuation magnitude, σ, scales linearly with the velocity fluctuation magnitude, ε. Here this aspect of the flame response will not be discussed, because it is a matter of a special investigation. Nevertheless, in the frame of the FTF dependency to the slot temperature attention is paid to the following question: is the FTF linearity affected by the slot temperature?

Considering the flame as a black box in which a physical mechanism transforms any input signal (*e.g.* flow velocity oscillation) into an output signal (*e.g.* heat release rate fluctuation) one can write:

$$\dot{q}(t) = G(v(t)) \tag{A.1}$$

The G operator can be linear or nonlinear. In the frequency domain, a signal has a linear response if most of the energy is stored in the fundamental harmonic of the excitation frequency. On the contrary, the signal has a nonlinear response if its energy is distributed between the fundamental of the excitation frequency and its harmonics.
One may think that the slot temperature can change the energy distribution of the flame response. In order to test the dependency of the flame response nonlinearity to the slot temperature, we perform a test in which we study the response of the second harmonic coefficient for different excitation frequencies and different slot temperatures. The second

harmonic coefficient is defined as:

$$k_n = \frac{\mathcal{S}(nf_{ex})}{\mathcal{S}(f_{ex})} \tag{A.2}$$

where $\mathcal{S}$ is the the amplitude of the signal power spectrum, f_{ex} is the frequency of excitation and n is the number of the harmonic ($n = 2$ for the second harmonic). Figure A.1 presents an example of a frequency dependency of k_2 for a flame submitted to velocity excitations.

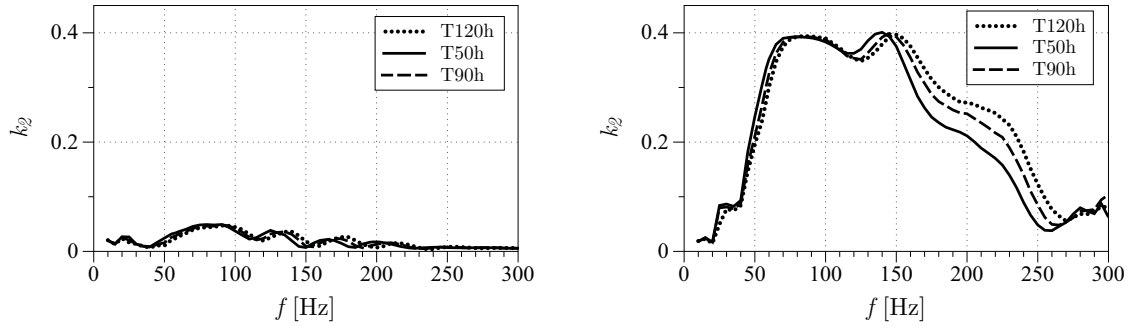

(a) Second harmonic coefficient of the velocity signal.

(b) Second harmonic coefficient of the CH* signal.

Figure A.1: Linearity of the signals: T50h (——); T90h (- - - -) and T120h (·····). Flow velocity and equivalence ratio where $\bar{v} = 1.6$ ms^{-1} and $\Phi = 0.95$ respectively. The modulation level was kept constant at $\varepsilon = 0.1$.

Figure A.1(a) shows the second harmonic coefficient for the velocity signal. Here k_2 is independent of the excitation frequency and the slot temperature. The second harmonic is less that 5 % of the fundamental for the whole range of frequency, confirming that the linear acoustic approximations is suitable in this experiment.

On the other hand, Fig. A.1(b) shows k_2 for the CH* intensity signals. In this case, k_2 depends on the excitation frequency. k_2 behaves has a band-pass filter with a maximum response for the frequency band of $f_{ex} \in [75, 150]$ Hz. In this range of frequency almost 40 % of the energy of the signal is stored in the second harmonics. One can also notice from Fig. A.1(b) that for low frequency of excitation typically less than 150 Hz the response of k_2 is independent of the slot temperature. However, for frequencies of excitation above 150 Hz the response of k_2 depends on the slot temperature. k_2 increases with the increase on T_s. However, in this study we focus on frequencies close to the resonance frequency of the natural instability $f_r = 58$ Hz. Thus, from the results of the linearity test we can conclude that the behavior observed in Ch. 2 is not caused by a re-distribution of the energy to higher harmonics in the flame response, as k_2 at $f = 58$ Hz for the CH* signal does not change.

Appendix B

Equipment

Table B.1: Equipment

Item	**Brand**	**Model**
DAQ burner	National Istruments	PCI 6024
Burner connection block	National Istruments	BNC 2120
DAQ diagnostics	National Istruments	PCI 6052E
Diagnostics connection block	National Istruments	BNC 2110
DAQ thermocouples	National Istruments	USB 9213
Air mass flow controller	Bronkhorst	F-201 AV-AAD-33-V, 100 ln/min
CH_4 mass flow controller	Bronkhorst	F-201 AV-AAD-33-V, 20 ln/min
Water temperature regulator	MGW Lauda	RCS
Hot wire probe	Dantec Dynamics	55P16
CTA	Dantec Dynamics	Mini-CTA 54T30
Photomultiplier + Conditioner	Thorlabs	PMM01
Microphone	Behringer	EMC8000
Microphone alimentation	Behringer	MIC100
Thermocouples	TC Direct	Type K 405-050
Loudspeaker	Focal	100VRS
Loudspeaker amplifier	Yamaha	K8081
Camera	pco	dimax
Lens	Nikon	Micro-Nikkor $f/2.8$ 105 mm

Appendix C

Proceedings of the Combustion Institute 2014 (Accepted)

Wall-temperature effects on flame response to acoustic oscillations

D. Mejia[a], L. Selle[a,b,*], R. Bazile[a], T. Poinsot[a,b]

[a] *Université de Toulouse; INPT, UPS; IMFT (Institut de Mécanique des Fluides de Toulouse); Allée Camille Soula, F-31400 Toulouse, France*
[b] *CNRS; IMFT; F-31400 Toulouse, France*

Abstract

This paper presents an experimental investigation of combustion instabilities for a laminar premixed flame stabilized on a slot burner. For certain operating conditions, the system exhibits an unstable mode locked on the Helmholtz mode of the burner. It is shown that the instability can be controlled and even suppressed by changing solely the temperature of the burner rim. A theoretical model accounting for this parameter in the flame transfer function is devised and the physical mechanisms for the temperature dependance of the flame response are investigated.

Keywords: Combustion instabilities, Flame transfer function, Wall temperature

1. Introduction

The occurrence of combustion instabilities (CI) is a major problem for the design and operation of many power-generation systems such as gas turbines, aeronautical engines and rocket engines [1]. The constructive coupling between acoustic waves and unsteady heat release rate constitutive of CI is responsible for loss of performance, restriction in operating conditions and sometimes catastrophic failures. The challenge for understanding and predicting CI lies in the multiplicity of physical phenomena involved in the unstable loop [2]: acoustics, vortex dynamics, mixing, chemistry, two-phase flows, etc. One of the canonical configurations for the study of CI is the laminar premixed flame, which has been extensively studied [3, 4, 5]. Recent theoretical developments [6, 7] propose analytical solutions for the flame response to acoustic perturbation, which is a central element for the prediction of CI. For linear-stability analysis, the flame response is assumed to depend only on the frequency of the incident perturbations, nevertheless its response may depend on many other parameters. The present study focuses on the impact of heat transfer on the flame response, based on the experimental observation that most systems behave differently at cold start and in the permanent regime. We therefore investigate the response of a laminar premixed flame where the temperature of the burner at the flame anchoring point can be controlled and monitored.

The manuscript is organized as follows: in Sec. 2 the experimental setup and diagnostics are presented, while in Sec. 3 presents a self-sustained CI, dependent on the burner-rim temperature. Section 4 is devoted to the derivation of a low-order model for the prediction of the stability map and the input parameters for this model are measured in Sec. 5. Finally, in Sec. 6 the impact of the flame-root dynamics on the overall flame response is scrutinized.

2. Experimental setup and diagnostics

The experiment is a slot burner [8] with a laminar premixed methane/air flame stabilized at the burner outlet (*cf.* Fig. 1). The four main components are: a mixing chamber, a plenum, a convergent nozzle and a rectangular-cross-section slot (width $w_s = 10$ mm and length $l_s = 100$ mm) with a height $h_s = 70$ mm. The flow rates of air and methane are controlled and measured via individual mass flow meters: Bronkhorst F-201 AV-AAD-33-V. The reactants are injected at the bottom of the mixing chamber in a cross-flow configuration to maximize mixing. The premixed flow is then laminarized in the plenum by an array of small glass balls and three honeycomb panels. Finally, it passes through the converging nozzle and the slot. In order to control the temperature of the burner rim, the long sides of the slot are water-cooled by two pairs of cylindrical passages (*cf.*

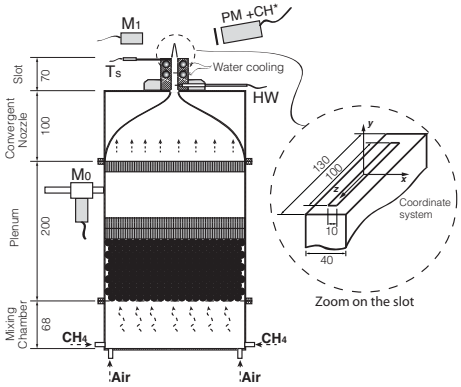

Figure 1: Sketch of the burner: transverse cut and experimental diagnostics. The four main components are: the mixing chamber, the plenum, the nozzle and the slot. M_0 and M_1 are 1/2" microphones. PM + CH* is a photomultiplier equipped with CH* filter. HW corresponds to a hotwire. T_W is K-type thermocouple.

*Corresponding author
Email address: laurent.selle@imft.fr (L. Selle)

Fig. 2) with a 5 mm cross-section, centered 7 mm and 21 mm below the burner rim, *i.e.* at $x = \pm 12.5$ mm, $y = -7$ mm and $y = -21$ mm in the reference coordinates of Fig. 1. The water temperature, T_w, in the upper channels ($y = -7$ mm) can be set between 1 and 99 °C, with a mass flow rate up to 1 kg/min. In the lower channels ($y = -21$ mm) water at ambient temperature flows at 5 kg/min. A K-type thermocouple is placed 1 mm below the burner outlet ($x = -6$ mm, $y = -1$ mm and $z = 0$ mm). It gives the temperature, T_s, of the material as close as possible to the flame base. The purpose of this dual-channel cooling system is to be able to control T_s, while maintaining the lower part of the slot and the burner under ambient conditions.

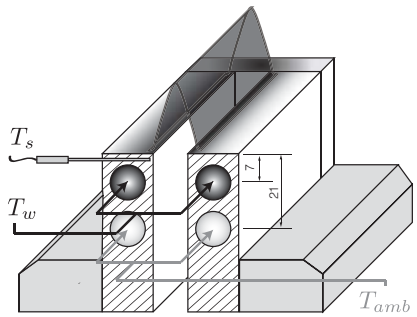

Figure 2: Perspective view of the slot with a cut through the material at $z = 0$. The upper and lower cooling channels allow a water flow at T_w and T_{amb}, respectively.

A hot wire probe, labeled HW in Fig. 1, is used to measure the unsteady axial velocity $v_1(t)$, located 55 mm upstream of the slot outlet ($x = 0$ mm, $y = -55$ mm and $z = 0$ mm). A photomultiplier, labeled PM in Fig. 1, measures the unsteady intensity, $I(t)$, of spontaneous emission of CH^* radicals. The PM is equipped with a narrow-band filter centered on a wavelength $\lambda = 430$ nm and is placed 400 mm away from the flame, aligned with the z axis ($x = 0$ mm, $y = 10$ mm and $z = 400$ mm). It has been shown that for lean premixed flames, $I(t)$ is proportional to the heat release rate [9]. Two microphones, M_0 and M_1, are used to record the acoustic pressure fluctuation, $p'_0(t)$ and $p'_1(t)$, respectively. M_0 is placed in a waveguide connected to a pressure plughole in the middle of the plenum ($x = -100$ mm, $y = -270$ mm and $z = 0$ mm), while M_1 is located 300 mm away from the burner ($x = 0$ mm, $y = 10$ mm and $z = 300$ mm).

3. Description of the unstable behavior

Configurations similar to Fig. 1 typically exhibit instabilities locked on the Helmholtz mode of the cavity [10, 11, 12] . For a given flame, which has its own response to acoustic perturbations, stability depends on the Helmholtz frequency and the level of dissipation in the system. Because of its direct impact on both effects, the main parameter controlling the occurrence of instabilities is the height, h_s, of the slot [13].

In this study, however, an other parameter has been identified: the temperature, T_s, of the burner rim. Indeed, for a slot height $h_s = 70$ mm, the flame is unstable when the slot is cold and stable once hot. This behavior is illustrated in Fig. 3, which presents the joint evolution of pressure fluctuation in the plenum and slot temperature versus time. The operating point for this test is an equivalence ratio $\Phi = 0.95$ and a bulk velocity in the slot $\bar{u} = 1.6$ m.s^{-1}. Temperature and pressure correspond to ambient conditions $T_{amb} = 20$ °C and $P_{amb} = 0.993$ bar, respectively. As shown in Fig. 3, at $t = 0$, the whole experiment is at ambient temperature and the cooling system is off. Combustion is initiated at $t = 20$ s and an instability develops immediately at a frequency $f_r = 58$ Hz, corresponding to the Helmholtz mode of the burner (*cf.* Sec. 4). The pressure fluctuation inside the plenum reaches 113 dB and decreases gradually as the the slot temperature, T_s, increases. Around $t = 300$ s, the instability reduces drastically and the flame is fully stable past $t = 400$ s. Meanwhile, T_s is over 100 °C and still increasing. At $t = 480$ s, the cooling system is started with water at $T_w = 3$ °C flowing through the slot, resulting in a sharp drop of T_s. The instability rises back up and the whole system reaches a steady state around $t = 800$ s, with $\|p'_0\| = 110$ dB and $T_s = 50$ °C. This behavior is fully repeatable and the instability can be controlled only using the cooling system, demonstrating that the burner-rim temperature is one of the parameters controlling the instability. To study the transition between stable and unstable modes, a quasi-steady-state analysis was performed. By

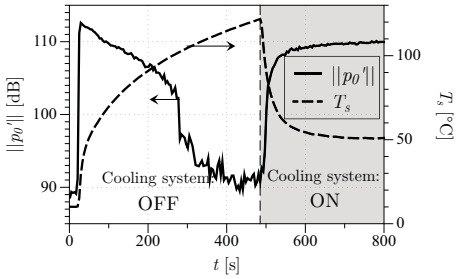

Figure 3: Experimental evidence of the effect of wall temperature on the amplitude of combustion instabilities: acoustic pressure fluctuation and slot temperature versus time. The flame is ignited at $t = 20$ s, without the cooling system, which is turned on at $t = 480$ s.

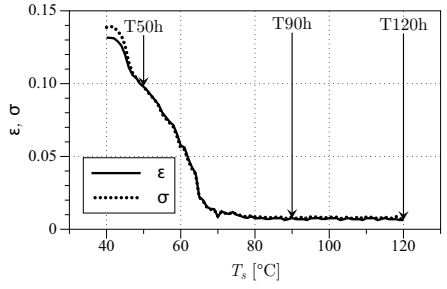

Figure 4: Influence of slot temperature, T_s on the magnitude of velocity and heat release rate fluctuations, ϵ and σ, respectively. Steady-state test where T_s is controlled via the cooling-water temperature, T_w.

varying the cooling-water temperature and waiting for a steady state, one can determine the amplitude of the instability versus slot temperature. The relative velocity fluctuation, $\varepsilon = v_1'^{rms}/\bar{v}$, and heat release rate fluctuation, $\sigma = I'^{rms}/\bar{I}$, are presented in Fig. 4 versus T_s. With maximum cooling, corresponding to $T_s = 48$ °C, ε and σ reach as much as 10 %. For $T_s = 60$ °C the fluctuation levels are down to 5 % and lower than 1 % past $T_s = 70$ °C. The instability is shut down by increasing the wall temperature by less than 20 °C, showing how sensitive flames are to heat transfer.

4. Low-order Model

Because the instability described in Sec. 3 is locked on the Helmholtz mode of the burner, one can derive an analytical model as described in [10]. For harmonic perturbations, $v_1' = \|v_1'\|e^{-i\omega t}$, Eq. 6 in [10] reduces to an equation for the pulsation ω:

$$\left[1 + Cne^{i\omega\tau}\right]\omega^2 + 2i\delta\omega - \omega_0^2 = 0 \tag{1}$$

where ω_0 is the Helmholtz mode pulsation and δ the damping coefficient, both under non-reacting conditions. The relative response of the flame to acoustic velocity perturbations is modeled by an interaction index, n, and a time delay, τ. Note that n and τ are not necessarily constants: they measure the amplitude and phase of the flame transfer function $\mathcal{F}$ (*cf.* Eq. 5). The factor C is derived from combustion-noise theory [14] and depends on the burner geometry and the operating conditions through

$$C = \frac{A_s}{4\pi h_e}\frac{E-1}{r} \tag{2}$$

where A_s is the slot outlet area, $h_e = h_s + e$ the effective height of the slot (e is an end-correction for acoustic waves) and E is the ratio of the fresh to the burnt-gases density. The distance, r, between the noise source and the burner outlet is difficult to evaluate. Here, we define the source as the location where the flame pinches [13]. The numerical values used to compute C are recalled in Tab. 1.

With the assumption that the pulsation, ω, is close to the Helmholtz mode, ω_0, of the burner, Eq. 1 can be simplified as:

$$[1 + Cn\ \cos(\omega_0\tau)]\,\omega^2 + i\omega\,[2\delta + Cn\,\omega_0\sin(\omega_0\tau)] - \omega_0^2 = 0 \tag{3}$$

which is a second-order polynomial equation. The combustion is unstable if the imaginary part of ω is negative, which according to Eq. 3, is equivalent to

$$n\ \sin(\omega_0\tau) < -\frac{2\delta}{\omega_0 C} \tag{4}$$

Equation 4 is a linear stability criterion, which indicates that in the presence of dissipation (*i.e.* $\delta \neq 0$), the occurrence of a combustion instability depends on both the phase-lag, $\omega_0\tau$, and the magnitude, n, of the flame response.

The resolution of Eq. 1 requires the determination of four parameters:

1. ω_0 and δ, which are related to the acoustic properties of the burner.
2. n and τ, which account for the flame response.

These parameters are evaluated experimentally in Sec. 5 in order to predict the stability map of the apparatus with respect to the slot temperature, T_s.

5. Experimental Results

5.1. Burner Acoustics

The determination of $\omega_0 = f_0/2\pi$ and δ is conducted under non-reacting conditions with a bulk velocity of air in the slot $\bar{v} = 1.6$ m/s. Two methods are considered:

1. **Impulse response (IR)**: a short impulse is delivered by the loudspeaker at the bottom of the plenum and the velocity signal is recorded with the hot wire. The response of the system is presented in Fig. 5. An optimal fit with the analytical solution of Eq. 1 (taking $n = 0$) yields the values of f_0 and δ, given in Tab. 2.
2. **Two-microphone method (2M)**: the signal of microphones M_0 and M_1 are simultaneously recorded while a harmonic perturbation is applied via a loudspeaker, outside of the burner. The ratio of the power spectral densities (PSD) is presented in Fig. 6 versus the excitation frequency: the maximum corresponds to the value of f_0 and the half-maximum width to δ/π. The corresponding values are also reported in Tab. 2.

The two methods give exactly the same value for the Helmholtz frequency but not for the dissipation. This experimental difficulty is known to be one of the weakest points of the prediction of combustion instabilities. For the validation of Sec. 5.3 an intermediate value between the IR and 2M methods is used for the dissipation. A discussion on the sensitivity of the stability map to uncertainties in model parameters is beyond the scope of this paper.

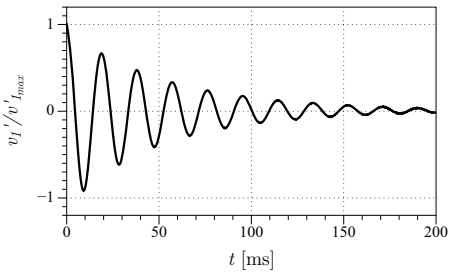

Figure 5: Impulse response of the system under non-reacting conditions with a bulk velocity $\bar{v} = 1.6$ ms^{-1}. Hot-wire probe normalized velocity fluctuation signal $v_1'/v_{1_{max}}'$.

Under non-reacting conditions, the slot temperature is controlled by flowing hot water in the 'cooling' passages (*cf.* Fig. 2). Consequently, values of T_s larger than 100 °C could not be reached. Nevertheless, both acoustic characteristics of the burner proved to be independent of the slot temperature.

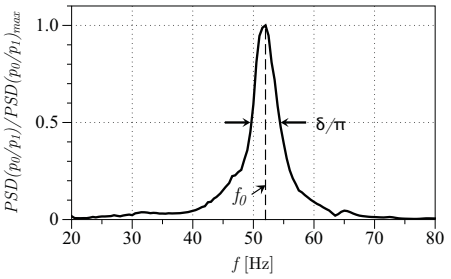

Figure 6: Two-microphone method for the determination of the acoustic parameters ω_0 and δ under non-reacting conditions. Ratio of the power spectral densities of microphones M_0 and M_1.

5.2. Flame Transfer Function

The response of the flame to acoustic perturbations is represented by a Flame Transfer Function (FTF), which is the ratio of the relative heat release rate perturbations, $\dot{q}'/\bar{\dot{q}}$, to the upstream velocity fluctuations, $v'/\bar{v}$. For linear-stability analysis, the FTF is a function of a single variable: the pulsation ω. In order to predict limit-cycle amplitudes and more complex phenomena, the dependance to the amplitude of the velocity fluctuation may be added, resulting in a so-called Flame Describing Function (FDF) [15, 16, 11, 17, 18]. Here, we explore how the FTF may depend on the slot temperature:

$$\mathcal{F}(\omega, T_s) = \frac{\dot{q}'/\bar{\dot{q}}}{v'/\bar{v}} = ne^{i\varphi} \tag{5}$$

where $\varphi = \omega\tau$ is the phase difference associated with the time delay of the flame.

Measuring the complex number $\mathcal{F}(\omega, T_s)$, requires a stable configuration that can be pulsated. For this purpose, it is sufficient to increase the height of the slot to $h_s = 150$ mm. Indeed, the resulting decrease in the Helmholtz frequency brings this configuration back to an unconditionally stable region. The forcing signal is generated by a 130 mm loudspeaker, fitted at the bottom of the plenum. The explored frequency range is $[10, 300]$ Hz. Heat release rate and velocity fluctuations are recorded simultaneously by the photomultiplier (PM) and the hot-wire probe (HW) represented in Fig. 1, respectively. The level of rms velocity fluctuation is kept constant at $\varepsilon = 10$ % of the bulk velocity for all frequencies, which corresponds to the value observed in the self-sustained oscillation test when the slot is cold (*cf.* Fig. 4). The bulk velocity and equivalence ratio are $\bar{v} = 1.6$ m/s and $\Phi = 0.95$, respectively. The cooling system allows to control the wall temperature in the range $T_s = 40$ to 150 °C. Three relevant temperatures were chosen to measure the FTF: $T_s = 50$, 90 and 120 °C. These operating conditions are labeled T50h, T90h and T120h, respectively.

The amplitude and phase of the FTF are presented in Fig. 7. For all slot temperatures, the gain features a characteristic low-pass-filter shape and the phase grows almost lineally with the frequency. However, as T_s is increased, n decreases for frequencies below 100 Hz while it increases past 100 Hz. The potential causes for this peculiar behavior are discussed in Sec. 6.

The phase, φ, is however marginally affected despite a slight

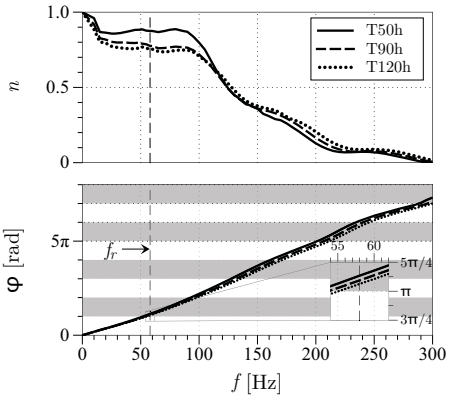

Figure 7: Flame transfer function. Top: gain, bottom: phase, for three wall temperatures T50h, T90h and T120h. Flow velocity and equivalence ratio are $\bar{v} = 1.6$ ms^{-1} and $\Phi = 0.95$ respectively. Velocity fluctuation is keep constant for all frequencies at $\varepsilon = 0.10$.

decrease as T_s increases. This behavior is consistent with previous findings that the phase of the flame response is mostly controlled by the flame height [19, 7]. Indeed, thanks to the dual-channel cooling system (*cf.* Fig. 2), the increase in slot temperature has very little impact on the fresh gases resulting in virtually identical flame height. For cases T90h and T120h, the decrease in flame height relative to case T50h are 0.5 % and 1.7 %, respectively.

The unstable zones corresponding to a case without dissipation (*i.e.* Eq. 4 with $\delta = 0$) are shaded in Fig. 7. At the Helmholtz-mode frequency, the three values of T_s correspond to an unstable condition. However, as reported in Fig. 4, only the case T50h should be unstable. As discussed in Sec. 5.1, the damping δ and Helmholtz pulsation ω_0 are not affected by the slot temperature. Therefore, Eq. 4 hints that the mechanism responsible for the stabilization is the decrease of n when T_s is increased. The underlying mechanisms of this decrease are discussed in Sec. 6.

5.3. Validation of the analytical model

The values of n, τ, and f_0 given in Tab. 2 are used for a numerical resolution of Eq. 1. For the dissipation, we use $\delta = 15$, which is between the IR and 2M values.[1] The solution is the complex-valued pulsation, $\omega = \omega_r + i\,\omega_i$, which is reported in Tab. 3 for the three cases. The low-order model is consistent with the experimental observation (*cf.* Fig. 7) that the flame is unstable for case T50h whereas it is stable for T90h and T120h.

This results shows the ability of low-order models –or more generally acoustic solvers using a FTF to describe the flame response– to account for additional parameters, such as the slot

[1] The stability map is the same with both methods except that with the IR value, case T50h has a lower amplification rate and with the 2M value, case T90h is marginally damped.

temperature. Despite their versatility, these methods still require input parameters, which can only be obtained through experiments or detailed numerical simulations.

6. Flame-root dynamics

In this section we investigate the mechanisms that may be responsible for the modification of the flame response by the slot temperature. Theoretical and experimental studies have shown how the response of conical flames is essentially controlled by the flame aspect ratio [19, 20, 17]. However, in the present configuration, it has been observed that the flame height and shape are marginally affected by changes in T_s, which is due to the limited impact of the slot temperature on the fresh gases temperature (*cf.* Sec. 5.2).

Nevertheless, multiple studies show that flames nearby a solid surface respond differently to acoustic perturbation, depending on the surface temperature [21, 22, 23, 24, 25, 26, 27]. We therefore seek how the flame-root region, which is close to the solid boundary, may alter the flame response. Recent work on conical flames [28] explains how the FTF is the sum of two contributions, one from the flame-root motion and the other one from the interaction of the flame front with a convective perturbation. We propose to explore experimentally how the slot temperature affects the flame-root movement.

6.1. Experimental technique

A high-speed camera (pco.dimax) is used to track the flame root when submitted to an acoustic modulation. The camera is equipped with a Micro-Nikkor $f/2.8$ 105 mm Nikon lens, located at $x = 0$ mm, $y = 10$ mm and $z = 350$ mm. Images zoomed on the flame base of 624-by-928 pixel with a resolution of 70 px/mm were acquired at a sampling frequency of $f_{cam} = 3000$ fps and an exposure time of 0.30 ms, during 2 s. For each pulsating frequency, 6000 images are acquired. A LabVIEW program is used as a signal generator, to drive the loudspeaker at the bottom of the burner and to send a synchronized TTL signal to trigger the camera. Thanks to this synchronization, the images can be phase-averaged with respect to the acoustic modulation. A flame-front detection algorithm is designed to track the flame rood during the harmonic excitation. The flame-root location is chosen as the intersection of the crest of light intensity with the iso-contour at 65 % of the maximum pixel value over the whole image. A typical image is presented in Fig. 8.

6.2. Flame root movement

The phase-averaged location of the flame base is presented in Fig. 9, at the frequency f_r of the instability. The coordinates (x', y') are relative to the location of the flame root without excitation, which means that the influence of T_s on the mean flame-root position has been removed from Fig. 9. For the three values of the burner-rim temperature, the horizontal flame displacement is virtually identical and equal to 0.85 mm. However, the vertical displacement is reduced, at least by a factor 3 when T_s increases form 50 °C to 120 °C. Qualitatively, it means that

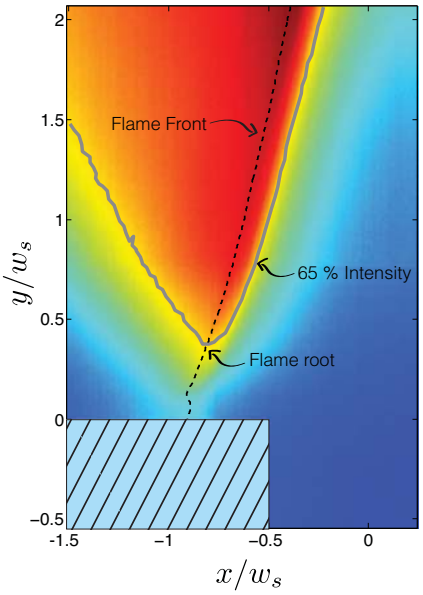

Figure 8: Typical phase-averaged image for the determination of the flame-root location.

for this frequency, when the slot is hot, the flame base is more resilient to acoustic velocity perturbations.

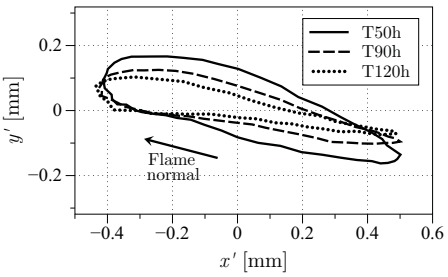

Figure 9: Phase-averaged flame base trajectory, relative to the flame root position without excitation, at the frequency, f_r, of the instability.

Together with the theoretical developments of [28], this behavior of the flame root sheds light on the influence of T_s on the gain of the FTF presented in Fig. 7. The damping of the flame-root movement at f_r, translates into a diminution of the FTF gain.

6.3. Flame root transfer function

The trajectories plotted in Fig. 9 are only representative of one frequency. The experiment is replicated over the frequency range [10, 200] Hz and a flame-root transfer function is devised. In the theoretical developments for the flame response, only the displacement normal to the flame front is relevant. Consequently, the gain and phase of the flame-root displacement

normal to the mean flame angle (based on the slot width and the flame height) are presented in Fig. 10. For all values of T_s, the gain is small at low and high frequencies and presents a single peak between 100 Hz and 120 Hz. The frequency at the peak increases with T_s. The most interesting feature is that while for frequencies below 120 Hz the gain decreases with increasing T_s, the opposite trend is observed past 120 Hz. This feature replicates the trends observed on the FTF in Fig. 7, strongly suggesting that the alteration of the flame-root movement by the burner-rim temperature is the key to the modification of the global flame response.

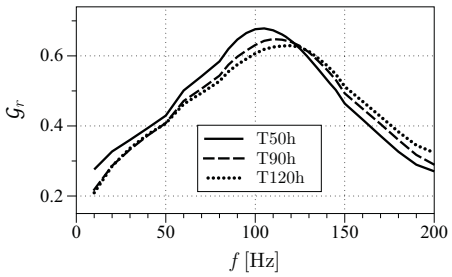

Figure 10: Gain of the flame-root displacement normal to the mean flame position.

7. Conclusion

A laminar premixed flame stabilized on a slot burner has been investigated experimentally, which exhibits a combustion instability dependent on the the temperature of the burner at the flame anchoring point. When the slot is cold, the flame is unstable but as it heats up the instability is damped. Flame Transfer Functions for various burner-rim temperatures were measured showing that the phase of the FTF is marginally affected while its gain is reduced at low frequency and increased at higher frequencies. Together with measurements of acoustic damping in the apparatus, a low-order model that can predict the influence of the burner-rim temperature on the stability was derived. Finally, the influence of temperature on the FTF was attributed to the dynamics of the flame root at the anchoring point and its dynamic interaction with heat transfer in the material.

Acknowledgments

The authors would like to thank Daniel Durox from Ecole Centrale Paris for his insights on flame dynamics.

References

[1] T. Lieuwen, Unsteady Combustor Physics, Cambridge University Press, 2012.
[2] F. E. C. Culick, P. Kuentzmann, Unsteady Motions in Combustion Chambers for Propulsion Systems, NATO Research and Technology Organization, 2006.
[3] L. Boyer, J. Quinard, Combust. Flame 82 (1) (1990) 51–65.
[4] T. Schuller, D. Durox, S. Candel, Combust. Flame 128 (2002) 88–110.
[5] H. Wang, C. Law, T. Lieuwen, Combust. Flame 156 (4) (2009) 889–895.
[6] A. Cuquel, D. Durox, T. Schuller, Theoretical and experimental determination of the flame transfer function of confined premixed conical flames, 7th Mediterranean Combustion Symposium, 2011.
[7] R. S. Blumenthal, P. Subramanian, R. Sujith, W. Polifke, Combust. Flame 160 (7) (2013) 1215–1224.
[8] L. Selle, T. Poinsot, B. Ferret, Combust. Flame 158 (1) (2011) 146–154.
[9] M. Vagelopoulos, F. H. Jonathan, Proc. Combust. Inst. 30 (1) (2005) 241–249.
[10] D. Durox, T. Schuller, S. Candel, Proc. Combust. Inst. 29 (2002) 69–75.
[11] N. Noiray, D. Durox, T. Schuller, S. Candel, J. Fluid Mech. 615 (2008) 139–167.
[12] D. Durox, T. Schuller, N. Noiray, A. Birbaud, S. Candel, Combust. Flame 155 (3) (2008) 416–429.
[13] T. Schuller, D. Durox, S. Candel, Combust. Flame 135 (2003) 525–537.
[14] P. Clavin, E. D. Siggia, Combust. Sci. Tech. 78 (1991) 147–155.
[15] A. P. Dowling, J. Fluid Mech. 346 (1997) 271–290.
[16] T. Lieuwen, S. Preetham, AIAA Paper (2004) 1–16.
[17] V. Kornilov, R. Rook, P. D. Goey, Proc. Combust. Inst. 1 (3) (2009) 1–6.
[18] F. Boudy, D. Durox, T. Schuller, S. Candel, Proc. Combust. Inst. 33 (2011) 1121–1128.
[19] T. Schuller, D. Durox, S. Candel, Combust. Flame 134 (2003) 21–34.
[20] V. Kornilov, K. Schreel, L. de Goey, Proc. Combust. Inst. 31 (2007) 1239–1246.
[21] M. Fleifil, Combust. Flame 106 (4) (1996) 487–510.
[22] K. Schreel, R. Rook, L. de Goey, Proc. Combust. Inst. 29 (2002) 115–122.
[23] R. Rook, L. D. Goey, L. Somers, K. Schreel, R. Parchen, Combust. Theory and Modelling (2002) 37–41.
[24] R. Rook, L. de Goey, Combust. Flame 133 (1-2) (2003) 119–132.
[25] H. Altay, S. Park, D. Wu, D. Wee, A. Annaswamy, A. Ghoniem, Proc. Combust. Inst. 32 (1) (2009) 1359–1366.
[26] K. Kedia, H. Altay, A. Ghoniem, Proc. Combust. Inst. 33 (2011) 1113–1120.
[27] L. de Goey, J. van Oijen, V. Kornilov, J. ten Thije Boonkkamp, Proc. Combust. Inst. 33 (2011) 863–886.
[28] A. Cuquel, D. Durox, T. Schuller, Comptes Rendus Mécanique 341 (2013) 171–180.

Tables

A_s [m^2]	e [m]	E [1]	r [m]	C [1]
10^{-3}	10^{-2}	7.07	0.022	0.274

Table 1: Numerical values for the evaluation of the combustion-noise parameter C (Eq. 2).

			T_s [°C]		
			50	90	120
Acoustics	f_0 [Hz]	IR	52		
		2M	52		
	δ [s^{-1}]	IR	16.9		
		2M	15.7		
FTF	n		0.87	0.77	0.75
	φ		3.56	3.43	3.33

Table 2: Experimental values for the resolution of Eq. 1. Acoustic parameters, ω_0 and δ are determined under non-reacting conditions, either with the impulse-response (IR) or the two-microphone (2M) methodologies.

Case	ω_r [rad/s]	ω_i [rad/s]	Experiment
T50h	369	2.45	Instable
T90h	366	-6.27	Stable
T120h	365	-11.22	Stable

Table 3: Numerical determination of $\omega = \omega_r + i\,\omega_i$ from Eq. 1 for three values of the slot temperature T_s. The experimental observation of the stability is inferred from Fig. 4.

List of Figures